Design and Synthesis of Fluorinated Porous Molecular Crystals

---

A Dissertation Presented to

the Faculty of the Department of Chemistry

University of Houston

In Partial Fulfillment

of the Requirements for the Degree

Doctor of Philosophy

By

Mohamed Hashim

December 2018

Design and Synthesis of Fluorinated Porous Molecular Crystals

_____

Mohamed Hashim

_____

Dr. Ognjen Š. Miljanić, Chairman

_____

Dr. Olafs Daugulis

_____

Dr. Judy I-Chia Wu

_____

Dr. P. Shiv Halasyamani

_____

Dr. Jeffrey Rimer

_____

Dean, College of Natural Sciences and Mathematics

ACKNOWLEDGMENTS

My PhD journey began back in August 2013 and I was extremely fortunate to have joined the Miljanić group. In this group I found an advisor and mentor who was extremely supportive and encouraging along with group members whom I consider to be like an extended family. I have met people from many different walks of life that have interacted with me and enabled me to grow into a better scientist and person. I am extremely grateful for the conversation, guidance, encouragement, and friendship provided to me by these mentors and colleagues.

First, I would like to express my deepest gratitude and appreciation to my advisor Dr. Ognjen Š. Miljanić for accepting me into his group. He has encouraged and pushed me to work harder. I appreciate his mentorship approach which gave me the freedom to work on the projects I desired and his patience with my numerous failures. The time spent under his tutelage has allowed me to work with different instruments and develop critical thinking skills that will help me in the lab as well as in the real world. I cannot even find the words to express my sincere appreciation to my advisor.

I would like to thank my colleagues from the Miljanić group: Dr. Teng-Hao Chen, Dr. Musabbir Saeed, Dr. Ljubodrag Vujisić, Dr. Merry Smith, Dr. Rio Carlo Lirag, Dr. Qing Ji, Dr. Ha Le, Dr. Chia-Wei Hsu, Nadia El-Hamdi, Maymounah Alrayyani, Cotton Starr, Corie McHale, Andrew Eisterhold, Zhenglin Zhang, Thamon Puangsamlee, and Sumitra Karki for their numerous conversations, questions and help. I also want to thank Dr. Ilya Popov, Dr. Maria Marquez, Dr. Mike Adams, Po-An Chen, Krit Setthakarn,

Parastou Mehrani, Daniela Rodriguez, and numerous other friends and faculty in the department. They have provided me with help, fun, and entertainment inside and outside of the research lab.

I am extremely grateful to Dr. James Korp and Dr. Xiqu Wang for their help with crystal analysis and solving crystal structures. I apologize for always bothering them with single crystal questions and issues. I am thankful for their patience and detailed explanations. In addition, I would like to thank Dr. Charles Anderson and Dr. Scott Smith for teaching about the NMR and trusting me with so called "keys" to the NMR facility when they were on vacation. I would also like to thank Dr. Jeffrey Rimer's group for allowing me to use the ASAP 2020 for porosity and surface area measurements.

I also want to express my sincere gratitude to my parents, Isameldin and Ibtisam, for their love, support, and allowing me to act on my ambitions. This accomplishment would not have been possible without you.

Finally, I would like to acknowledge my committee members Dr. Olafs Daugulis, Dr. Judy I-Chia Wu, Dr. P. Shiv Halasyamani, and Dr. Jeffrey Rimer for their respective comments and suggestions.

Financial support for this research was provided by the National Science Foundation and Robert A. Welch Foundation and both of these foundations are very much appreciated.

Design and Synthesis of Fluorinated Porous Molecular Crystals

---

An Abstract of a Dissertation

Presented to

the Faculty of the Department of Chemistry

University of Houston

In Partial Fulfillment

of the Requirements for the Degree

Doctor of Philosophy

By

Mohamed Hashim

December 2018

ABSTRACT

Porous molecular crystals are an emerging class of porous materials that are built from discrete molecules rather than being polymeric in nature. In this thesis, the effects of the molecular structure of the precursors on the formation of porous solid-state structures were examined. One of the trigonal fluorinated porous molecular crystals displayed aggregation-induced emission and this discovery was studied in more detail.

Chapter One, summarizes the research literature that discusses the work and applications conducted on crystalline porous materials. The porous materials that are discussed herein are metal-organic frameworks, covalent organic frameworks, and porous organic molecular crystals that are held together by non-covalent interactions.

Chapter Two, discusses the synthetic strategies and methodology utilized in the preparation of six novel fluorinated porous molecular crystal precursors of different geometries. The insights and lessons learned from the successful and failed synthetic attempts are also discussed.

Chapter Three**,** describes the solvothermal synthesis and characterizations of molecular crystals. The gas sorption isotherms and hydrophobic properties of the porous variants are also discussed.

Chapter Four, describes the investigations of the fluorescent properties of fluorinated trispyrazole compounds that make up porous molecuclar crystal frameworks. It was found that in a DMF/H_2O mixed solvent system one of the compounds displays

aggregation-induced emission (AIE), while its iso-structural counterpart does not. The reason for this difference was investigated. Further research conducted on the AIE active compound also led to the discovery that it can discriminate between dicarboxylic acids through assembly induced emissions.

In summary, this study the grometry and dimensions of the precursors was varied, resulting in six crystallographically characterized derivatives. Among these derviatives two were found to be porous and posessed surface areas of 903 $m^2 g^{-1}$ and 1821 $m^2 g^{-1}$. It was also revealed that the rigid trigonal geometry plays a key role in the design and prepararation porous molecular crystals.

TABLE OF CONTENTS

*Note: Chapter 1 contains compounds labeled **1** through **36**. A separate numbering system is used for Chapters 2–4. The compounds are numbered **1** through **45**.*

ABBREVIATIONS AND ACRONYMS

1D	one-dimensional
2D	two-dimensional
3D	three-dimensional
ATR	attenuated total reflection
BDC	1,4-benzenedicarboxylate (terephthalate)
BET	Brunauer-Emmett-Teller
BOC	*tert*-butyloxycarbonyl
BTC	benzene-1,3,5-tricarboxylic acid
Bu	butyl
CH_2Cl_2	dichloromethane
CIF	crystallographic information files
CFC	chlorofluorocarbon
CMP	conjugated macroporous polymers
COF	covalent organic framework
CuCl	copper(I) chloride
DCC	dynamic covalent chemistry

DMA	*N,N*-dimethylacetamide
DMF	*N,N*-dimethylformamide
DMSO	dimethyl sulfoxide
DNA	deoxyribonucleic acid
Et_3N	triethylamine
Et_2O	ether
EtOAc	ethyl acetate
EtOH	ethanol
FT-IR	Fourier-transform
Hex	hexane
HCP	hypercrosslinked polymers
HOF	hydrogen-bonded organic framework
IR	infrared
Me	methyl
MeOH	methanol
MOF	metal-organic framework
MOFF	fluorinated metal-organic framework
NMR	nuclear magnetic resonance

PCP	porous coordination polymers
$Pd(Ph_3)_4$	Tetrakis(triphenylphosphine)palladium(0)
PIFA	Phenyliodine bis(trifluoroacetate)
PIM	polymers of intrinsic microporosity
SBU	secondary building unit
SOF	supramolecular organic framework
t-BuOK	potassium *tert*-butyl
THF	tetrahydrofuran
TLC	thin layer chromatography
UV	ultraviolet

Chapter One

Crystalline Porous Materials

1.1 Introduction

Porous materials can be defined as materials possessing voids within their structures that are large enough to house guest molecules.[1] Such materials can be categorized according to their respective pore diameters as microporous (<2 nm), mesoporous (2–50 nm), and macroporous (>50 nm).[2] Of the three categories, the microporous class of materials are of the most importance as they have been extensively studied and applied industrially in the fields of catalysis, separation, filtration, and ion-exchange processes.[3,4,5] This class of materials has generated so much attention due to their uniform porosities, large surface areas, high adsorption capacities for various gases, as well as their size- and shape- selectivity that can be altered in order to cater to specific molecules.

Research in the field of crystalline porous materials began with an emphasis on inorganic compounds, mainly zeolite—microporous frameworks. Zeolites are still widely used in the petrochemical industry as catalysts.[1,5] The name zeolite was first coined by Cronstedt in 1756 [6] and it means "boiling stone," based on the observation that upon heating a natural zeolite, large amounts of steam were released.[1] The adsorption properties of natural zeolites have been extensively studied. In the late-1940s research into their synthesis, along with the characterization of various natural and artificial zeolites, led to the further development of this field.[1,6] As this field began to generate more interest, the focus began to shift from purely inorganic materials to the

incorporation of organic molecules resulting in hybrid metal organic frameworks (MOFs)[7,8,9] and all the way to the development of entirely organic frameworks such as covalent organic frameworks (COFs)[10,11] and porous molecular crystals (PMCs).[12,13,14] This shift resulted in easier solution-phase characterization as well as the introduction of hydrophilic or hydrophobic character within the pores. This caused the research into development of new porous materials to become one of the most active areas in materials chemistry. This chapter will briefly introduce the three kinds of porous materials mentioned above, setting the stage for the subsequent chapters, which explore the synthesis, characterization, and applications of PMCs.

1.2 Metal-Organic Frameworks (MOFs)

1.2.1 Brief History of MOFs

Metal organic frameworks (MOFs) consist of metal clusters coordinated with organic linker molecules into an "infinite" one-, two-, or three-dimensional framework. MOFs represent a class of coordination compounds and thus it seems appropriate to briefly discuss the history of coordination chemistry in this section as well. Coordination compounds have been used since ancient times in the form of pigments such as Prussian blue ($Fe_7(CN)_{18}$) and ochre (iron oxide earth based pigments). However, the chemical structure of these compounds remained unclear until 1893 when Alfred Werner published the most accepted version of the coordination theory.[15] His research into the structure of coordination compounds resulted in him being awarded the 1913 Nobel Prize in chemistry. The chemical composition of such compounds at that time could be established by existing analytical methods, but their chemical configuration was puzzling.

The major problem was that these transition metal compounds had higher valences than necessary. Werner postulated that metal ions have two different kinds of valence:

1. a primary valence which is essentially an oxidation number that matches the positive charge on the metal ion.

2. a secondary valence that characterizes the coordination number or the total number of ligands bound to the metal ion.

He also made the distinction between charged and neutral ligands, and proposed the octahedral configuration of transition metal complexes. Due to his great contribution to this field and that most of his work was with metal-amines these are commonly referred to as Werner complexes.

The first coordination network to be synthesized was the Hofmann complex, discovered in 1897 by Hofmann and Küspert.[16] The original complex was formed by the addition of benzene to a solution of nickel cyanide in aqueous ammonia, resulting in a nickel amine complex. The structure of this complex could not be determined at that time but it was found that the benzene molecule was firmly retained within and could only be partially removed after repeated washing with ether as well as evolved by heating the compound to 120 °C.[16,17] Over the years there were speculations about the structure of this complex by Pfeiffer[18] and Feigel[19] which assumed that the benzene molecule was coordinated to the nickel complex. It was not until 1952 when the structure of this complex was determined by x-ray analysis conducted by Rayner and Powell.[17] They reported that the unit cell dimensions of the crystal were $a = b$ =7.242 Å, c = 8.277 Å and that $\alpha = \beta = \gamma = 90$ º. The crystal structure was a square $P4/m$ network that was bridged

by CN groups with an encapsulated benzene molecule within the channel as depicted in Figure 1.1.

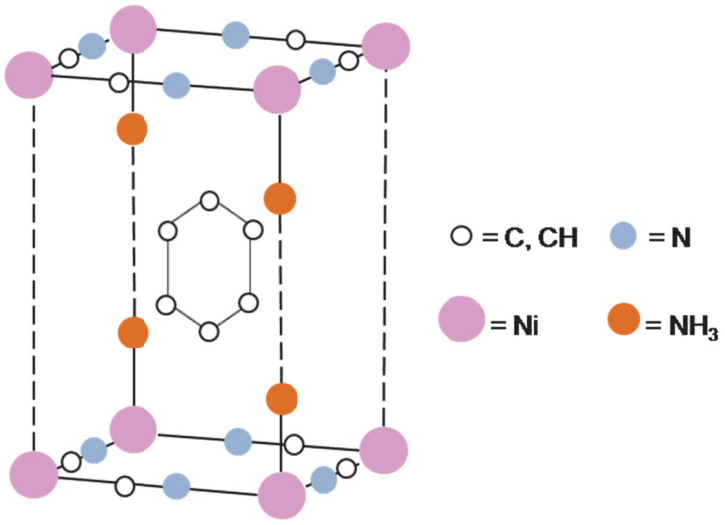

Figure 1.1 A partial crystal structure of the Hofmann complex showing benzene molecule encapsulated within the channel.[17]

Afterwards, in 1967, Hawthorne et al. replaced the ammonia ligand with an *n*-alkylamine[20] and this opened the door for Iwamoto et al. to further develop variations of these complexes by the incorporation of an ethylene diamine linker into these networks. This ethylene diamine unit functioned as a linker that connected different $M(CN)_2$ layers together allowing for the encapsulation of different aromatic guests such as benzene, aniline, thiophene, or pyrrole.[21,22] In 1977, Mathey et al. took it a step further and showed that varying the length of the diamine linker allows for the specific encapsulation of aromatic guest molecules and solvents.[23] These are early examples of the effect of linker length and design on the selective encapsulation of guest molecules within the pores of complexes and thus laying the groundwork for the modular design of MOFs.

The term MOF was invented in 1995 by Yaghi, and it initially refered to an extended crystalline framework that was composed of Cu(I) and 4,4'-bipyryidine.[24] Prior to that, similar compounds were called porous coordination polymers (PCPs).[25] Throughout this time numerous PCPs that displayed porosity in the solution phase were synthesized but it was not until 1998 when Yaghi et al. reported the adsorption isotherms of MOF-2 establishing that it demonstrated permanent microporosity.[26] They utilized a $Zn_2(–COO)_4(H_2O)_2$ cluster that was connected with a 1,4-benzendicarboxylate (BDC) linker to form an extended structure resulting in MOF-2 (Figure 1.2). Gas sorption studies indicated that this MOF displayed a type I isotherm and a Langmuir surface area between 270 and 310 $m^2\ g^{-1}$. This discovery launched a new era in the direction of MOF research with an emphasis on permanent porosity.

The following year, two key MOFs with even higher surface areas were reported in the literature. The first was HKUST-1, which was a framework composed of Cu nodes connected with benzene-1,3,5-tricarboxylic acid (BTC) struts between the nodes, displaying a Brunauer–Emmett–Teller (BET) surface area of 692 $m^2\ g^{-1}$ and a Langmuir surface area of 918 $m^2\ g^{-1}$, which were comparable to the surface areas of zeolites.[27] The second was MOF-5, which was a framework constructed from Zn nodes attached to BDC linkers resulting in a porous framework with a reported Langmuir surface area of 2900 $m^2\ g^{-1}$ which was even higher than the surface area for most zeolites.[28] These two MOFs set the standard for this field, and throughout the course of the years, numerous MOFs have been synthesized with an emphasis on increasing their respective surface area (Table 1.1). This was done by the synthesis of new MOF structures as well as revisiting

previous MOF structures and activating the porous frameworks under milder conditions thus minimizing the collapse of pores upon solvent removal.

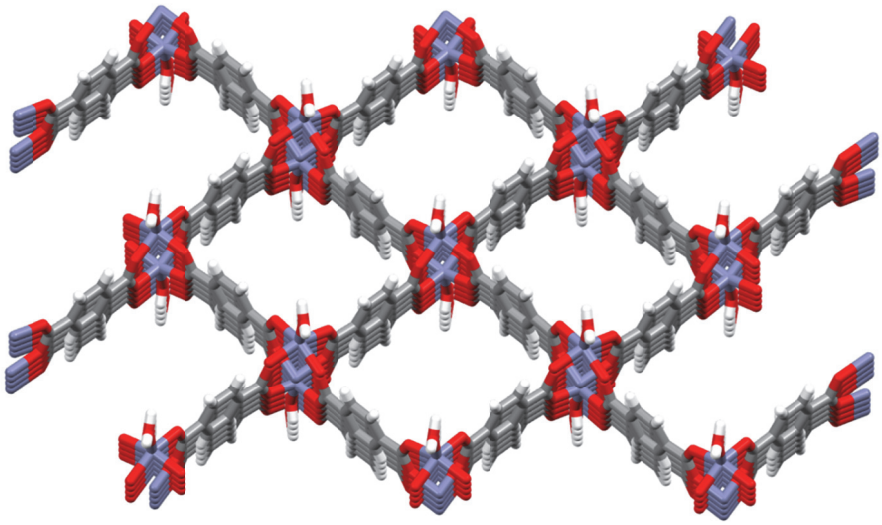

Figure 1.2 A graphical representation of MOF-2 displaying the large rectangular pores along the crystallographic a-axis. Element colors: C—gray, H—white, O—red, Zn—purple.[26]

Material Name	**BET Surface Area (m^2 g^{-1})**
Zeolite Y	970
Activated Carbons	2040
MFU-4 L	2750
NOTT-102	2940
PCN61	3000
$Cu_{24}(TPBTM)_8(H_2O)_{24}$	3160
SNU-77	3670
NOTT-112	3800
MOF-5	3800
UMCM-1-NH_2	3920
PCN-66	4000
$Be_{12}(OH)_{12}(BTB)_{24}$	4030

UMCM-1	4160
MIL-101c	4230
Bio-MOF-100	4300
MOF205	4460
MOF-177	4750
DUT-23-Co	4850
NOTT-116	4660
PCN-68	5110
UMCM-2	5200
NU-100	6140
MOF-210	6240
NU-109E	7010
Nu-110E	7140
Highest Predicted Surface Area Value of MOFs	14600

Table 1.1 BET Surface area of highly porous MOFs and other porous materials. Data collected from references 29, 30, and 31.

1.2.2 MOF Synthesis

The conventional method utilized for the synthesis of MOFs involves the heating of a solution of an organic linker and a metal salt in a high-boiling solvent without stirring or agitation. After a certain point, the MOFs usually precipitate out of solution and are of sufficiently high crystallinity most of the time, allowing for analysis by X-ray crystallography. This approach seems quite straightforward but there are many synthetic factors that can influence the formation of the desired crystal structure of MOFs. Such factors include the molar ratio of starting materials, nature of the solvent, pH of the

solution along with temperature, pressure reaction rate and cooling time. All of these can influence the morphology and overall structure of a MOF. One of the most challenging tasks for using MOFs in an industrial setting is maintaining their desired properties such as high porosity, thermal and chemical stability, phase uniformity, and crystallinity while scaling up the reactions. This may result in altering the conventional synthetic methods used in the laboratory. The fundamental difference stems from the approach used by each to tackle the problem.

The conventional method of MOF synthesis takes place in a solvent at varying temperatures depending on the procedure the energy that is introduced to this reaction is heat via a hot plate or oven. However, energy can also be introduced to this chemical reaction by other means such as electric potential, microwave radiation, sonochemical radiation or mechanochemically.[32] Each of these methods will be discussed below.

1. The potential from an electrochemical cell presents a method for the rapid synthesis of MOFs under mild conditions. This process does not require metal salts as the metal ions are continuously introduced to the reaction mixture via anodic dissolution.[33] The solvent can also be recycled without prior treatment in this process due to the absence of anion/counter ion salts making this approach quite green and appealing for scale up in an industrial setting. This method has been utilized by BASF to synthesize MOFs as early as 2005.[34]

2. The microwave irradiation has been utilized by organic synthetic chemists since at least 1986.[35] The application of a suitable frequency results in the increase of

collisions between molecules in an electric field thereby resulting in an energy-efficient form of heating. These reactions can be carried out at temperatures up to 100 ºC above the boiling point of the solvent and with reaction times under an hour. Also providing the chemist with the option of utilizing more environmentally friendly solvents as the boiling point is no longer a variable for solvent selection. For example, Vivani et al. utilized microwave irradiation to optimize and scale up the synthesis of UiO-66.[36]

3. Sonochemistry involves the use of ultrasonic radiation to cause a chemical or physical change to take place. The ultrasonic frequencies do not add vibrational energy through the chemical bonds but instead the change arises from a phenomenon called acoustic cavitation. This involves the formation, growth and instantaneous collapse of bubbles within the solvent,[37] thereby resulting in a buildup of energy within the bubble and the creation of regions of high temperature and pressure with short lifetimes. These methods can generate homogenous nucleation centers and result in a dramatic decrease in MOF preparation time. This can be seen in the work of Ahn et al.,[38] in a sonochemical synthesis of MOF-5 crystals that were prepared in 30 mins (compared to the 24 h it took via conventional methods). Nair et al. also prepared a MOF using sonochemical methods.[39] This method shows promise as it can lead to the rapid scale up of MOFs but this method requires much exploration as it is quite underutilized in the current literature.

4. Mechanochemistry can be defined as a branch of chemistry by which chemical reactions take place in the solid state due to the application of mechanical energy. The ball milling method is the most widely used process to apply mechanical energy in order to achieve a chemical transformation.[40,41] This is the most environmentally friendly synthetic method mentioned, as it avoids the use of bulk solvents. It also possesses the added benefit of avoiding all the limitation of solvent chemistry such as solubility, solvent complexation, and solvolysis. The ball milling methodology has also shown that it can undergo the same molecular assembly phenomena shown in solution via liquid-assisted grinding. Moreover, in some cases metal salts can be replaced with metal oxides as a starting material, resulting in the formation of water as the only side product.[42]

1.2.3 MOF Design and Postsynthetic Modification

The initial discovery of new MOFs has been quite coincidental in the sense that the mixing of metals with organic linkers yielded a novel MOF with interesting properties. But as the years progressed more attention has been given to the development and design of MOF chemistry in the form of reticular synthesis. This represents a design strategy for the assembling of molecular building blocks into an ordered structure of predetermined geometry.[43] This process begins with the assembly of metal ions with multidentate linkers such as carboxylates to form a rigid cluster that locks the metal in place as well as serves as the vertex of the extended framework. This vertex is known as a secondary building block (SBU).

The SBUs are then connected by organic linkers to form the MOF as depicted in Figure 1.3. This strategy works quite well as different SBUs have yielded a select number of preferred topologies that can be targeted. Then based on the size and geometry of the organic linker used, one can manipulate the pore size and properties of the framework. Based on this, one can understand that reticular synthesis has played a central role in the development of frameworks with permanent porosity. In order to obtain a better appreciation of this role one can compare it to the traditional method of expanding pore size. This involves the uses of longer organic linkers to expand the size of the pores. This in theory works but often yields interpenetrated pores or the collapse of pores during the evacuation of solvent molecules. Both outcomes result in lower than expected porosity.

Meanwhile, the use of SBUs in the framework result in minimal interpenetration as they function as vertices guiding the organic linkers and their rigid nature suppresses the collapse of pores upon solvent evacuation. The only downside to this strategy is that metal ions with high oxidation states (e.g. V^{4+}, Zr^{4+}, and Fe^{3+}) can adopt multiple coordination geometries leading to the formation of complicated SBUs that can result in polycrystalline or amorphous products. Thus in order to avoid this outcome an alternative approach is to treat these metal ions with monotopic ligands leading to the formation of the desired SBU. Once the desired SBU precursor has been obtained it can be subjected to a solution containing the polytopic organic linkers thus replacing the monotopic ones. Finally, bridging the SBUs leads to the formation of the desired MOF.[44]

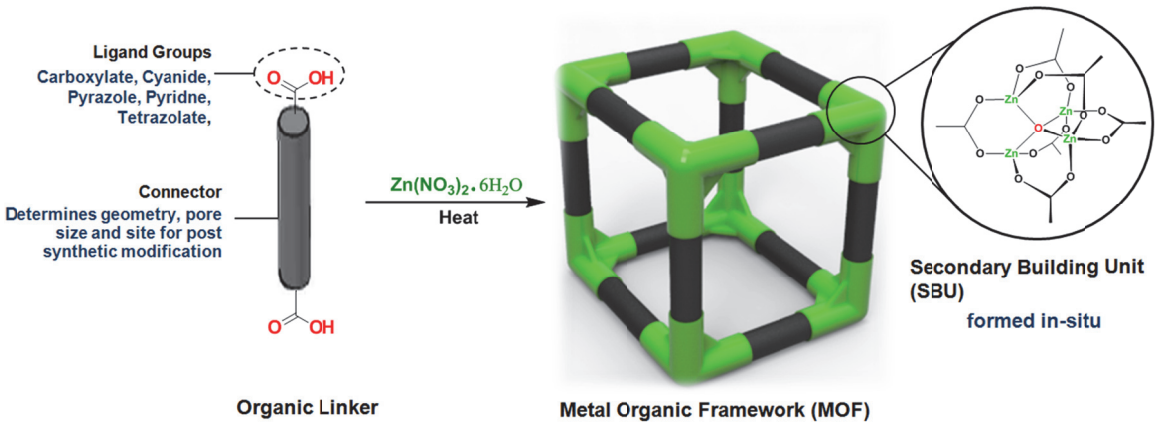

Figure 1.3. A graphical depiction of the conceptual design of a MOF.

Another strategy for the design of MOFs is postsynthetic modification (PSM). This synthetic strategy can be used when it is difficult to obtain a MOF product due to the thermal and/or chemical sensitivity of the organic linkers, as well as high reactivity of reaction materials. This protocol can be broken down into three subgroups which are organic linker modification, metal exchange, and ligand exchange. In order to modify the organic linker it should bear two sets of functional groups: one with purpose of binding to the metal thereby creating a MOF, and the other will engage in a secondary reaction once the MOF is already formed. For example Telfer et al.[45] used the thermolysis of –NHBoc (Boc = *tert*-butyloxycarbonyl) groups within a low-porosity MOF to remove the Boc protecting group, in turn increasing the empty space within the framework. This spatial protecting group approach (Figure 1.4) can be used to synthesize non-interpenetrated versions of MOFs for which the direct synthesis resulted in an interpenetrated framework. This methodology can also allow for the introduction of new functional groups to the linker as well via known chemical reactions to the linker such as acetylation, alkylation, and metathesis.

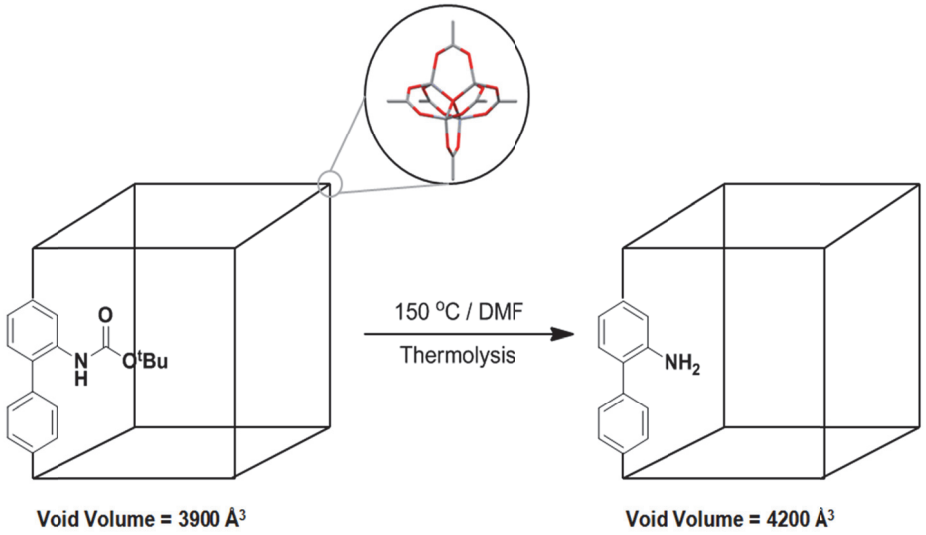

Figure 1.4 Postsynthetic Modification via thermolysis of a Zn_4O-based MOF.[45]

PSM can also be utilized to exchange the metal ion within the SBU of MOFs by taking advantage of the kinetically labile nature of metal–ligand coordination bonds. This is done by soaking the MOF crystal in a solution of the new metal as shown by Dincă et al. during the preparation of a metastable cobalt variant of MOF-5 (Scheme 1.1).[46] Cation exchange within SBUs was reviewed by Dincă et al.[47] This emerging protocol has been utilized to alter metal compositions of zeolites and nanocrystals and has been known to geochemists and mineralogists for some time. The appeal of this protocol is that it offers milder conditions to access MOFs that may not be accessible via direct synthesis, or which require harsh conditions to synthesize. There is also the added benefit that the topology of the original framework remains unaltered. The same strategy can also be utilized to exchange the ligands within a MOF framework. This was demonstrated by Rosi et al.,[48] displaying the in situ ligand exchange of bio-MOF-100 with longer linkers that resulted in larger pore sizes and an increase in the surface are of these new MOFs.

Hence it can be seen that PSM is a powerful protocol that offers an alternative path for the introduction of desired functionalities to MOFs as well as increasing MOF variability.

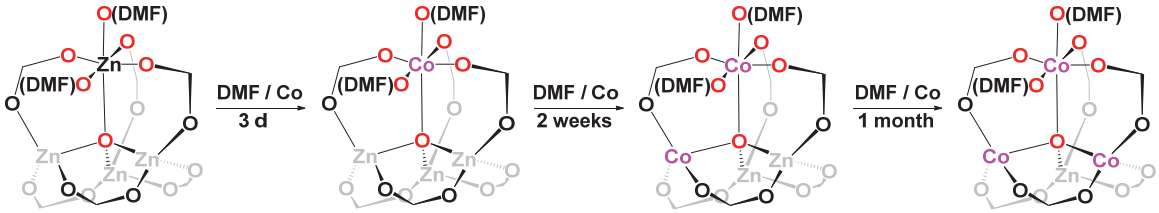

Scheme 1.1 Postsynthetic modification via metal exchange of the Zn_4O cluster of MOF-5 with cobalt.[46]

1.2.4 Applications of MOFs

Since the discovery of the permanent porosity of MOFs in 1998, the scientific literature has been filled with potential applications to utilize these highly porous materials. These applications include gas storage and separation,[49] sensing,[50] catalysis,[51] and drug delivery.[52] In this section a few of these applications will be highlighted as well as the emerging industrial applications.

The most widely explored application for MOFs is gas storage. In this section there will be an emphasis on hydrogen and methane gas storage due to their potential use as alternative energy sources. Hydrogen has a very high energy output and is quite green as its combustion product is only water. But the disadvantages of this fuel source exist in its difficulty to store and transport in large quantities. Initial reports indicated high storage capacities of hydrogen in MOFs at room temperature and this produced great interest, but the lack of reproducibility shifted the focus towards cryogenic storage.[53] Research into the cryogenic storage of hydrogen has been conducted with a variety of different MOFs. It was MOF-210 which displayed a reversible uptake of 8.0 wt %

hydrogen at 77 K.[54] This is still far from the Department of Energy (DoE) desired goals for an energy storage system. There has also been a trend in MOF research to increase the surface area of these materials (refer to Table 1.1); with the logic being that this increase will result in higher uptake of guest molecules. But this is not always true, as in the case of UMC-2, whose hydrogen uptake is actually 7 wt% at 77 K even though it possesses a larger surface area than MOF-5.[55] This means that factors other than surface area should be taken into consideration such as pore dimensions (i.e. size, shape, and volume), the metal in use, as well as other properties that are yet to be determined. Thus, there remain opportunities to increase the hydrogen storage capacities of MOFs.

The second target gas is methane, which is currently in use as an energy source in compressed natural gas vehicles. The combustion of methane with oxygen from the air releases water and carbon dioxide as products. It is not as green as hydrogen due to the release of carbon dioxide, but the amount of carbon dioxide released is lower when compared to other hydrocarbon fuel sources. Methane is also safer to use when compared hydrogen, due to it not being as flammable, consequently being safer to store and transport. There have been many MOFs utilized to uptake methane at 298 K and 65 bar with the record holder being HKUST-1.[56,57,58] In the original methane uptake study conducted by Yildirim et al.,[57] they utilized the theoretical crystal density of HKUST-1 to determine that it was capable of maximum uptake of 270 cm^3(STP)/ cm^3. But the experimental results indicated that the maximum was 189 cm^3(STP)/ cm^3 and it was hypothesized that this was due to the mechanical internal collapse of the pores. In order to circumvent this issue, Fairen-Jimenez et al.[58] prepared a sol-gel variant of HKUST-1. This modification was done by taking a mother solution of the metal and organic linkers

in ethanol and allowing particles to form. This solution was then centrifuged and allowed to dry overnight at room temperature resulting in a gel form of HKUST-1. The gel was then washed to remove any unreacted precursors. It was found that this gel form displayed an uptake capacity of 259 cm^3 of methane per cm^3. This result may make the use MOFs in natural gas vehicles more efficient and affordable.

In recent years there have also been attempts to commercialize MOF technologies in the form of startups and even partnerships with larger corporations. For example, Omar Farha and colleagues founded NuMat Technologies to commercialize his academic MOF research. In 2016 the company announced the launch of their first product ION-X. Ion-X is a gas cylinder that contains proprietary MOFs that encapsulate toxic gases such as arsine, phosphine and boron trifluoride which are used as dopants in the electronics industry. Also in 2014, MOF Technologies and Decco (a food company) launched TruPick which consists of a MOF that holds 1-methylcyclopropene. This chemical slows down the ripening of fruit and thereby extends its shelf life. The MOF releases 1-methylcyclopropene which binds to the active site of enzymes in the fruit preventing ethylene from accessing this site. There are other companies utilizing MOFs as well such as MOF Technologies and MOFgen. There also exist partnerships between academia and industry such as Yaghi's partnership with BASF. This partnership resulted in a MOF-containing fuel tank for methane powered cars. This technology did produce a working prototype, but this partnership has not introduced any commercial products into the market as of late.

1.2.5 Conclusion and Outlook

In summary, the field of MOF chemistry is maturing and expanding in scope. This was demonstrated by the new and emerging methods of MOF synthesis that could allow for scale-up. Along with the detailed study of SBUs and organic linkers which has led to a better understanding of MOF connectivity, and the development of reticular chemistry that serves as a guide for designing MOFs with different topologies. There have even been attempts at the commercialization of products that utilize MOFs recently. With this progress the future of MOF chemistry seems to be bright and contains opportunities for innovation. However, more research efforts are needed to bring down the cost of MOF synthesis and more precise control over the assembly of MOFs needs to be developed allowing for the synthesis of more sophisticated, hierarchical topologies. If both conditions are met, this could lead to the practical utilization of MOF applications outside of the laboratory.

1.3 Covalent Organic Frameworks

Covalent organic frameworks (COFs) are generally microcrystalline[59] two- or three-dimensional frameworks built from light elements (H, B, C, N, and O), that are held together by strong covalent bonds and thus have much lower densities than MOFs. Prior to the discovery of COFs in 2005 by Yaghi et al.[60] there were other attempts at porous organic materials that were focused on the use of polymers resulting in materials such as hypercrosslinked polymers (HCPs),[61] polymers of intrinsic microporosity (PIMs),[62] and conjugated macroporous polymers (CMPs).[63] These polymeric materials were porous but generally amorphous and therefore possessed a highly disordered extended structure

along with a wide pore size distribution. This limited their applications. Hence the discovery of microcrystalline COFs with their ordered extended structures and porosity was a crucial turning point for the field. This allowed for COFs to become a new class of porous materials for gas storage, catalysis, and optoelectronic applications. The syntheses and development of COFs is based on dynamic covalent chemistry. This section will briefly describe the basic design concepts and synthesis of COFs along with a few selected applications.

1.3.1 Dynamic Covalent Chemistry

Dynamic covalent chemistry (DCC) involves the use of reversible covalent reactions to exchange molecules at equilibrium in order to obtain a more stable thermodynamic product. This reversible nature can allow for "error checking" and proofreading when applied to molecular assemblies.[64] It is primarily for this reason that DCC is used in the synthesis of COFs and Scheme 1.2 represents several reversible reactions used in their preparation.

The first COF synthesized was based on dynamic boroxine B–O linkages (Figure 1.5 A). It was prepared from the self-condensation of 1,4-phenylenediboronic acid resulting in a 2D layered framework with hexagonal pores of 7Å in diameter and a BET surface area of 711 m^2 g^{-1}.[60] The slow removal of water was essential for the error-correction process and resulted in an environment that was favorable towards crystal growth. Most COFs at that time were synthesized from building blocks with boronic acids resulting in B–O linkages, from either self-condensation or reactions with dialcohols to give boronate esters (Scheme 1.2 and Figure 1.5 A and B). Recently, other

dynamic functional motifs based on C-N linkages came into prominence in order to avoid the fragile nature of boron-containing COFs (Scheme 1.2 and Figure 1.5 C, D, and E).

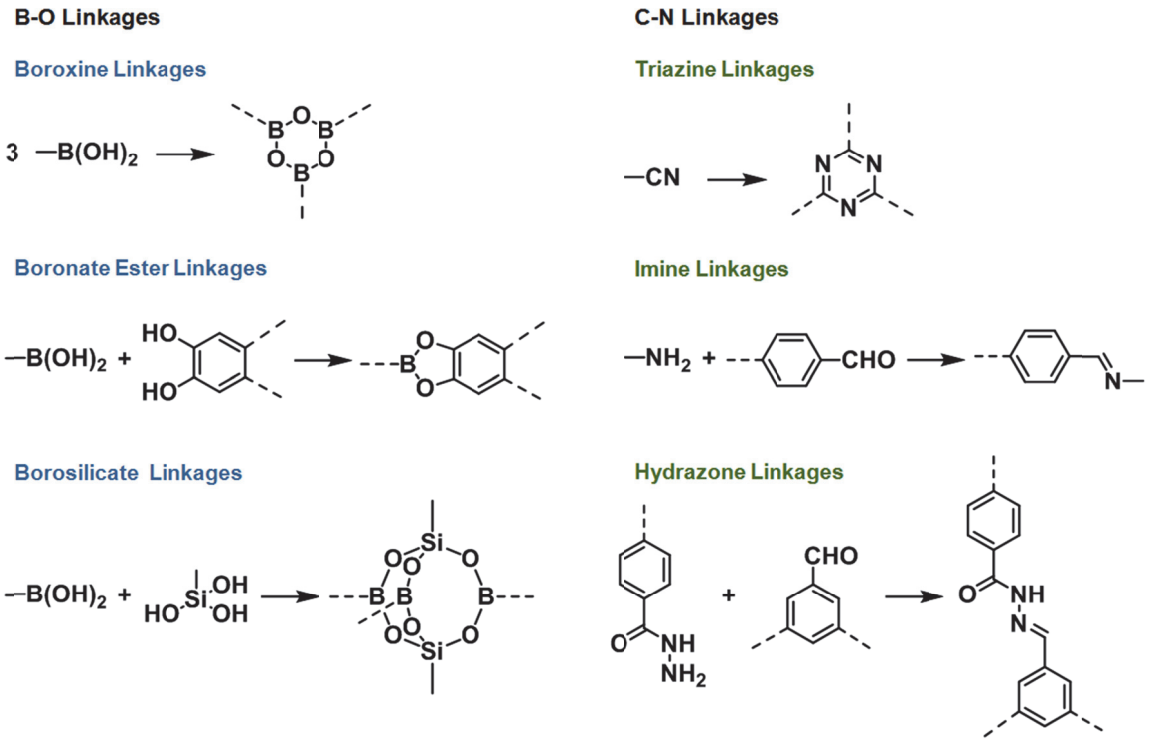

Scheme 1.2 Representation of several DCC reactions used in COF preparations.

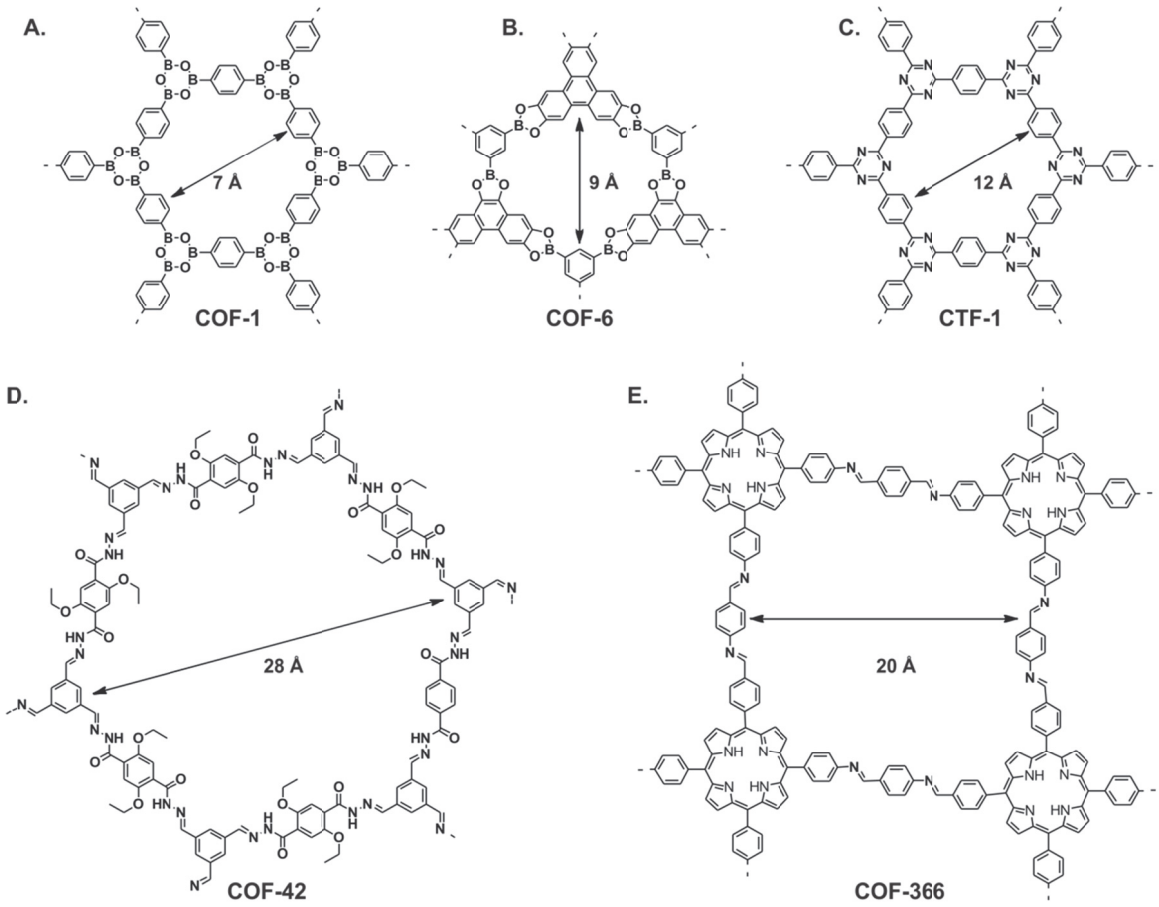

Figure 1.5 Representation of COF motifs based on boroxine (**A**), boronate ester (**B**), triazine (**C**), hydrazine (**D**) and imine linkages (**E**).

1.3.2 COF Synthesis and Design

Similarly to MOF chemistry, there have been attempts within the literature to expand the synthetic methodology of COF chemistry. These include the synthesis of COFs via solvothermal, ionothermal, microwave, and mechanochemical reactions. Within this section, solvothermal and ionothermal reactions will be discussed in more detail as microwave and mechanochemical reactions were discussed in the MOF section and the applications in COF synthesis parallel those.

The conventional method for the synthesis of COFs is solvothermal. In this methodology, a reaction is usually conducted in a sealed vessel and requires heating at temperatures ranging from 80 to 120 °C for several days. Yaghi et al.[60] discovered the pressure inside of the reaction vessel plays a key role and significantly effects reaction yields, with the optimal pressure determined to be at 150 mBar (which is equal to 0.15 atms). A year later, Lavigne et al.[65] developed a reflux procedure that could be run at ambient pressure for the synthesis of COFs. Another development to the solvothermal methodology toolkit involved the use of acetonide-protected catechols in the presence of Lewis acids by Dichtel et al.[66] This improvement expanded the scope of COF synthesis as it avoids the use of unstable and/or insoluble catechols. Dichtel et al.[67] have also developed a solvothermal method for the production of thin film COF materials on single-layer graphene (SLG). These materials have demonstrated improved crystallinity over the powder samples synthesized from traditional solvothermal methods. This method has the potential to broaden the application of COFs in particular involving their prospective use in electronic devices.

Ionothermal reactions involve the use of an ionic liquid in an autoclave or sealed vessel at high temperature (up to 400 °C) and pressure, and have been used to prepare COFs. Thomas et al.[68] utilized this method to synthesize triazine-based COFs in molten $ZnCl_2$. This resulted in a COF with a high degree of crystallinity that was also chemically and thermally stable. The molten $ZnCl_2$ serves as both a solvent and catalyst for the cyclotrimerization reaction of the nitrile building units. This method has an apparent disadvantage over the solvothermal method as it required harsh conditions and high temperatures, thus narrowing the choice of building blocks that can be used in COF

synthesis. This substantially limited the application of this methodology in COF synthesis. Recently, Qiu et al.[69] have synthesized a COF at ambient temperature and pressure under ionothermal conditions in an open system.

A key design strategy for the preparation of crystalline COFs is the geometry of the building blocks, as it is vital in maintaining an ordered structure. These building blocks should be conformationally rigid, symmetric and contain reactive functional groups that can trigger dynamic covalent bond formation without any irreversible side reactions (ideally no side reactions). The use of rigid building blocks will lock the conformation and allow the prediction and computational simulation of the COF topologies. These symmetric building blocks can be classified into different geometries, which include linear, triangular, cross-shaped, or tetrahedral. These geometries refer to the directionality of the reactive groups (Figure 1.6) and can also determine the overall structure of the subsequent COF. Therefore, the different combinations and geometries of linkers can result in the assembly of COFs with varying shapes and pore sizes. For example, the combinations of planar building blocks (e.g., linear, triangular, and cross-shape linkers) can result in 2D COFs with 1D channels of different shapes and pore sizes (Figure 1.7). Combinations of tetrahedral linkers only or tetrahedral and linear linkers can lead to the formation of 3D COFs. The rigid nature and distinct bonding direction of arenes enables the layering of 2D COFs via aromatic [$\pi\cdots\pi$] stacking. The advances in synthetic organic chemistry and the diversity of aromatic systems should allow for the discovery of novel linkers and various building block combinations.

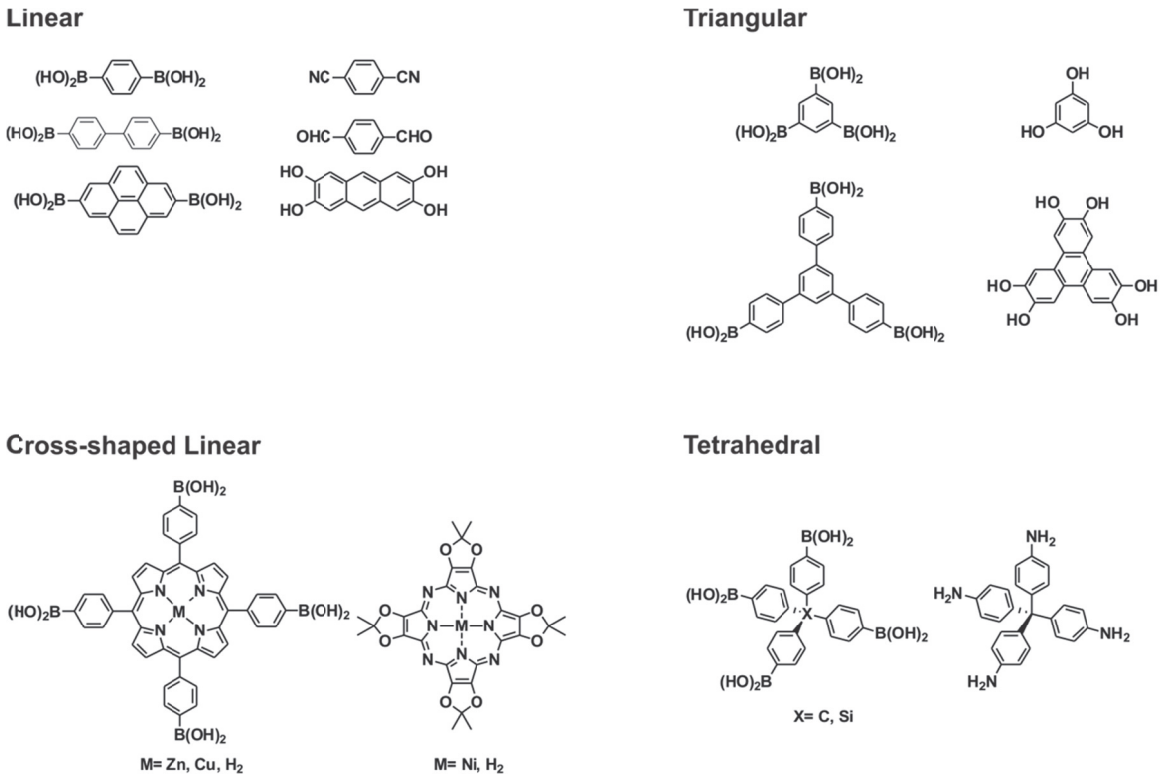

Figure 1.6 Commonly used COF building blocks of different geometries.

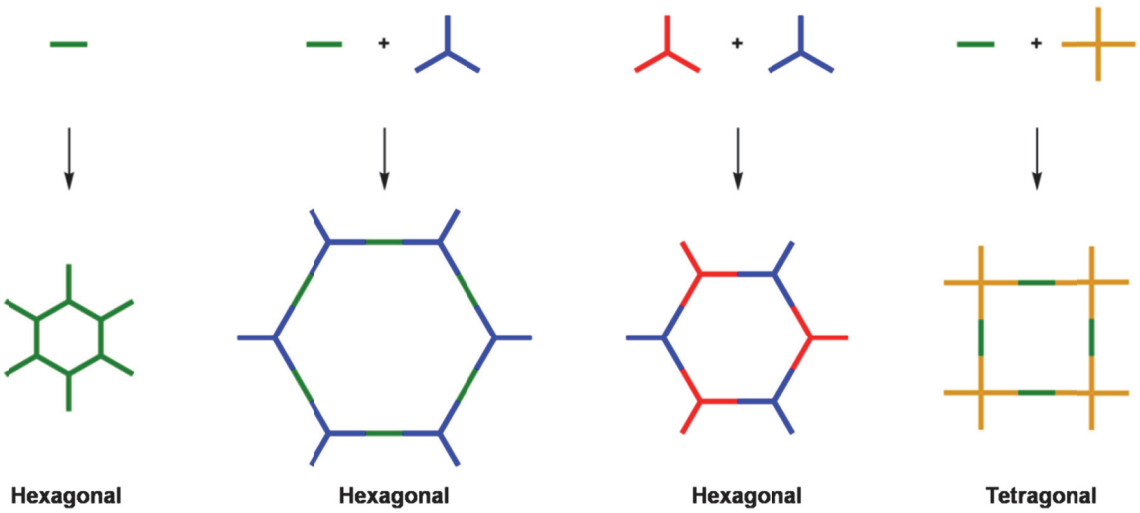

Figure 1.7 Different combinations of building blocks showing the effect of geometry on the synthesis of 2D COFs.

Another design strategy for the synthesis of COFs is the postsynthetic modification inspired by the same approach applied in MOF chemistry. Jiang et al.[70] were the first to apply the organic linker modification strategy towards the synthesis of COFs for the functionalization of the pore walls with various organic groups (Figure 1.8). They used an azide-anchored linker for the COF synthesis. These azide units underwent a quantitative click reaction with alkynes to modify pore surfaces with the desired functional groups and properties. A more recent example of postsynthetic modification of COFs was conducted by Valtchev et al.,[71] wherein they converted a 3D COF with a hydroxyl functionality into a carboxy functionality. This was accomplished by reacting the hydroxyl anchored linker groups on the pore walls with succinic anhydride, resulting in a ring opening reaction. This yielded a carboxy functionalized COF that displayed a high degree of crystallinity and exceptional lanthanide selectivity. Another modern example was conducted by Horike et al.[72] who utilized a novel DCC and post synthetic approach towards the modification of imine COFs. They prepared two 2D imine-bonded COFs with different aromatic groups and mixed them together. This resulted in two structures with various compositions: a homogeneously mixed-linker structure and a heterogeneously core-shell hollow structure. These modified COFs were more crystalline and displayed twice the BET surface area when compared to the original parent COFs.

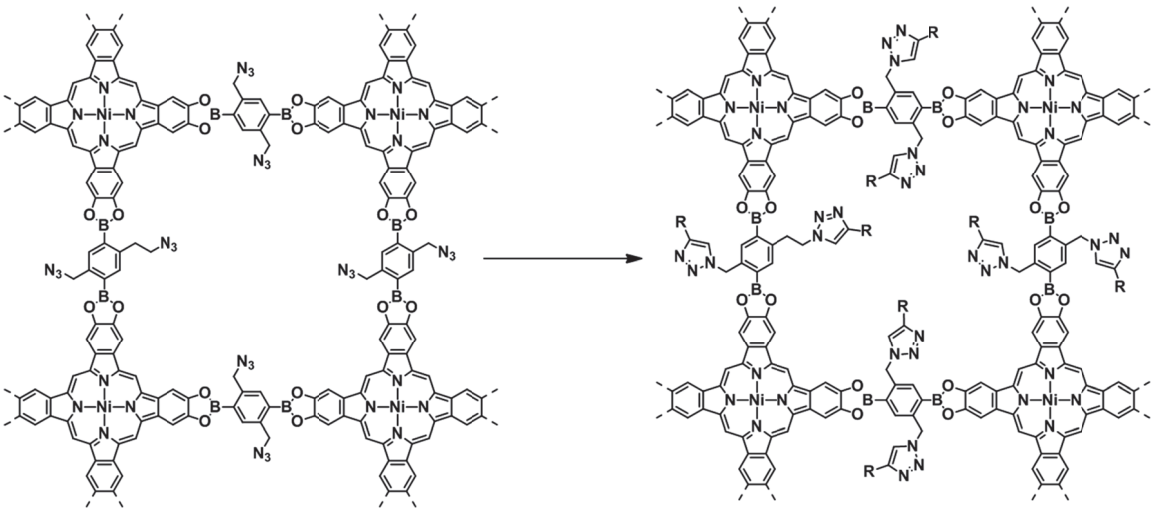

Figure 1.8 Postsynthetic modification of tetragonal NiPc-COF via azide alkyne Huisgen cycloaddition reaction.[70]

The newest design strategy innovation within this field is called weaving and it is inspired by the way we weave and stitch together fabric, with the major difference being that this weaving is occurring at the molecular level. In this process the organic linker molecules are treated as threads and they are stitched together forming a new COF. The first example of a woven COF was reported by Yaghi et al.[73] utilizing a copper(I) complex as a template to bring together the organic threads of phenanthroline resulting in an imine-based framework called COF-505. The covalently linked organic threads are woven together by Cu(I) ions while the threads themselves are dispersing in two different directions. This resulted in helices with opposite chirality, giving rise to a racemically woven framework of the same topology. Heating this COF in a KCN methanol-water solution resulted in the demetalation of the COF. This resulted in a decrease in crystallinity but an unexpected increase in elasticity of the material which is believed to be attributed to the loose interaction between the organic threads after metal removal.

Furthermore this material can also be remetalated with Cu(I) ions to restore the crystallinity of COF-505. This methodology can allow for increasing the complexity of crystal structure modification by the weaving of organic threads to provide both strength and flexibility into the new structure.

1.3.3 COF Applications

Because of their similarity to MOFs and the strong covalent linkages holding the framework together resulting in higher stabilities, COFs have gathered an increase in interest within the scientific literature in the form of applications. These applications include gas storage and separation,[74,75] catalysis,[76] and electrochemical devices.[77]

The applications discussed in this section will focus on gas storage with an emphasis on hydrogen and methane gas as was discussed in the MOF section. Gas storage is also the most widely explored application of COFs and just like MOFs they show the capability for hydrogen storage. Since their inception, theoretical studies conducted by Yaghi et al.[78] predicted the hydrogen uptakes at 77 K are 10.0 wt % at 80 bar for COF-105, and 10.0 wt % at 100 bar for COF-108, which represent the highest values reported for associative hydrogen storage of any material. Previous simulations conducted by Goddard et al.[79] also indicated that the benzene rings of the organic linkers of MOFs play an important role during hydrogen uptake which is more important than the presence of heavy metals. For these reasons, COFs emerged as promising candidates within this field. But in actuality the experimental results have them closer to each other, as the COF-102 displays the highest hydrogen uptake of 7.24 wt% at 77 K and 55 bar.[80]

This is comparable to MOF-210 which has a hydrogen uptake of 8 wt% under the same conditions.

A more recent development in this field[81] has shown that COFs doped with lithium could show improved hydrogen storage capacity at ambient temperature due to the increased binding energy between the H_2 and the Li atoms. The practical challenge for use of COF materials toward the hydrogen uptake is still far away. The same can be said for methane uptake as well since COF-102 also has the highest methane uptake capacity of 230 cm^3 of methane per cm^3 which is slightly less than HKUST-1.

1.3.4 Conclusions and Outlook

In summary, COFs embody a newer arrival to the field of porous crystalline frameworks. This field is thriving due to the similarities between COFs and MOFs such as modular synthesis, permanent porosity, and controllable pore size. The field is still in its early stages and has yet to reach maturation hence there is still room for the further development of synthetic strategies, linkers and methods of post-synthetic modification. More detailed studies into improving the crystallinity of COFs also need to be conducted, as well as mechanistic studies to provide more insight and control over the morphologies of these materials.

1.4 Organic Molecules with Porous Crystal Structures[12]

Porous molecular crystals (PMC) are composed of discrete molecules that pack in the solid state in an inefficient manner that leaves behind large voids. These discrete molecules are held together by non-covalent interactions making this group unique among the other classes of porous materials; as molecules tend to pack efficiently in the

solid state due to entropic considerations and to maximize attractive intermolecular contact. Thus, porous structures of this variety are quite rare. Even amongst cases when pores are observed they are usually filled with disordered solvents and tend to collapse upon solvent removal. The interest in PMCs stems from the fact that they are generally solution-processable allowing for the study of their mode of assembly and function via solution phase spectroscopic tools. In addition, the fact that there are no strong covalent bonds holding individual molecules together makes these crystals 'rubbery', allowing for the distances between the molecules to change even in the solid state. This feature is applicable in the motion and transport of guests through the pores, as well as in guest sensing.

PMCs can further be divided into two categories: intrinsically and extrinsically porous.[82] Intrinsically porous PMCs are composed of molecules that already possess porosity in the form of a large, shape-persistent voids such as molecular cages and macrocycles. Extrinsically porous PMCs are formed from molecules that do not possess voids, but whose inefficient packing in the solid state results in large empty voids. In other words, molecules that bring their voids with them into the crystal structure are intrinsically porous; while extrinsically porous crystals are a product of crystal packing. Combinations of these two categories are possible as well.

1.4.1 Early Days of PMCs

Many organic compounds display porosity in the solution phase in which these apparent pores are usually filled with disordered solvent or guest molecules. In the vast majority of cases, these pores collapse as the included guests are removed; the reasons for

this are thermodynamic as the more stable close-packed structure (with included guests) gives rise to the less stable structure with voids. This section will focus on systems that resist structural collapse upon solvent or guest removal and maintain porosity discovered prior to 2011.

One of the earliest examples was Dianin's compound (Figure 1.9 compound **1**) reported in 1914.[83] This compound was capable of sorbing a series of gases (Ar, Kr, Xe, CO_2, CH_4, C_2H_6, C_3H_8, *n*-C_4H_{10}, *iso*-C_4H_{10}, and *neo*-C_5H_{12}) despite the lack of apparent porosity within the crystal structure.[84] This interesting behavior was called "porosity without pores" and has been observed in other molecules, such as calixarenes.[85] This phenomenon has been explained as taking place through dynamic van der Waals cooperativity, allowing for guest transport through the crystal.[85] Another organic molecule that has shown porosity is tris(*o*-phenylenedioxy)cyclotriphosphazene (TPP) (Figure 1.9, compound **3**). The crystal structure revealed that the molecular TPP crystal possessed hexagonal pores along the *c*-axis and that it was capable of adsorbing Ar, N_2, O_2, H_2, CH_4, and CO_2, gases under isothermal conditions.[86] Another group of organic molecules that have been discovered to be capable of organizing into porous structures in the solid state were hydrophobic dipeptides such as *L*-alanyl-*L*-valine and *L*-valyl-*L*-alanine.[87]

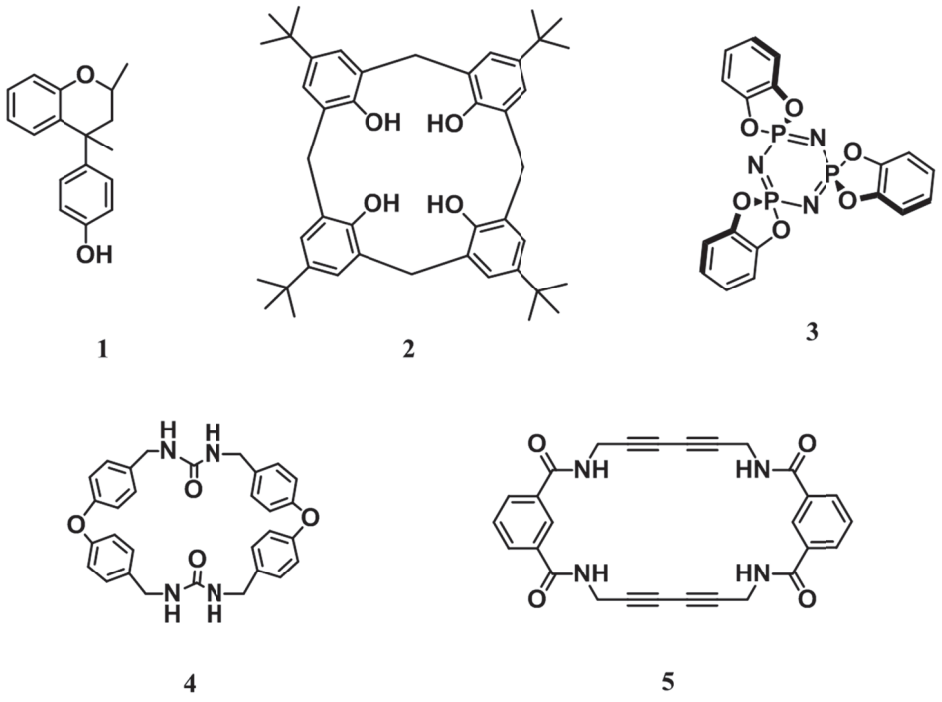

Figure 1.9 Organic compounds with porous solid state structures, reported prior to 2011.

In 2003 Shimizu's group reported[88] the synthesis of a porous bis-urea macrocycle (Figure 1.9, compound **4**). This macrocycle assembled into columnar stacks that were held together by hydrogen bonding between the individual urea moieties. It was found to be capable of the reversible adsorption of AcOH and possessed a BET surface area of 316 $m^2\ g^{-1}$. This group also reported the synthesis of a tetrayne-based macrocycle (figure 1.9, compound **5**) with a BET surface area of ~350 $m^2\ g^{-1}$ that is capable of polymerization when heated.[89]

In 2009, McKeown et al.[90] reported the porous crystal structure of a biphenyl-based tetrayne compound (Figure 1.10A, compound **6**). This structure was not designed and then synthesized, but was instead discovered through careful examination of the Cambridge Structural Database by following a set of criteria that McKeown et al.

proposed.[90] These criteria include: (a) crystal density lower than 0.9 g cm^{-3}, (b) crystal composed of rigid aromatic molecules, and (c) small pore sizes. The BET surface area of this compound was determined to be 278 m^2 g^{-1} and the crystal structure seemed to be stabilized mostly by [C–H···π] interactions. Additionally, the crystal structure benefited from the bicontinuous microporous surface which reduced sensitivity towards mechanical stress. Recently, Doonan et al.[91] utilized machine learning to analyze a set of 150,000 previously reported organic molecular crystal structures and identified 481 potentially porous organic molecular crystals. This result provided proof that this methodology for the identification of the porosity of PMCs is general and that PMCs of the organic variety are quite rare.

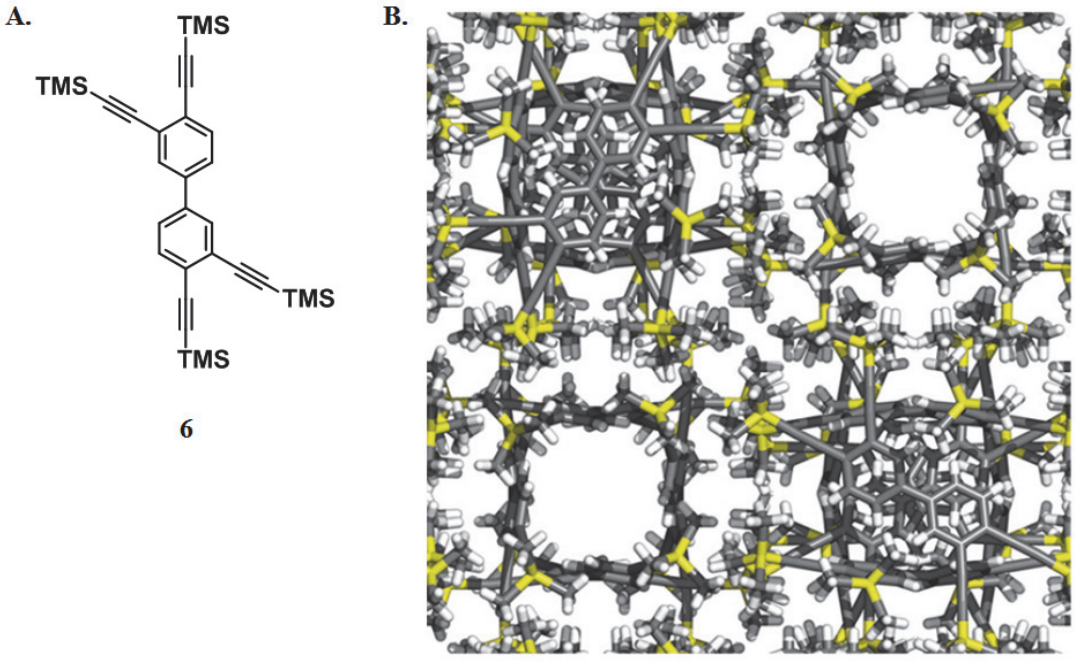

Figure 1.10 (A) Compound ([1,1'-biphenyl]-3,3',4,4'-tetrayltetrakis(ethyne-2,1-diyl))tetrakis (trimethylsilane)) crystallizes as a porous structure, a segment of which is shown (B) Element colors: Si—yellow, C—gray, H—white.[90]

1.4.2 Intrinsically Porous Molecular Crystals

1.4.2.1 Porous Imine Cages

In 2009, Cooper et al.[92] reported the synthesis of porous organic cages based on imine linkages. These tetrahedral imine cages (compounds **11–14** in Scheme 1.3) were synthesized through a [4+6] cyclocondensation reaction between 1,3,5-triformylbenzene and four vicinal diamines: 1,2-ethanediamine (**7**), 1,2-propanediamine (**8**), (*R*,*R*)-1,2-diaminocyclohexane (**9**), and (*R*,*R*)-1,2-diaminocyclopentane (**10**) (Scheme 1.3).[92,93] The respective BET surface areas of these cages were found to be in the 500–600 $m^2\ g^{-1}$ range. These cages were also found to be thermally stable as they did not decompose below 320 °C. The crystal porosity of these PMCs was caused both by the intrinsic porosity of the imine cages as well as the inefficient packing of the cages.[80] In this case the crystal packing and arrangement of the pores depended heavily on the vertices of the cage which were derived from the functional groups on the imine linkers. The bulkiness of these functional groups dictated whether the pores were isolated or connected (Figure 1.11).

Take, for example, cage **11**: it packs in a window-to-arene stack with no inter-cage window connectivity and is hence non-porous even though it has isolated lattice voids (Figure 1.11 A). Even though **12** has analogous packing to **11**, owing to the steric hindrance of the methyl groups over six vertices, cage **12** features a one-dimensional undulating pore channel running between the cages, but not connecting with the cage voids (Figure 1.11 B).[94] Conversely, cage **13** packs in a window-to-window arrangement that is a result of the interlocking of the cyclohexyl groups thereby producing an interconnected three-dimensional diamondoid homochiral pore network (Figure 1.11C).[94]

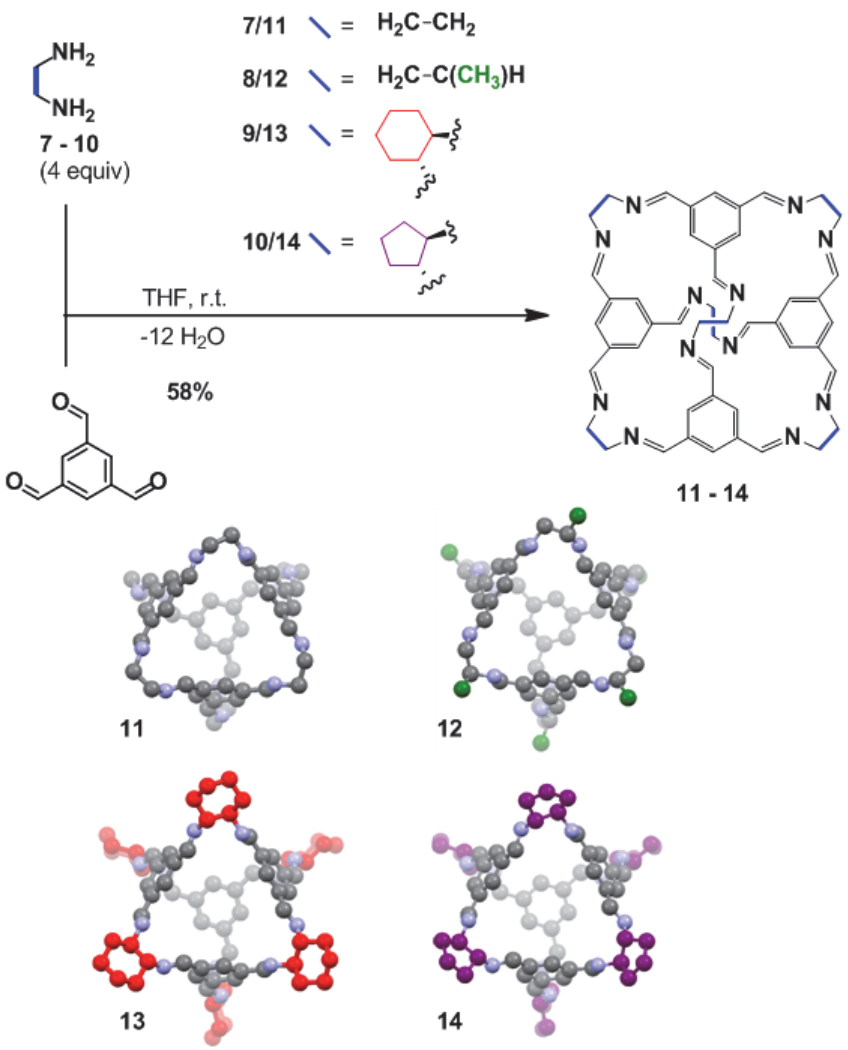

Scheme 1.3 Synthesis of porous imine cages **11**–**13** by Cooper et al. [92,93]

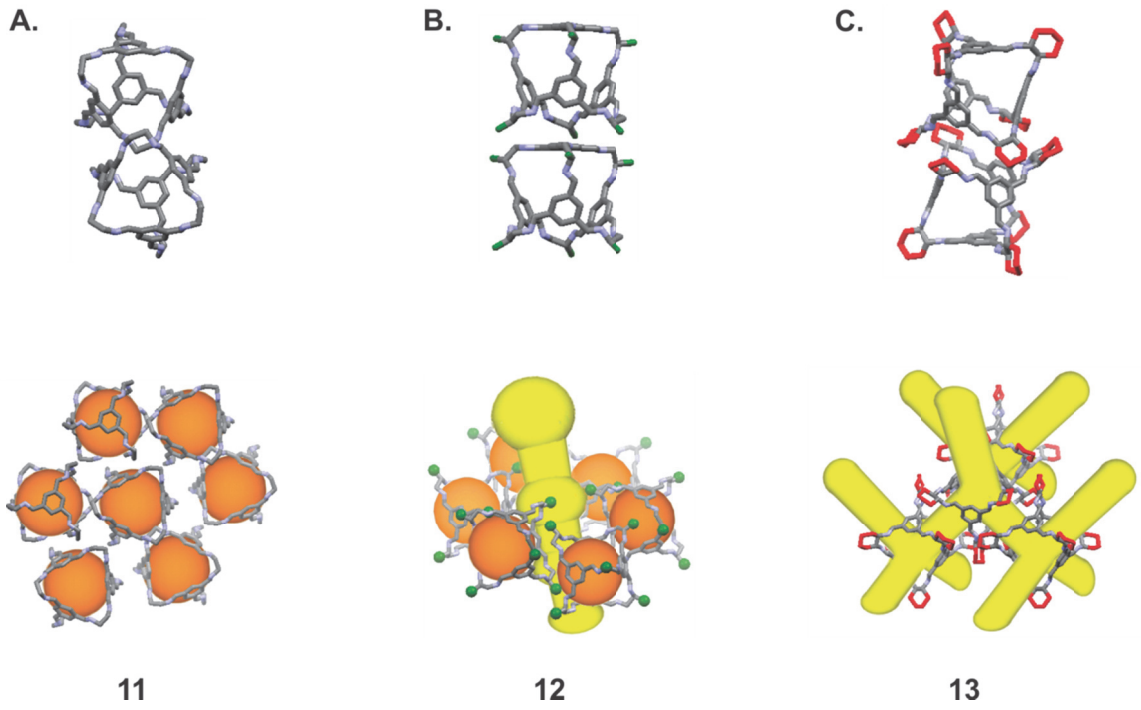

Figure 1.11 The differences in crystal packing of porous imine cages **11**–**13**.[94]

Interestingly, these cages can experience morphological changes in response to chemical stimuli under different recrystallization conditions. For example, the porosity of cage **11** can be switched on and off between three different polymorphs: nonporous **11α** (SA_{BET}=23 m^2 g^{-1}); selectively porous to hydrogen gas **11β** (SA_{BET}=30 m^2 g^{-1}); and highly porous **11γ** (SA_{BET}=550 m^2 g^{-1}). Organic solvents serve as the trigger for switching between these three polymorphs (as depicted in Figure 1.12). The switching procedure was achieved by exposing the desolvated nonporous **11α** (after its isolation from EtOAc) to DCM in order to yield **11β**, or *o*-xylene to yield **11γ** respectively.[92,94]

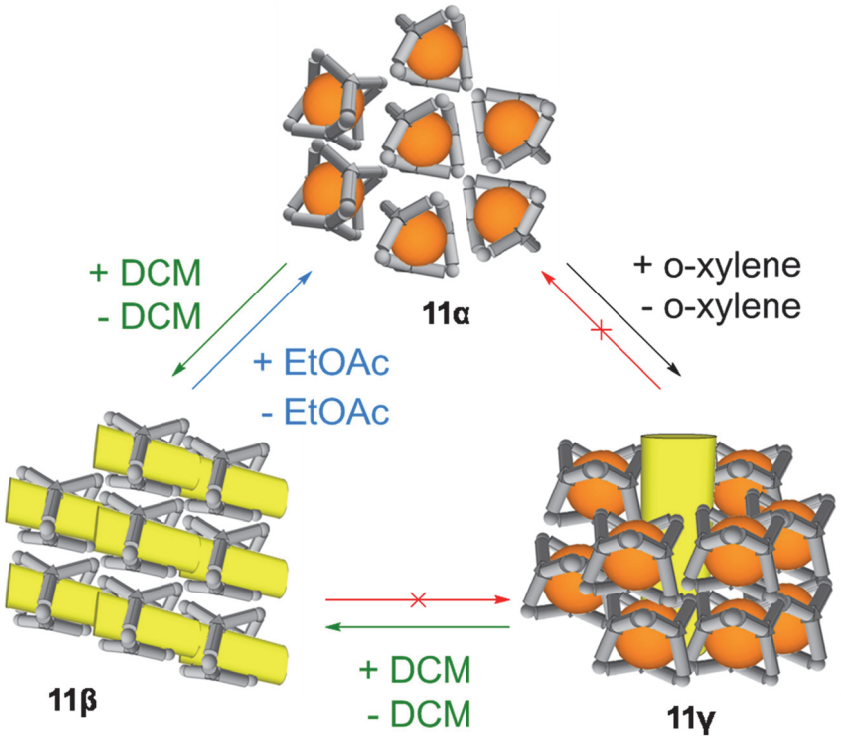

Figure 1.12 Porosity on–off switching of the different polymorphs of imine cage **11**.[92,94]

Postsynthetic modification of imine cage **11** into an amine was achieved in quantitative yield with the use of $NaBH_4$. This amine cage is of interest as it is more stable than the precursor cage and can be further functionalized by acylation with acid halides to generate dodecamide cages. Cooper et al.[95] have proposed using it as a unique and porous node for the preparation of novel dendrimers, MOFs, and COFs. It was also discovered that cage **13** is capable of hosting organometallic guests when exposed to vapors of OsO_4; resulting in a doped crystal that contained 2.5 molecules of OsO_4 per cage. In the very same study, Cooper et al.[96] showed that exposing cage **13** to iodine vapors resulted in the formation of an oxidized cage that acted as a counterion to the V-shaped pentaiodide. This host-guest interaction was found to be a completely reversible

process as iodine can be liberated either by heating to a temperature above 60 °C or in the presence of organic solvent.

Cooper et al.[97] also discovered that porous organic cocrystals can be prepared in a modular fashion, simply by combining the previously mentioned imine cages in solution followed by the slow evaporation of the mother liquor. For example, evaporation of an equimolar solution of imine cage **11** and homochiral (*R*)-**13** led to a quasiracemic cocrystal composed of (*S*)-**11** and (*R*)-**13**. Cage **11** is a racemic mixture of helically chiral (*R*)-**11** and (*S*)-**11** enantiomers, which rapidly interconvert, allowing complete amplification of (*S*)-**11** in the presence of (*R*)-**13**. In the solid state, (*S*)-**11** and (*R*)-**13** alternate in a face-centered cubic ZnS crystal lattice, yielding a porous cocrystal (SA_{BET} = 437 $m^2\ g^{-1}$) as they pack in a window-to-window arrangement.[97] Notably, this work involved crystal structure prediction and yielded a larger imine-based cage from *tris*(4-formylphenyl) amine and chiral (*R*,*R*)-1,2-cyclopentadiamine. This cage possessed a BET surface area of 1333 $m^2\ g^{-1}$. Ternary porous cocrystals were also prepared via an extension of this strategy.[98] These were dubbed 'porous organic alloys', and 50% of the lattice positions were occupied by (*S*)-**11**, while alternating positions were occupied by a disordered mixture of (*R*)-**13** and (*R*)-**14** in various ratios ranging from 0 to 1 producing $\mathbf{11}\cdot\mathbf{13}_n\cdot\mathbf{14}_{1-n}$ cocrystal compositions. It was found that the BET surface area increases almost linearly with the proportion of **14** incorporated into the cocrystal, ranging from 373 (0% of **14**) to 670 (50% of **14**) $m^2\ g^{-1}$.

The effort to build larger cages resulted in propeller imine cage structure **15**. This imine cage was synthesized by the application of a one-pot [2+3] cycloimination reaction between 1,3,5-tris(4-formylphenyl)benzene with 1,5-pentanediamine in methanol.[99] This

new cage was expected to provide additional flexibility due to the presence of long chain diamines and yield larger pores sizes compared to the previous cages. However, it crystallized as a closely packed structure with small voids within the cage due to favorable [π···π] stacking between the central phenyl rings. Interestingly, extrinsic networks along the *a*-axis that correspond to 10% of the crystal structure volume were observed as the result of the imperfect extended packing of the propeller-shaped molecules (Figure 1.13). Further attempts to increase the size of imine cages were conducted by Cooper et al.[100] by the use of an [8+12] cycloimination of tris(4-formylphenyl) amine with chiral diamines (*R,R*)-1,2-cyclohexanediamine and (*R,R*)-1,2-cyclohex-4-enediamine. This resulted in two large cubic assemblies with inner diameters of 1.2 nm and a calculated volume of 1500 Å^3. Unfortunately, these highly porous structures were found to collapse upon desolvation.

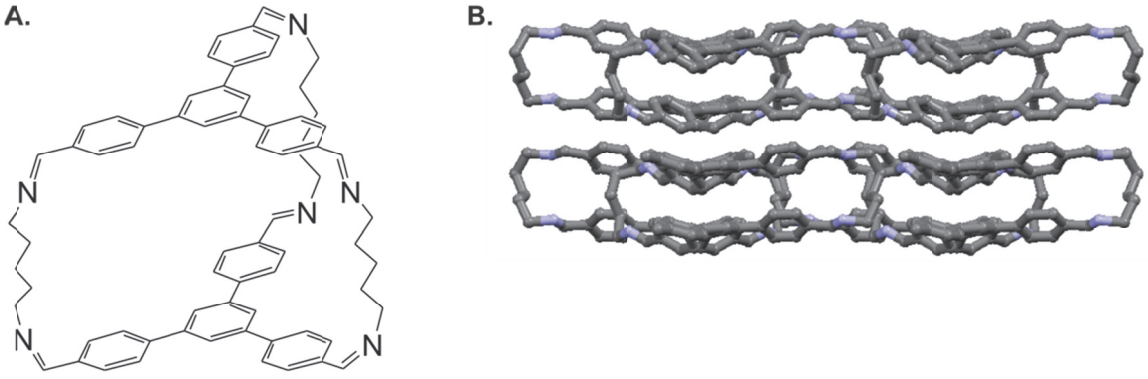

15

Figure 1.13 (A) Propeller-shaped cage **15**. (B) Molecular packing of cage **14** viewed along the c-axis, hydrogen atoms have been removed for clarity (Element colors: O— red, N— blue, C—gray).[99]

These imine-based cages could also be functionalized with long alkyl chains to produce materials with lowered melting points allowing access to liquid and/or glassy phases. However, it was found that the liquids were not porous due to the penetration of the long alkyl chains into neighboring cavities.[101] An alternative strategy proved successful in producing liquids with permanent porosity: the dissolution of imine-based molecular cages in 15-crown-5, which is a solvent whose molecules are too large to enter the pores.[102] This porous liquid displayed an 8-fold increase in methane capture when compared to the pure solvent. It was also shown that a dynamic covalent scrambling approach could be used to prepare porous liquids.[103] The underlying principle was that vertex-disordered cage mixtures show an increase in solubility when compared to cages derived from a single diamine. This could be attributed to a reduction in lattice energy as scrambled mixtures show a reduced tendency towards crystal formation.[99] This approach has resulted in porous liquids with lower viscosity, increased solubility and improved gas uptake.

Another class of imine cages based on tetrahedral salicylimine **18** was prepared by Mastalerz et al.[104] This cage was synthesized by the condensation reaction of triaminotriptycene **16** with salicyldialdehyde **17** (Scheme 1.4) and crystallized. Porosity measurements revealed that this PMC possessed a BET surface area of 1375 $m^2 g^{-1}$ and selective CO_2 uptake in the presence of CH_4.[105] In a following full paper, Mastalerz et al.[106] reported the preparation of a series of substituted derivatives of **18**. Wherein, these derivatives contained peripheral groups of varying degrees of steric bulk. It was found that most of the prepared cages had similar BET surface areas of approximately ~700 $m^2 g^{-1}$ in the amorphous state. Nonetheless, upon crystallization, dramatic changes in the

surface area were observed, with some cages almost doubling their surface areas, while other cages having their surface area decrease by half. This was believed to be due to the dominant contributions of the cages' internal surface to the porosity in the amorphous state. Where as in the crystalline state, orientation of the large bulky groups had to be taken into consideration as some of them could not pack efficiently and this it led to an increase in the surface area.[106] These molecular cages were shown to be solution-processable and could be deposited onto quartz crystal microbalances via an electrospray procedure. Thus they can be exploited into porous coatings on thin films that can uptake and release vapors of aromatic solvents as well as enhance selectivity and can be applied to specific chemical sensing.[107] This approach was also used to gravimetrically sense γ-hydroxybutyric acid (GHB).[108]

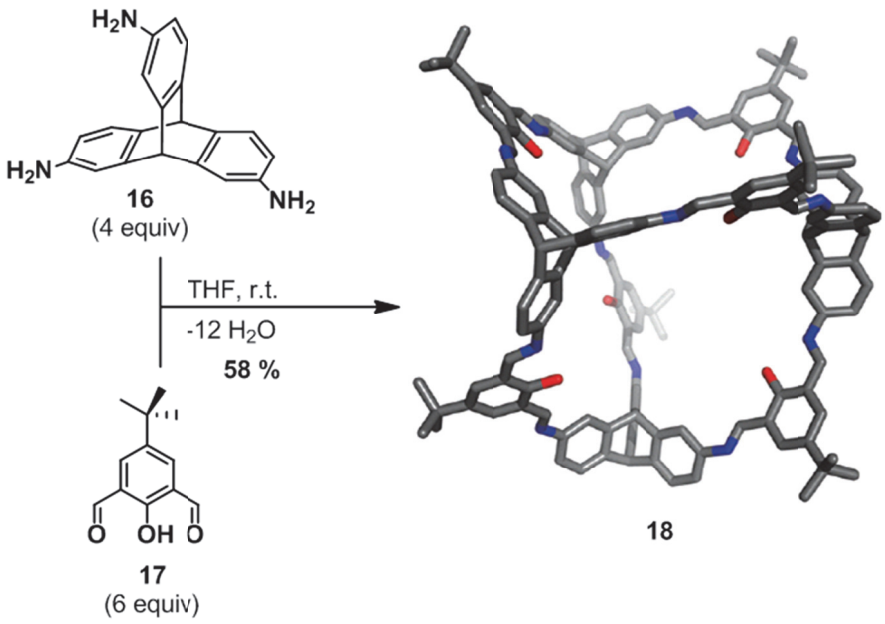

Scheme 1.4 Synthesis of an imine-based cage **18** by condensation of triamine **16** and dialdehyde **17** (in the crystal structure of **18**, hydrogen atoms have been removed for clarity; Element colors: O— red, N—blue, C—gray).[104]

Using the two triptycene-based precursors, triamine **16** and tricarboxaldehyde **19**, the same group discovered the self-assembly of molecular cube **20** (Scheme 1.5).[109] In this strategy, each of the triptycene building blocks acted as a corner of the cube, convergently positioning the three reactive functionalities. The two precursors alternate as corners of the final cubic assembly. Mastalerz's work on porous imine-based cages has been highlighted in *Synlett*.[110] Zhang et al.[111] also reported a synthesis of imine-based cages through a [2+3] cycloimination. These cages resulted in low BET surface areas, but displayed high selectivity for the adsorption of CO_2 in the presence of N_2.[111]

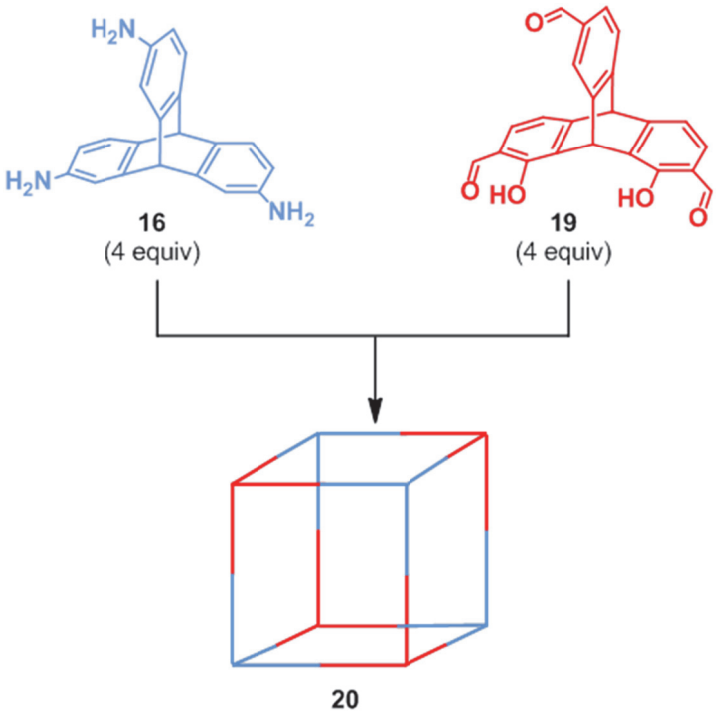

Scheme 1.5 Synthesis of molecular cube **20** via cycloimination of triptycene compounds **16** and **19** (for simplicity, the cube is shown schematically, with each precursor color retained in the final structure).[109]

1.4.2.1 Porous Cages Based on Boronate Esters

The dehydration of boronic acids and diols into boronate esters was the first reaction to be used in the synthesis of COFs[60] (discussed in the DCC section of this thesis). Mastalerz et al.[112] adapted the reversible chemistry of boronate ester based COFs to give discrete molecular capsules. Using triptycene-derived tetraol **21** (which positioned its two catechol moieties in a convergent fashion at a 120° angle) and trisboronic acid **22**, Mastalerz et al.[113] prepared molecular cage **23** (Scheme 1.6), whose crystal structure revealed a large void in the center. The surface area of this material was found to be 3758 $m^2\ g^{-1}$, the highest thus far reported for porous molecular crystals. Surprisingly, with a minimally modified derivative of **21**, in which the two ethyl groups are moved to the bridgehead positions of triptycene and replaced with hexyl substituents, a different outcome of condensation was observed in the solid state.[113] Instead of discrete cages being formed, two of them quadruply interlocked to create catenated structure **25** (Scheme 1.7). The authors[113] postulated that the interlocked structure allowed greater close contact between alkyl groups; as expected, its porosity is quite a bit lower than that of **23**: 1540 $m^2\ g^{-1}$.

Recently, this same group[114] also prepared shape-persistent [4+6] tetrahedral boronic ester cages with varying the degrees of fluorination on the sp^2 centered aromatic diboronic acid. It was found that direct relationship existed between the fluorine content and the reaction rate. This corresponds well with the theory that fluorinated diboronic acids are more Lewis acidic, thereby increasing the reaction rate. It was also found that the non-fluorinated cage demonstrated the highest surface area of the synthesized cages.

The surface area was reported to be 511 m^2 g^{-1} and the cage displayed gas-sorption selectivity for ethane over ethylene and acetylene.

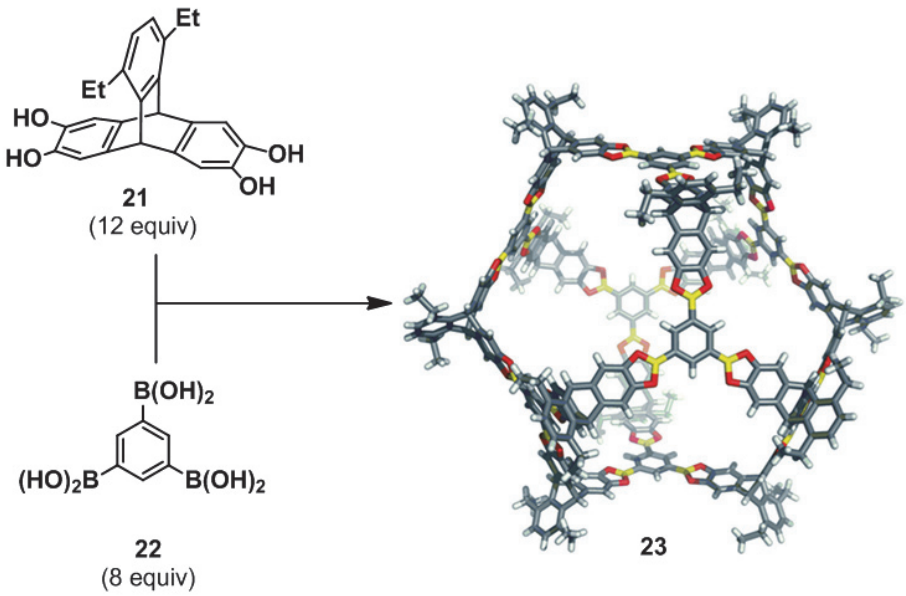

Scheme 1.6 Synthesis of boronate ester cage **23** from **30** and **22** (Element colors : O—red, C—gray, B—yellow, H—white).[113]

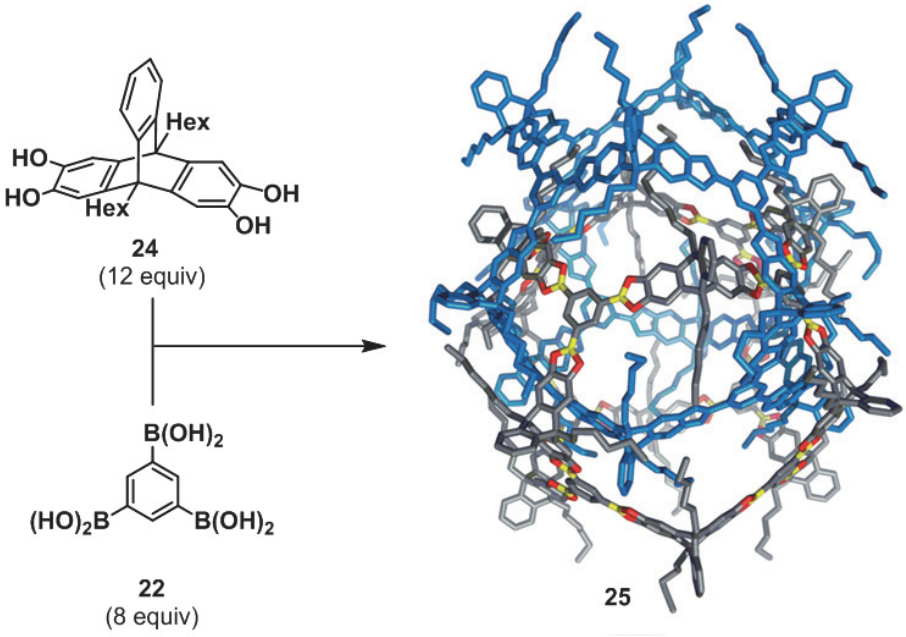

Scheme 1.7 Synthesis of boronate ester catenane **25** (in the crystal structure of the catenane, hydrogens have been removed and one of the cages is colored in blue for clarity. Element colors: O—red, C—gray, B—yellow.[113]

1.4.3 Extrinsically Porous Molecular Crystals

Extrinsically porous molecular crystals existed[84,86] before intrinsically porous molecular crystal cages. Some of the prominent extrinsically porous molecular crystals based on triptycene molecules were developed by Mastalerz et al.[110] In 2012, they synthesized trisbenzimidazolone **27** from the reaction of hexaammonium triptycene hexachloride with carbonyldiimidazole (Scheme 1.7).[115] This molecule was selected for the preparation of extrinsically porous crystals for two reasons: (1) benzimidazolones are known to form planar ribbon like structures in the solid state[116] and (2) incorporation of the D_{3h}-symmetric triptycene subunit could allow for the trigonal orientation of these hydrogen bond donors resulting in an extended porous framework. This strategy did

indeed result in a crystalline and highly porous molecular crystal with a BET surface area of 2796 m^2 g^{-1}, which is the current world record for extrinsically porous molecular crystals. This PMC possesses two distinct types of pores: large roughly circular pores and smaller rectangular ones (Figure 1.14). This PMC was also found to adsorb high amounts of CO_2 (15.9 wt%) at 273 K and 1 bar which was comparable to MOFs[117] at that time. It was hypothesized that this high amount of CO_2 uptake was due to attractive interactions between the polar surface of the benzimidazolone subunits and the quadrupole of CO_2, as significantly smaller amounts of nonpolar CH_4 (1.5 wt%) were adsorbed. Examination of the crystal structure of **27** revealed that this PMC was held together by infinite tapes of hydrogen bonds between the N–H and C=O groups of the benzimidazolone moieties (Figure 1.15).

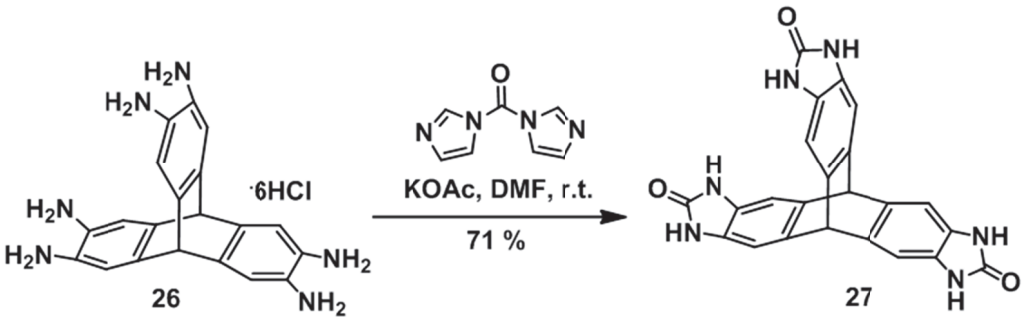

Scheme 1.8 Synthesis of tris-benzimidazolone **27**.[115]

Mastalerz et al.[118] further expanded upon the triptycene based PMCs by synthesizing another class of trigonal based molecules that self-assemble through [π···π] stacking (Figure 1.15). This class of molecules displayed BET surfaces areas that range from 206 to 754 m^2 g^{-1} depending on the R substituents. They also found that these molecules were fluorescent which could facilitate their future use in applications that involve organic electronic devices and uses as sensors. Due to the weak interactions

between the molecules most of the members of this class are amorphous solids with the exception being compound **28e.** This derivative is end-capped with three triptycenylene units and was found to much more soluble than the other members. The slow evaporation of **28e** in a concentrated solution of mesitylene resulted in the single crystals of four polymorphs, with void volumes ranging from 63 to 72%.[119] As the four polymorphs were obtained under the same conditions this suggests that no strongly directing interactions were involved in the self-assembly of these frameworks.[118] Similar to this compound McKeown et al.[120] have also reported triptycene based organic molecules of intrinsic microporosity (OMIM) with BET surface areas ranging from range 515–702 m^2 g^{-1}, that were unfortunately amorphous in nature.

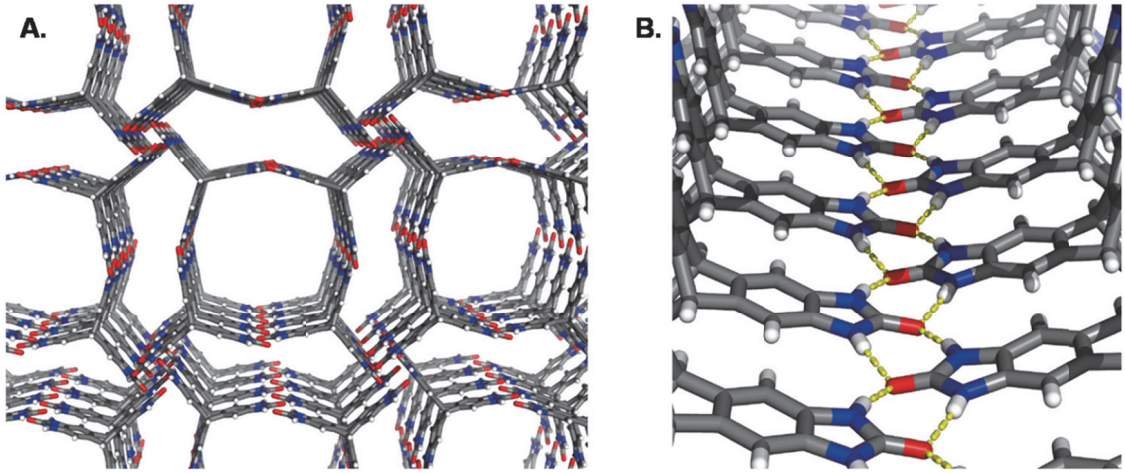

Figure 1.14 (A) Crystal structure of tris-benzimidazolone **27**, highlighting the pores. (B) Segment of the crystal structure displaying [C=O···H–N] hydrogen bonding which stabilize the structure. Element colors: O—red, N—blue, C—gray, H—white. Hydrogen bonds are highlighted in yellow.[115]

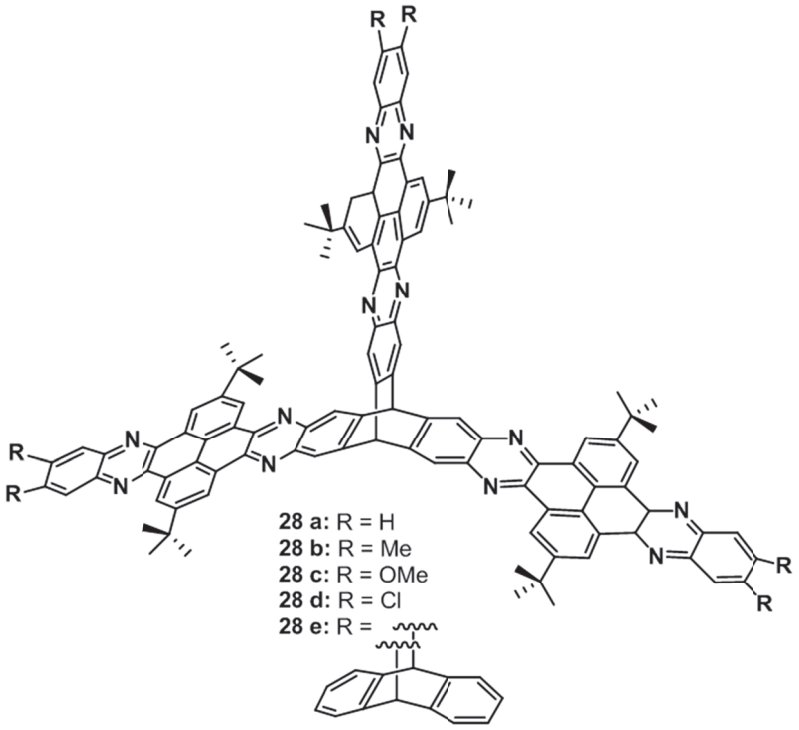

Figure 1.15 Trigonal precursors to [π···π]-stacked fluorescent porous materials prepared by Mastalerz et al. [118]

Another class of extrinsically porous molecular crystals are hydrogen bonded organic frameworks (HOFs) which were discovered by Chen et al.[121] They decided to utilize terminal 2,4-diamino-1,3,5-triazin-6-yl (DAT) groups as hydrogen bond donors and acceptors in the assembly of an extended porous framework. These DAT groups were previously shown by Wuest et al.[122] as being capable of forming multiple hydrogen bonds behaving as reliable tectons (building blocks) for the construction of frameworks. Chen et al.[121] synthesized compound **29** (Figure 1.16), in three steps from tetraphenylmethane and crystallized it resulting in a porous network (SA_{BET} = 359 m^2 g^{-1}). This framework was dubbed HOF-1 and it displayed a high selectivity for acetylene in its challenging separation from ethene. Due to the initial success of HOF-1 displaying

permanent porosity Chen et al. continued the use of the DAT group as an end group and to vary the core resulting in the synthesis of HOF-2,[123] HOF-3,[124] HOF-4,[125] HOF-5,[126] HOF-6,[127] HOF-7.[128] Recently, HOF-11[129] was also synthesized but the end group used was a carboxylic acid group was used instead of the DAT moiety. Most of these HOFs have shown potential application in gas separation with a few displaying other applications all of which will be highlighted below.

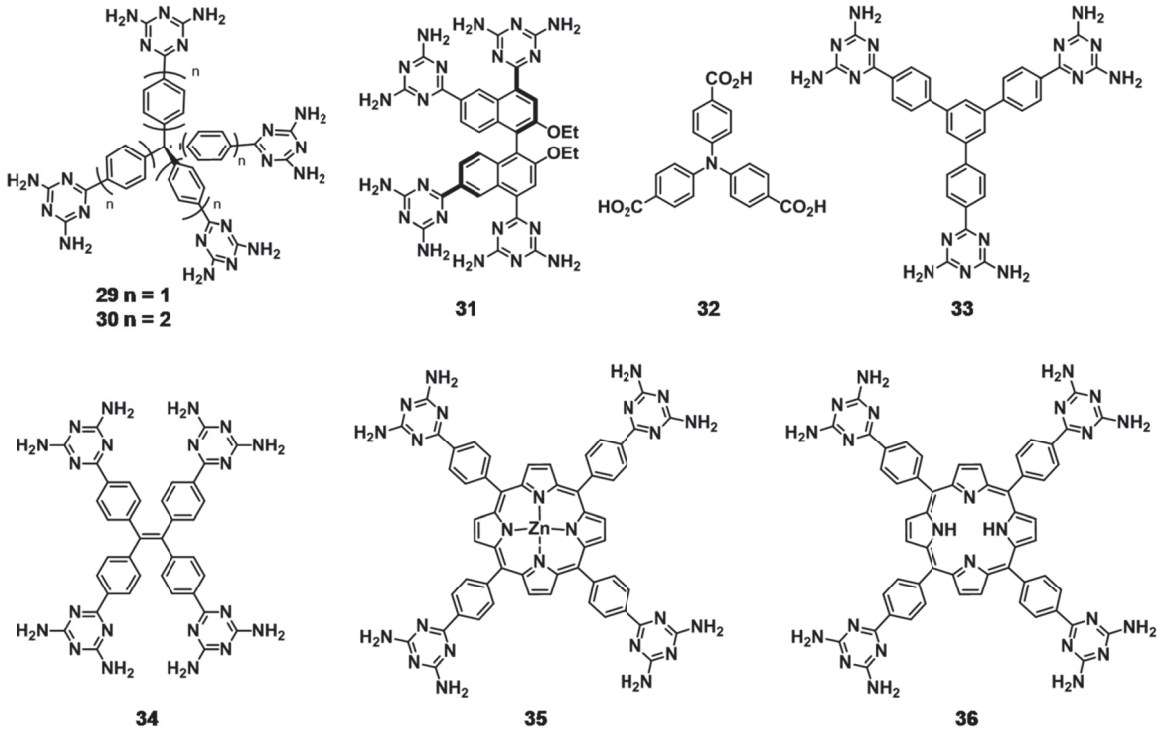

Figure 1.16 Structures of the precursors to other HOFs synthesized by Chen et al.[121–129]

1.4.4 Applications of Hydrogen-Bonded Organic Frameworks (HOFs)

Similar to MOFs and COFs, PMCs can also be utilized in applications that take advantage of their porous nature. PMCs are the youngest member of this family of crystalline porous materials, hence not as much research has been conducted on their application. That is why this section will focus on the applications of HOFs as they have

been studied the most and have shown potential applications in gas separations and other fields.

1.4.4.1 HOFs with Potential Gas Separation Applications

Compound **30** (HOF-4)[125] is an extended tetrahedral DAT-terminated tecton of HOF-1, which crystallized as a sixfold interpenetrated HOF with a BET surface area of SA is 312 m^2 g^{-1}. Interpenetration is usually not viewed in a favorable light as it decreases in pore volume and overall porosity of frameworks. However, the interpenetration of this extended framework has proven to be favorable as it resulted in it possessing superior properties for the separation of ethene from ethane. It was experimentally determined that HOF-4 adsorbed 17.3 cm^3 g^{-1} at 273 K and 11.1 cm^3 g^{-1} at 296 K . This was found to be three times higher than quantity of ethane adsorbed which was 5.1 cm^3 g^{-1} at 273 K and 3.6 cm^3 g^{-1} at 296 K at 1 atm. Furthermore, calculations indictated that at a total pressure of 100 kPa and 296 K, HOF-4 displayed adsorption selectivity of ethene from ethane that was comparable to that of zeolites.

Compound **33** (HOF-3),[124] base on a trigonal planar DAT-terminated tecton was then reported. It crystallized into a rodpacking HOF with a BET surface area of 165 m^2 g^{-1} and displayed a twofold preference for binding acetylene in the presence of CO_2. This selectivity, while moderate, is still extremely unusual since the two gases have similar geometries, dimensions, and boiling points.

Shortly afterwards, compound **34** (HOF-5)[126] a framework based on the tetraphenylehtylene tecton was prepared. This HOF was both porous (SA_{BET} = 1101 m^2 g^{-1}) and flexible, as well as displaying the highest CO_2 uptake of all the HOFs reported by Chen's group. HOF-5 displayed a stepwise nitrogen adsorption isotherm and this was an

indication of the flexible nature of this compound as similar stepwise isotherms were documenteded for flexible MOFs.

Then came the porphyrin-based compound **35** (HOF-7)[128] which was based on a metalloporphyrin tecton and possessed a surface are of 124 $m^2 g^{-1}$. This HOF displayed a CO_2/N_2 selectivity of 15:85 in a total pressure of 0–1 bar at 273 K. This selectivity is quite high and is comparable to that reported for some MOFs.[130,131]

Recently compound **32** was reported by Chen and et al.[129] It is a HOF based on a trigonal triphenylamine tecton with carboxyl acids endgroups and was dubbed HOF-11. Compound **32** possessed a surface area of 687 $m^2 g^{-1}$. It also exhibited selective capture of acetylene over methane, CO_2 over methane, and CO_2 over N_2 demonstrating its potential for the use in gas separation application.

1.4.4.2 Other applications of HOFs

The literature has also shown that HOFs have applications other than gas storage and separations, such as the separation of enantiomers and proton conductivity which will be discussed in this section.

Compound **31** (HOF-2)[123] consists of the DAT end group attached to the chiral scaffold of 1,1′-bi-2-naphthol (BINOL) to produce a precursor to a homochiral and microporous framework. The BET surface area of this framework was 238 $m^2 g^{-1}$, but its chiral porous nature allowed for its use in the separation of enantiomers of secondary alcohols. In general, higher enantiomeric excesses of the *R*-enantiomers were observed for alcohols with aromatic groups (92% ee for 1-phenylethanol) relative to their aliphatic counterparts (ee's ranging from <4% for 2- heptanol to 77% for 2-butanol).

Compound **36** (HOF-6)[127] which is based on metal-free porphyrin tecton with DAT endgroups and resulted in a microporous framework with a BET surface area of 130 $m^2\ g^{-1}$. This displays proton conductivity in the hydrated form, which can be attributed to the metal-free porphyrin core as studies have shown them to be effective proton donors.[132] Chen et al.[133] speculated that the combination of the metal free porphyrin core protons and the DAT endgroups in this framework might be able to serve as Lewis acids to effectively provide protons as well and thus afford special proton-conducting pathways. The end result proved this postulate to be correct resulting in a framework with proton conductivity values comparable to polyoxometalate-based nanotubes[133] and MOF UiO-66[134] indication this HOF has the potential to be used in proton conduction materials.

1.4.4 Conclusions and Outlook

In, summary, this class of porous crystalline materials offers the distinct advantage of solution processability over MOFs and COFs. Unfortunately this property has been under explored in the literature with a few examples such as the use of an organic cage in solution for the formation of composite membranes.[135] Overall, this field is still in its infancy when compared to MOFs and COFs as molecular crystals can either form crystalline structures with voids or amorphous solids with interconnected and disordered pores. The most porous of these molecular crystals so far are the intrinsically porous triptycene benzimidazolone (SA_{BET} = 2796 $m^2\ g^{-1}$) developed by Mastalerz et al.[115] This value is somewhat comparable to the levels of porosity found in COFs but not as comparable to the levels of porosity found in MOFs. Even with all of these initial shortcomings the future for this field still looks bright as numerous applications for PMCs other than gas separations have appeared in the literature. These include fullerene

capture,[127] uranium capture,[136] fluorocarbon capture,[137,138] ion absorption,[139] proton conduction,[140] enantioseparations,[123] and hydrocarbon separation.[141] Also the unpredictable nature of noncovalent supramolecular assembly that has made the specific design of molecular crystals difficult could be set to change in the near future thanks to computational studies[142] and the use of energy-structure-function maps.[143]

References

1. Schüth, F.; Sing, K. S. W.; Weitkamp, J. *Handbook of Porous Solids,* John Wiley & Sons: Hoboken, NJ, **2002**.
2. Rouquerol, J.; Avnir, D.; Fairbridge, C. W.; Everett, D. H.; Haynes, J. H.; Pernicone, N.; Ramsay, J. D. F.; Sing, K. S. W.; Unger, K. K. *Pure Appl. Chem.* **1994**, *66*, 1739–1758.
3. Akhtar, F.; Andersson, L.; Ogunwumi, S.; Hedin, N.; Bergström, L. *J. Eur. Ceramic Soc.* **2014**, 34, 1643–1666.
4. Król, M.; Mozgawa, W.; Jastrzębski, W. *J. Porous Mater.* **2016**, *23*, 1–9.
5. Degnan Jr., T. F. *Top. Catal.* **2000**, *13*, 349–356.
6. Cronstedt, A. F., *Akad. Handl. 18*, *Stockholm* **1756**, *18*, 120–125.
7. Cui, Y.; Li, B.; He, H.; Zhou, W.; Chen, B.; Qian; G. *Acc. Chem. Res.* **2016**, *49*, 483−493.
8. Bosch, M.; Yuan, S.; Rutledge, W.; Zhou, H.-C. *Acc. Chem. Res.* **2017**, *50*, 857−865.
9. Liu, D.; Zou, D.; Zhu, H.; Zhang, J. *Small* **2018**, *14*, 1801454.
10. Diercks, C. S.; Kalmutzki, M. J.; Yaghi, O. M. *Molecules* **2017**, 22, 1575, doi:10.3390/molecules22091575.
11. Zhao, F.; Liu, H.; Mathe, S. D. R.; Dong, A.; Zhang, J. *Nanomaterials* **2018**, *8*, 15, doi:10.3390/nano8010015.
12. Hashim, M. I.; Hsu, C.-W.; Le, H. T. M.; Miljanić, O. Š. *Synlett* **2016**, *27*, 1907–1918.

13. Han, Yi-Fei; Yuan, Ying-Xue; Wang, Hong-Bo *Molecules* **2017**, *22*, 266, doi:10.3390/molecules22020266.

14. Hassell, T.; Copper, A. I. *Nat. Rev. Mater.* **2016**, *1*, 16053, doi:10.1038/natrevmats2016.53.

15. Werner, A. *Z. Anorg. Chem.* **1893**, *3*, 267–330.

16. Hofmann, K. A., Küspert, F. *Z. Anorg. Chem.***1897**, *15*, 204–207.

17. Rayner, J. H.; Powell, H. M. *J. Chem. Soc.* **1952**, 319–328.

18. Pfeiffer, P. *Organic Molecular Compounds*, Stuttgart, **1927**, 213.

19. Feigl, F. *Anais Assoc. Quim. Brasil*, **1944**, 3, 72.

20. Walker, F. G.; Hawthrone, D. G. *Trans. Faraday Soc.* **1967**, *63*, 166–174.

21. Iwamoto, T.; Miyoshi, T.; Miyamoto, T.; Sasaki, Y.; Fujiwara S. *Bull. Chem. Soc. Jpn.* **1967**, *40*, 1174–1178.

22. Iwamoto, T.; Nakano, T.; Morita, M.; Miyoshi, T.; Miyamoto, T.; Sasaki, Y. *Inorg. Chim. Acta.* **1968**, *2*, 313–316.

23. Mathey, Y.; Mazières, C.; Setton, R. *Inorg. Nucl. Chem. Lett.* **1977**, *13*, 1–3.

24. Yaghi, O.M.; Li, H. *J. Am. Chem. Soc.* **1995**, *117*, 10401–10402.

25. Tomic, E. A. *J. Appl. Polym. Sci.* **1965**, *9*, 3745–3752.

26. Li, H.; Eddaoudi, M.; Groy, T. L.; Yaghi, O. M.; *J. Am. Chem. Soc.* **1998**, 120, 8571–8572.

27. Chui, S. Y.; Lo, S. M.-F.; Charmant, J. P. H.; Orpen, A. G.; Williams, I. D. *Science* **1999**, *283*, 1148–1150.

28. Li, H., Eddaoudi, M., O'Keeffe, M., Yaghi, O.M. *Nature* **1999**, *402*, 276–279.

29. Farha, O. K.; Eryazici, I.; Jeong, N. C.; Hauser, B. G.; Wilmer, C. E.; Sarjeant, A. A.; Snurr, R. Q.; Nguyen, S. T.; Yazaydin, A. O.; Hupp, J. T. *J. Am. Chem. Soc.* **2012**, 134, 15016–15021.

30. Ma, X.; Yang, H.; Yu, L.; Chen, Y.; Li, Y. *Materials* **2014**, *7*, 4431–4441.

31. García-Martínez, J.; Johnson, M.; Valla, J.; Kunhao, L.; Ying, J. Y. *Catal. Sci. Technol.* **2012**, *2*, 987–994.

32. Dey, C.; Kundu, T.; Biswal, B. P.; Mallick, A.; Banerjee, R. *Acta. Cryst*. **2014**, *B70*, 3–10.

33. Joaristi, A. M.; Juan-Alcañiz, J.; Serra-Crespo, P.; Kapteijn, F.; Gascon, J. *Cryst. Growth. Des*. **2012**, *12*, 3489 –3498.

34. Müeller, U.; Puetter, H.; Hesse, M.; Wessel, H. *Patent* WO 2005/049892, 2005.

35. Geydye, R.; Smith, F.; Westaway, K.; Ali, H.; Baldisera, L.; Laberge, L.; Rousell, J. *Tetrahedron Lett.* **1986**, *27*, 279–282.

36. Taddei, M.; Dau, P. V.; Cohen, S. M.; Ranocchiari, M.; van Bokhoven, J. A.; Costantino, F.; Sabatini, S.; Vivani, R. *Dalton Trans.* **2015**, *44*, 14019–14026.

37. Suslick, K. S.; Flannigan, D. J. *Annu. Rev. Phys. Chem.* **2008**, *59*, 659–683.

38. Son, W.-J.; Kim, J.; Kim, J.; Ahn, W.-S. *Chem. Commun.* **2008**, *47*, 6336–6338.

39. Carson, C. G.; Brown, A. J.; Sholl, D. S.; Nair, S. *Cryst. Growth Des.* **2011**, *11*, 4505–4510.

40. Carlier, L.; Baron, M.; Chamayou, A.; Couarraze, G. *Tetrahedron Lett.* **2011**, *52*, 4686–4689.

41. Friščić, T. *Chem. Soc. Rev*. **2012**, *41*, 3493–3510.

42. Stock, N.; Biswas, S. *Chem. Rev*. **2012**, *112*, 933–969.

43. Yaghi, O. M.; O'Keeffe, M.; Ockwig, N. W.; Chae, H. K.; Eddaoudi, M.; Kim, J.; *Nature* **2003**, *423*, 705–714.

44. Guillerm, V.; Gross, S.; Serre, C.; Devic, T.; Bauer, M.; Férey, G. *Chem. Commun.* **2010**, *46*, 767–769.

45. Deshpande, R. K.; Minnaar, J. L.; Telfer, S. G. *Angew. Chem. Int. Ed.* **2010**, *49*, 4598–4602.

46. Brozek, C. K.; Michaelis, V. K.; Ong, T.-C.; Bellarosa, L.; López, N.; Griffen, R. G.; Dincă, M. *ACS Cent. Sci.* **2015**, *1*, 252 – 260.

47. Brozek, C. K.; Dincă, M. *Chem. Soc. Rev*. **2014**, *43*, 5456–5467.

48. Li, T.; Kozlowski, M. T.; Doud, E. A.; Blakely, M. N.; Rosi, N. L. *J. Am. Chem. Soc.* **2013**, *135*, 11688–11691.

49. Ahmad, M. Z.; Navarro, M.; Lhotka, M.; Zornoza, B.; Tellez, C.; de Vos, W. M.; Benes, N. E.; Konnertz, N. M.; Visser, T.; Semino, R.; Maurin, G.; Fila,V.; Coronas, J. *J. Memb. Sci.* **2018**, *558*, 64–77.

50. Assen, A. H.; Yassine, O.; Shekhah, O.; Eddaoudi, M. *ACS Sens.* **2017**, *2*, 1294–1301

51. Wu, C.-D.; Zhao, M. *Adv. Mater.* **2017**, *29*, 1605446.

52. Jiang, K.; Zhang, L.; Hu, Q.; Yang, Y.; Lin, W.; Cui, Y.; Yang, Y.; Qian, G. *Matter. Lett.* **2018**, *225*, 142–144.

53. Murray, L. J.; Dincă, M.; Long, J. R. *Chem. Soc. Rev.* **2009**, *38*, 1294–1314.

54. Furukawa, H.; Ko, N.; Go, Y. B.; Aratani, N.; Choi, Y. B.; Choi, E.; Yazaydin, A. O.; Snurr, R. Q.; O'Keeffe, M.; Kim, J.; Yaghi, O. M. *Science* **2010**, *329*, 424–428.

55. Koh, K.; Wong-Foy, A. G.; Matzger, A. J. *J. Am. Chem. Soc.* **2009**, *131*, 4184–4185.

56. He, Y.; Zhou, W.; Qian, G.; Chen, B. *Chem. Soc. Rev.* **2014**,*43*, 5657–5678.

57. Peng, Y.; Krungleviciute, V.; Eryazici, I.; Hupp, J. T.; Farha, O. K.; Yildirim, T. *J. Am. Chem. Soc.* **2013**, *135*, 11887–11894.

58. Tian, T.; Zeng, Z.; Vulpe, D.; Casco, M. E.; Divitini, G.; Midgley, P. A.; Silvestre-Albero, J.; Tan, J.-C.; Moghadam, P. Z.; Fairen-Jimenez, D. *Nat. Mater.* **2018**, *17*, 177–180.

59. Beaudoin, D.; Maris, T.; Wuest, J. D. *Nat. Chem.* **2013**, *5*, 830–834.

60. Côté, A. P.; Benin, A. I.; Ockwig, N. W.; O'Keeffe, M.; Matzger, J.; Yaghi, O. M. *Science* **2005**, *310*, 1166–1170.

61. Tsyurupa, M. P.; Davankov, V. A. *React. Funct. Polym.* **2002**, *53*, 193–203.

62. Budd, P. M.; Ghanem, B. S.; Makhseed, S.; McKeown, N. B.; Msayib, K. J.; Tattershall, C. E. *Chem. Commun.* **2004**, 230–231.

63. Jiang, J.-X.; Su, F.; Trewin, A.; Wood, C. D.; Campbell, N. L.; Niu, H.; Dickinson, C.; Ganin, A. Y.; Rosseinsky, M. J.; Khimyak, Y. Z.; Cooper, A. I. *Angew. Chem. Int. Ed.* **2007**, *46*, 8574–8578.

64. Rowan, S. J.; Cantrill, S. J.; Cousins, G. R. L.; Sanders, J. K. M.; Stoddart, J. F. *Angew. Chem. Int. Ed.* **2002**, *41*, 898−952.

65. Tilford, R. W.; Gemmill, W. R.; zur Loye, H.-C.; Lavigne, J. J. *Chem. Mater.* **2006**, *18*, 5296–5301.

66. Spitler, E. W; Dichtel, W. R. *Nat. Chem.* **2010**, *2*, 672–677.

67. Colson, J.W.; Woll, A. R.; Mukherjee, A.; Levendorf, M. P.; Spitler, E. L.; Shields, V. B.; Spencer, M. G.; Park, J.; Dichtel, W. R. *Science* **2011**, *332*, 228–231.

68. Kuhn, P.; Antonietti, M.; Thomas, A. *Angew. Chem. Int. Ed.* **2008**, *47*, 3450–3453.

69. Guan, X.; Ma, Y.; Li, H.; Yusran, Y.; Xue, M.; Fang, Q.; Yan, Y.; Valtchev, V.; Qiu, S. *J. Am. Chem. Soc.* **2018**, *140*, 4494−4498.

70. Nagai, A.; Guo, Z.; Feng, X.; Jin, S.; Chen, X.; Ding, X.; Jiang, D. *Nat. Commun.* **2011**, *2*, 536–543.

71. Lu, Q.; Ma, Y.; Li, H.; Guan, X.; Yusran, Y.; Xue, M.; Fang, Q.; Yan, Y.; Qiu, S.; Valtchev, V. *Angew. Chem. Int. Ed.* **2018**, *57*, 604 –6048.

72. Zhang, G.; Tsujimoto, M.; Packwood, D.; Duong, N. T.; Nishiyama, Y.; Kadota, K.; Kitagawa, S.; Horike, S. *J. Am. Chem. Soc.* **2018**, *140*, 2602−2609.

73. Liu, Y.; Ma, Y.; Zhao, Y.; Sun, X.; Gándara, F.; Furukawa, H.; Liu, Z.; Zhu, H.; Zhu, C.; Suenaga, K.; Terasaki, O.; Yaghi, O. M. *Science* **2016**, *351*, 365–369.

74. Han, X.; Huang, J.; Yuan, C.; Liu, Y.; Cui, Y. *J. Am. Chem. Soc.* **2018**, *140*, 892–895.

75. Pramudya, Y.; Mendoza-Cortes, J. L.; *J. Am. Chem. Soc.* **2016**, *138*, 15204–15213.

76. Wang, X.; Han, X.; Zhang, J.; Wu, X.; Liu, Y.; Cui, Y. *J. Am. Chem. Soc.* **2016**, *138*, 12332–12335.

77. Xu, H.; Tao, S.S.; Jiang, D.L. *Nat. Mater.* **2016**, *15*, 722–726.

78. Han, S. S.; Furukawa, H.; Yaghi, O. M.; Goddard, W. A. *J. Am. Chem. Soc.* **2008**, *130*, 11580–11581.

79. Han, S. S.; Deng, W.-Q.; Goddard, W. A. *Angew. Chem. Int. Ed.* **2007**, *46*, 6289–6292.

80. El-Kaderi, H. M.; Hunt, J. R.; Mendoza-Cortés, J. L.; Côté, A. P.; Taylor, R. E.; O'Keeffe, M.; Yaghi, O. M.; *Science* **2007**, *316*, 268–272.

81. Cao, D.; Lan, J.; Wang, W.; Smit, B. *Angew. Chem. Int. Ed.* **2009**, *48*, 4730–4733.

82. Holst, J. R.; Trewin, A.; Cooper, A. I. *Nat. Chem.* **2010**, *2*, 915–920.

83. Dianin, J. *J. Russ. Phys. Chem. Soc.* **1914**, *46*, 1310–1319.

84. Barrer, R. M.; Shanson, V. H. *J. Chem. Soc., Chem. Commun.* **1976**, 9, 333–334

85. Atwood, J. L.; Barbour, L. J.; Jerga, A.; Schottel, B. L. *Science* **2002**, *298*, 1000–1002.

86. Sozzani, P.; Bracco, S.; Comotti, A.; Ferretti, L.; Simonutti, R. *Angew. Chem. Int. Ed.* **2005**, *44*, 1816–1820.

87. Soldatov, D. V.; Moudrakovski, I. L.; Ripmeester, J. A. *Angew. Chem. Int. Ed.* **2004**, *43*, 6308–6311.

88. Shimizu, L. S.; Hughes, A. D.; Smith, M. D.; Davis, M. J.; Zhang, B. P.; zur Loye, H.-C.; Shimizu, K. D. *J. Am. Chem. Soc.* **2003**, *125*, 14972–14973.

89. Xu, Y.; Smith, M. D.; Geer, M. F.; Pellechia, P. J.; Brown, J. C.; Wibowo, A. C.; Shimizu, L. S. *J. Am. Chem. Soc.* **2010**, *132*, 5334–5335.

90. Msayib, K. J.; Book, D.; Budd, P. M.; Chaukura, N.; Harris, K. D. M.; Helliwell, M.; Tedds, S.; Walton, A.; Warren, J. E.; Xu, M.; McKeown, N. B. *Angew. Chem. Int. Ed.* **2009**, *48*, 3273–3277.

91. Evans, J. D.; Huang, D. M.; Haranczyk, M.; Thornton, A. W.; Sumby, C. J.; Doonan, C. J. *CrystEngComm* **2016**, *18*, 4133–4141

92. Tozawa, T.; Jones, J. T. A.; Swamy, S. I.; Jiang, S.; Adams, D. J.; Shakespeare, S.; Clowes, R.; Bradshwa, D.; Hasell, T.; Chong, S. Y.; Tang, C.; Thompson, S.; Parker, J.; Trewin, A.; Bacsa, J.; Slawin, A. M. Z.; Steiner, A.; Cooper, A. I. *Nat. Mater.* **2009**, *8*, 973–978.

93. Mitra, T.; Wu, X.; Clowes, R.; Jones, J. T. A.; Jelfs, K. E.; Adams, D. J.; Trewin, A.; Bacsa, J.; Steiner, A.; Cooper, A. I. *Chem. Eur. J.* **2011**, *17*, 10235–102040.

94. Jones, J. T. A.; Holden, D.; Mitra, T.; Hasell, T.; Adams, D. J.; Jelfs, K. E.; Trewin, A.; Willock, D. J.; Day, G. M.; Bacsa, J.; Steiner, A.; Cooper, A. I. *Angew. Chem. Int. Ed.* **2011**, *50*, 749–753.

95. Culshaw, J. L.; Cheng, G.; Schmidtmann, M.; Hasell, T.; Liu, M.; Adams, D. J.; Cooper, A. I. *J. Am. Chem. Soc.* **2013**, *135*, 10007–10010.

96. Hasell, T.; Schmidtmann, M.; Cooper, A. I. *J. Am. Chem. Soc.* **2011**, *133*, 14920–14923.

97. Jones, J. T. A.; Hasell, T.; Wu, X.; Bacsa, J.; Jelfs, K. E.; Schmidtmann, M.; Chong, S. Y.; Adams, D. J.; Trewin, A.; Schiffman, F.; Cora, F.; Slater, B.; Steiner, A.; Day, G. M.; Cooper, A. I. *Nature* **2011**, *474*, 367–371.

98. Hasell, T.; Chong, S. Y.; Schmidtmann, M.; Adams, D. J.; Cooper, A. I. *Angew. Chem. Int. Ed.* **2012**, *51*, 7154–7157.

99. Jiang, S.; Bacsa, J.; Wu, X.; Jones, J. T. A.; Dawson, R.; Trewin, A.; Adams, D. J.; Cooper, A. I. *Chem. Commun.* **2011**, *47*, 8919–8921.

100. Jelfs, K. E.; Wu, X.; Schmidtmann, M.; Jones, J. T. A.; Warren, J. E.; Adams, D. J.; Cooper, A. I. *Angew. Chem. Int. Ed.* **2011**, *50*, 10653–10657.

101. Giri, N.; Davidson, C. E.; Melaugh, G.; Del Pópolo, M. G.; Jones, J. T. A.; Hasell, T.; Cooper, A. I.; Horton, P. N.; Hursthouse, M. B.; James, S. L. *Chem. Sci.* **2012**, *3*, 2153–2157.

102. Giri, N.; Del Pópolo, M. G.; Melaugh, G.; Greenaway, R. L.; Rätzke, K.; Koschine, T.; Pison, L.; Costa Gomes, M. F.; Cooper, A. I.; James, S. L. *Nature* **2015**, *527*, 216–220.

103. Greenway, R. L.; Holden, D.; Eden, E. G. B.; Stephenson, A.; Yong, C. W.; Bennison, M. J.; Hasell, T.; Briggs, M. E.; James, S. L.; Cooper, A. I.; *Chem. Sci.* **2017**, *8*, 2640–2651.

104. Mastalerz, M. *Chem. Commun.* **2008**, 4756–4758.

105. Mastalerz, M.; Schneider, M. W.; Oppel, I. M.; Presly, O. *Angew. Chem. Int. Ed.* **2011**, *50*, 1046–1051.

106. Schneider, M. W.; Oppel, I. M.; Ott, H.; Lechner, L. G.; Hauswald, H.-J. S.; Stoll, R.; Mastalerz, M. *Chem. Eur. J.* **2012**, *18*, 836–847.

107. Brutschy, M.; Schneider, M. W.; Mastalerz, M.; Waldvogel, S. R. *Adv. Mater.* **2012**, *24*, 6049–6052.

108. Brutschy, M.; Schneider, M. W.; Mastalerz, M.; Waldvogel, S. R. *Chem. Commun.* **2013**, *49*, 8398–8400.

109. Elbert, S. M.; Rominger, F.; Mastalerz, M. *Chem. Eur. J.* **2014**, *20*, 16707–16720.

110. Mastalerz, M. *Synlett* **2013**, *24*, 781–786.

111. Jin, Y. H.; Voss, B. A.; Jin, A.; Long, H.; Noble, R. D.; Zhang, W. *J. Am. Chem. Soc.* **2011**, *133*, 6650–6658.

112. Zhang, G.; Presly, O.; White, F.; Oppel, I. M.; Mastalerz, M. *Angew. Chem. Int. Ed.* **2014**, *53*, 1516–1520.

113. Zhang, G.; Presly, O.; White, F.; Oppel, I. M.; Mastalerz, M. *Angew. Chem. Int. Ed.* **2014**, *53*, 5126–5130.

114. Elbert, S. M.; Regenauer, N. I.; Schindler, D.; Zhang, W.-S.; Rominger, F.; Schröder, R. R.; Mastalerz, M. *Chem. Eur. J.*, **2018**, *24*, 11438–11443.

115. Mastalerz, M.; Oppel, I. M. *Angew. Chem. Int. Ed.* **2012**, *51*, 5252–5255.

116. Schwiebert, K. E.; Chin, D. N.; MacDonald, J. C.; Whitesides, G. M. *J. Am. Chem. Soc.* **1996**, *118*, 4018–4029.

117. Sumida, K.; Rogow, D. L.; Mason, J. A.; McDonald, T. M.; Bloch, E. D.; Herm, Z. R.; Bae, T.-H.; Long, J. R. *Chem. Rev.* **2012**, *112*, 724–781.

118. Kohl, B.; Rominger, F.; Mastalerz, M. *Org. Lett*. **2014**, *16*, 704–707.

119. Kohl, B.; Rominger, F.; Mastalerz, M. *Chem. Eur. J.* **2015**, 21, 17308–17313.

120. Taylor, R. G. D.; Carta, M.; Bezzu, C. G.; Walker, J.; Msayib, K. J.; Kariuki, B. M.; McKeown, N. B. *Org. Lett.* **2014**, *16*, 1848–1851.

121. He, Y.; Xiang, S.; Chen, B. *J. Am. Chem. Soc.* **2011**, *133*, 14570–14573.

122. Brunet, P.; Simard, M.; Wuest, J. D. J. *Am. Chem. Soc.*, **1997**, 119, 2737–2738.

123. Li, P; He, Y.; Guang, J.; Weng, L.; Zhao, J. C.-G.; Xiang, S.; Chen, B. *J. Am. Chem. Soc.* **2014**, *136*, 547–549.

124. Li, P.; He, Y.; Zhao, Y.; Weng, L.; Wang, H.; Krishna, R.; Wu, H.; Zhou, W.; O'Keeffe, M.; Han, Y.; Chen, B. *Angew. Chem. Int. Ed.* **2014**, *54*, 574–577.

125. Li, P.; He, Y.; Arman, H. D.; Krishna, R.; Wang, H.; Weng, L.; Chen, B. *Chem. Commun.* **2014**, *50*, 13081–13084.

126. Wang, H.; Li, B.; Wu, H.; Hu, T.-L.; Yao, Z.; Zhou, W.; Xiang, S.; Chen, B. *J. Am. Chem. Soc.* **2015**, *137*, 9963–9977.

127. Yang, W.; Yang, F.; Hu, T.-L.; King, S. C.; Wang, H.; Wu, H.; Zhou, W.; Li, J.-R.; Arman, H. D.; Chen, B. *Cryst. Growth Des.* **2015**, *16*, 5831–5835.

128. Yang, W; Li, B.; Wang, H.; Alduhaish, O.; Alfooty, K.; Zayed, M A.; Li, P.; Arman, H. D.; Chen, B. *Cryst. Growth Des.* **2015**, *15*, 2000–2004.

129. Yang, W.; Wang, J.; Wang, H.; Bao, Z.; Zhao, J. C.-G.; Chen, B. *Cryst. Growth Des.* **2017**, *17*, 6132–6137.

130. Dietzel, P. D. C.; Besikiotis, V.; Blom, R. *J. Mater. Chem.* **2009**, *19*, 7362–7370.

131. Bae, Y.-S.; Farha, O. K.; Hupp, J. T.; Snurr, R. Q. J. *Mater. Chem.* **2009**, *19*, 2131–2134.

132. Motoyama, S.; Makiura, R.; Sakata, O.; Kitagawa, H. *J. Am. Chem. Soc.* **2011**, *133*, 5640−5643.

133. Xu, H.; Tao, S.; Jiang, D. *Nat. Mater.* **2016**, *15*, 722−726.

134. Yang, F.; Huang, H.; Wang, X.; Li, F.; Gong, Y.; Zhong, C.; Li, J.-R. *Cryst. Growth Des.* **2015**, *15*, 5827−5833.

135. Jiang, S.; Chen, L.; Briggs, M. E.; Hasell, T.; Cooper, A. I. *Chem. Commun.* **2016**, *52*, 6895−6898.

136. Li, B.; Bai, C. Y.; Zhang, S.; Zhao, X. S.; Li, Y.; Wang, L.; Ding, K.; Shu, X.; Li, S. J.; Ma, L. J. *J. Mater. Chem. A* **2015**, *3*, 23788−23798.

137. Chen, T.-H.; Popov, I.; Kaveevivitchai, W.; Chuang, Y. C.; Chen, Y. S.; Daugulis, O.; Jacobson, A. J.; Miljanić, O. Š. *Nat. Commun.* **2014**, *5*, doi: 10.1038/ncomms6131.

138. Chen, T.-H.; Kaveevivitchai, W.; Jacobson, A. J.; Miljanić, O. Š. *Chem. Commun.* **2015**, *51*, 14096–14098.

139. Tian, J.; Zhou, T. Y.; Zhang, S. C.; Aloni, S.; Altoe, M. V.; Xie, S. H.; Wang, H.; Zhang, D. W.; Zhao, X.; Liu, Y.; Li, Z. T. *Nat. Commun.* **2014**, *5*, doi: 10.1038/ncomms6574.

140. Yang, W. B.; Greenaway, A.; Lin, X. A.; Matsuda, R.; Blake, A. J.; Wilson, C.; Lewis, W.; Hubberstey, P.; Kitagawa, S.; Champness, N. R.; Schroder, M. *J. Am. Chem. Soc.* **2010**, *132*, 14457−14469.

141. Jelfs, K. E.; Cooper, A. I. *Solid State Mater. Sci.* **2013**, *17*, 19−30.

142. Evans, J. D.; Jelfs, K. E.; Day, G. M.; Doonan, C. J. *Chem. Soc. Rev.* **2017**, *46*, 3286–3301.

143. Pulido, A.; Chen, L.; Kaczorowski, T.; Holden, D.; Little, M. A.; Chong, S. Y.; Slater, B. J.; McMahon, D. P.; Bonillo, B.; Stackhouse, C. J.; Stephenson, A.; Kane, C. M.; Clowes, R.; Hasell, T.; Cooper, A. I.; Day, G. M. *Nature* **2017**, *543*, 657−664.

Chapter Two

Synthesis of Fluorinated Organic Precursors to Porous Molecular Crystals (PMCs)

2.1 Fluorinated Porous Materials

Fluorine is the element with the highest electronegativity and a small electric polarizability. Hence, the incorporation of C–F bonds into a material can result in a variety of unique characteristics such as high thermal and chemical stability, low polarity, hydrophobicity and weak intermolecular interactions.[1,2] This has led to the utilization of fluorination to further the development of materials such as liquid crystals,[3,4] polymers,[5,6] surfactants,[7] membranes,[8,9] thin films,[10,11] agrochemicals,[12] and ionic liquids.[13]

There has also been a growing interest in the development of fluorinated MOFs as well, mainly in the hopes of preparing frameworks that possess higher thermal and chemical stability as well as enhanced hydrophobicity. The first fluorinated MOF called FMOF-1 (Fluorinated Metal Organic Framework-1), was developed by Omary et al.[14] in 2007. It was prepared by the reaction of Ag(I) with 3,5-bis (trifluoromethyl)-1,2,4-triazolate (Tz) in MeOH to yield colorless crystals upon evaporation. These crystals were then recrystallized from MeCN and PhMe. Examination of the crystal structure revealed a three-dimensional porous framework consisting of tetranuclear $[Ag_4(Tz)_6]$ clusters connected by three coordinate Ag(I) centers, displaying a BET surface area of 810 $m^2\ g^{-1}$.

This MOF also possessed large rectangular channels (~12.2 and 7.3 Å) and small diamond-shaped cavities (~6.6 and 4.9 Å) both coated with CF_3 groups of the fluorinated Tz ligands. This resulted in hydrophobic pores that adsorbed a negligible amount of water even at >90% relative humidity. These pores also remained intact when soaked in water

for days. Gas sorption of FMOF-1 showed a unique hysteretic sorption of H_2 and high uptake of O_2. This unique hysteretic sorption behavior was found to be indicative of the flexible nature of this framework. A later study conducted by the same group[15] found that the reversible breathing nature induced by gaseous guest molecules in FMOF-1 was due to the flexibility of Ag(I) coordination clusters and the fluorinated surface.[15] In particular the fluorinated surface with its low surface free energy and surface tension, was deemed necessary to further stabilize surface bending allowing for the storage of a large amount of mechanical energy during the breathing processes. It was also found that an annealed variant of FMOF-1 called FMOF-2, was capable of a high degree of adsorption of C6–C8 hydrocarbons such as benzene, toluene, *p*-xylene, cyclohexane and *n*-hexane, which are common oil components.[16]

Further research conducted by Omary et al.,[17] found that the hydrophobic cavities of FMOF-1 were suitable for studying the properties of water clusters within them. This ability to study water clusters within the pores was due to the negligible interaction of water molecules with the pore walls. Water molecules were confined in the hydrophobic cavities of FMOF-1. The MOF was then studied using Raman spectroscopy, IR spectroscopy, and theoretical calculations. The results suggested that a small number of pentameric water clusters were formed within the cavities at low pressures (800 mTorr). Theoretical calculations indicated that the binding energy between the water clusters and the CF_3-decorated walls was weakest and that hydrogen bonding of the water species dominates, leading to water cluster formation. The above mentioned properties represent some of the reasons for the increased interest in the preparation of fluorinated porous MOFs.

In the field of selective gas sorption, Bu et al.[18] developed a fluorinated MOF that displayed a high uptake of H_2 and CO_2 (5 and 40 wt %). In the field of gas separation, Chen et al.[19] reported a fluorinated MOF with a high adsorption capacity for acetylene (2.1 millimoles per gram at 0.025 bar) and high selectivity for the separation of acetylene/ethylene mixtures. Other applications that fluorinated MOFs are capable of also include the uptake of perfluoroalkanes,[20] ionic conduction,[21] proton conduction,[22] catalysis,[23] and oil/water separation.[24] With all of these unique properties resulting from the use of fluorinated linkers it seems worthwhile to explore and develop the field of fluorinated PMCs.

2.2 Fluorinated Porous Molecular Crystals [25]

Our group's journey in the field of PMCs began quite accidentally, with the initial goal being the preparation of rigid fluorinated organic ligands to be used in the synthesis of MOFs. These ligands were expected to form metal—ligand coordination bonds to yield robust porous three-dimensional networks. The focus was mainly on extensively fluorinated precursors as those showed the potential to result in porous materials with unique physicochemical properties, and because they were synthetically inaccessible targets at that time. A series of extensively fluorinated aromatic linkers with carboxylic acid, tetrazole and pyrazole end groups were synthesized (Figure 2.1A) and successfully incorporated into fluorinated MOFs (which we dubbed MOFFs).[26] An example of these synthesized MOFs is MOFF-5[27] (crystal structure is depicted in Figure 2.1B). This MOF was assembled from a trigonal tetrazolate ligand (compound **3**) and Cu^{2+}. It displayed a

BET surface area of 2445 m^2 g^{-1} which was the highest among fluorinated porous materials at that time.[28]

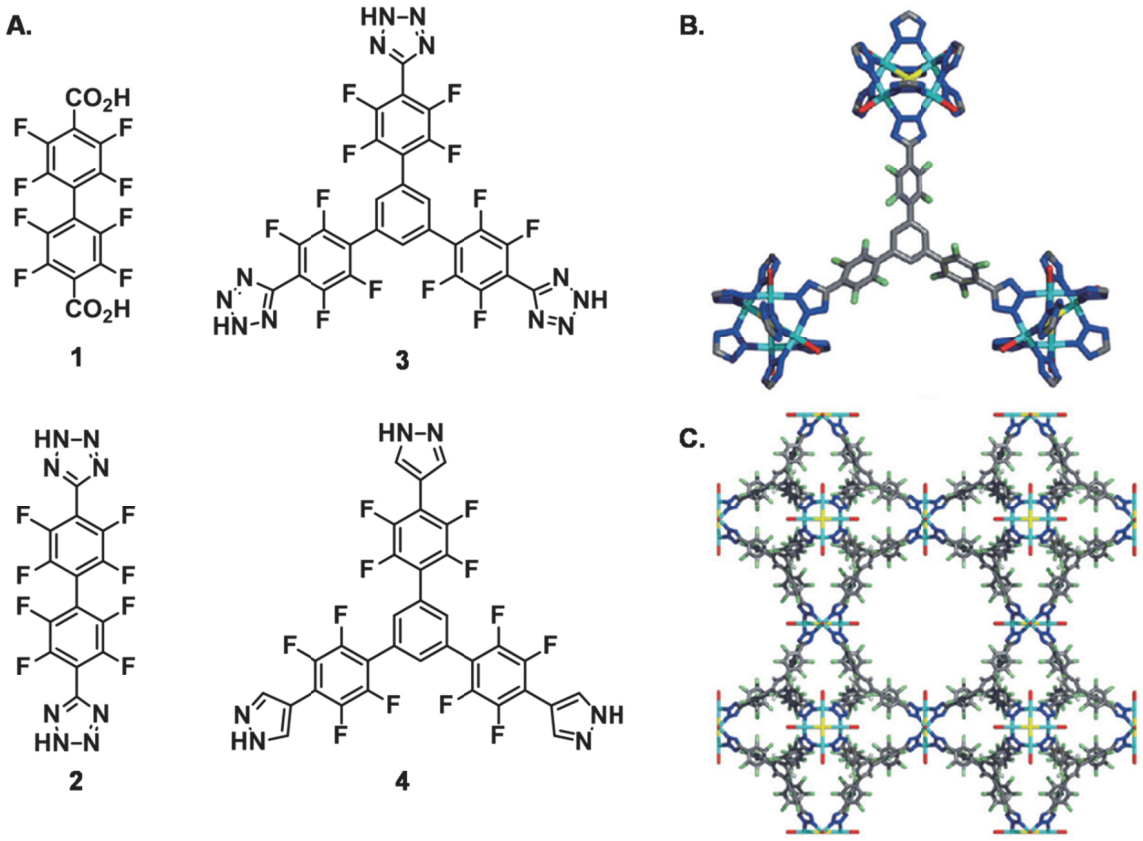

Figure 2.1 (A) A few selected extensively aromatic linkers used in MOFF preparation. (B) Structure of organic linker 3 attached to Cu metal node. (C) Overall crystal structure of MOFF-5. Element colors: Cu—cyan, C—gray, F—lime green, N—blue, O—red, Cl—yellow.[26]

The high porosity of MOFF-5 allowed high uptake of Freons, halocarbons, and fluorocarbons, but it was found to be somewhat labile in the presence of water and even moist air. This behavior could be attributed to the lower basicity of fluorinated tetrazolates when compared to the respective non-fluorinated counterparts, resulting in

the formation of weaker coordination bonds to the metal. To avoid this issue and improve the stability of our MOFs the tris-tetrazole linker **3** was substituted with the more basic trispyrazolate linker (**4** deprotonated), which was synthesized according to Scheme 2.1. The starting material for this synthesis was 1,2,4,5-tetrafluorobenzene; one of its two C–H bonds was first activated with copper to couple with *N*-protected iodopyrazole **6**, giving intermediate compound **7**. This species was then subjected to a threefold coupling with 1,3,5-triiodobenzene to give compound **8**. The trityl protecting groups in compound **8** were then exchanged for the more thermolabile Boc groups in order to yield a MOF precursor linker **9**. With this precursor in hand, a standard protocol for the in-situ removal of the Boc group to synthesize a MOF was attempted. The underlying theory was that in hot DMF, thermolysis of the Boc group was anticipated, thus yielding compound **4** with three free N–H functionalities. This compound could then be slowly deprotonated into its pyrazolate form by the dimethylamine formed in situ by the thermolysis of DMF. This pyrazolate compound could then slowly coordinate to the metal yielding the desired MOF crystals.

The exposure of compound **8** to $ZrCl_4$ (which served as the metal source) under solvothermal conditions resulted in single crystals that were poorly diffracting. Therefore, the structure had to be resolved at the Argonne National Laboratory synchrotron facility. Initial examination of the crystal data revealed the absence of the metal within the crystal structure and that only the linker was present. Further examination of the crystal structure revealed that it was indeed porous and had hexagonal pores that protrude through the crystal along the *c*-axis (Figure 2.2).[28] The new framework was held together by a triplet of [N–H···N] hydrogen bonds that connected three pyrazoles (Figure 2.2) at every other

trigonal junction, forming an infinite two-dimensional hexagonal sheet. These sheets stacked on top of each other through electronically favorable [π···π] stacking between the electron-rich pyrazoles and electron-poor tetrafluorobenzenes (Figure 2.2).

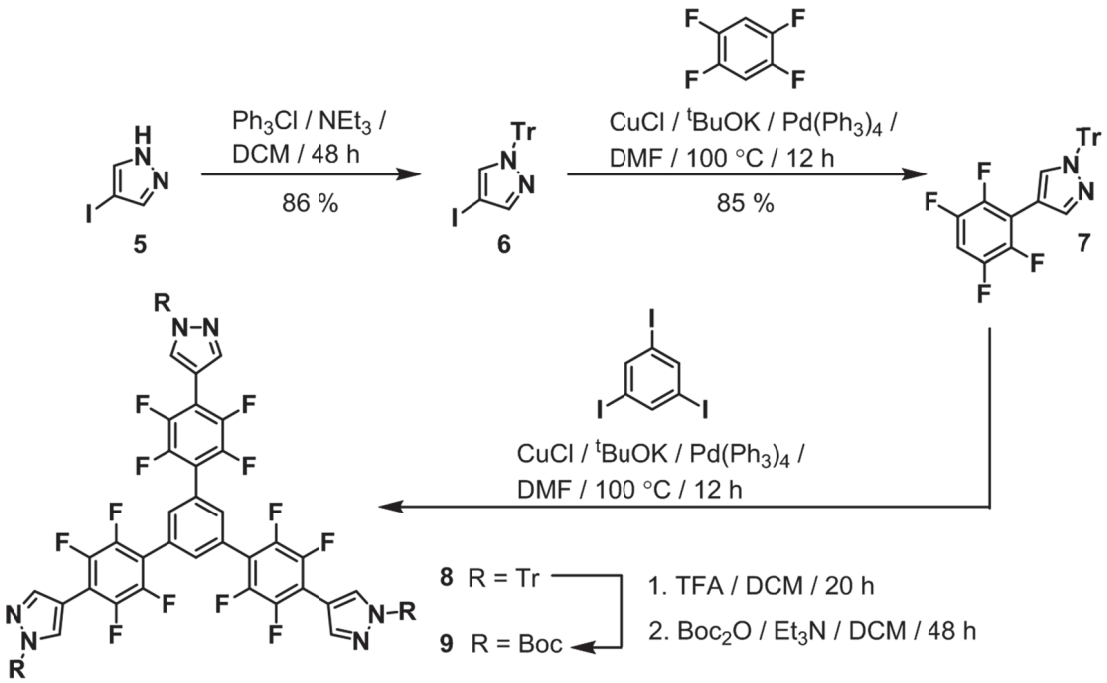

Scheme 2.1 Synthesis of a trigonal extensively fluorinated pyrazole precursor to porous molecular crystals.

As this extended structure was only connected by weak noncovalent bonds, initially there was a concern that it would be unstable and the pores would collapse upon activation. Fortuitously, this did not take place as thermogravimetric and variable-temperature powder X-ray diffraction analyses confirmed the stability of the structure up to 250 °C. Gas sorption studies also indicated that this framework possessed a BET surface area of 1159 m^2 g^{-1}. Furthermore, this framework was found to be chemically resistant towards water, as well as dilute acids and bases.[28] In hindsight, this outcome was not completely unexpected as pyrazoles do not react with water and are weakly acidic

and basic. This discovery meant that our framework was more stable than MOFs and COFs which possessed hydrolytically labile linkers such as imines or boronate esters. These extrinsically porous crystals were also capable of adsorbing fluorocarbons, hydrocarbons, and Freon halocarbons, with weight capacities in the range of 50–70%.[28] Furthermore, the crystals were also capable of capturing commonly used fluorinated inhalation anesthetics, such as sevoflurane, isoflurane, and enflurane, with similar weight capacities.[29]

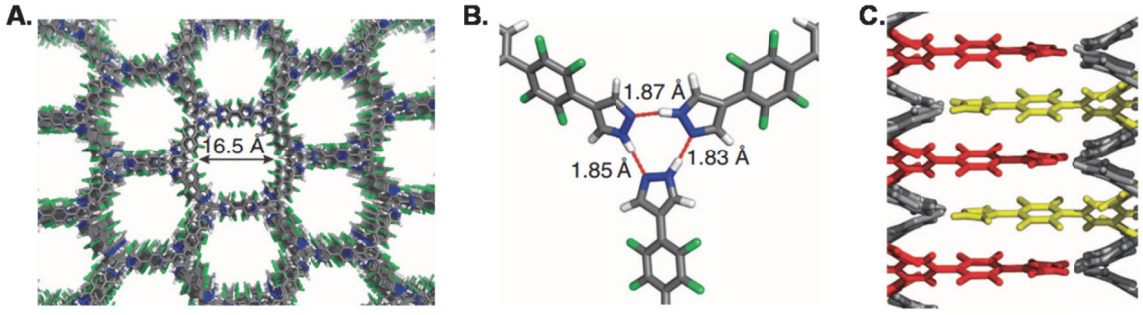

Figure 2.2 (A) Crystal structure of tris-pyrazole **4** displaying large hexagonal pores along *c*-axis (B) that are held together by hydrogen bonding between pyrazoles and (C) [π···π] stacking between pyrazoles and tetrafluorobenzenes. (Element colors: F—lime green, N—blue, C—gray, H—white; hydrogen bonds are highlighted in red; coloring in (C) structure is to illustrate stacking only).

In another collaborative study, it was revealed that the adsorption of a guest within the pores of the above framework leads to the contraction of the framework along the hydrogen-bonding plane, but expansion along the [π···π] stacking direction.[30] This elastic behavior could be further quantified by indexing powder X-ray diffraction patterns and through solid state UV/vis spectroscopy, thus representing an innovative piezochromic sensing mechanism. This physicochemical response that was dependent on

analyte uptake along with the electronic calculations used to predict it, could lay the fundamental ground work for the further development of tunable porous frameworks for specific guest uptake.

2.3 Synthesis of Fluorinated PMCs Precursors

The major focus of the work conducted in this section and the next was in trying to determine the generality of the supramolecular organization of derivatives of compound **4**.[31] This research was conducted via a modular approach towards the synthesis of different fluorinated precursors to PMCs utilizing Cu- and Pd-mediated reactions. The geometry changes were probed through the synthesis of linear, triangular, tetrahedral, and other analogs of **4**. All of the analogs were designed with both the hydrogen-bonding pyrazole endgroups and the 1,2,4,5-tetrafluorobenzene moieties needed for aromatic stacking.

The linear analogs were designed to be of varying lengths (Compounds **10**–**12**) and degrees of twisting between the aromatic rings (Scheme 2.2). The synthesis of **10** was accomplished by Cu- and Pd-mediated coupling reactions of 1,2,4,5-tetrafluorobenzene with a slight excess of two equivalents of **6**. This was followed by the replacement of the trityl (Ph_3C–) group with a Boc protecting group. Synthesis of **11** was conducted in the same way, the only difference being the initial coupling step in which 2,2′,3,3′,5,5′,6,6′-octafluorobiphenyl was coupled with **6** instead of 1,2,4,5-tetrafluorobenzene. It is worthwhile mentioning that the initial coupling step was not as effective, therefore a larger amount of $Pd(Ph_3)_4$ was used in this reaction. Synthesis of **12** involved the Cu- and Pd-mediated coupling reactions between **7**[31] and 1,4-diiododurene.

The following step involved the replacement of the trityl (Ph_3C–) group with a Boc protecting group as conducted for the preparation of **10** and **11**.

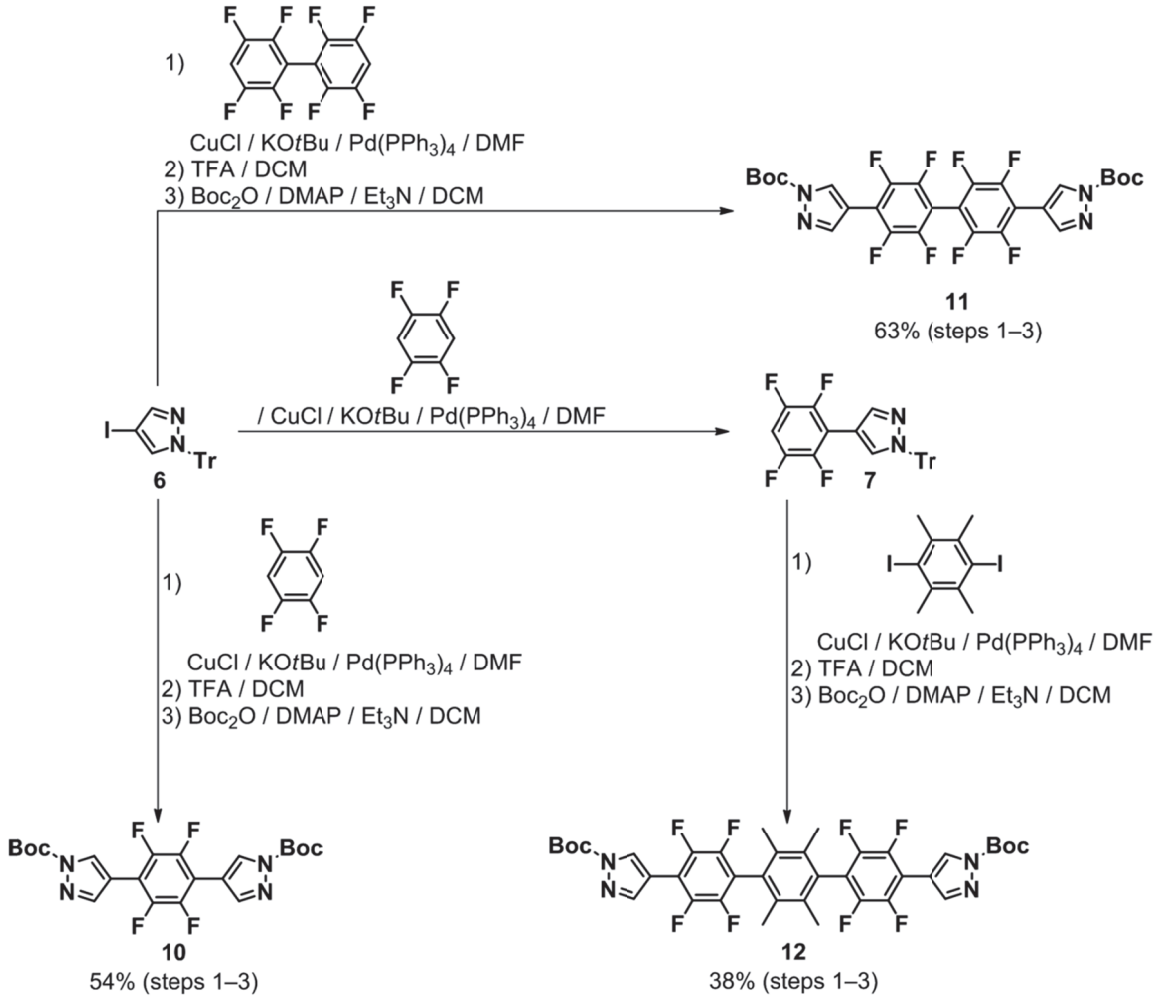

Scheme 2.2 Synthesis of linear fluorinated pyrazole precursors **10** –**12**.

The triangular analogs that were synthesized in this section can also be broken down into two categories based on the central core or the modified pyrazole end groups used in their respective syntheses. The first category was characterized by the central 1,3,5-triazine ring system and the second by a central benzene ring system with the

presence of 3,5-dimethylpyrazole end group. The two categories were synthesized in a slightly different manner when compared to the linear precursors.

In the first category, the installation of the triazine core was initially rather challenging. The original idea involved the utilization of the readily available cyanuric chloride and its reaction with **7** in order to synthesize **15** via the Cu- and Pd-mediated coupling reactions. This resulted in a complicated reaction mixture that did not contain the desired product. It was believed that activation of the aryl C–Cl bonds of cyanuric chloride occurred in negligible amounts or not at all. The next course of action would be to think of potential ways to successfully activate this bond. Thus the next idea was to utilize aryl C–I bonds instead, as our group has shown success coupling to ary iodides.[28] Attempts at the synthesis of cyanuric iodide were abandoned after a literature search showed that this compound was unstable, had not been prepared in a highly purified state and is insoluble in most solvents.[32]

Further research of the literature did show that the substitution of the chloride atoms was possible by Grignard reagents,[32] Friedel-Crafts reaction,[33] and amination.[34] With this knowledge in hand, substitution of the chlorides of the triazine ring system was attempted by the use of aryl lithium reagents derived from 1,2,4,5-tetrafluorobenzene and **7**. These attempts also resulted in reaction mixtures that did not yield **15**. It was then decided that a completely different approach all together should be utilized for the synthesis of the triazine core, and the literature revealed that triazines can also be synthesized by trimerization of benzonitriles.[35] Initial findings indicated that these trimerization reactions were conducted under high temperature and pressure and the

aromatic substituents were not fluorinated.[35] Further exploration of the literature showed that trimerization of aryl nitriles could be conducted under milder conditions, utilizing $ZnCl_2$,[36] SmI_2,[37] and fluorosulfuric acid at room temperature.[38,39] All of these methods were attempted for the trimerization of the known benzonitrile **13**.[40] Only the trimerization of **13** under acidic conditions with fluorosulufric acid resulted in the successful synthesis of triazine **14**. This was followed by the Cu- and Pd-mediated coupling reaction of **6** to **14** yielding compound **15**. The final steps of this scheme involved the replacement of the trityl (Ph_3C–) group with a Boc protecting group (Scheme 2.3).

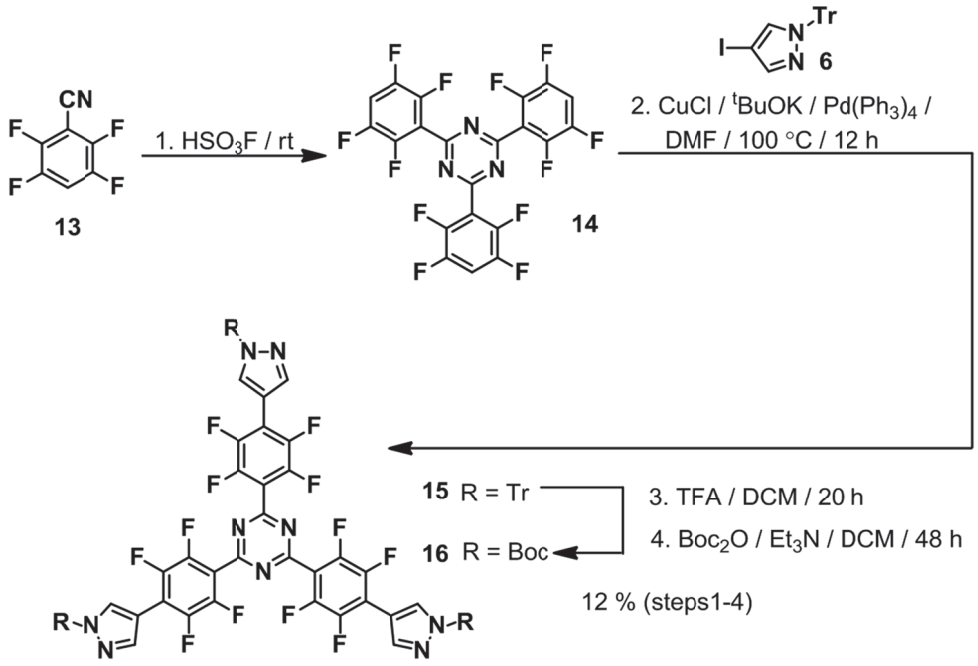

Scheme 2.3 Synthesis of a trigonal fluorinated pyrazole precursor **16**.

After the successful synthesis of **16**, a second triazine core with extended aromatic "arms" was synthesized. This core was synthesized in much the same way starting from the trimerization of known benzonitrile **17**[41] in the presence of

fluorosulfuric acid to yield known triazine **18**.[39] The Cu- and Pd-mediated coupling reaction of **7** to **18** yielded compound **19**. The trityl protecting group was successfully removed but the Boc protection step did not succeed (Scheme 2.4). This failure was attributed to to the low solubility and numerous conditions were attempted to yield the desired product but these attempts were not successful. It may be worth attempting to run this reaction under ultrasonic or microwave conditions to see if that will result in an improvement in the solubility of the pyrazolate product prior to Boc protection.

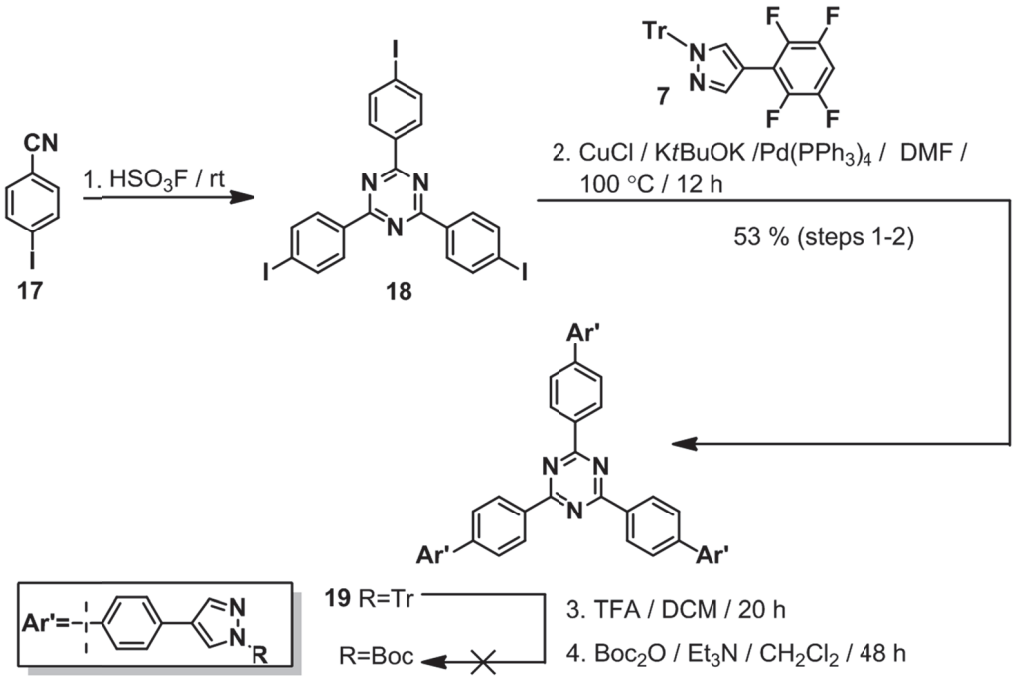

Scheme 2.4 Synthesis of a trigonal fluorinated pyrazole precursor **19**.

The second category involved 1,3,5-triiodobenzene and coupling it to *N*-trityl-3,5-dimethyl pyrazole **21** to yield compound **22** which was also successfully deprotected and reprotected with a Boc protecting group yielding PMC precursor **23** (Scheme 2.5). This resulted in the successful synthesis of two trigonal PMC precursors where compound **16**

is very similar to the original PMC precursor. Due to the presence of the bulky dimethyl groups on the terminal pyrazoles of **23** that twist out of the plane due to the presence of the bulky methyl groups in the 3 and 5 positions. This twist could thereby disrupt any [π···π] stacking that would occur during the assembly process.

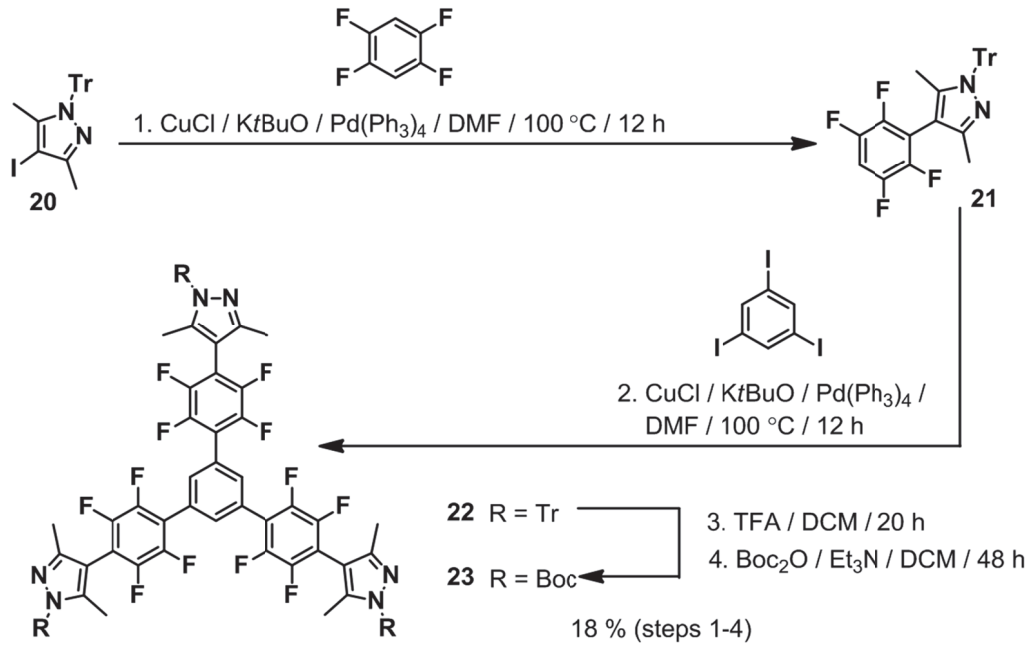

Scheme 2.5 Synthesis of a trigonal fluorinated pyrazole precursor **23.**

Other triangular analogs based on triphenyl borane were targeted as well. There was initial success with the synthesis of *tris*(4-iodophenyl)borane[42] (Scheme 2.6A), which was synthesized by the treatment of 1,4-diiodobenzene with one equivalent of butyllithium. This *in situ* generated aryllithium was reacted with BBr_3 yielding the desired product. Unfortunately, Cu- and Pd-mediated coupling reaction of *tris*(4-iodophenyl)borane with **7** did not yield the desired coupling product. Based on the initial successful generation of *tris*(4-iodophenyl)borane, preparation of a fluorinated variant of this borane was attempted in much the same manner (Scheme 2.6B). This fluorinated

borane could not be successfully prepared and the synthesis of these analogs was abandoned.

However, these analogs are worth revisiting as the coupling reaction (Scheme 2.7A) could have failed due to the electron poor boron p_z orbital being easily accessible and readily attacked by nucleophiles such as water during the work up of the reaction. This nucleophilic attack could potentially result in bond cleavage or the formation of a four coordinate borate species. In order to avoid this issue during the coupling reaction bulky aryl groups (such as mesityl) should be placed around the central boron, thereby blocking access to the p_z orbital.[43]

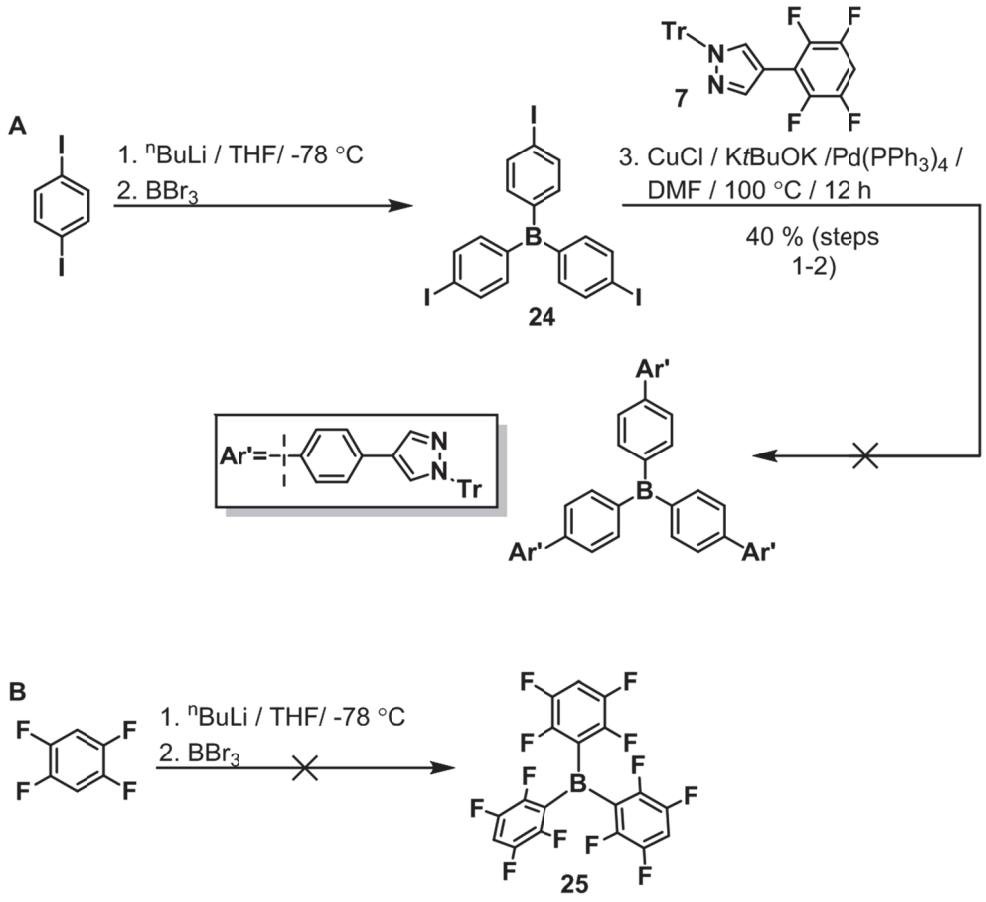

Scheme 2.6 Attempts at the synthesis of trigonal boron precursors.

The four-armed symmetric analogs were targeted next. The first target was of the tetrahedral geometry which would yield a three-dimensionally porous PMC. Initial attempts at targeting this geometry through a tetraphenylmethane core were not successful. Then, structurally analogous silanes were examined as potential alternatives, but there was difficulty in the preparation of the desired tetrakisaryl substituted silanes as well. Therefore, in order to gain access to this tetrahedral geometry a new synthetic route was devised aiming for an adamantyl central core (Scheme 2.7). Utilizing **25**, a literature procedure was followed for the preparation of **26**.[44] This compound was insoluble in all common organic solvents and could not be characterized by solution-phase NMR. It was taken to the next step and iodinated by treatment with phenyliodine bis(trifluoroacetate) and iodine, yielding the known compound **27**.[44] This was followed by the Cu- and Pd-mediated coupling reaction of **7** to **27** yielding **28**, which was then deprotected and reprotected with a Boc protecting group, yielding PMC precursor **29**. It is also worth revisiting this precursor and attempting to synthesize an adamantyl core with completely fluorinated arms and this could be achieved by the synthesis of 1,3,5,7-tetraiodoadamantane and coupling it to **7**. Initial attempts at directly iodinating adamantane ended in failure. But it may be worthwhile to change the approach and brominate adamantane to obtain 1,3,5,7-tetrabromoadamantane and then to attempt the iodination of this compound in the presence of a Lewis acid.

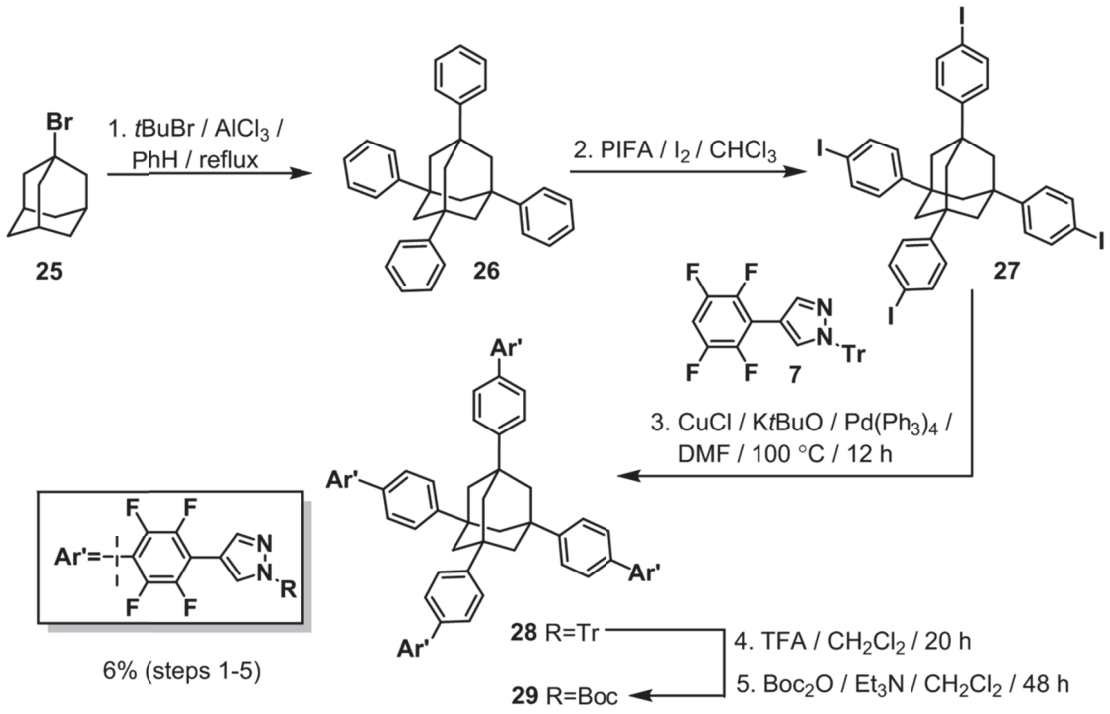

Scheme 2.7 Synthesis of a trigonal fluorinated pyrazole precursor **23.**

The other four-armed precursor was of the square planar geometry. It was synthesized starting from a 1,2,4,5-tetraiodobenzene and coupling it to **7** in order to yield compound **31** according to Scheme 2.8. The yield of the coupling step was low and this seems to be indicative of a trend noticed with PMC precursors that have been synthesized thus far: an increase in the number of coupling sites or arms results in a decrease in the yield. It is anticipated that the steric bulk of the fluorinated benzene rings will cause the arms of the PMC derived from **31** to twist out of the plane possibly hampering any [π···π] stacking that would occur during the assembly process.

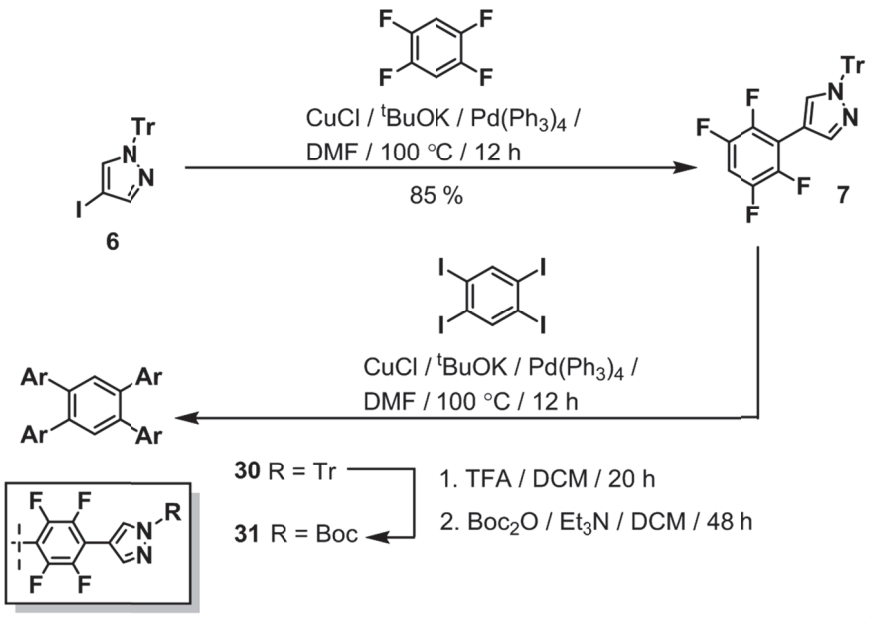

Scheme 2.8 Synthesis of a square planar fluorinated pyrazole precursor **31**.

The final analog that was attempted was based on a hexasubstituted benzene core. This core was anticipated to display a twisted paddlewheel like geometry. The initial synthetic route involved the use of hexaiodobenzene and to couple **7** to this core via the Cu- and Pd-mediated coupling reaction. This did not yield the desired product, possibly due to this product being too sterically hindered or this being the limit of the currently used the Cu- and Pd-mediated coupling reaction. Thus, the strategy was changed in order to relieve the possible steric congestion at the central benzene ring. This could be done by switching the core to hexakis(4-iodophenyl)benzene and coupling **7** to this core. The first strategy attempted to synthesize hexakis(4-iodophenyl)benzene was the cyclo-trimerization of diphenylacetylenes[45] and this did not yield the desired product. The next strategy was to conduct a Diels-Alder reaction between tetraphenylcyclopentadienone and diphenylacetylene in benzophenone to yield hexaphenylbenzene.[46] Treatment of hexaphenylbenzene with phenyliodine bis(trifluoroacetate) and iodine yielded hexakis(4-

iodophenyl)benzene. Initial attempts at coupling **7** to hexakis(4-iodophenyl)benzene seem promising but at the moment are inconclusive. Synthesis of hexakis(4-iodophenyl)benzene needs to be scaled up and further attempts at coupling with **7** should be conducted.

2.4 Conclusions and Outlook

The initial goal of synthesizing PCM precursors with different geometries was achieved successfully resulting in the synthesis of **10**, **11**, **12**, **16**, **23**, **29**, and **31**. These precursors were be utilized for the solvothermal preparation of PCMs. This represents a small number of compounds and it is this author's hope that more PMC precursors can be synthesized in the future. It would also be ideal if the synthetic route for the preparation of PMC precursors was altered to remove the deprotection and protection steps. This would increase the overall yield of the precursor synthesized, minimize waste and result in a more elegant synthetic route.

2.5 Experimental Section

2.5.1 General Methods and Materials

Vials with PTFE/Liner caps were used as reaction vessels for the synthesis of precursors. Solvents THF, Et_2O, and hexane were dried over activated alumina in an mBraun solvent purification system. Column chromatography was carried out on silica gel 60, 32–63 mesh and basic aluminum oxide Act. 1, 50–200μm (Sorbent Technologies). Analytical TLC was performed on J. T. Baker plastic-backed silica gel IB-F plates and aluminum oxide IB-F plates. The ^{1}H and ^{19}F NMR spectra were recorded on JEOL ECA-600, ECA-500, or ECX-400P spectrometers, with working frequencies (for ^{1}H nuclei) of 600, 500, and 400 MHz, successively, and using the peaks of tetramethylsilane or residual solvent as standards. Trifluorotoluene ($PhCF_3$, $\delta = -63.72$ ppm) was used as the internal standard in ^{19}F NMR spectra. ^{13}C NMR spectra were not included since they are not informative, due to the poor solubility of the prepared compounds and the extensive coupling between ^{13}C and ^{19}F nuclei; low intensities and many missing peaks were observed. Melting points were measured in a Barnstead International Mel-TEMP apparatus, and are uncorrected. Analytical thin-layer chromatography was performed on Fluka silica gel/TLC plates with a fluorescent indicator that emitted when irradiated at 254 nm. Infrared spectra were recorded on a Nicolet iS10 FT-IR spectrometer equipped with a Thermo Scientific iTR for multi-purpose ATR sampling. Microanalyses were conducted by Intertek USA Inc.

All reactions were performed under nitrogen atmosphere in oven-dried glassware. The following starting materials and solvents were obtained from the respective

commercial sources and used without further purification: Boc_2O (Alfa Aesar); triphenylchloromethane (TrCl, AK Scientific); *N,N*-dimethylformamide (DMF), potassium *t*-butoxide (*t*-BuOK) (Oakwood); 2,3,5,6-tetrafluorobenzene, triethylamine (Et_3N), tetrakis(triphenylphosphine) palladium(0) ($Pd(PPh_3)_4$), 4-iodopyrazole, trifluoroacetic acid (TFA) (Matrix Scientific); CH_2Cl_2 (Aldrich); water (Milli-Q, deionized). All gases were purchased from Matheson Tri-Gas.

2.5.2 Synthesis of Precursors to PMCs

Compound 10

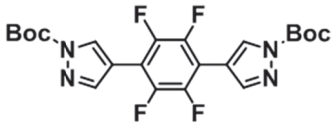

A 100 mL screw cap pressure vessel was equipped with a magnetic stir bar and charged with CuCl (2.18 g, 22.0 mmol) and *t*-BuOK (2.47 g, 22 mmol). Dry DMF (25 mL) was added, and the vessel was sealed and the contents stirred at 25 °C for 1 h inside the glovebox. Next, 1,2,4,5-tetrafluorobenzene (1.50 g, 10.0 mmol) was added in one portion and then the reaction mixture was stirred at 25 °C for 1 h. Catalyst $Pd(PPh_3)_4$ (115 mg, 0.10 mmol) was added, followed by 4-iodo-1-trityl-1H-pyrazole (**7**, 9.60 g, 22.0 mmol). The reaction vessel was sealed, taken out of the glovebox and placed inside an oil bath preheated to 100 °C, where it was stirred for 22 h. Reaction mixture was cooled to 25 °C, diluted with CH_2Cl_2 (400 mL) and poured into a beaker that contained aq. NH_4OH (100 mL), eight spatula scoops of NH_4Cl, and deionized H_2O (300 mL). This mixture was stirred in the beaker for 30 min. The blue aqueous layer was poured out and the organic layer was vacuum filtered. The grey solid that remained on the filter paper was

washed with CH_2Cl_2 and left to air dry overnight, yielding a greyish white solid. This compound was used crude in the subsequent step.

The crude trityl-protected dipyrazole intermediate was dissolved in CH_2Cl_2 (200 mL) in a 500 mL round bottom flask equipped with a magnetic stir bar. The resulting clear solution was stirred and then TFA (12 mL, 131 mmol) was added, resulting in an orange solution. Stirring was continued for 24 h at 25 °C. The salt that precipitated out of solution was filtered off and washed with fresh CH_2Cl_2 (3×50 mL), resulting in a light tan solid that was vacuum dried for 3 h.

A 500 mL round bottom flask equipped with a magnetic stir bar was charged with the crude isolated salt (4.70 g) and CH_2Cl_2 (230 mL). This suspension was cooled to 0 °C followed by the slow addition of NEt_3 (18.4 mL, 130 mmol) over 10 min. This reaction mixture was allowed to stir and maintained at 0 °C for another 10 min and then the ice bath was removed, followed by the addition of 4-(*N,N*-dimethylamino)pyridine (DMAP, 1.13 g, 9.25 mmol), and finally di-*tert*-butyl dicarbonate (12.0 g, 55.0 mmol) was added to the reaction mixture. The round bottom flask was then sealed with a septum and connected to a bubbler, to visually monitor the evolution of CO_2 gas. The reaction mixture was stirred at 25 °C until the evolution of CO_2 ceased (~24 h). Upon completion, the reaction mixture was dry-absorbed on silica gel. After purification by column chromatography on silica gel, using CH_2Cl_2/hexanes (gradient from 5% to 100% of CH_2Cl_2) as the eluent, the product was obtained as a white solid (2.63 g, 54%) mp: >350 °C. IR (neat): 3190 (w), 3116 (w), 2999 (w), 2982 (w), 2941 (m), 1742 (s, $\tilde{\upsilon}_{C=O}$), 1586 (w), 1494 (m), 1473 (m), 1394 (s), 1342 (s), 1306 (s), 1285 (s), 1227 (s) 1139 (s) 964 (s) 842 (s) cm^{-1}. ^1H NMR (600 MHz, $CDCl_3$): δ 8.65 (s, 2H), 8.23 (s, 2H), 1.69 (s,

18H) ppm. ^{19}F NMR (564 MHz, $CDCl_3$): δ –140.67 (s, 4F) ppm. HRMS (ESI/Q-TOF) *m*/*z*: $[M+Na]^+$ Calc'd for $C_{22}H_{22}F_4N_4O_4Na$: 505.1475; Found: 505.1469. Anal. Calc'd for $C_{22}H_{22}F_4N_4O_4$: C, 54.77; H, 4.60; N, 11.61. Found: C, 54.39; H, 4.37; N, 11.54.

Synthesis of Compound 11

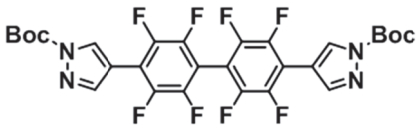

Inside a glovebox, a 100 mL screw cap pressure vessel was equipped with a magnetic stir bar and charged with CuCl (2.18 g, 22.0 mmol) and *t*-BuOK (2.47 g, 22.0 mmol). Dry DMF (25 mL) was added, and the vessel was sealed and stirred at 25 °C for 1 h. Next 2,2',3,3',5,5',6,6'-octafluorobiphenyl (2.98 g, 10.0 mmol) was added in one portion and then the reaction mixture was stirred at 25 °C for 1 h. Catalyst $Pd(PPh_3)_4$ (463 mg, 0.40 mmol) was added, followed by 4-iodo-1-trityl-1H-pyrazole (9.60 g, 22.0 mmol). The reaction vessel was sealed, taken out of the glovebox and placed inside an oil bath preheated to 100 °C, where it was stirred for 22 h. Reaction mixture was cooled to 25 °C, diluted with CH_2Cl_2 (400 mL) and poured into a beaker that contained aq. NH_4OH (100 mL), eight spatula scoops of NH_4Cl, and deionized H_2O (300 mL). This mixture was stirred in the beaker for 30 min. The blue aqueous layer was poured out and the organic layer was filtered out through a Celite pad, resulting in a yellow-orange solution. This organic solution was dried with $MgSO_4$ and then concentrated, resulting in a yellow solid. This yellow solid was not purified or characterized and was used the next step.

The crude trityl-protected dipyrazole intermediate was dissolved in CH_2Cl_2 (300 mL) in a 500 mL round bottom flask equipped with a magnetic stir bar. The following

clear solution was stirred vigorously, then TFA (10 mL, 131 mmol) was added, followed by the addition of trifluoromethanesulfonic anhydride (4.00 mL, 8.45 mmol), resulting in an orange-green solution. Stirring was continued for 24 h at 25 °C. The salt that precipitated was filtered off and washed with fresh CH_2Cl_2 (3×50 mL), resulting in a light tan solid that was vacuum dried for 3 h.

A 500 mL round bottom flask equipped with a magnetic stir bar was charged with the crude isolated salt (14.0 g) and CH_2Cl_2 (250 mL). This suspension was cooled to 0 °C followed by the slow addition of NEt_3 (21.0 mL, 150 mmol) over 10 min. This reaction mixture was stirred at 0 °C for another 10 min and then the ice bath was removed, followed by the addition of DMAP (2.50 g, 20.0 mmol), and finally di-*tert*-butyl dicarbonate (27.0 g, 126 mmol) was added to the reaction mixture. The round bottom flask was then sealed with a septum and connected to a bubbler, to visually monitor the evolution of CO_2 gas. The reaction mixture was stirred at 25 °C until the evolution of CO_2 ceased (~24 h). Upon completion, the reaction mixture was dry-absorbed on silica gel. After purification by column chromatography on silica gel, using CH_2Cl_2/hexanes (gradient from 5% to 100% of CH_2Cl_2) as the eluent, the product was obtained as a white solid (4.20 g, 61% yield over 3 steps), mp: >350 °C. IR (neat): 3190 (w), 3116 (w), 2999 (w), 2982 (w), 2941 (m), 1742 (s, ϑC=O), 1586 (w), 1494 (m), 1473 (m), 1394 (s), 1342 (s), 1306 (s), 1285 (s), 1227 (s) 1139 (s) 964 (s) 842 (s) cm^{-1}. ^1H NMR (600 MHz, $CDCl_3$): δ 8.65 (s, 2H), 8.23 (s, 2H), 1.69 (s, 9H) ppm. ^{19}F NMR (564 MHz, $CDCl_3$): δ –138.13 to –138.16 (m, 4F), –139.47 to –138.49 (m, 4F) ppm. HRMS (ESI/Q-TOF) *m*/*z*: [M+Na]+ Calc'd for $C_{28}H_{22}F_8N_4O_4Na$: 653.1411; Found 653.1406. Anal. Calc'd for $C_{28}H_{22}F_8N_4O_4$: C, 53.34; H, 3.52; N, 8.89. Found: C, 53.22; H, 3.41; N, 8.67.

Synthesis of Compound 12

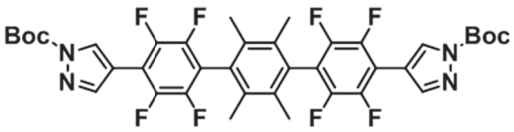

Inside a glovebox, a 100 mL screw cap pressure vessel was equipped with a magnetic stir bar and charged with CuCl (1.64 g, 16.5 mmol) and *t*-BuOK (1.85 g, 17.0 mmol). Dry DMF (40 mL) was added and the reaction mixture was sealed, taken out of the glovebox, sonicated for 5 min, and then stirred at 25 °C for 1 h. Pressure vessel was placed back inside glovebox. *N*-Trityl protected pyrazole **8** (7.56 g, 16.5 mmol) was added in one portion, and after that the reaction mixture was sealed, taken out of the glovebox, sonicated for 5 min, and then stirred at 25 °C for 1 h. The pressure vessel was placed back inside glovebox. Then, $Pd(PPh_3)_4$ (347 mg, 0.30 mmol) was added, followed by 2,3,5,6-tetramethyl-1,4-diiodobenzene (2.90 g, 7.50 mmol).

Reaction mixture was sealed, taken out of the glovebox and then placed inside an oil bath preheated to 100 °C, where it was stirred for 24 h. Reaction mixture was cooled to 25 °C, diluted with $CHCl_3$ (150 mL) and an aqueous solution of citric acid (3%, 100 mL) was added. Reaction mixture was filtered through the plug of Celite to remove the copper salts. Filter cake was washed with additional $CHCl_3$ (3×25 mL). Combined organic layer was separated and washed with deionized H_2O (5×100 mL), followed by brine (100 mL). Finally, the organic layer was dried over anhydrous $MgSO_4$, filtered and dry-absorbed on silica gel. Purification of the reaction mixture by column chromatography on silica gel using $CHCl_3$/hexanes (gradient from 30% to 100% of $CHCl_3$) as the eluent and evaporation of the fractions containing the product afforded 4.07 g of trityl-protected dipyrazole intermediate.

Next, a 250 mL flask equipped with magnetic stirring bar was charged with thus obtained trityl-protected dipyrazole intermediate (4.07 g, 5.34 mmol) and $CHCl_3$ (60 mL). The resulting clear solution was treated with TFA (10 mL) under vigorous stirring, resulting in a color change from colorless to yellow. Reaction mixture was stirred at 25 °C for 20 h. All volatiles were evaporated in vacuo and the resulting residue was triturated with hexanes/EtOAc mixture (1/1, 50 mL). The salt that formed was filtered off and dried in vacuo for 2 h.

A 100 mL flask equipped with a magnetic stirring bar was charged with the previously isolated salt and CH_2Cl_2 (20 mL) was added. Resulting suspension was treated with Et_3N (3 mL), followed by the addition of DMAP (0.24 g, 2.00 mmol). Then, Boc_2O (2.00 g, 11.0 mmol) was added to the open flask, via syringe, over 2 min. **CAUTION!!!** DURING THE ADDITION RAPID EVOLUTION OF CO_2 WAS OBSERVED!!! After the addition of Boc_2O was complete, the reaction flask was capped with a septum connected to a bubbler. Reaction mixture was stirred at 25 °C until the evolution of CO_2 ceased (typically 12–36 h), and was then dry-absorbed on silica gel. After purification by column chromatography on silica gel using EtOAc/CH_2Cl_2 (gradient from 1% to 8% of EtOAc) as eluent and evaporation of the fractions containing the product, the title compound was obtained as a white solid **5** (2.2 g, 38% over three steps). ^{1}H NMR (500 MHz, $CDCl_3$): δ 8.65 (s, 2H), 8.25 (s, 2H), 2.07 (s, 12H), 1.70 (s, 18 H) ppm. ^{19}F NMR (471 MHz, $CDCl_3$): δ –140.1 to –140.2 (m, 4F), –140.4 to –140.6 (m, 4F) ppm. HRMS (ESI/Q-TOF) *m*/*z*: $[M+Na]^+$ Calc'd for $C_{38}H_{34}F_8N_4O_4Na$: 785.2350. Found 785.2345. Anal. Calc'd for $C_{38}H_{34}F_8N_4$: C, 59.84; H, 4.49; N, 7.35. Found: C, 59.02; H, 4.44; N, 7.03.

Synthesis of Compound 14

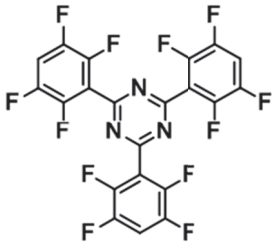

Compound 2,3,5,6-tetrafluorobenzonitrile (**13**, 6.00 g, 34 mmol) and fluorosulfuric acid (5.6 mL, 103 mmol) were placed in a 20 mL Schlenk flask with stirring at room temperature for 3 d. The mixture was poured into cold water with ice (30 mL) and the precipitated solid was collected, washed with H_2O until neutral, then washed with EtOH (15 mL), and Et_2O (2×5 mL) and air dried for 12 h. This sequence of steps yielded 3.39 g (57%) of a white powder, mp 229–230 °C. ^{1}H NMR (600 MHz, DMSO-d_6): δ 8.23–8.29 (m, 3H) ppm. ^{19}F NMR (564 MHz, DMSO-d_6): δ –137.76 to –137.83 (m, 6F), –141.73 to –141.77 (m, 6F) ppm. FT-IR (neat): $\tilde{\upsilon}$ 3059, 1525, 1501, 1481, 1461, 1391, 1346, 1239, 1270, 1189, 1174, 1002, 935, 867, 840, 735, 715 698, 664, 565 cm^{-1}. ESI MS *m*/*z*: 526 (100 %), 441 (10 %), 417 (20 %), 401 (5 %).

Synthesis of Compound 15

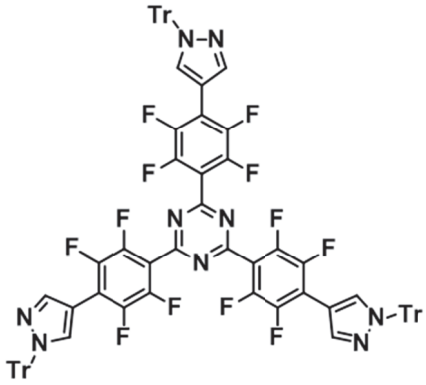

A 100 mL screw cap pressure vessel was equipped with a magnetic stir bar and charged with CuCl (1.68 g, 17 mmol) and *t*-BuOK (1.91 g, 17 mmol) inside the glovebox. Dry DMF (20 mL) was added, and the vessel was sealed and vigorously stirred at 25 °C for 1 h. Next, compound **14** (2.63 g, 5 mmol) was added in one portion and then the reaction mixture was vigorously stirred at 25 °C for 1 h. Catalyst $Pd(PPh_3)_4$ (174 mg, 0.15 mmol) was added, followed by 4-iodo-1-trityl-1H-pyrazole (8.73 g, 20 mmol). The reaction vessel was sealed, taken out of the glovebox and placed inside an oil bath preheated to 100 °C, where it was stirred vigorously for 22 h. The reaction mixture was cooled to 25 °C, diluted with DCM (400 mL) and poured into a beaker that contained 100 mL NH_4OH (aq), eight spatula scoops of $NH_4Cl_{(s)}$, and 300 mL of deionized H_2O. This mixture was stirred in the beaker for 30 min. The blue aqueous layer was poured out and the organic layer was filtered out through a celite pad, dried with $MgSO_4$ and was dry-absorbed on silica gel. After purification by column chromatography on silica gel (using hexanes/CH_2Cl_2 as eluent) and evaporation of the fractions containing the product, compound **15** was obtained (5.00 g, 69%). ^{1}H NMR (400 MHz, $CDCl_3$): δ 8.25 (s, 3H), 8.04 (s, 3H), 7.37–7.35 (m, 27H), 7.23–7.20 (m, 15H) ppm. ^{19}F NMR (376 MHz, $CDCl_3$): δ –139.87 to –139.96 (m, 6F), –142.00 to –142.08 (m, 6F) ppm.

Synthesis of Compound 16

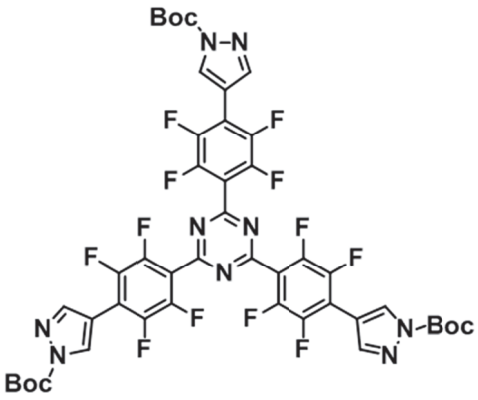

Compound **15** (6.60 g, 4.55 mmol) was dissolved in 100 mL of DCM in a 250 mL round bottom flask equipped with a magnetic stir bar. The following clear solution was stirred vigorously, then TFA (10 mL, 131 mmol) was added resulting in a green solution. Stirring was continued for 24 h at 25 °C. The resulting salt that precipitated was filtered off and washed with fresh CH_2Cl_2 (3 × 50 mL). Resulting tan solid was then vacuum dried for 3 h. A 250 mL round bottom flask equipped with a magnetic stir bar was charged with the crude isolated salt (3.4 g, 4.70 mmol) and 70 mL of DCM. This suspension was cooled to 0 °C followed by the slow addition of NEt_3 (6 mL, 81 mmol) over 10 min. This reaction mixture was allowed to stir and maintained at a temperature of 0 °C for another 10 min and then the ice bath was removed, followed by the addition of dimethylaminopyridine (0.38 g, 3 mmol), and finally di-*tert*-butyl dicarbonate (7.00 g, 33 mmol) was added to the reaction mixture. The round bottom flask was then sealed with a septum and connected to a bubbler, to monitor the evolution of CO_2 gas. The reaction mixture was stirred vigorously at 25 °C until the evolution of CO_2 ceased (~24 h). Upon completion, the reaction mixture was dry-absorbed on silica gel. After purification by

column chromatography on silica gel (using hexanes/EtOAc as eluent) and evaporation of the fractions containing the product was obtained as a yellowish solid (1.40 g, 30% over two steps). Mp: >350 °C (decomp). ^{1}H NMR (400 MHz, $CDCl_3$): δ 8.60 (s, 3H), 8.20 (s, 3H), 1.69 (s, 27H) ppm. ^{19}F NMR (376 MHz, $CDCl_3$): δ –138.97 to –139.05 (m, 6F), –141.04 to –141.13 (m, 6F) ppm. FT-IR (neat): $\tilde{\upsilon}$ 2982, 2360, 1794, 1758, 1643, 1566, 1522, 1475, 1372, 1357, 1340, 1288, 1259, 1233, 1214, 1145, 1038, 965, 874, 839, 812, 751, 743, 707, 672, 657, 636, 596, 513 cm^{-1}.

Synthesis of Compound 18

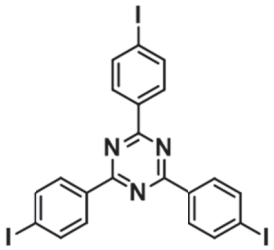

Compound 4-iodobenzonitrile (**18**, 2.06 g, 9.00 mmol) and fluorosulfuric acid (1.66 mL, 30.60 mmol) were placed in a 10 mL Schlenk flask with stirring at room temperature for 3 h. The viscous mixture was poured into cold water with ice (10 mL) and the precipitated brown solid was collected, washed with water until neutral, EtOH (10 mL), Et_2O (2×5 mL) and air dried for 12 h. The remaining brown solid was insoluble in organic solvents therefore it could not be characterized by NMR. mp > 300 °C.

Synthesis of Compound 19

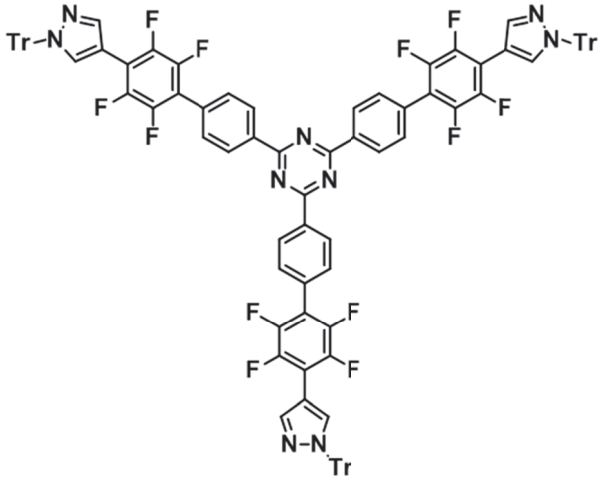

A 100 mL screw cap pressure vessel was equipped with a magnetic stir bar and charged with CuCl (1.47g, 14.9 mmol) and *t*-BuOK (1.67 g, 14.9 mmol) inside the glovebox. Dry DMF (25 mL) was added, and the vessel was sealed and vigorously stirred at 25 °C for 1 h. Next, compound **18** (7.00 g, 15.3 mmol) was added in one portion and then the reaction mixture was vigorously stirred at 25 °C for 1 h. Catalyst $Pd(PPh_3)_4$ (200 mg, 0.175 mmol) was added, followed by compound **11** (3.00 g, 4.37 mmol). The reaction vessel was sealed, taken out of the glovebox and placed inside an oil bath preheated to 100 °C, where it was stirred vigorously for 22 h. The reaction mixture was cooled to 25 ^{o}C, diluted with CH_2Cl_2 (400 mL) and poured into a beaker that contained 100 mL $NH_4OH_{(aq)}$, eight spatula scoops of $NH_4Cl_{(s)}$ and 300 mL of deionized H_2O. This mixture was stirred in the beaker for 30 min.

The blue aqueous layer was poured out and the organic layer was filter out through a Celite pad, dried with $MgSO_4$ and dry-absorbed on silica gel. After purification by column chromatography on silica gel (using hexanes/CH_2Cl_2 as eluent) and

evaporation of the fractions containing the product, compound **12** was obtained (3.16 g, 62.8% yield). ^{1}H NMR (400 MHz, $CDCl_3$): δ 8.90 (d, 2H, *J* = 8Hz), 8.22 (s, 1H) 7.98 (s, 1H), 7.72 (d, 2H, *J* = 8Hz), 7.40–7.30 (m, 18H), 7.22–7.15 (m, 12H) ppm. ^{19}F NMR (376 MHz, $CDCl_3$): δ –140.95 to –141.04 (m, 6F) and –144.91 to –141.58 (m, 6F) ppm.

Synthesis of Compound 21

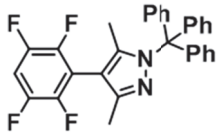

Inside a glovebox, a 100 mL screw cap pressure vessel was equipped with a magnetic stir bar and charged with CuCl (7.00 g, 75 mmol) and *t*-BuOK (8.42 g, 75 mmol). Dry DMF (120 mL) was added and the reaction mixture was sealed, taken out of the glovebox, and then stirred at 25 °C for 1 h. Tetrafluorobenzene (26.30 g, 175 mmol) was added in one portion, and then stirred at 25 °C for 1 h. Then, $Pd(PPh_3)_4$ (575 mg, 0.50 mmol) was added, followed by protected dimethyl-4-iodopyrazole **20** (23.2 g, 50 mmol). Reaction mixture was sealed, taken out of the glovebox and then placed inside an oil bath preheated to 100 °C, where it was stirred for 24 h. The reaction mixture was cooled to 25 °C, diluted with CH_2Cl_2 (400 mL), and poured into a beaker that contained aq. NH_4OH (100 mL), eight spatula scoops of NH_4Cl, and deionized H_2O (300 mL). This mixture was stirred in the beaker for 30 min. The blue aqueous layer was poured out and the organic layer was filter out through a Celite pad, resulting in a yellow-orange solution. This organic solution was dried with $MgSO_4$ and dry sorbed onto silica. After purification by column chromatography on silica gel using CH_2Cl_2/hexanes (gradient from 50 to 90% of CH_2Cl_2) as eluent and evaporation of the fractions containing the product, title

compound was obtained as a light yellow solid (17.2 g, 71%). R_f = 0.48 (SiO2, hexanes/CH_2Cl_2 1/1). ^{1}H NMR (400 MHz, $CDCl_3$): δ 7.32–7.25 (m, 9H), 7.17–7.15 (m, 6H), 7.05–6.98 (s, 1H), 2.12 (s, 3 H) 1.36 (s, 3 H) ppm. ^{19}F NMR (376 MHz, $CDCl_3$): δ –139.4 to –139.5 (m, 2F), – 139.6 to –139.7 (m, 2F) ppm.

Synthesis of Compound 23

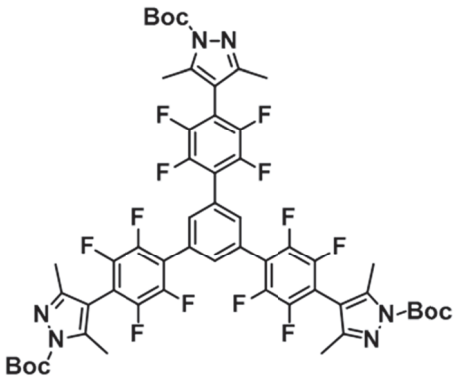

Inside a glovebox, a 100 mL screw cap pressure vessel was equipped with a magnetic stir bar and charged with CuCl (1.06 g, 10.7 mmol) and *t*-BuOK (1.20 g, 10.7 mmol). Dry DMF (40 mL) was added and the reaction mixture was sealed, taken out of the glovebox, and then stirred at 25 °C for 1 h. Then, *N*-trityl protected dimethyl pyrazole **21** (5.00 g, 10.8 mmol) was added in one portion, and the reaction mixture was then stirred at 25 °C for 1 h. Then, $Pd(PPh_3)_4$ (115 mg, 0.10 mmol) was added, followed by 1,3,5-triiodobenzene (1.45 g, 3.18 mmol). Reaction mixture was sealed, taken out of the glovebox and then placed inside an oil bath preheated to 100 °C, where it was stirred for 24 h.

The reaction mixture was cooled to 25 °C, diluted with CH_2Cl_2 (400 mL) and poured into a beaker that contained aq. NH_4OH (100 mL), eight spatula scoops of NH_4Cl, and deionized H_2O (300 mL). This mixture was stirred in the beaker for 30 min. The blue

aqueous layer was poured out and the organic layer was filter out through a Celite pad, resulting in a yellow-orange solution. This organic solution was dried with $MgSO_4$ and then concentrated, resulting in an orange solid. This solid was not purified and was used as such in the next step.

Next, a 250 mL flask equipped with magnetic stirring bar was charged with thus obtained trityl-protected dipyrazole intermediate (3.00 g, 1.96 mmol) and $CHCl_3$ (60 mL). The resulting clear solution was treated with TFA (10 mL) under vigorous stirring, resulting in a color change from colorless to yellow. Reaction mixture was stirred at 25 °C for 20 h. All volatiles were evaporated in vacuo and solution was filtered off and dried in vacuo for 2 h.

A 100 mL flask equipped with a magnetic stirring bar was charged with the previously isolated salt (800 mg, 0.99 mmol) and CH_2Cl_2 (30 mL) was added. Resulting suspension was treated with Et_3N (2 mL), followed by the addition of DMAP (0.18 g, 1.49 mmol). Then, Boc_2O (1.95 g, 8.9 mmol) was added to the open flask, via syringe, over 2 min. **CAUTION!!!** DURING THE ADDITION RAPID EVOLUTION OF CO_2 WAS OBSERVED!!! After the addition of Boc_2O was complete, the reaction flask was capped with a septum connected to a bubbler. Reaction mixture was stirred at 25 °C until the evolution of CO_2 ceased (typically 12–36 h), and was then dry-absorbed on silica gel. After purification by column chromatography on silica gel using EtOAc/CH_2Cl_2 (gradient from 1% to 8% of EtOAc) as eluent and evaporation of the fractions containing the product, the title compound was obtained as a pearly white solid **23** (0.4 g, 18% over three steps). ^{1}H NMR (500 MHz, $CDCl_3$): δ 7.83 (s, 3H), 2.45 (s, 9H), 2.25 (s, 9H), 1.68 (s, 27 H) ppm. ^{19}F NMR (471 MHz, $CDCl_3$): δ –138.65 to –139.04 (m, 6F), – 143.22 to –

143.31 (m, 6F) ppm. HRMS (ESI/Q-TOF) *m/z*: $[M+K]^+$ Calc'd for $C_{54}H_{48}F_{12}N_6O_6K$: 1143.3081. Found 1143.3075. Anal. Calc'd for $C_{54}H_{48}F_{12}N_6O_6$: C, 56.92; H, 4.38; N, 7.40. Found: C, 58.70; H, 4.38; N, 7.61.

Synthesis of Compound 28

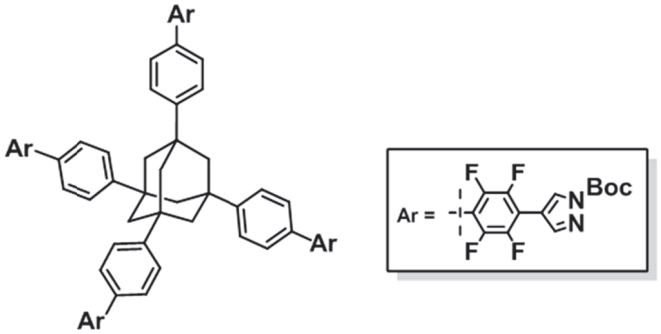

A 100 mL screw cap pressure vessel was equipped with a magnetic stir bar and charged with CuCl (2.10 g, 21.2 mmol) and *t*-BuOK (2.38 g, 21.2 mmol) inside the glovebox. Dry DMF (25 mL) was added, and the vessel was sealed and vigorously stirred at 25 °C for 1 h. Next compound **26** (9.71 g, 21.2 mmol) was added in one portion and then the reaction mixture was vigorously stirred at 25 °C for 1 h. Catalyst $Pd(PPh_3)_4$ (245 mg, 0.212 mmol) was added, followed by compound **14** (4.00 g, 4.24 mmol). The reaction vessel was sealed, taken out of the glovebox and placed inside an oil bath preheated to 100 °C, where it was stirred vigorously for 22 h. The reaction mixture was cooled to 25 °C, diluted with CH_2Cl_2 (400 mL) and poured into a beaker that contained 100 mL $NH_4OH_{(aq)}$, eight spatula scoops of $NH_4Cl_{(s)}$ and 300 mL of deionized H_2O. This mixture was stirred in the beaker for 30 min. The blue aqueous layer was poured out and the organic layer was filter out through a Celite pad, dried with $MgSO_4$ and concentrated. This compound was taken crude to the next step.

Crude compound **27** (6.50 g, 2.87 mmol) was dissolved in 180 mL of dichloromethane in a 250 mL round bottom flask equipped with a magnetic stir bar. The following clear solution was stirred vigorously, then trifluoroacetic acid (10 mL, 130.6 mmol) was added resulting in a yellowish orange solution. Stirring was continued for 24 hours at 25 °C. The resulting salt that precipitated out of solution was filtered off and washed with fresh CH_2Cl_2 (3×50 mL), resulting in a yellow solid was then vacuum dried for 3 h. A 250 mL round bottom flask equipped with a magnetic stir bar was charged with the crude isolated salt (5.30 g, 2.81 mmol) and 150 mL of CH_2Cl_2. This suspension was cooled to 0 °C followed by the slow addition of NEt_3 (14.42 mL, 103 mmol) over 10 min. This reaction mixture was stirred at 0 °C for another 10 min and then the ice bath was removed, followed by the addition of dimethylaminopyridine (1.753 g, 14.35 mmol), and finally di-*tert*-butyldicarbonate (12.00 g, 55 mmol) was added to the reaction mixture. The round bottom flask was then sealed with a septum and connected to a bubbler, to visually monitor the evolution of CO_2. The reaction mixture was stirred vigorously at 25 °C until the evolution of CO_2 ceased (~24 h). Upon completion, the reaction mixture was dry-absorbed on silica gel. After purification by column chromatography on silica gel (using hexanes/EtOAc as eluent) and evaporation of the fractions containing the product, compound **2** was obtained (1.50 g, 30% yield over two steps). ^{1}H NMR (400 MHz, $CDCl_3$): δ 8.61 (s, 4H), 8.22 (s, 4H), 7.68 (d, 8H, *J*=8.4 Hz) 7.58 (d, 8H, *J*=8.4Hz), 1.69 (s, 36H). ^{19}F NMR (376 MHz, $CDCl_3$): δ –140.79 to –140.82 (m, 8F) and –144.06 to –144.09 (m, 8F). Anal. Calc'd for $C_{90}H_{72}F_{16}N_8O_8$: C, 74.63; H, 3.77; N, 7.23. Found: C, 75.13; H, 3.78; N, 7.51.

Synthesis of Compound 32

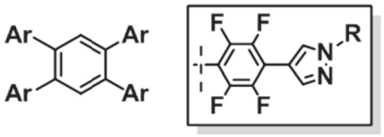

A 100 mL screw cap pressure vessel was equipped with a magnetic stir bar and charged with CuCl (2.10 g, 21.2 mmol) and *t*-BuOK (2.38 g, 21.2 mmol) inside the glovebox. Dry DMF (25 mL) was added, and the vessel was sealed and vigorously stirred at 25 °C for 1 h. Next compound **7** (9.71 g, 21.2 mmol) was added in one portion and then the reaction mixture was vigorously stirred at 25 °C for 1 h. Catalyst $Pd(PPh_3)_4$ (245 mg, 0.212 mmol) was added, followed by 1,2,4,5-tetraiodobenzene (2.47 g, 4.24 mmol). The reaction vessel was sealed, taken out of the glovebox and placed inside an oil bath preheated to 100 °C, where it was stirred vigorously for 22 h. The reaction mixture was cooled to 25 °C, diluted with CH_2Cl_2 (400 mL) and poured into a beaker that contained 100 mL $NH_4OH_{(aq)}$, eight spatula scoops of $NH_4Cl_{(s)}$ and 300 mL of deionized H_2O. This mixture was stirred in the beaker for 30 min. The blue aqueous layer was poured out and the organic layer was filter out through a Celite pad, dried with $MgSO_4$ and concentrated. This compound was taken crude to the next step.

Crude compound **31** (5.39 g, 2.83 mmol) was dissolved in 180 mL of dichloromethane in a 250 mL round bottom flask equipped with a magnetic stir bar. The following clear solution was stirred vigorously, then trifluoroacetic acid (10 mL, 130.6 mmol) was added resulting in a yellowish orange solution. Stirring was continued for 24 h at 25 °C. The resulting salt that precipitated out of solution was filtered off and washed with fresh CH_2Cl_2 (3×50 mL). Resulting in a yellow solid that was then vacuum dried for

3 h. A 250 mL round bottom flask equipped with a magnetic stir bar was charged with the crude isolated salt (4.00 g, 2.87 mmol) and 150 mL of CH_2Cl_2. This suspension was cooled to 0 °C followed by the slow addition of NEt_3 (14.42 mL, 103 mmol) over 10 min. This reaction mixture was allowed stirred at 0 °C for another 10 min and then the ice bath was removed, followed by the addition of dimethylaminopyridine (1.753 g, 14.35 mmol), and finally di-*tert*-butyldicarbonate (12.00 g, 55 mmol) was added to the reaction mixture.

The round bottom flask was then sealed with a septum and connected to a bubbler, to monitor the evolution of CO_2. The reaction mixture was stirred vigorously at 25 °C until the evolution of CO_2 ceased (~ 24 h). Upon completion, the reaction mixture was dry-absorbed on silica gel. After purification by column chromatography on silica gel (using hexanes/EtOAc as eluent) and evaporation of the fractions containing the product, compound **32** was obtained (900 mg, 24% yield over two steps). ^{1}H NMR (400 MHz, $CDCl_3$): δ 8.60 (s, 4H), 8.19 (s, 4H), 7.71 (s, 2H), 1.67 (s, 36H). ^{19}F NMR (376 MHz, $CDCl_3$): δ –139.13 to –139.26 (m, 8F) and –141.40 to –141.47 (m, 8F). Anal. Calc'd for $C_{62}H_{46}F_{16}N_8O_8$: C, 55.96; H, 3.81; N, 8.24. Found: C, 55.78; H, 3.47; N, 8.24.

2.5.3 ^{1}H and ^{19}F NMR Spectra of Compounds

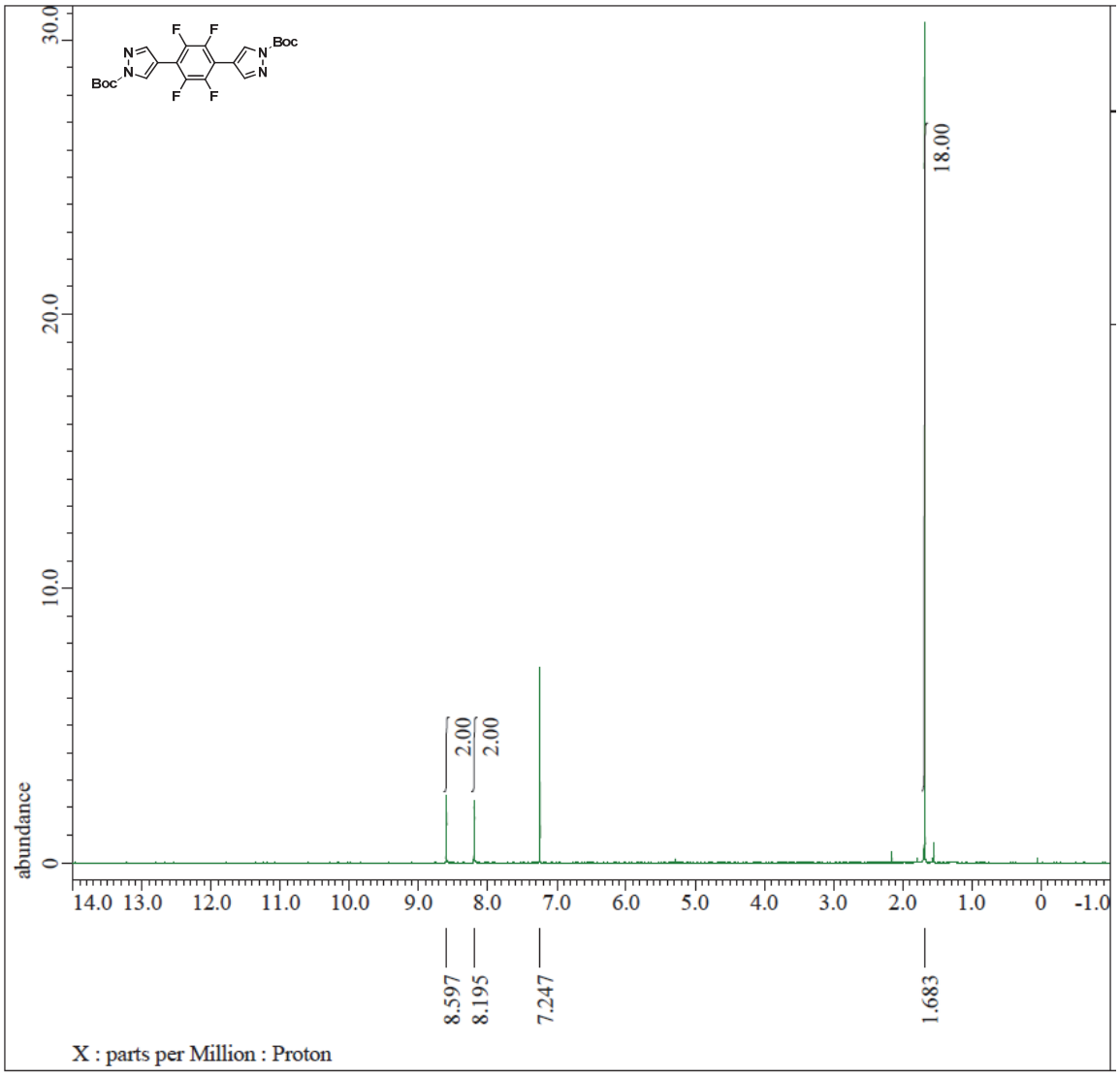

Figure 2.3 ^{1}H NMR Spectrum of compound **10**.

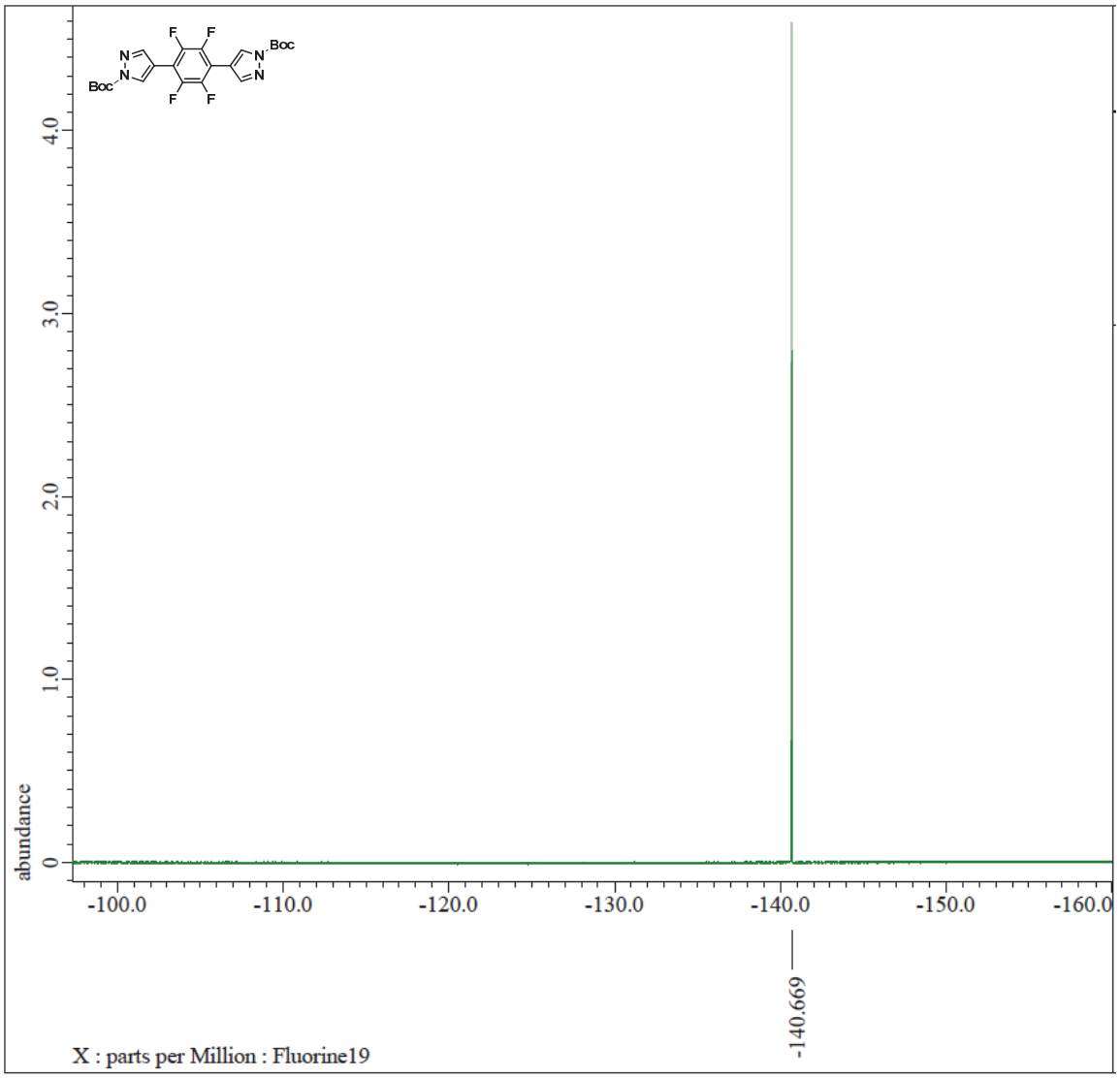

Figure 2.4 ^{19}F NMR Spectrum of compound **10**.

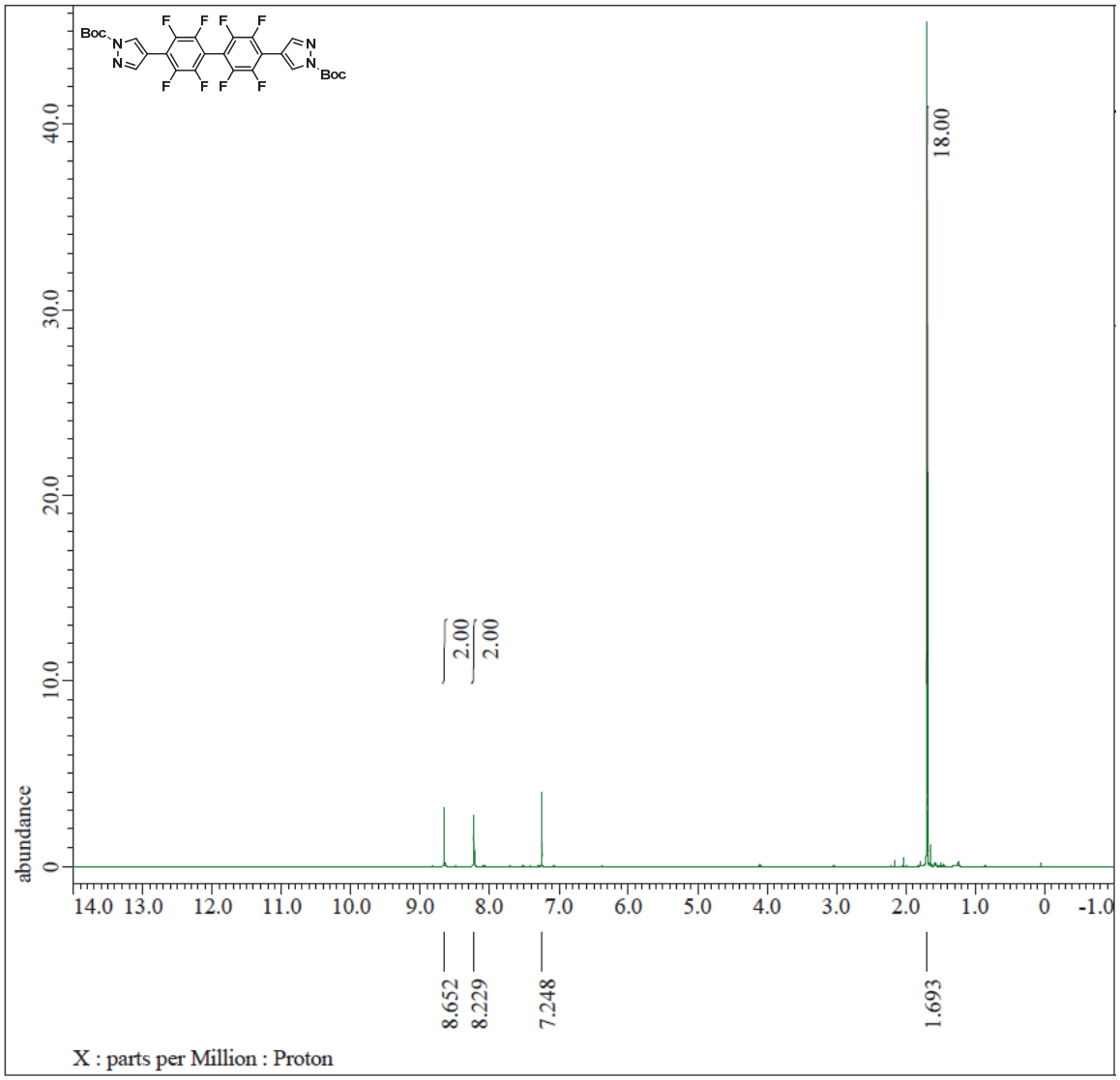

Figure 2.5 ^{1}H NMR Spectrum of compound **11**.

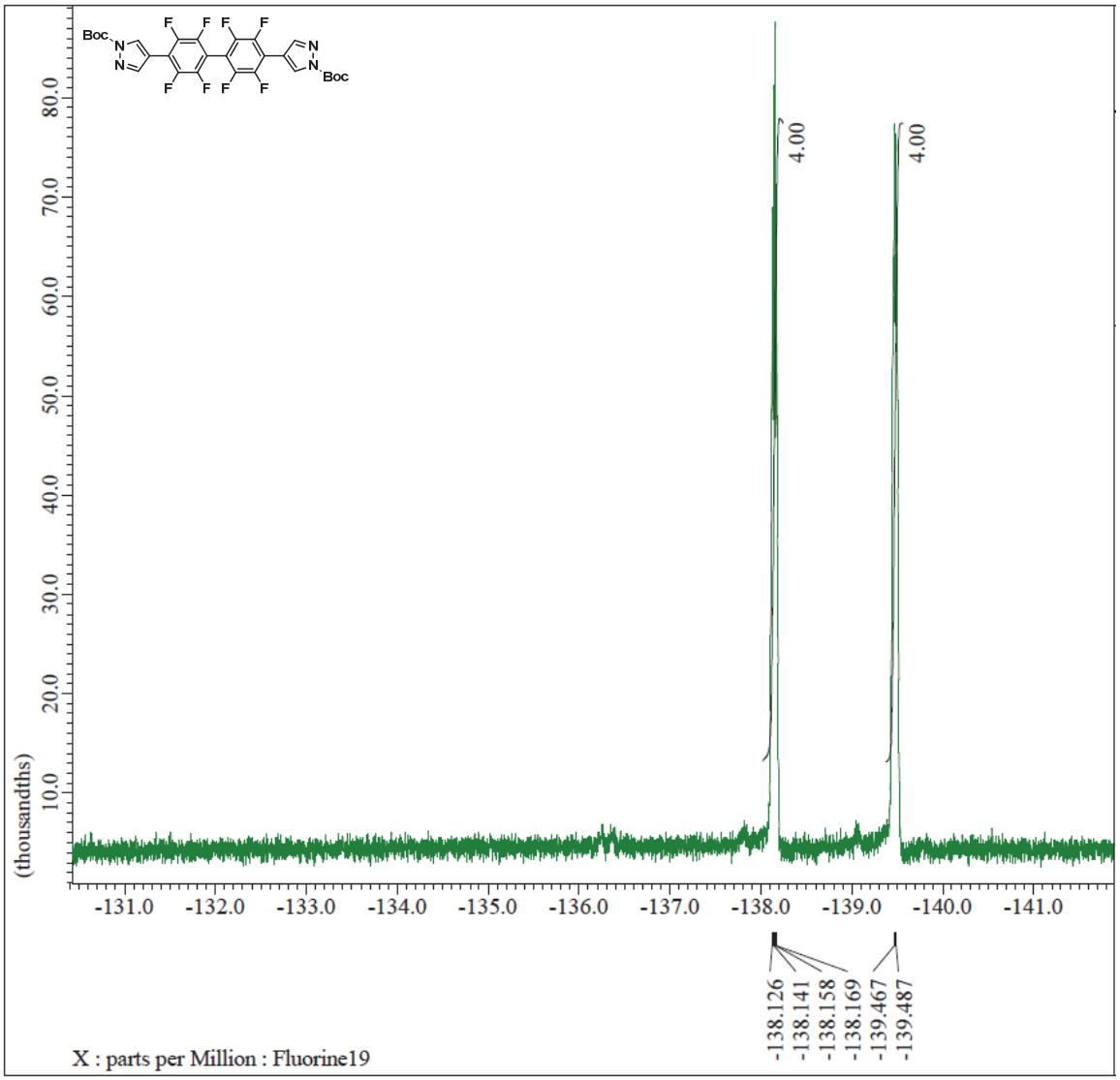

Figure 2.6 ^{19}F NMR Spectrum of compound **11**.

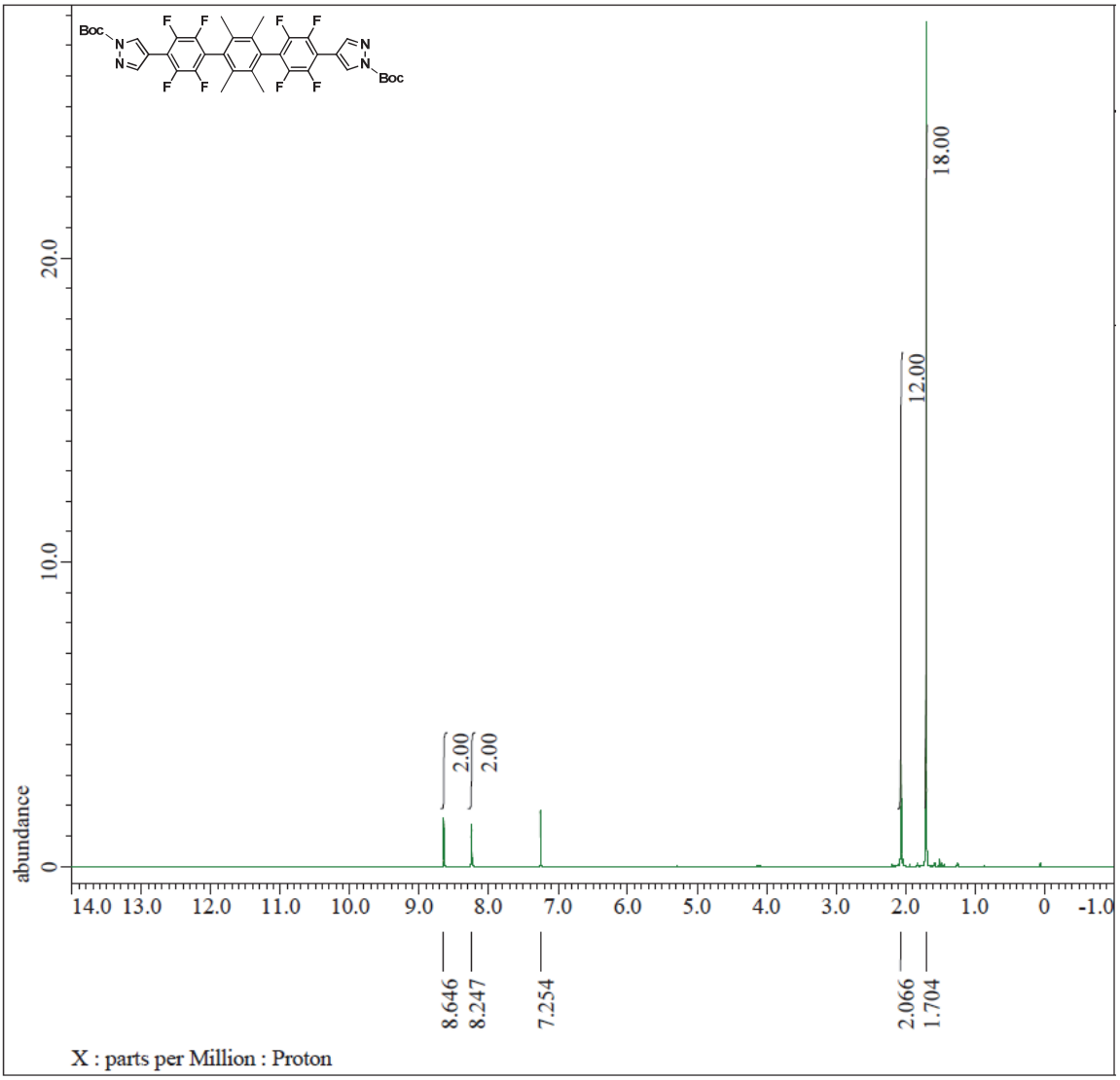

Figure 2.7 ^{1}H NMR Spectrum of compound **12**.

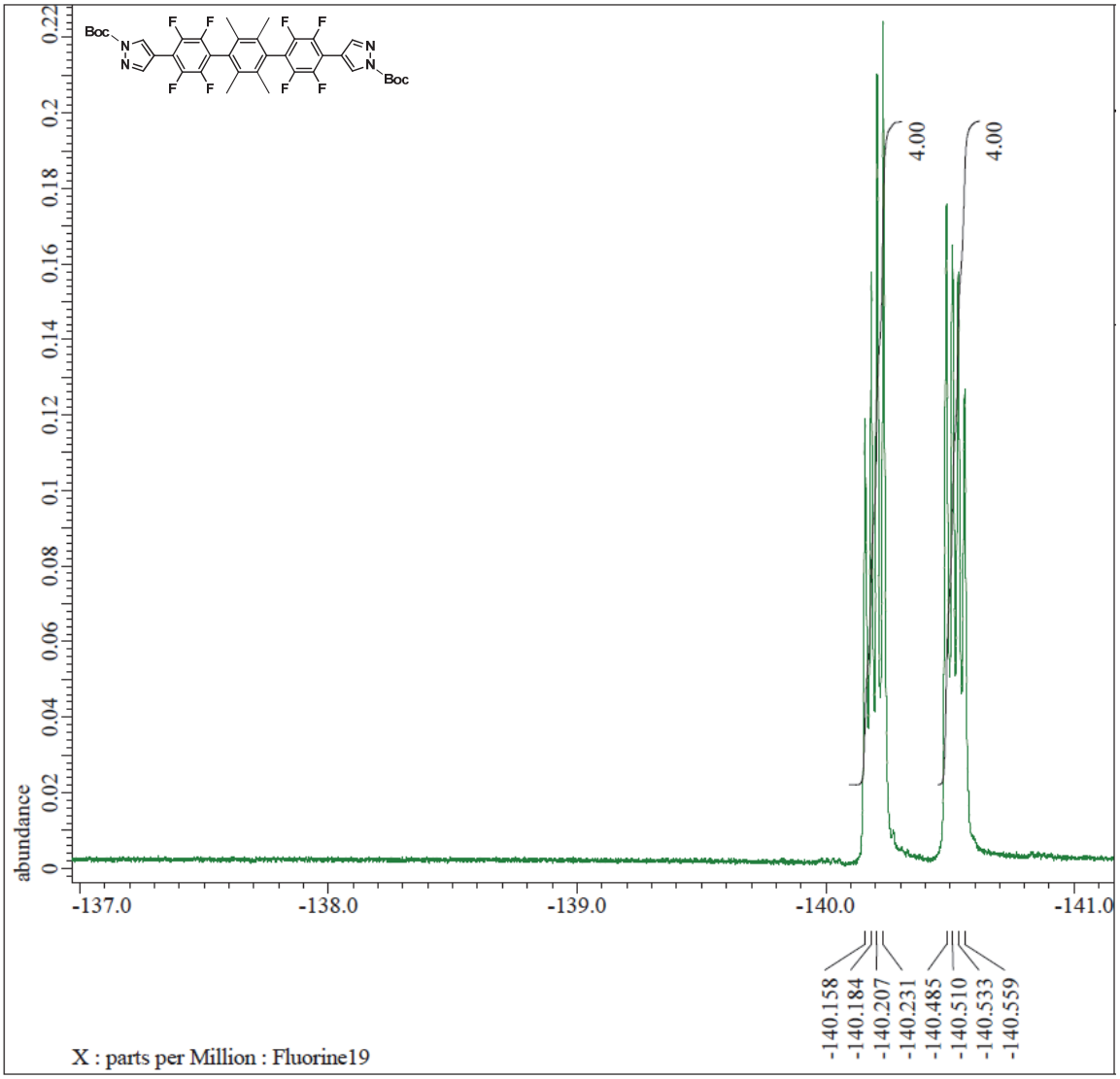

Figure 2.8 ^{19}F NMR Spectrum of compound **12**.

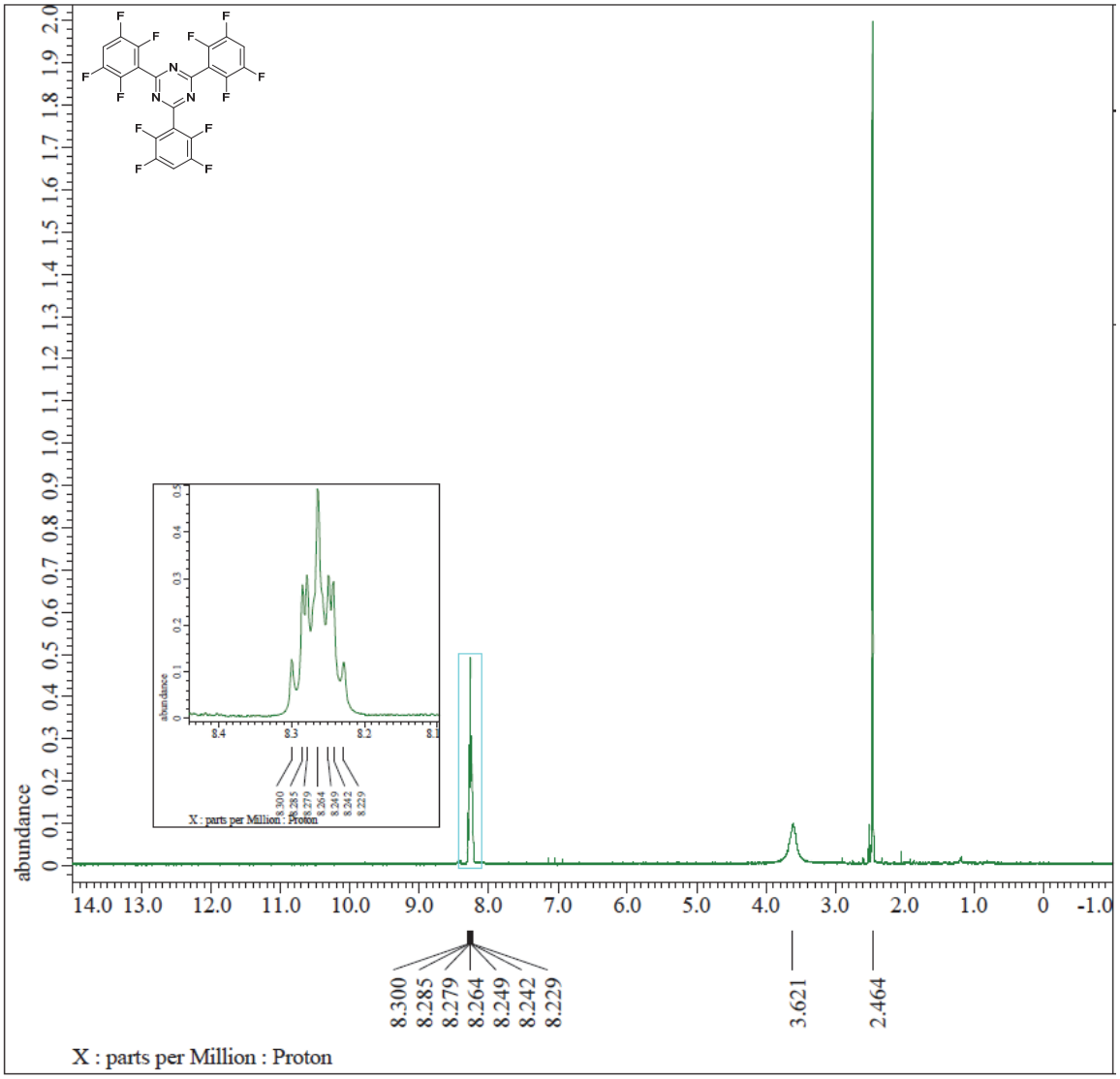

Figure 2.9 ^{1}H NMR Spectrum of compound **14**.

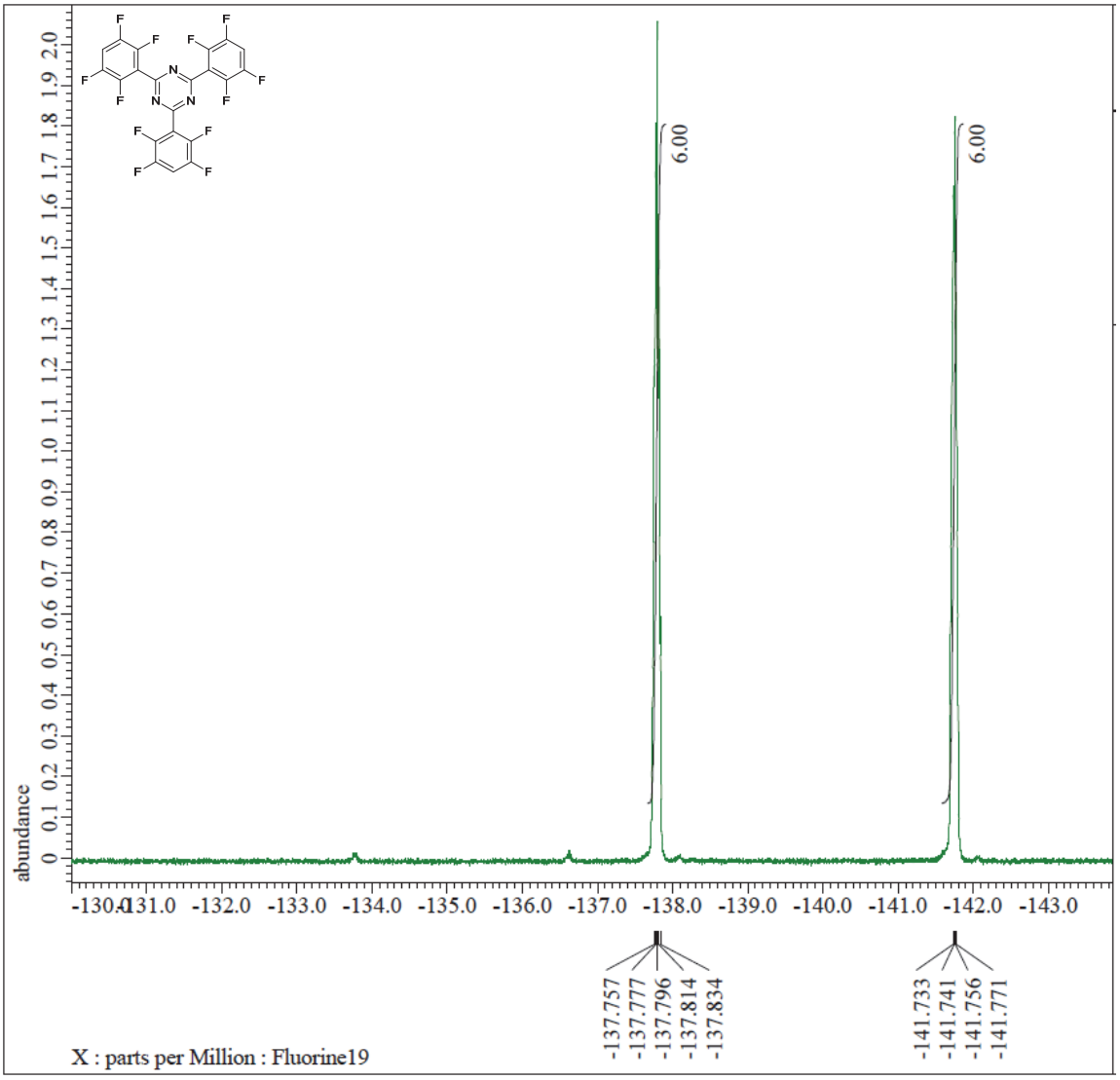

Figure 2.10 ^{19}F NMR Spectrum of compound **14**.

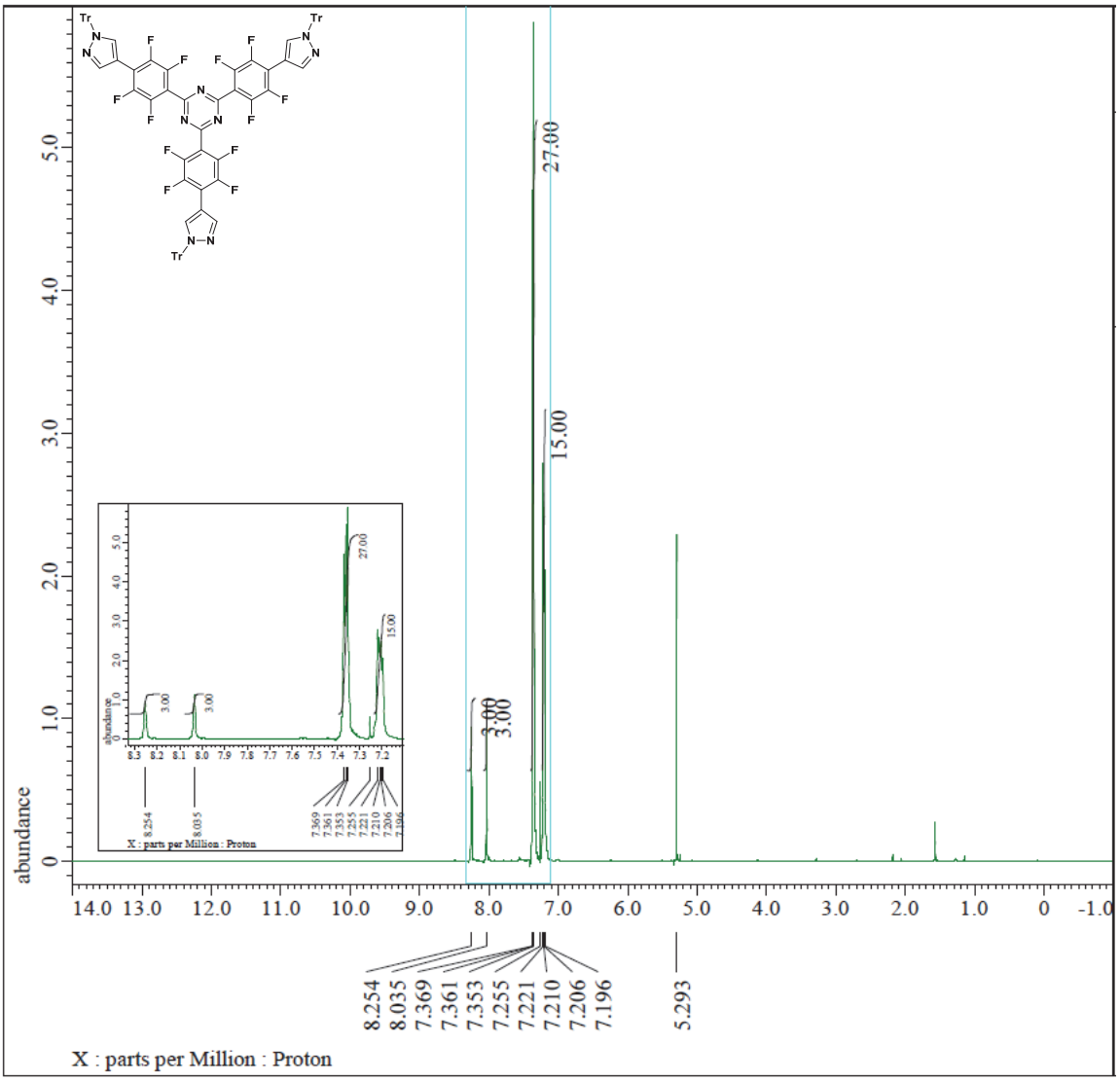

Figure 2.11 ^{1}H NMR Spectrum of compound **15**.

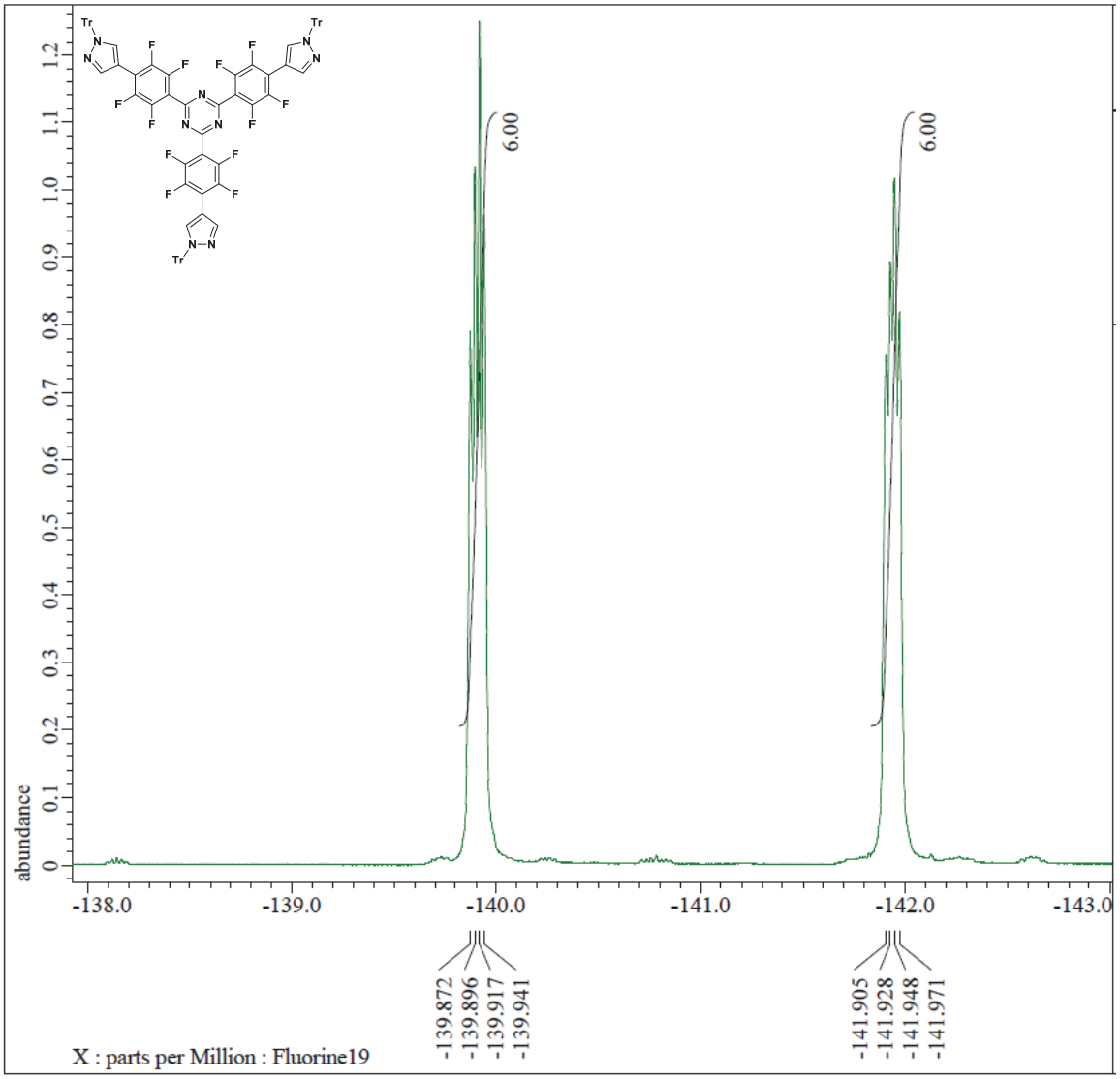

Figure 2.12 ^{19}F NMR Spectrum of compound **15**.

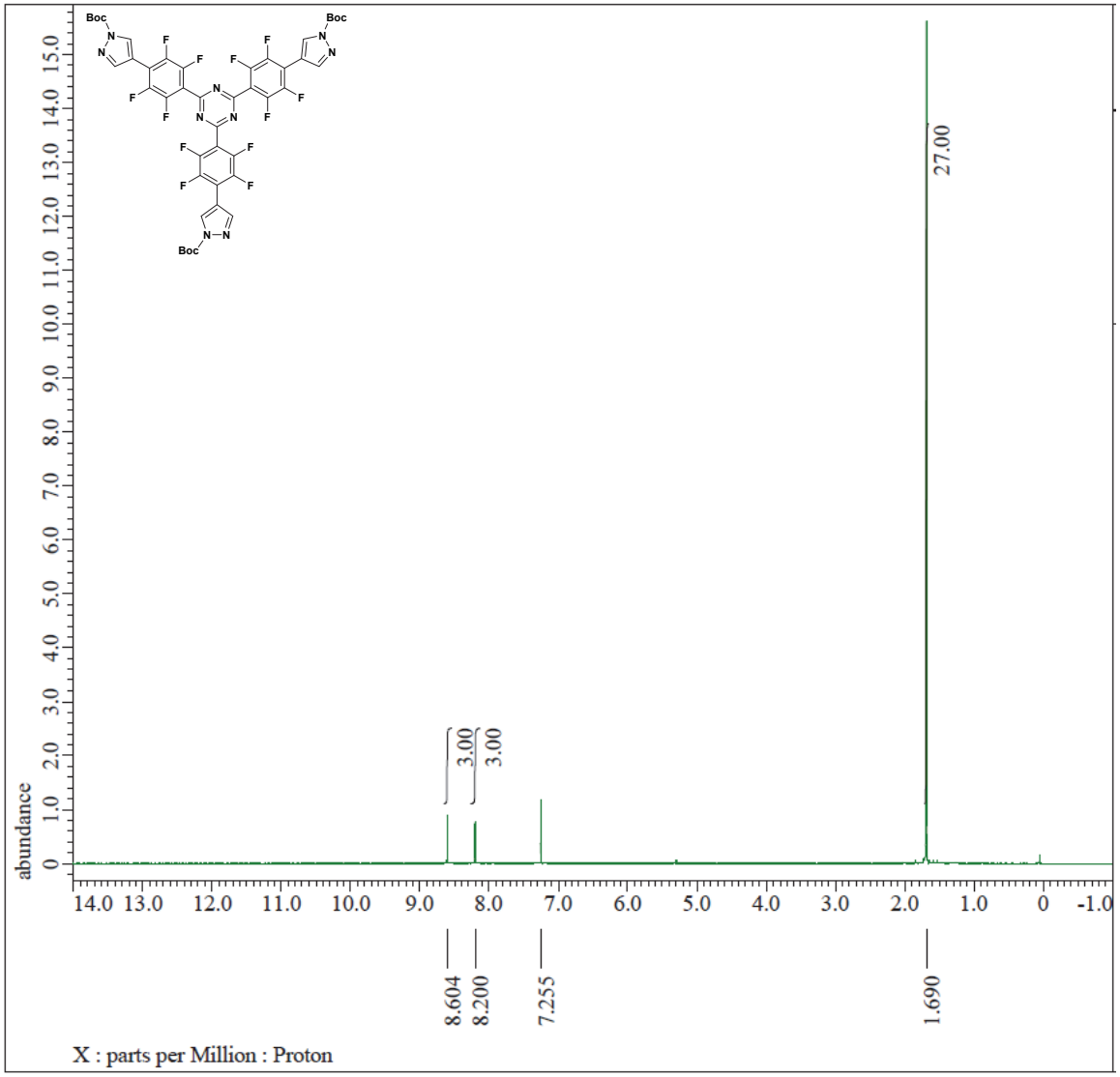

Figure 2.13 ^{1}H NMR Spectrum of compound **16**.

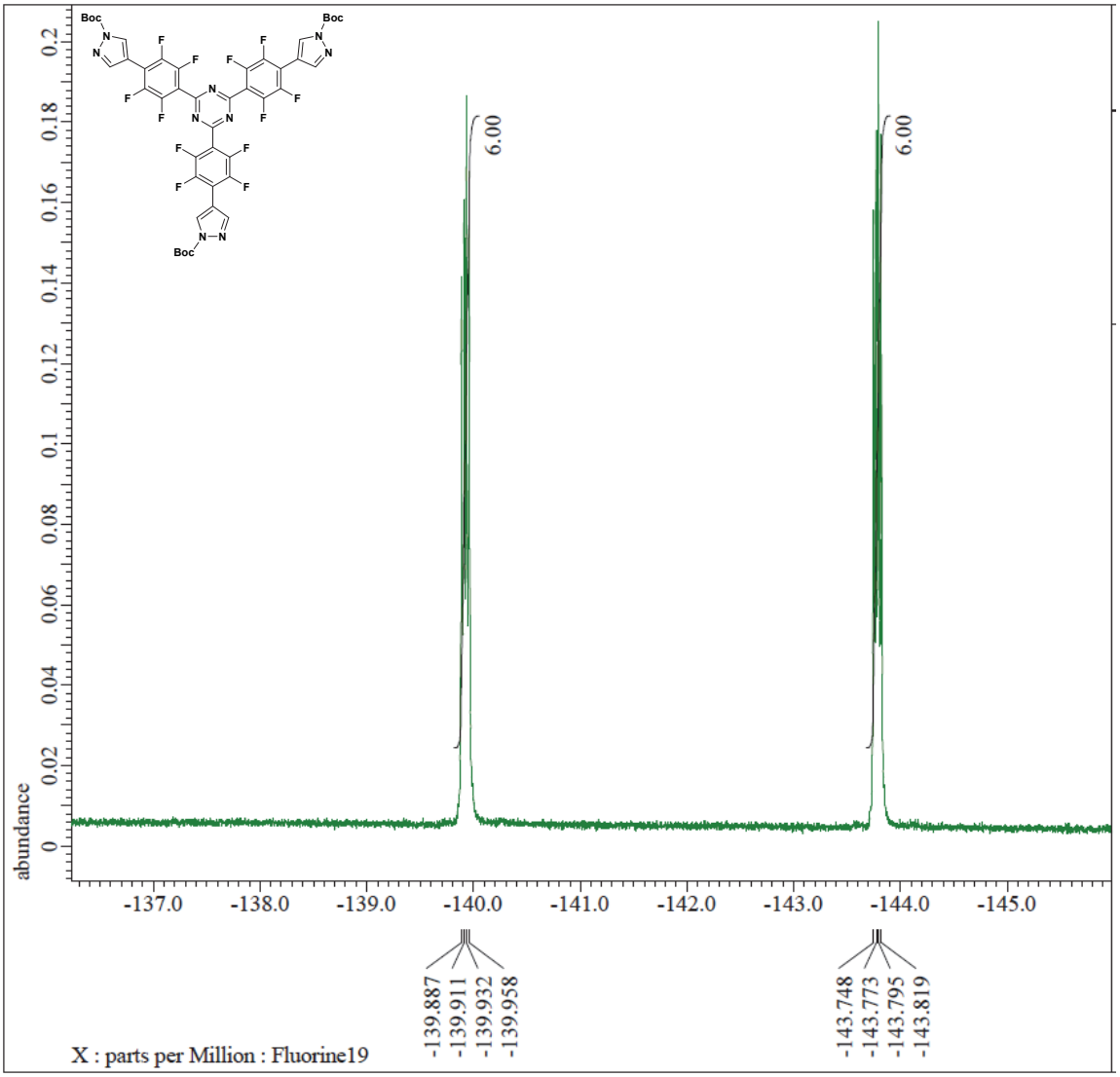

Figure 2.14 ^{19}F NMR Spectrum of compound **16**.

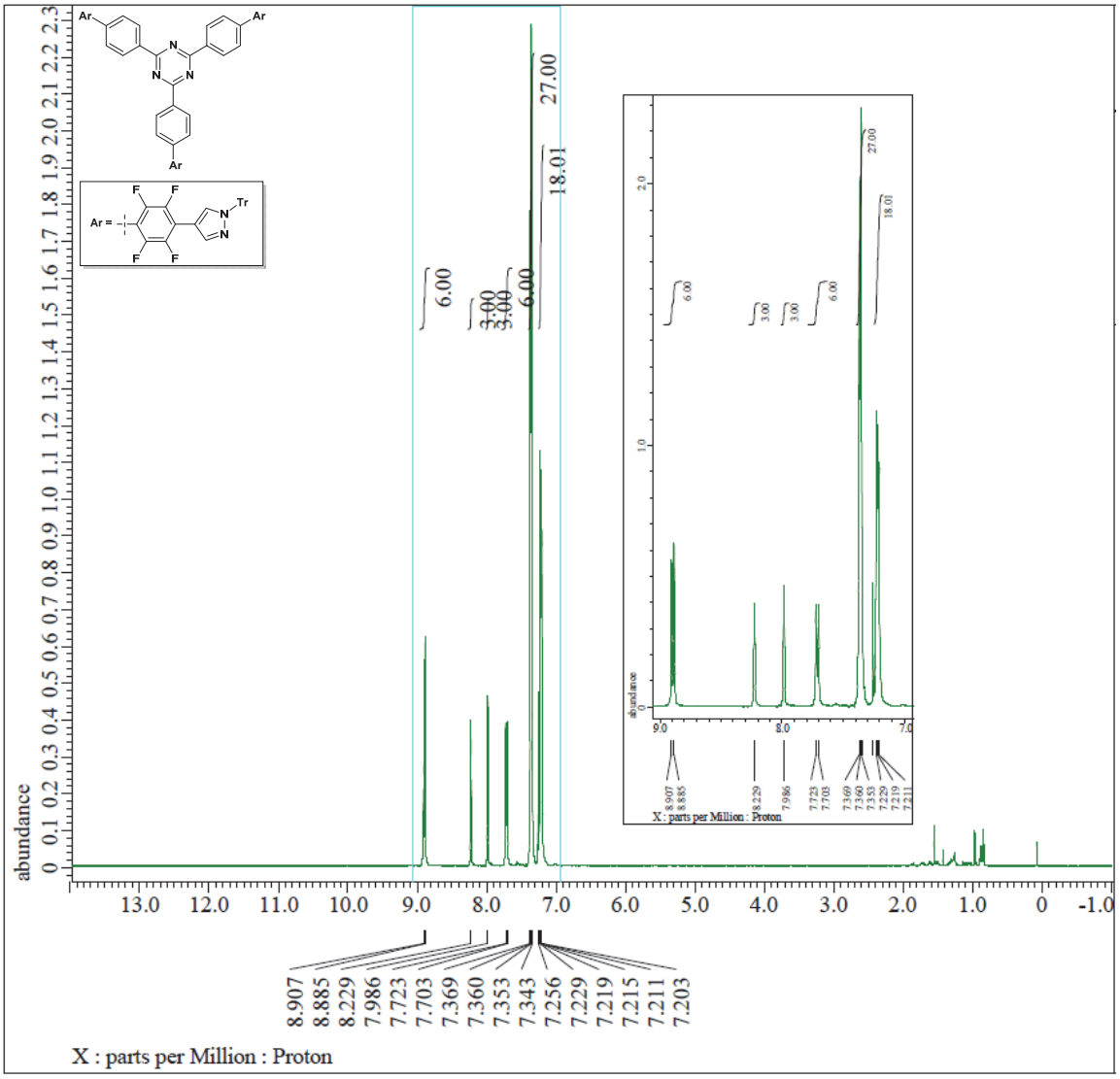

Figure 2.15 ^{1}H NMR Spectrum of compound **19**.

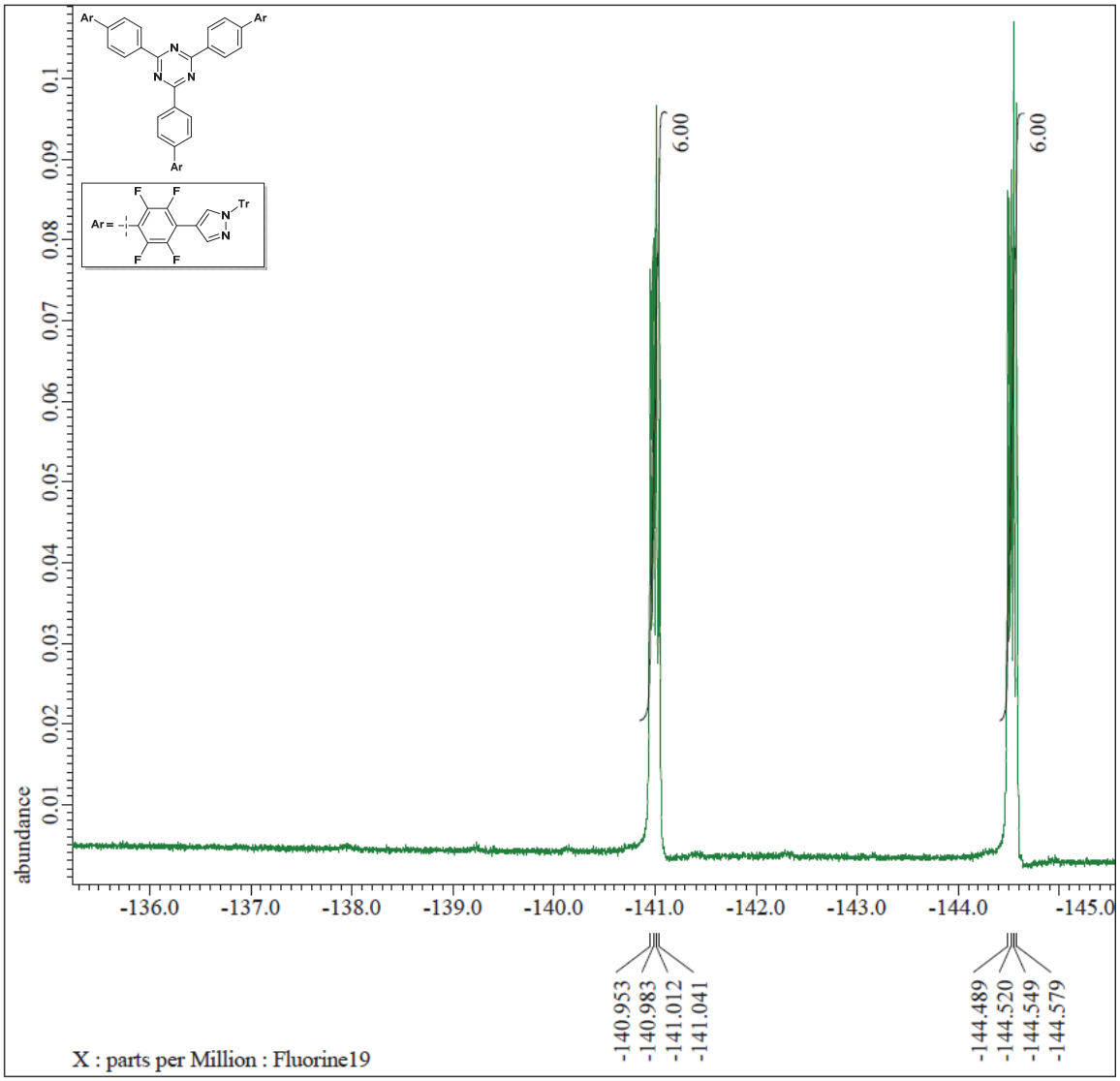

Figure 2.16 ^{19}F NMR Spectrum of compound **19**.

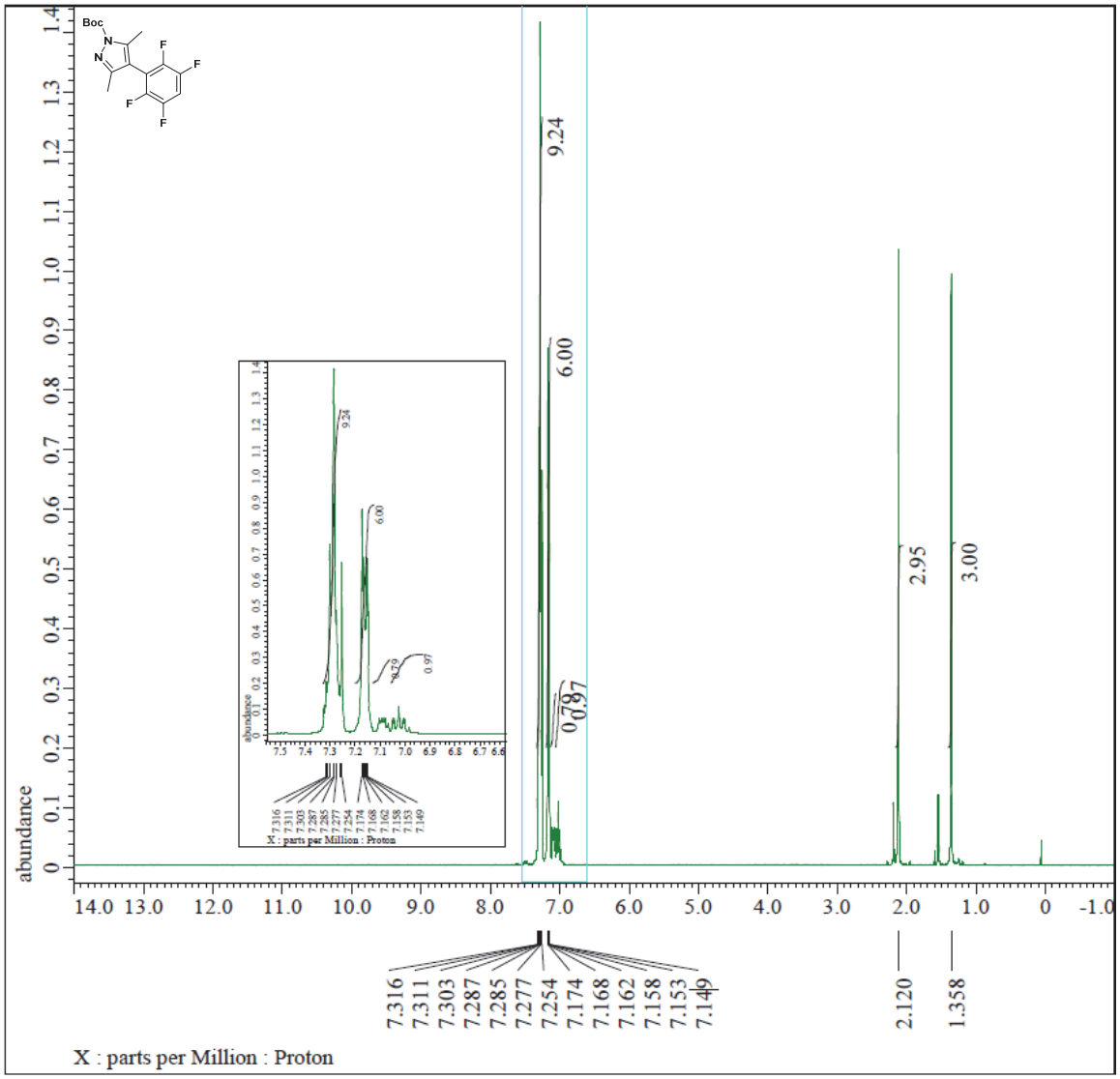

Figure 2.17 ^{1}H NMR Spectrum of compound **21**.

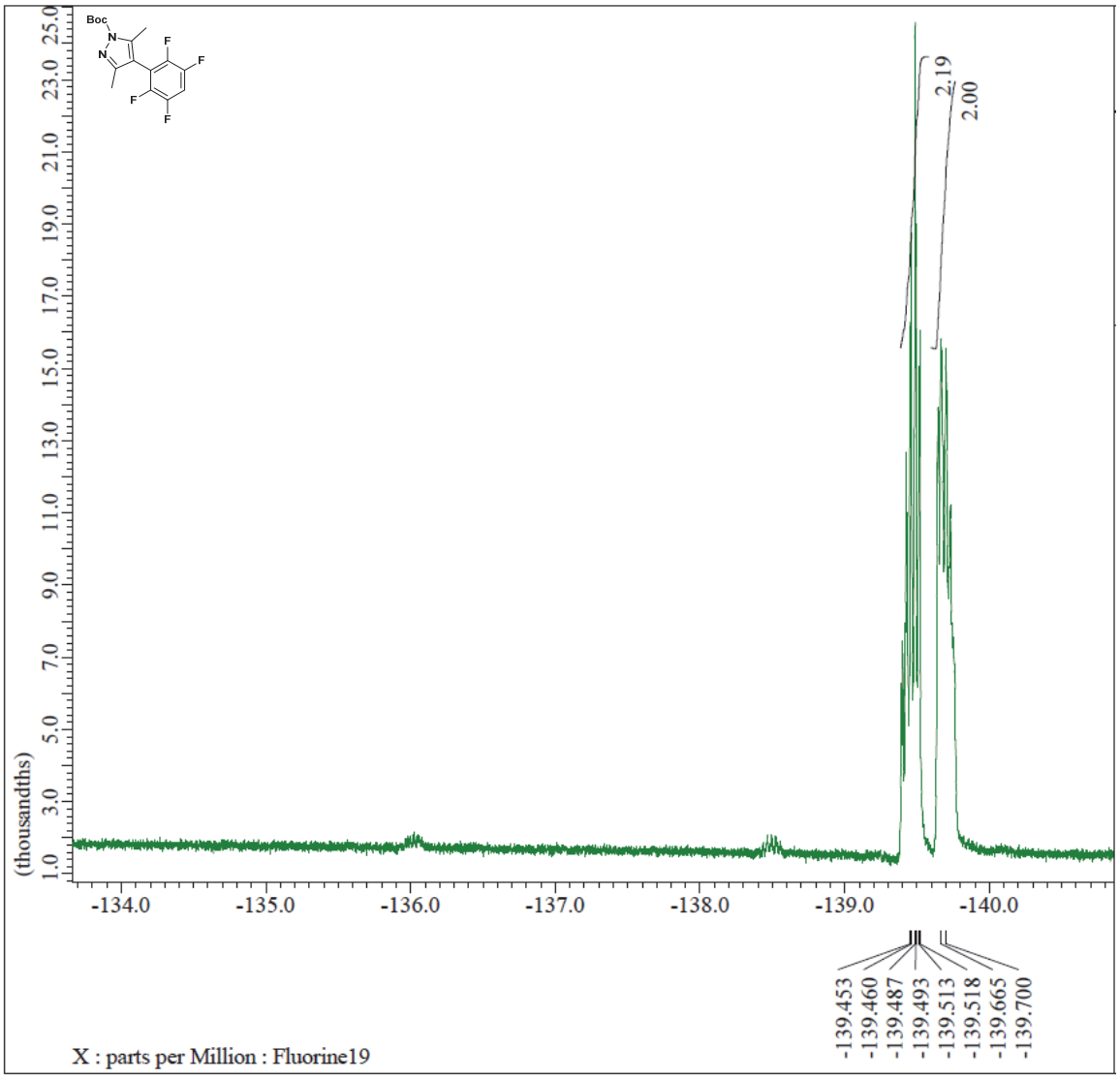

Figure 2.18 ^{19}F NMR Spectrum of compound **21**.

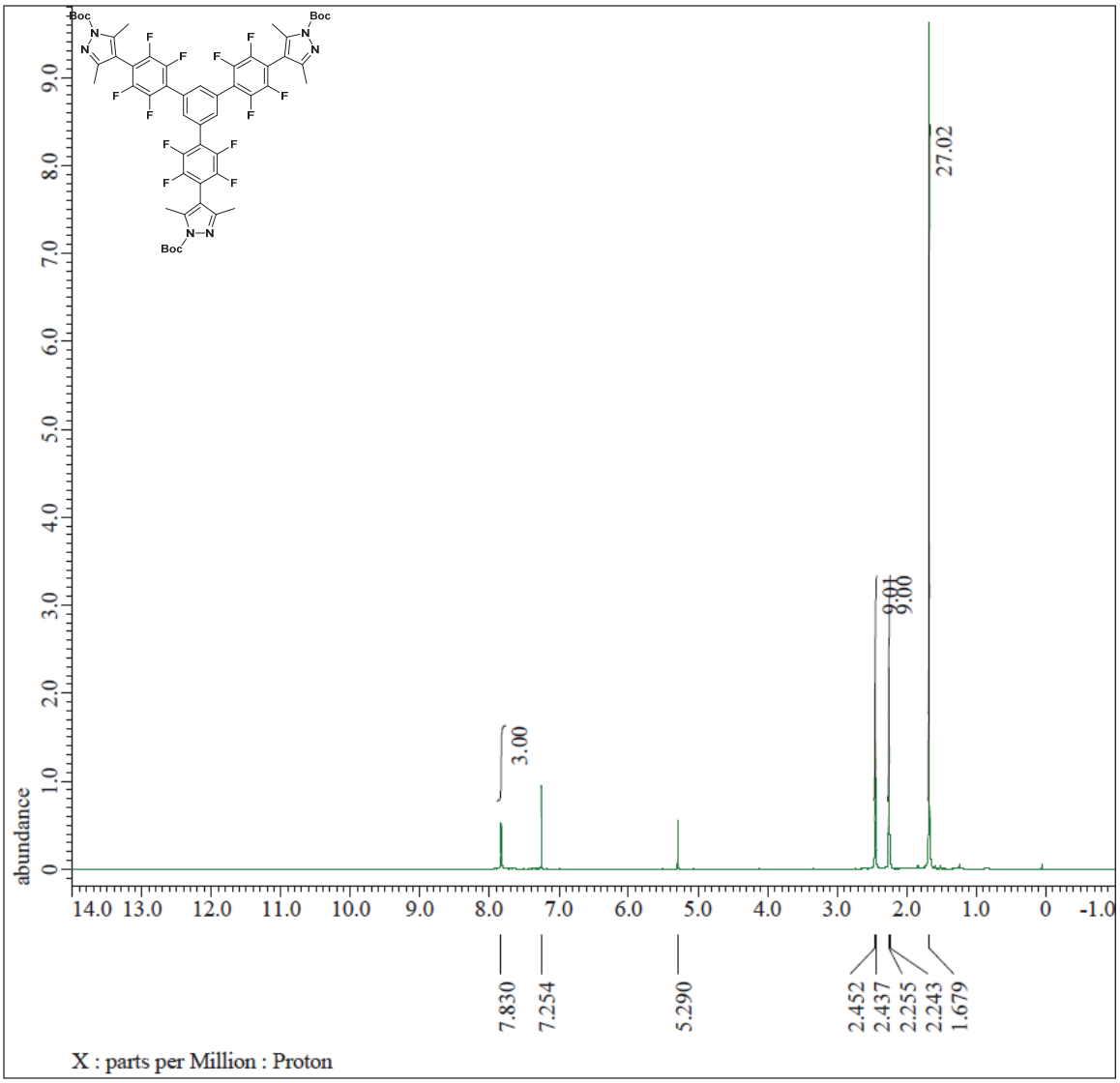

Figure 2.19 ^{1}H NMR Spectrum of compound **23**.

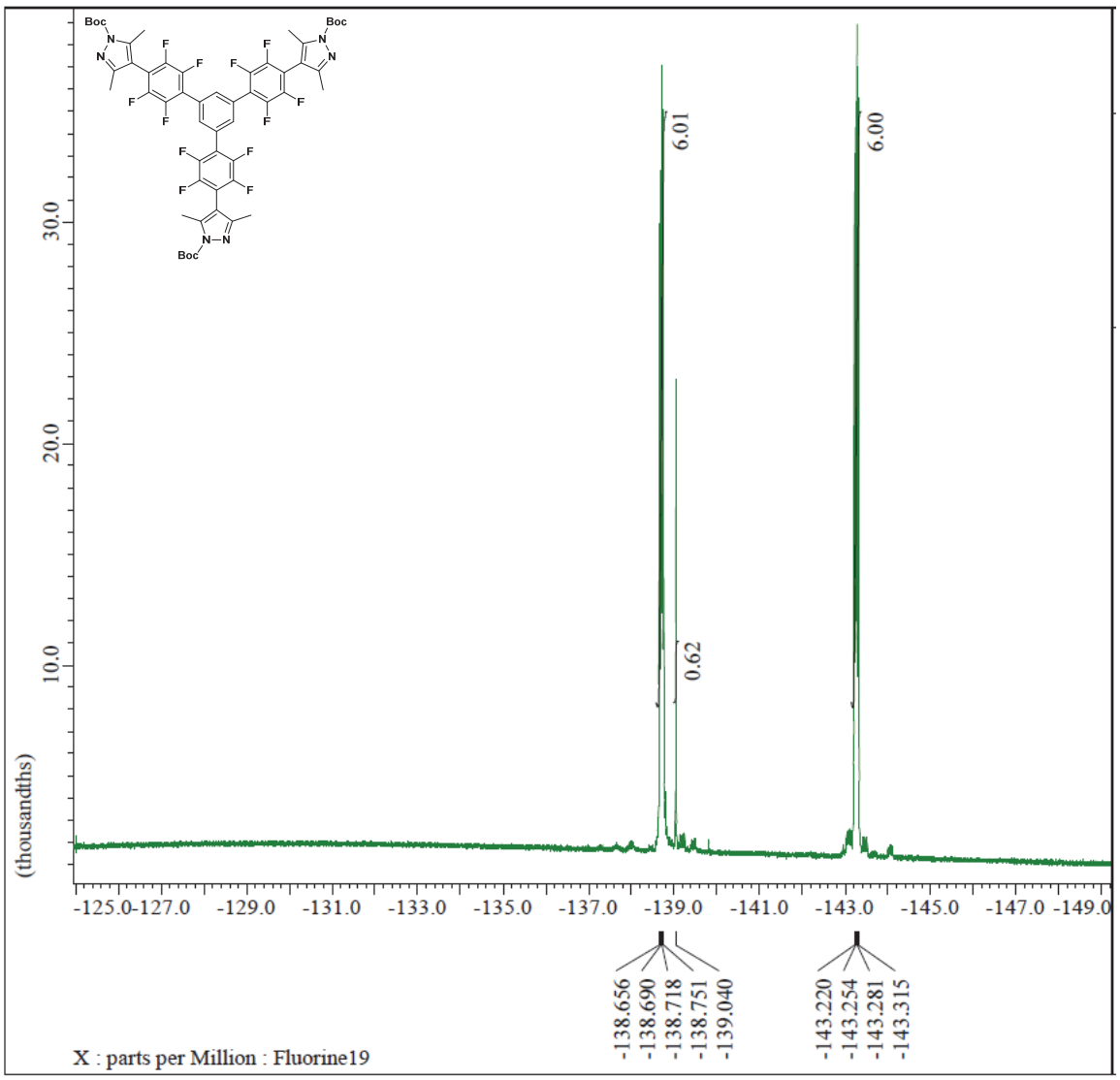

Figure 2.20 ^{19}F NMR Spectrum of compound **23**.

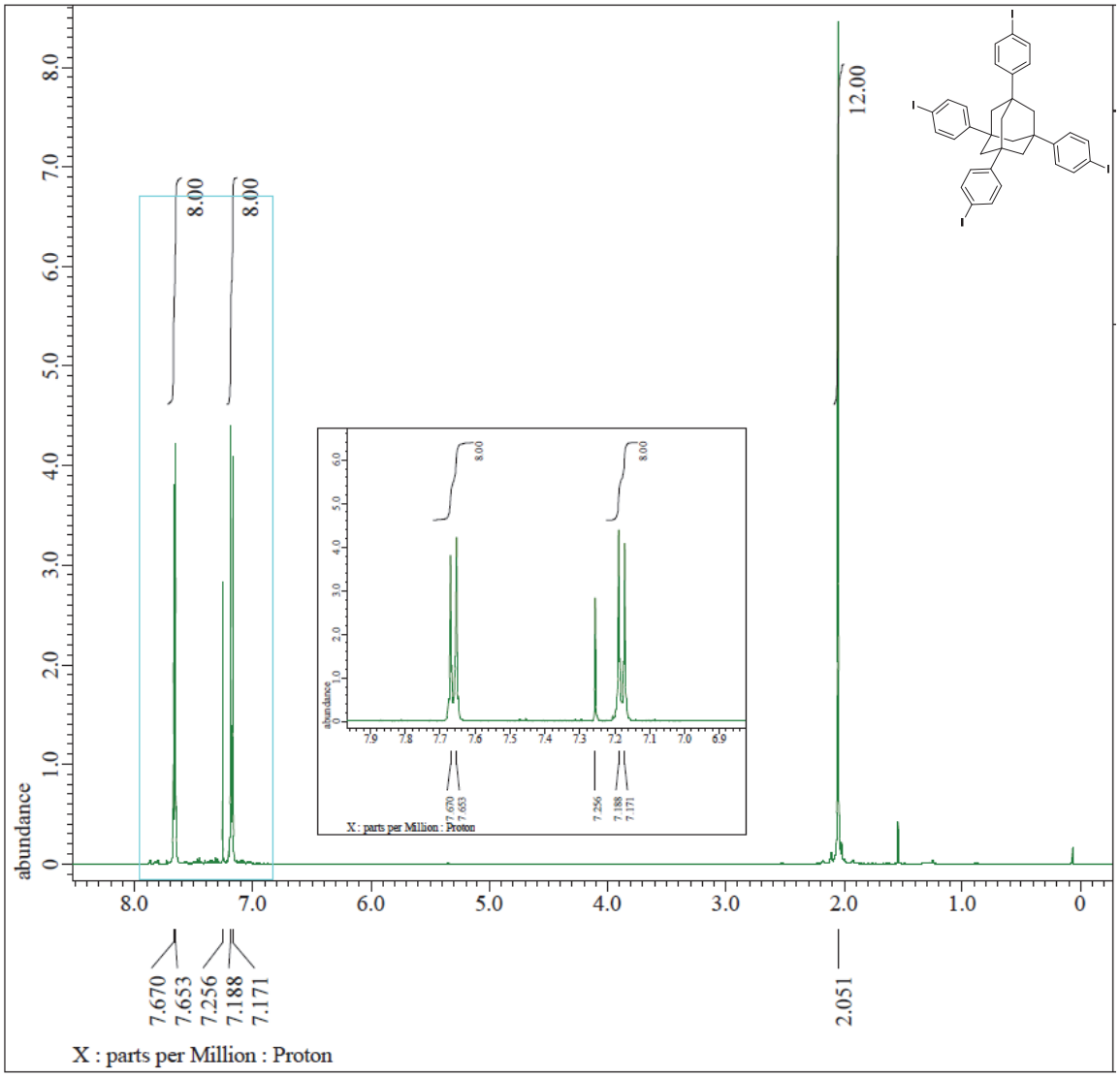

Figure 2.21 ^{1}H NMR Spectrum of compound **26**.

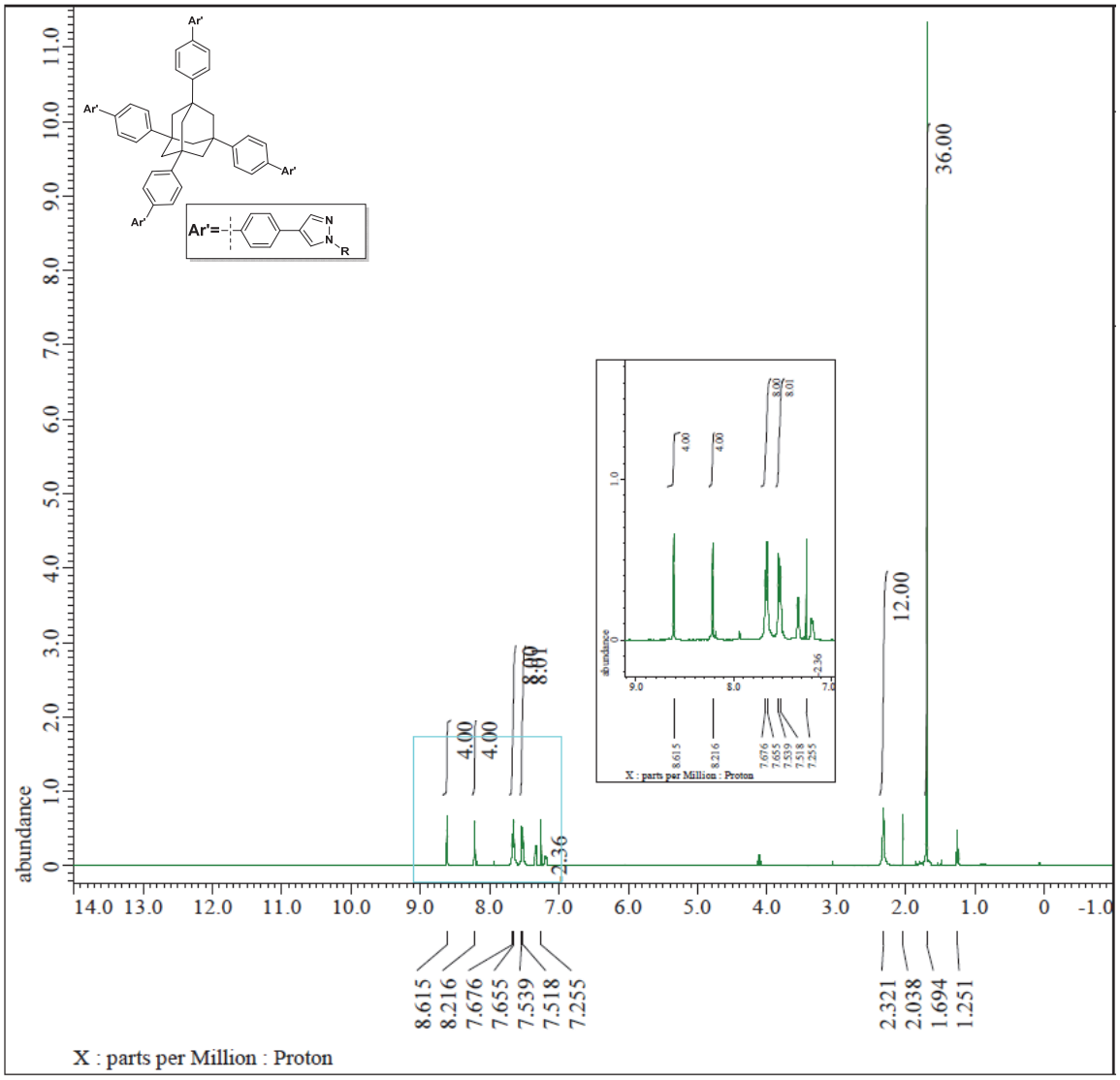

Figure 2.22[1]H NMR Spectrum of compound **28**.

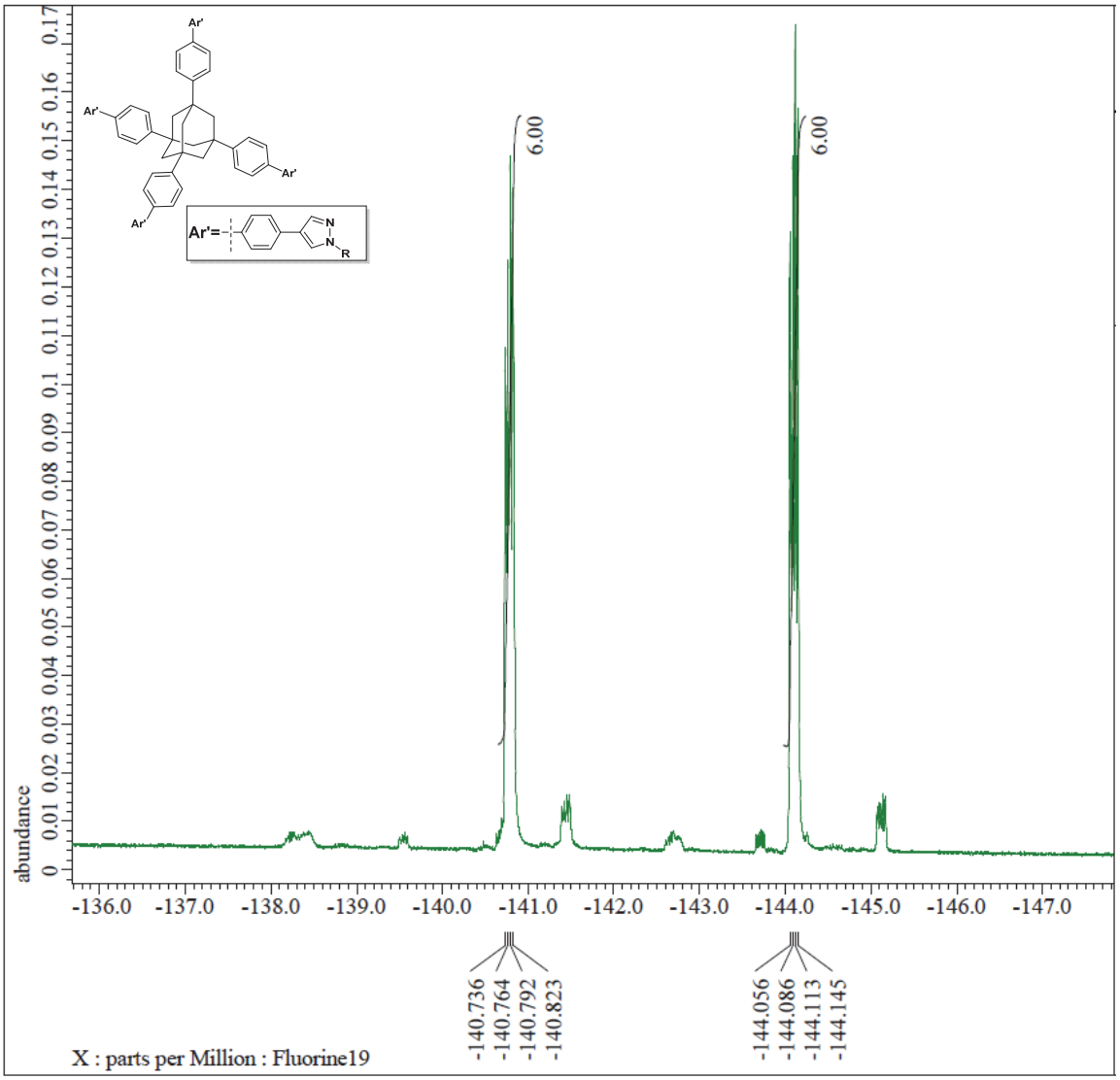

Figure 2.23 ^{19}F NMR Spectrum of compound **28**.

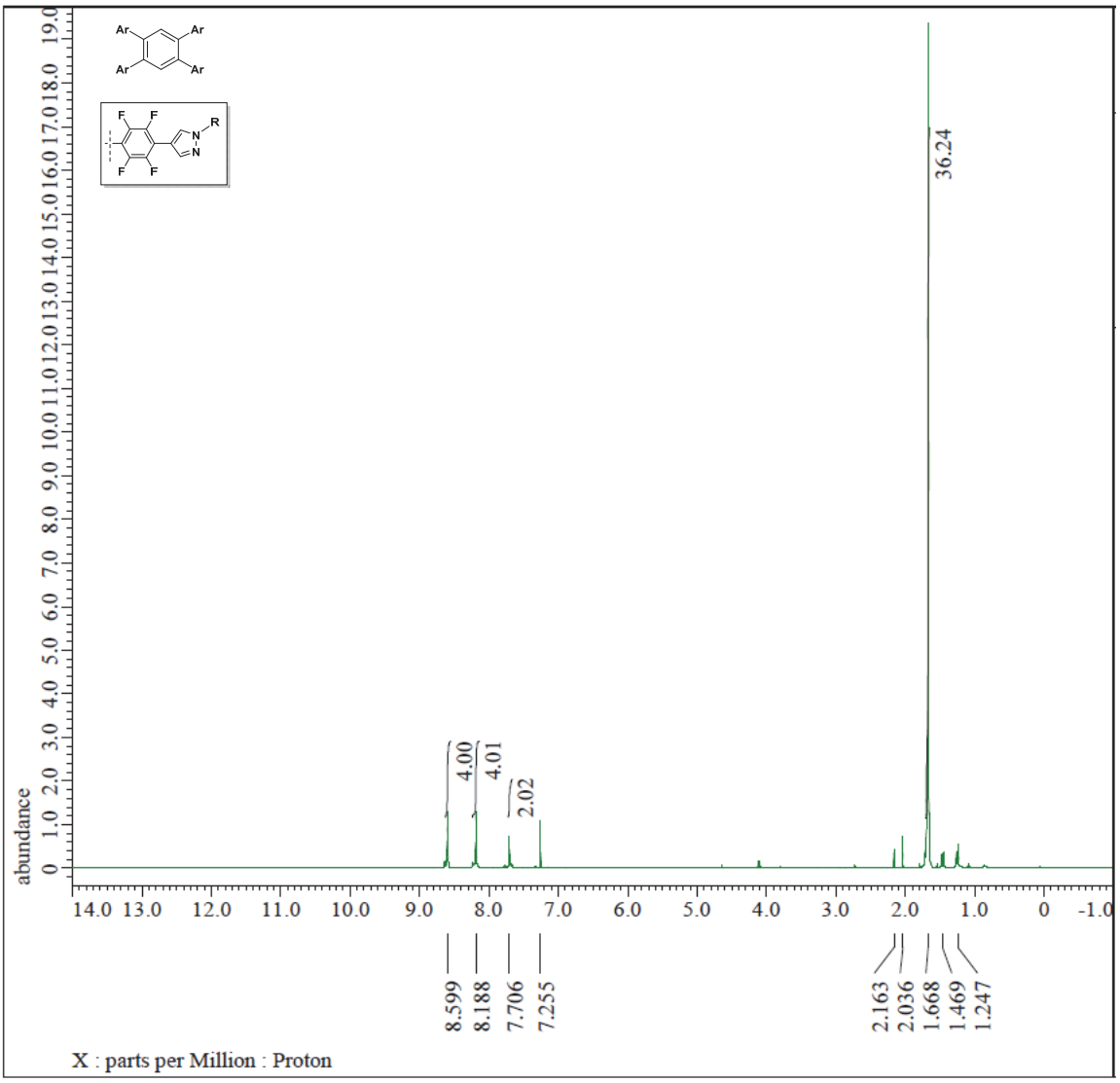

Figure 2.24 ^{1}H NMR Spectrum of compound **32**.

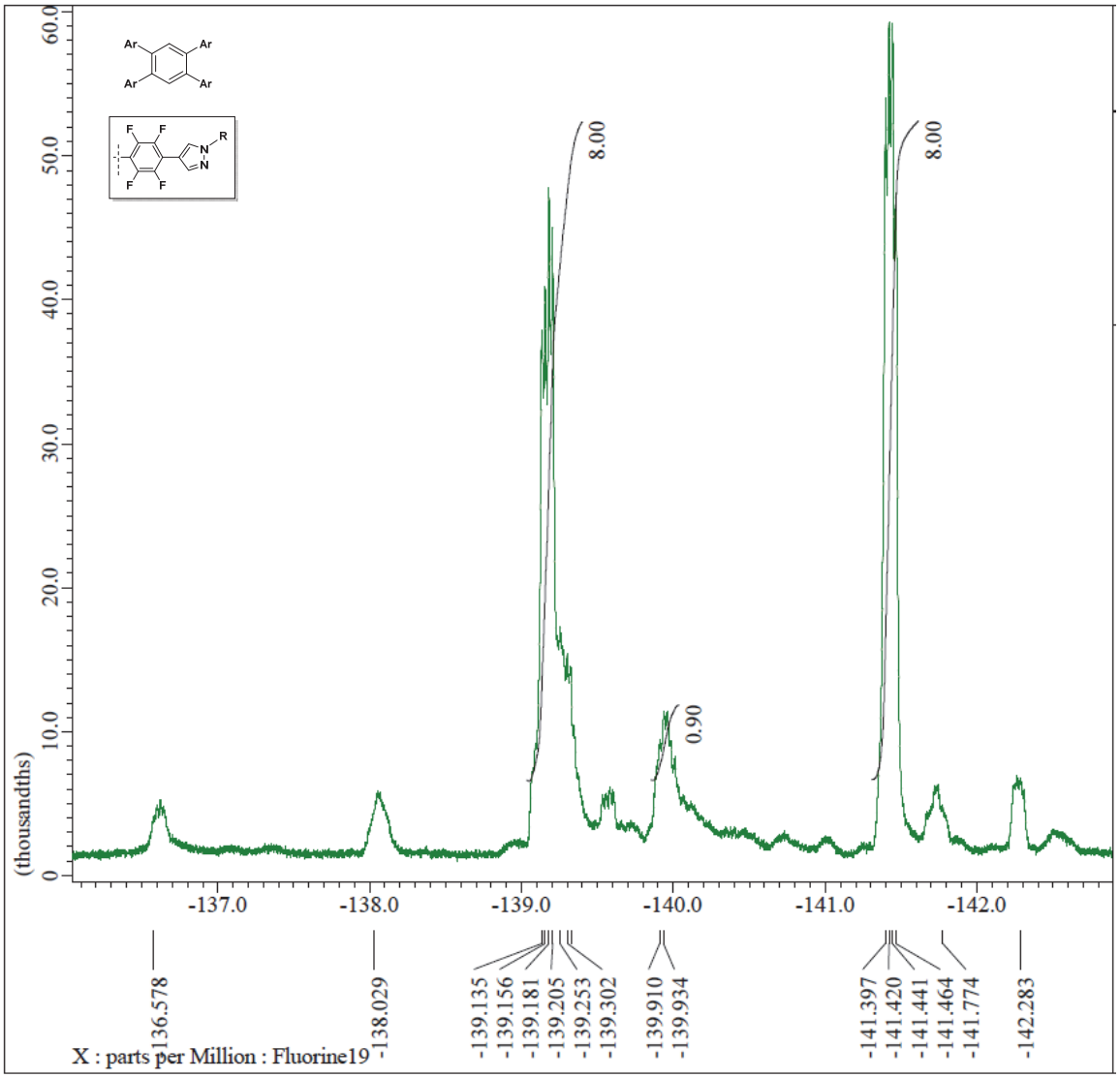

Figure 2.25 ^{19}F NMR Spectrum of compound **32**.

References

1. Kirsch, P. Modern Fluoroorganic Chemistry; Wiley-VCH: Weinhein, Germany **2004**.
2. Gladysz, J. A., Curran, D. P., Horváth, I. T., Eds. Handbook of Fluorous Chemistry; Wiley/VCH: Weinheim, Germany, **2004**.
3. Darmanin, T.; Taffin de Givenchy, E.; Amigoni, S.; Guittard, F. *J. Fluorine Chem.***2012**, *134*, 85–89.
4. Dasgupta, P.; Das, B.; Das, M. K. *Liq. Cryst.* **2012**, *39*, 1297–1304.
5. Sceirs, J. Modern Fluoropolymers: High Performance Polymers for Diverse Applications, ed. Wiley, Hoboken, NJ, **1997**.
6. Wu, P.; Zhang, S.; Yang, H.; Zhu, Y.; Chen, J. *J. Polym. Sci. A Polym. Chem.* **2018**, *56*, 1508–1515.
7. Scanga, R.; Chrastecka, L.; Mohammad, R.; Meadows, A.; Quan, P.-L.; Brouzes, E. *RSC Adv.* **2018**, *8*, 12960–12974.
8. Su, Y.; Zhao, Q.; Liu, J.; Zhao, J.; Li, Y.; Jiang, Z. *Desalin. Water Treat.* **2015**, *55*, 304 –314.
9. Shirdast, A.; Sharif, A.; Abdollahi, M. *Int. J. Hydrogen Energy* **2014**, *39*, 1760–1768.
10. Al Akhrass, S.; Damiron, D.; Carrot, G.; Drockenmuller, E. J. *Polym. Sci., Part A: Polym. Chem.* **2010**, *48*, 3888–3895.
11. Zuo, B.; Li, C.; Li, Y.; Qian, W.; Ye, X.; Zhang, L.; Wang, X. *Langmuir* **2018**, *34*, 3993–4003.

12. Fujiwara, H.; Chott, R. C.; Solsten, R. T. *Biol. Mass Spectrom.* **1992**, *21*, 431–440.

13. Bastos, J. C.; Carvalho, S. F.; Welton, T.; Canongia Lopes, J. N.; Rebelo, L. P. N.; Shimizu, K.; Araujo, J. M. M.; Pereiro, A. B. *Chem. Commun.* **2018**, *54*, 3524–3527.

14. Yang, C.; Wang, X.; Omary, M. A. *J. Am. Chem. Soc.* **2007**, *129*, 15454–15455.

15. Yang, C.; Wang, X.; Omary, M. A. *Angew. Chem. Int. Ed.* **2009**, *48*, 2500–2505

16. Yang, C.; Kaipa, U.; Mather, Q. Z.; Wang, X.; Nesterov, V.; Venero, A. F.; Omary, M. A. *J. Am. Chem. Soc.* **2011**, *133*, 18094–18097.

17. Nijem, N.; Canepa, P.; Kaipa, U.; Tan, K.; Roodenko, K.; Tekarli, S.; Halbert, J.; Oswald, I. W. H.; Arvapally, R. K.; Yang, C.; Thonhauser, T.; Omary, M. A.; Chabal, Y. J. *J. Am. Chem. Soc.* **2013**, *135*, 12615–12626.

18. Zhang, D.-S.; Chang, Z.; Li, Y.-F.; Jiang, Z.-Y.; Xuan, Z.-H.; Zhang, Y.-H.; Li, J.-R.; Chen, Q.; Hu, T.-L.; Bu, X.-H *Sci. Rep.* **2013**, 3, 3312, doi: 10.1038/srep03312.

19. Cui, X.; Chen, K.; Xing, H.; Yang, Q.; Krishna, R.; Bao, Z.; Wu, H.; Zhou, W.; Dong, X.; Han, Y.; Li, B.; Ren, Q.; Zaworotko, M. J.; Chen, B. *Science* **2016**, *353*, 141–144.

20. Jang, M.; Yamaguchi, T.; Ohara, K.; Kawano, M.; Fujita, M. *Chem. Asian J.* **2009**, *4*, 1524–1526.

21. Fujie, K.; Otsubo, K.; Ikeda, R.; Yamada, T.; Kitagawa, H. *Chem. Sci.* **2015**, *6*, 4306–4310.

22. Mileo, P. G. M.; Adil, K.; Davis, L.; Cadiau, A.; Belmabkhout, Y.; Aggarwal, H.; Maurin, G.; Eddaoudi, M.; Devautour-Vinot, S. *J. Am. Chem. Soc.* **2018**, *140*, 13156–13160.

23. Pal, T. K.; De, D.; Senthilkumar, S.; Neogi, S.; Bharadwaj, P. K. *Inorg. Chem.*, **2016**, *55*, 7835−7842.

24. Mukherjee, S.; Kansara, A. M.; Saha, D.; Gonnade, R.; Mullangi, D.; Manna, B.; Desai, A. V.; Thorat, S. H.; Singh, P. S.; Mukherjee, A.; Ghosh, S. K. *Chem. Eur. J.* **2016**, *22*, 10937–10943.

25. Hashim, M. I.; Hsu, C.-W.; Le, H. T. M.; Miljanić, O. Š. *Synlett* **2016**, *27*, 1907–1918.

26. Chen, T.-H.; Popov, I.; Zenasni, O.; Daugulis, O.; Miljanić, O. Š. *Chem. Commun.* **2013**, *49*, 6846–6648.

27. Chen, T.-H.; Popov, I.; Kaveevivitchai, W.; Chuang, Y.-C.; Chen, Y.-S.; Jacobson, A. J.; Miljanić, O. Š. *Angew. Chem. Int. Ed.* **2015**, *54*, 13902–13906.

28. Chen, T.-H.; Popov, I.; Kaveevivitchai, W.; Chuang, Y. C.; Chen, Y. S.; Daugulis, O.; Jacobson, A. J.; Miljanić, O. Š. *Nat. Commun.* **2014**, *5*, doi: 10.1038/ncomms6131.

29. Chen, T.-H.; Kaveevivitchai, W.; Jacobson, A. J.; Miljanić, O. Š. *Chem. Commun.* **2015**, *51*, 14096–14098.

30. Hendon, C.; Wittering, K.; Chen, T.-H.; Kaveevivitchai, W.; Popov, I.; Butler, K. T.; Wilson, C. C.; Cruickshank, D.; Miljanić, O. Š.; Walsh, A. *Nano Lett*. **2015**, *15*, 2149–2154.

31. Hashim, M. I.; Le, H. T. M.; Chen, T.-H.; Chen, Y.-S. Daugulis, O.; Hsu, C.-W.; Jacobson, A. J.; Kaveevivitchai, W.; Liang, X.; Makarenko, T.; Miljanić, O. Š.; Popovs, I.; Tran, H. V.; Wang, X.; Wu, C.-H.; Wu, J. I. *J. Am. Chem. Soc.* **2018**, *140*, 6014–6026.

32. Smolin, E. M.; Rapoport, L. *The chemistry of Hetrocyclic Compounds: s-Triazines and Derivatives*, Interscience Publishers Inc., New York, **1959**.

33. Fierz-David, H.; Matter, M. *J. Soc. Dyers and Colour.* **1937**, 53, 424–436.

34. Kolmakov, K. A.; J. *Heterocycl. Chem.* **2008**, *45*, 533–539.

35. Matsumoto, K.; Sera, A.; Uchida, T. *Synthesis* **1985**, 1–37.

36. Berger, R.; Hauser, J.; Labat, G.; Weber, E.; Huliger, J. *CrystEngComm* **2012**, *14*, 768–770.

37. Xu, F.; Sun, J.-H.; Yan, H.-B.; Shen, Q. *Synth. Commun.* **2000**, *30*, 1017–1022.

38. Naritomi, M.; Murofushi, H.; Nakashima, N. *Bull. Chem. Soc. Jpn.* **2004**, *77*, 2121–2127.

39. Rudenko, A. P.; Salfetnikova, Yu. N.; Vasil'ev, A. V. *Russ. J. Org. Chem.* **1996**, *32*, 1499–1521.

40. Krasnov, V. I.; Platonov, V. E. *Russ. J. Org. Chem.* **1993**, *29*, 895–896.

41. Xiang, Y.; Caron, P.-Y.; Lillie, B. M.; Vaidyanathan, R. *Org. Process Res. Dev.* **2008**, *12*, 116–119.

42. Tokoro, Y.; Nagai, A.; Chujo, Y. *Macromolecules* **2010**, *43*, 6229–6233.

43. Entwistle, C. D.; Marder, T. B. *Chem. Mater.* **2004**, *16*, 4574–4585.

44. Li, Q.; Rukavishnikov, A. V.; Petukhov, P. A.; Zaikova, T. O.; Keana, J. F. *Org. Lett.* **2002**, *4*, 3631–3634.

45. Hyatt, John A. *Org. Prep. Proced. Int.* **1991**, *23*, 460–464.

46. Fieser, L. F. *Org. Synth.* **1966**, 46, 44, doi: 10.15227/orgsyn.046.0044

Chapter Three

Crystal growth and Characterization of Fluorinated Porous Molecular Crystals

3.1 Crystal Growth and Engineering of PMCs

A crystal is a solid composed of atoms, molecules, or ions that are arranged in a periodic pattern that reflects its internal symmetry (quasicrystals[1] are a related class of ordered, but not periodic solids). The crystal consists of minimal repeating smaller structural units, called unit cells which are translationally repeated throughout the crystal. A fundamental property of crystals is their symmetry, and all crystals can be classified on the basis of their main symmetry elements into seven crystal systems: cubic, tetragonal, orthorhombic, monoclinic, triclinic, trigonal, and hexagonal.[2] Crystalline solids can be classified as single crystalline or polycrystalline. The single crystals possess a near ideal and continuous arrangement of basic building blocks that is unbroken all the way towards the edges of the sample with no grain boundaries (i.e. interfaces where crystals of different orientations come into contact with one another).

The above arrangement of atoms give single crystals unique mechanical, optical, and electrical properties. For example, single crystal silicon is used in the manufacture of semiconductors and single crystal nickel silicide/silicon heterostructure nanowires display ideal resistivity for the use in sharp metallic semiconductors.[3] As for the mechanical properties, face-centered-cubic nickel based single crystal super alloys[4,5,6] have been used in the manufacture of jet turbine blades with minimal thermal creep (deformation of the blades resulting in failure).[7] Polycrystalline materials are composed

of many aggregates of microscopic crystals. Of the two classes, we are more interested in single crystals of PMCs, as they permit easy determination of their internal structure through X-ray diffraction.

In order to prepare single crystals, we are taking advantage of crystal engineering principles to further our understanding of non-covalent molecular interactions. The term crystal engineering was first coined by Schmidt in 1971,[8] in regards to his work on photodimerization reactions of cinnamic acid. A more modern and broader definition of this term was proposed by Desiraju, stating that it is the utilization of supramolecular interactions in the context of crystal packing in order to design new solids with desired physicochemical properties.[9] The non-covalent intermolecular interactions we chose to focus on were hydrogen bonding and π–π stacking as both of these interactions were proven to be strong enough to support our very first synthesized PMC.[10] The directional nature of hydrogen bonds and the extensive studies conducted on pyrazoles in solution show that they can form hydrogen bonds leading to cyclic dimers, trimers, and tetramers.[11]

With this knowledge in hand we began growing crystals of our PMCs via solvothermal Boc (*tert*-butoxycarbonyl) deprotection reactions of the precursor molecules screened under various reaction conditions. The mechanism by which PMCs, COFs, and MOFs are formed is not well understood.[12,13,14] Initially, the Boc protecting group is thermally removed,[15] thereby exposing the N–H of the pyrazole end groups which can then form [N–H···N] hydrogen bonds with each other. Our understanding of the nucleation and crystal growth process that occur in our system after this point is deficient. Based on the mechanistic studies conducted by Dichtel et al. on COFs,[16] one could infer

that our PMCs may follow a similar mechanistic pathway, in which crystals may arise from the formation of large 2D sheets of [N–H···N] hydrogen bonded layers that eventually stack on top of each other. There also exists the possibility that one layer is formed and then smaller subunits of the [N–H···N] hydrogen bonded framework stack on top, initiating the formation of the next layer similar to a template. Either way, more detailed mechanistic and computational studies need to be conducted on our PMC systems.

3.2 Crystal Structures of PMCs Derived from the Synthesized Precursors

3.2.1 Crystal Structures derived from the Linear Precursors

This section examines the crystal structures of the PMCs that were obtained from the precursors previously synthesized in Chapter 2. The first crystal was obtained from the solvothermal deprotection of **10** yielding crystals of **32** (Scheme 3.1). The crystal structure of **32** (depicted in Figure 3.1), reveals an essentially planar molecule with angles between the planes of the central and terminal rings of 5.4 °. Pyrazoles on each side of the molecule form catemers in infinite zig-zagging arrays of hydrogen bonds (N–H···N distance of 1.88 Å,[17] NHN angle 174 °), wherein each molecule of **32** connects to four other molecules in the solid state (Figure 3.1A). Neighboring molecules of **32** are in planes that define a 54.4 ° angle; overall, the molecule organizes into corrugated 2D sheets (Figure 3.1B), which then stack on top of each other, resulting in an overall non-porous structure. Examination of the 2D sheet layers reveals that the individual molecules stack on top of each other at a distance of 3.72 Å from one another. This observation could indicate a stabilizing interaction due to [π···π] stacking as it is close to the upper

limits of 3.8 Å reported by Janiak,[18] or this could be due to the fluorine atoms interacting directly with the electron rich pyrazole ring system without the involvement of the π system being as suggested by Houk and Wheeler.[19] The latter seems to be a more accurate depiction. As the distance is close to the upper limit and more recent literature about rethinking the usage of the term [π···π] stacking,[20] causes one to consider this interaction as a direct substituent effect.

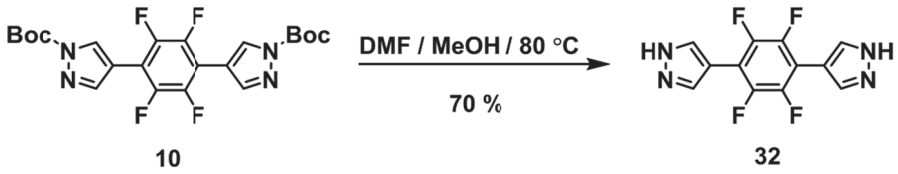

Scheme 3.1 Synthesis of **32**.

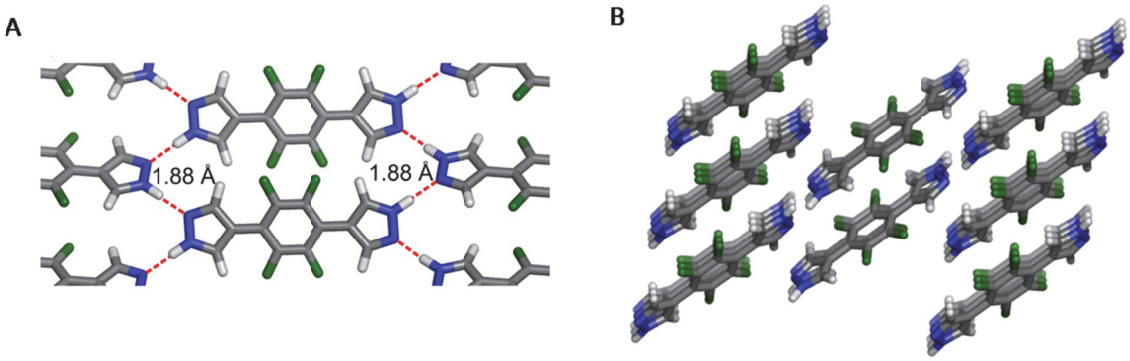

Figure 3.1 Crystal structure of **32**. (A) Hydrogen bonding pattern observed in the structure. (B) The molecule organizes into 2D corrugated sheet which stack to produce an overall nonporous 3D structure.

The second linear PMC compound **33** was synthesized according to Scheme 3.2. It is chemically similar to **32**, but its molecular structure is more deplanarized (Figure 3.2A). The two pyrazole rings are slightly distorted away from coplanarity with their tetrafluorobenzene neighbors (by 5.8 ° and 14.3 °). The largest distortion, however, is found in the deplanarization of the two 1,2,4,5-tetrafluorobenzene rings by 56.4° relative

to each other. This deplanarization minimizes steric interactions between neighboring fluorine atoms of the two 1,2,4,5-tetrafluorobenzene rings and the degree of deplanarization is quite similar to the 57.6 ° twist angle observed in the crystal structure of 2,2'-difluorobipohenyl.[21] Similar to **32**, each molecule of **33** also connects to four of its neighbors via hydrogen bonding (N−H···N distances of 1.82 and 1.94 Å, NHN angles of 158 ° and 170 °, respectively). This crystal structure is also overall nonporous and does not display [π···π] stacking between the pyrazoles and 1,2,4,5-tetrafluorobenzene moieties just like **32**.

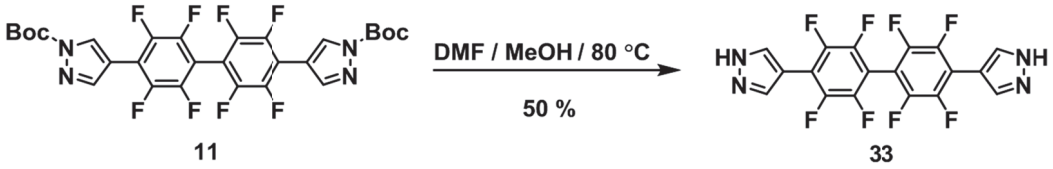

Scheme 3.2. Synthesis of **33**.

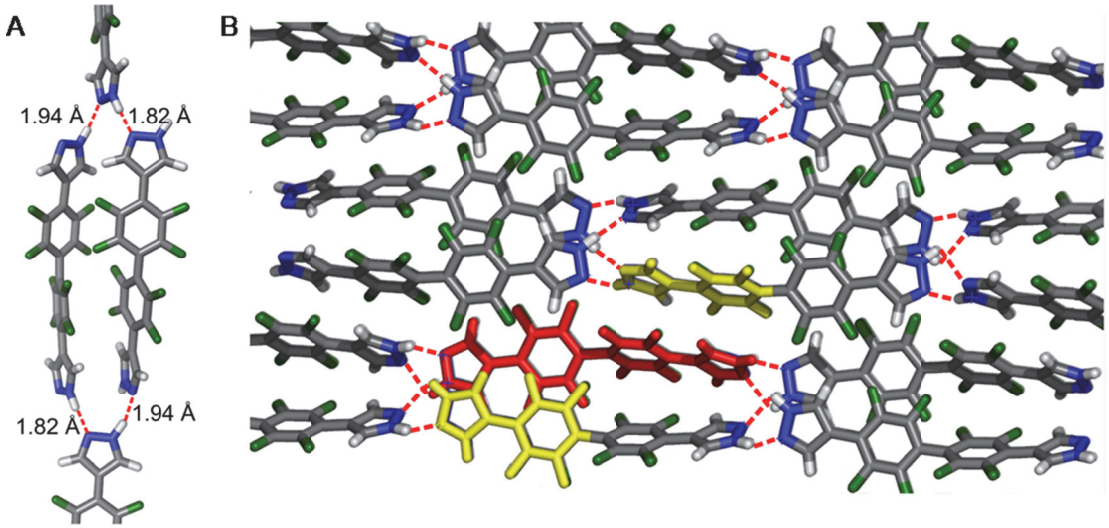

Figure 3.2 Crystal structure of **33**. (A) Hydrogen bonding pattern observed in the structure. (B) The molecule organizes into a nonporous structure.

The third crystal structure was of **34** and it was prepared by the solvothermal deprotection of **12** (Scheme 3.3). The crystal structure of **34** (Figure 3.3) shows that four out of five aromatic rings are almost coplanar, with pyrazole and 1,2,4,5-tetrafluorobenzene planes at angles of 16.5 °. As expected, the central tetramethylated benzene ring is distorted from coplanarity with its perfluorinated neighbors by 67.2 °. The crystal structure of **34** is unique in the linear series as it includes solvent molecules (MeOH) in the linear hydrogen-bonded catemers formed. This causes the pyrazole N−H groups not to hydrogen bond to N atoms from other pyrazoles, but instead to the oxygen atom in MeOH. Methanol's O−H group bridges the gap to the next pyrazole nucleus by establishing a hydrogen bond with its N atom, resulting in an infinite 1D chain of pyrazole/MeOH/pyrazoles; parallel packing of these in the solid state (Figure 3.3A) leaves no noticeable voids (Figure 3.3B).

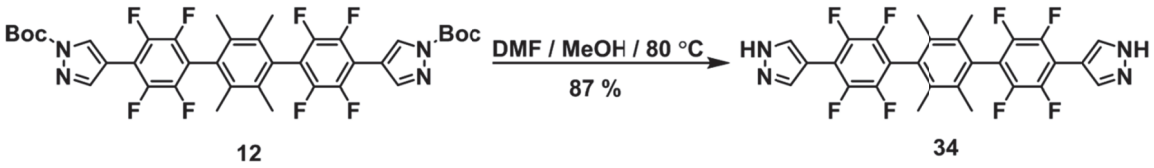

Scheme 3.3 Synthesis of **34**.

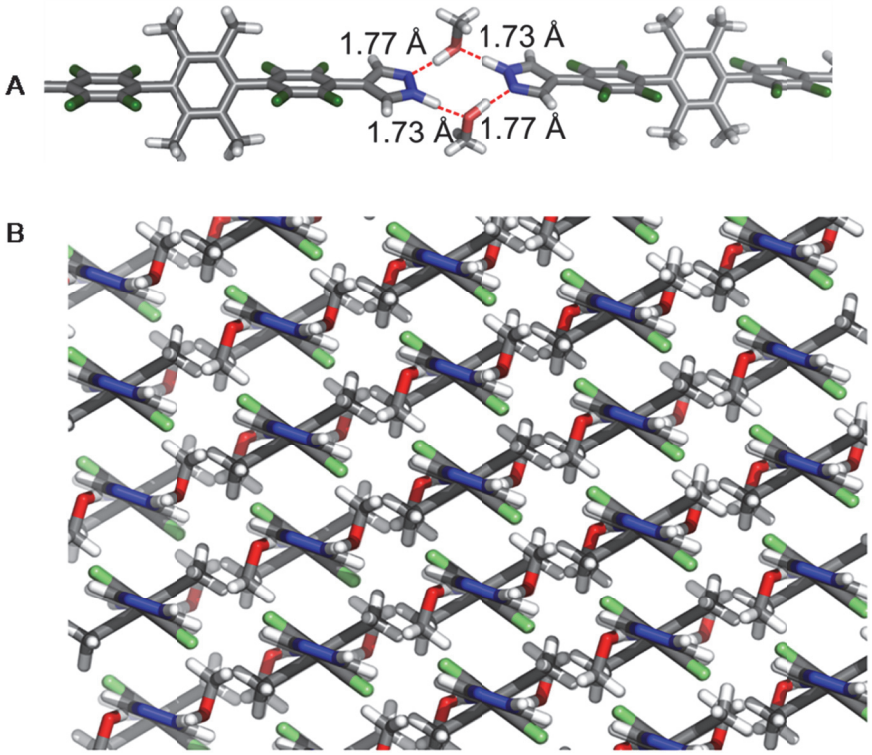

Figure 3.3 Crystal structure of **34**. (A) Hydrogen bonding pattern observed in the structure between **12** and MeOH, (B) resulting in a nonporous structure 3D. Oxygen atoms are shown in red.

The final crystal precursor in the linear series is a bipyridyl compound synthesized by our collaborator Dr. Nurbey Gulia. Compound **35** was also deprotected solvothermally (Scheme 3.4) yielding **36** (Figure 3.4). From the crystal structure data, the molecular structure was slightly deplanarized in regards to the perfluorinated rings and terminal pyrazoles as the planes of these rings were at angles of 13.5 ° to one another. It was significantly deplanarized at a twist angle of 42.3 ° with regards to the central bipyridyl ring and the perfluorinated ring. This twist minimizes the steric repulsion between fluorine and neighboring hydrogen atoms similar to the twist observed in **33**. Also the neighboring bipyridine rings were almost coplanar to one another, defining an

angle of 7.2 ° with each nitrogen atoms being placed trans to the other. This phenomena has been observed in the crystal structure of 2,2'-bipyridine and is the most stable configuration.[22] Similarly, each molecule of **36** also connects to four of its neighbors via hydrogen bonding (N−H···N distances of 1.92, 1.96, 1.99, and 2.01 Å, NHN angles of 158 °, 142 °, 149 °, and 135 ° respectively). This crystal structure is also overall nonporous and does not display [π···π] stacking between the pyrazoles and 1,2,4,5-tetrafluorobenzene moieties just like **33**.

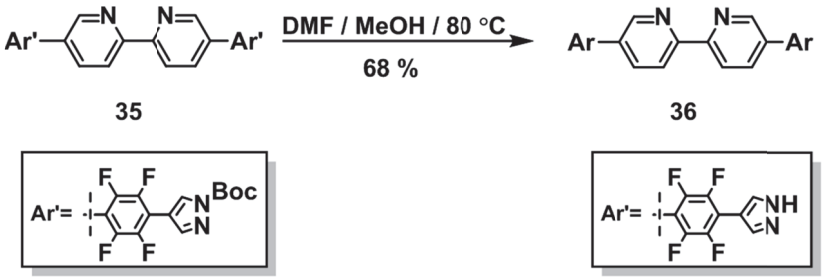

Scheme 3.4 Synthesis of **36**.

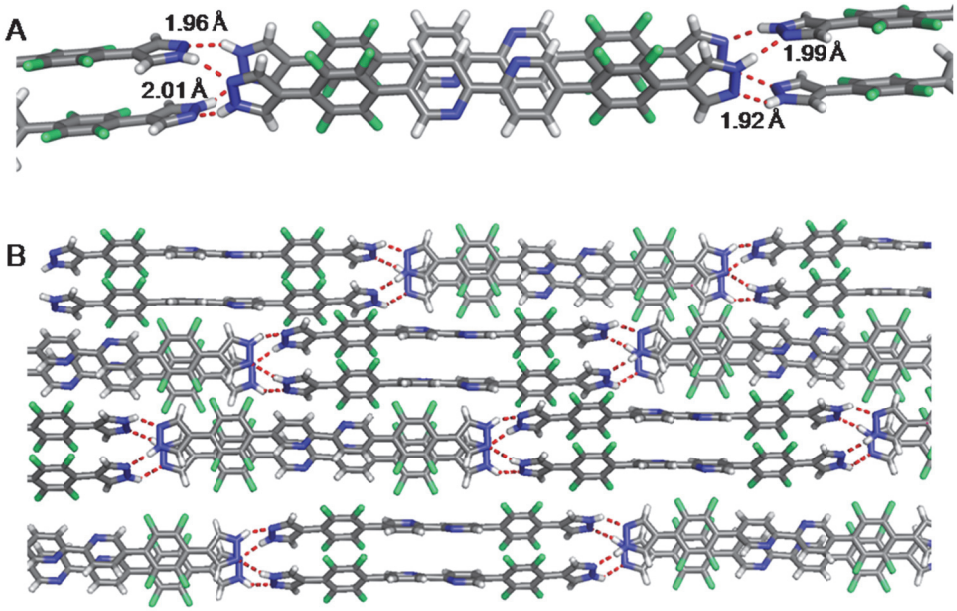

Figure 3.4 Crystal structure of **36**. (A) Hydrogen bonding pattern observed in the structure. (B) The resulting 3D structure is nonporous.

3.2.2 Crystal Structures derived from the Triangular Precursors

After the somewhat disappointing results observed with the linear precursors our attention was shifted towards the triangularly shaped precursor compounds. Crystals of the solvothermal deprotection derivative of **16** (Scheme 3.5) revealed a structure very similar to that of our original framework (**4**), shown in Figure 3.5. The two compounds are isostructural as both show twisting between the central trigonal ring and the tetrafluorobenzenes (Figure 3.5A and E; interplanar angles of 36.8−49.5 ° in **4** and 32.3−46.0 ° in **37**). The tetrafluorobenzene rings are almost coplanar with the terminal pyrazoles (interplanar angles of 10.1−12.6 ° in **4** and 9.8−11.5 ° in **37**). Both form triplets of hydrogen bonds, shown in Figure 3.5B and F. Both also form infinite head-to-tail [π···π] stacks between the electron-poor tetrafluorobenzenes and electron-rich pyrazoles (Figure 3.5C and G), characterized by the 3.44−3.47 (in **4**) and 3.38 (in **37**) Å distances between pyrazole centroids and averaged planes of the tetrafluorobenzene rings. Finally, this combination of stabilizing intermolecular interactions results in porous networks in the respective crystal structures (Figure 3.5D and H), displaying hexagonal pores with diameters of 16.5 and 15.8 Å diameters. Such similarity of the two structures bodes well for the preparation of porous organic alloys.[23]

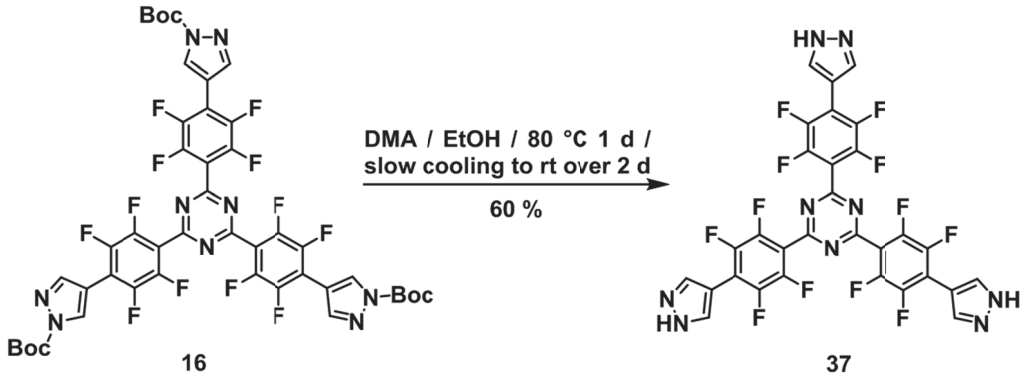

Scheme 3.5 Synthesis of **37**.

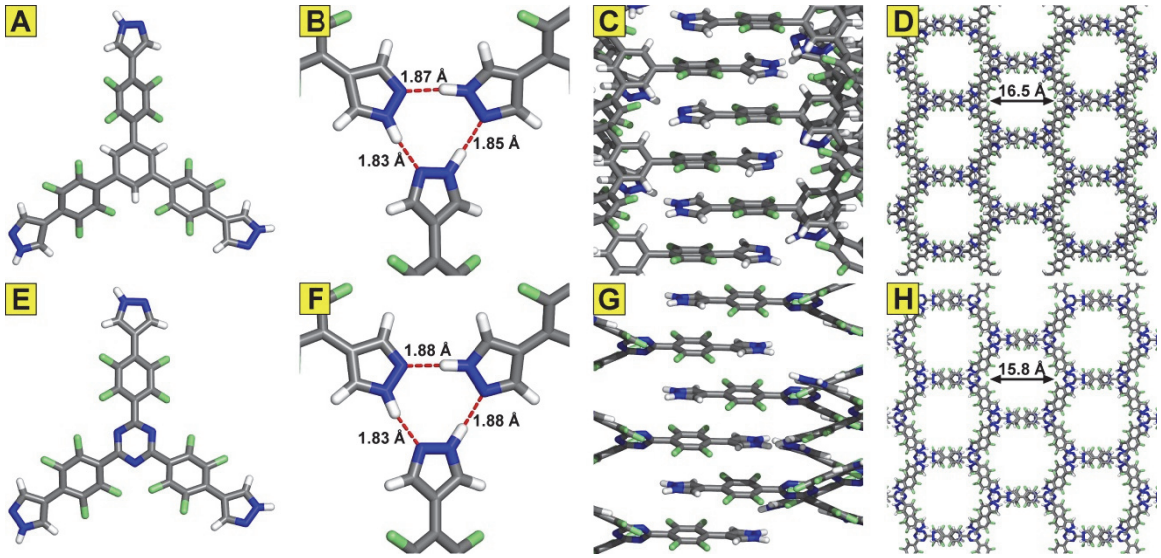

Figure 3.5 Crystal structures of **4** (A) and **37** (E) are isostructural. They both form triplets of N–H···N hydrogen bonds between pyrazoles (B and F), and display [π···π] stacking interactions between electron-rich pyrazoles and electron-poor tetrafluorobenzenes (C and G). Both organize into porous networks with hexagonal pores (D and H).

The crystal structure of compound **39** was obtained by the solvothermal deprotection of **38**, prepared by Dr. Le. The crystal structure revealed that the unit cell consisted of three independent molecules of **39** where two of those are connected through the disorder in their fluorinated rings. Relative to the plane on the central benzene ring, the three "internal" tetrafluorobenzene rings are deplanarized by an angle of 42.4−49.8 °. The twisting between internal and external tetrafluorobenzene rings is quite distinct, with corresponding angles in the range of 48.5−49.9 °. However, the external tetrafluorobenzene and pyrazole rings are almost coplanar, with interplanar angles between 4.5−12.5 °. The molecules of **39** engage in triplet of hydrogen bonds similar to those observed in the crystal structures of **4** and **37**, with [N−H···N] distances of 1.79, 1.82, and 1.88 Å (Figure 3.6A). The unusual structural feature of **39** is its [π···π] stacking pattern, shown in Figure 3.6C. Two molecules of **39** appear to have one of their arms positioned exactly on top of each other, and following that another pair of molecules oriented in the opposite direction stacks below and above them. This parallel "stacking of pairs" appears to oppose the electron-poor/electron-rich stacking model, as all of the "external" tetrafluorobenzenes seem to stack with each other (centroid−plane distance of 3.52 Å).

Similar stacking of electron-poor aromatic rings on top of each other had been observed when two fluoroarenes were constrained by binding to the same metal cluster.[24,25] As the molecules from separate pairs and are not parallel to one another other, some of this unfavorable interaction may be reduced, as half of the "internal" tetrafluorobenzenes and pyrazoles also appear to stack with each other (centroid−plane distance of 3.19 and 3.30 Å, respectively). These interactions alternate with favorable

stacking of pyrazoles with "internal" tetrafluorobenzenes, characterized by the centroid−plane distance of 3.70 Å. Overall, this complex stacking pattern works together with hydrogen bonding to generate a network of hexagonal pores (Figure 3.5D), with a pore diameter of 26.4 Å. In order to further study and understand this unexpected stacking of the arms we turned to computational experiments conducted by our collaborators in Dr. Wu's group.[26] The geometry optimization for a phenyl−perfluorophenyl−perfluorophenyl−pyrazole (Ph−Ph_F−Ph_F−Py) single-chain model was computed at B97XD/6-311+G-(2d,p) level of theory, and several parallel π-stacked Ph−Ph_F−Ph_F−Py dimer models were considered at the B97D/6-31G(d)level. The calculated energy for the parallel stacking observed in the crystal structure of **39** is −7.2 kcal mol^{-1} relative to the other coconformers. As a result, this arrangement benefits from some attractive electrostatic interactions.[27]

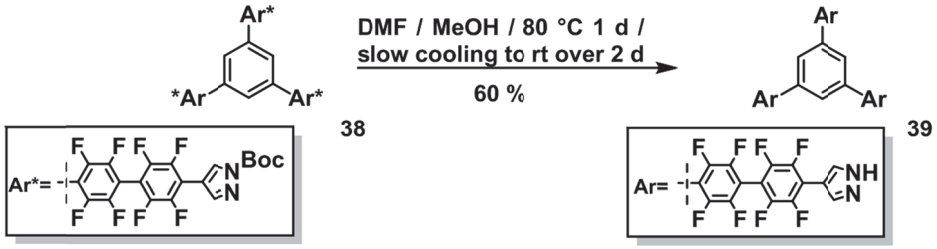

Scheme 3.6 Synthesis of **39**.

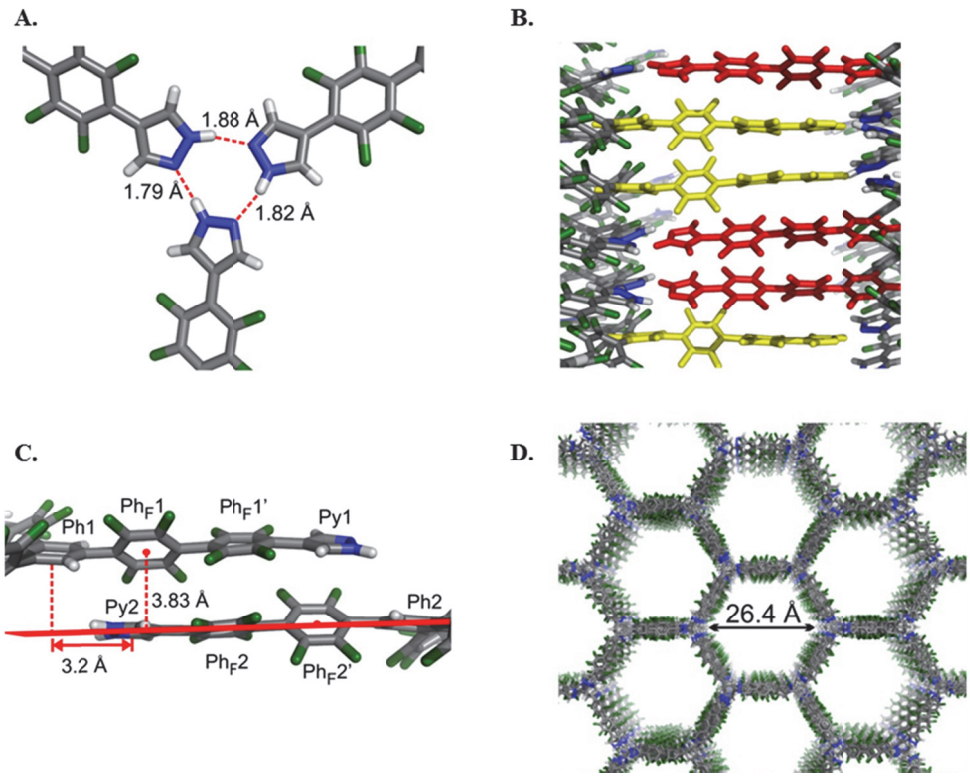

Figure 3.6 Crystal structures of **39** consists of (A) triplets of N–H···N hydrogen bonds between pyrazoles, and (B and C) displays unique pairwise [π···π] stacking interactions that alternates between electron-rich pyrazoles and electron-poor tetrafluorobenzenes (similar to **37**) and the unfavorable stacking of electron-poor aromatic rings on top of each other. (D) The overall structure possesses large hexagonal channels viewed along the crystallographic *a* axis.

As for the remaining PMC precursors that were discussed in Chapter 2 (compounds **28** and **31**) we were unfortunately unable to obtain any single crystals. These compounds were subjected to several solvothermal deprotection conditions and did successfully result in the deprotected product.

3.3 Properties of the Porous PMCs

As mentioned in Section 3.2, it was discovered that **37** and **39** are porous. In this section we will discuss the thermal stability, pore size and surface area along with hydrophobicity of these PMCs.

3.3.1 Thermal Stability

Thermogravimetric analysis (TGA) of **37** and **39** (experimental section Figure 3.26 and 3.27) was performed in both air and N_2 in order to determine their thermal stability. These compounds began losing weight around 380 °C in both air and N_2. The weight loss of **37** was initially about 6% and was followed by full decomposition slightly below 500 °C, as demonstrated by the featureless TGA trace. This behavior is very similar to that of **4**. Compound **39** also displays similar behavior with an initial weight loss of about 3%, followed by its complete decomposition slightly below 500 °C. But variable temperature powder X-ray diffraction (PXRD, Figure 3.28 in the experimental section) indicates that this framework is not thermally stable and begins to lose crystallinity at around 100 °C (due to the decrease in the intensity of all of its peaks). The sample finally becomes completely amorphous at 150 °C, as its diffraction peaks disappear. This also explains the unusually low porosity values that were initially obtained when the sample was activated at 120 °C.

3.3.2 Porosity Analysis

Gas sorption measurements were performed on **37** and **39**, as their respective crystal structures possess large pores. Nitrogen adsorption isotherm for **37** (experimental section, Figure 3.29 and 3.31) revealed a Brunauer-Emmett-Teller (BET) surface area of

903 m^2 g^{-1} and that it was capable of the sorption of N_2, O_2, and CO_2. Interestingly, it was revealed that **37** adsorbed 339 cm^3 g^{-1} at 195 K which was larger than 250 cm^3 g^{-1} adsorbed by **4** under the same conditions. This increase in CO_2 uptake could be due to the triazine nitrogen atoms in the pores of **37** forming interactions with the quadrupole of the CO_2 guest molecules. This phenomenon has been observed in nitrogen-containing MOFs[29,30] and COFs. [31,32]

Using nonlinear density functional theory (NLDFT) calculations the pore diameter was estimated to be ~11 Å (experimental section, Figure 3.32). This result is lower than the ~16.5 Å pore diameter measured from the crystal structure, but it has been reported that the existing models may not be well suited for fluorine-lined pores such as those of **37**, **39**, and **4**.[10] The surface area of **37** is also smaller than that of **4** (1159 m^2 g^{-1}), while the pore diameter appears slightly smaller than that measured from the crystal structure (~15.8 Å).

Gas sorption within the pores of **39** was measured after its crystals were activated by solvent exchange in acetone (4 × 24 h) followed by pentane (4 × 24 h), and degassing of the crystals by heating at 30 °C for 24 h in vacuo. The crystal structure of **39** has several analogous characteristics with the structure of **4**, and its pore size is about 26 Å in diameter, which is much larger than in **4** and this result is in good agreement with NLDFT simulations (~23 Å, experimental section, Figure 3.36). As expected, the BET surface area of **39** (experimental section, Figure 3.33 and 3.35) based on nitrogen adsorption isotherm is 1821 m^2 g^{-1}, which is much higher than in **4**. Compound **39** was also capable of the sorption of N_2, O_2, and CO_2 (experimental section, Figure 3.33).

The measured surface areas match quite well with the calculated values obtained from crystal structure data using the Materials Studio software package. These calculated surface areas are 1447 m^2 g^{-1} for **4**, 1371 m^2 g^{-1} for **37**, and 1598 m^2 g^{-1} for **39** (calculation shown in the experimental section 3.5.7).

3.3.3 Determining the Hydrophobicity of our PMCs

As crystalline **37** and **39** are extensively fluorinated it was expected that these compounds would display hydrophobic characteristics. In order to evaluate these properties, contact angles of these PMCs and water were measured with the aid of Dr. Maria Márquez and Daniela Rodriguez.

The contact angle measurement is a method that is commonly used to measure the wettability of a surface or a material. Here wettability or wetting refers to the study of how a droplet of liquid can spread out or ball up over a flat surface (Figure 3.6). If the liquid completely spreads out on the surface than the contact angle is 0 ° and the surface is considered to be perfectly wetting. If the liquid forms a perfect sphere on the surface and the contact angle is 180 ° then the surface is perfectly non-wetting. Finally, if the liquid droplet used is water then this method can serve as a method to measure hydrophobicity. It has been reported that if the water contact angle is in the range of $0° < \theta < 10°$, $10° < \theta < 90°$, $90° < \theta < 150°$, and $150° < \theta < 180°$ the material can then be termed as superhydrophilic, hydrophilic, hydrophobic, and superhydrophobic, respectively.[32] Recently there has been an interest in the development of superhydrophobic materials as they have applications in the fields of anti-corrision,[33,34] self-cleaning,[35,36] and anti-fouling.[37,38] Experimental results indicated that **37** was

hydrophobic and that **39** was superhydrophobic, with **37** displaying a contact angle of 113 ° and **39** a contact angle of 150 ° (experimental section, Figures 3.39 and 3.40). The results revealed that both **37** and **39** were hydrophobic, as was expected. The only unexpected result was that **37** was less hydrophobic than the isostructural **4** which displayed a contact angle of 132 °. This difference in hydrophobicity could be attributed to the nitrogen atoms of the triazine rings present in **37**. These nitrogen atoms could potentially form hydrogen bonds with water molecules resulting in a smaller contact angle. As for the increase in hydrophobicity in **39** compared to **4**, this could be attributed to an increase in the overall fluorination of this framework due to the presence of an additional tetrafluorophenyl ring on each arm of the parent molecule **38**.

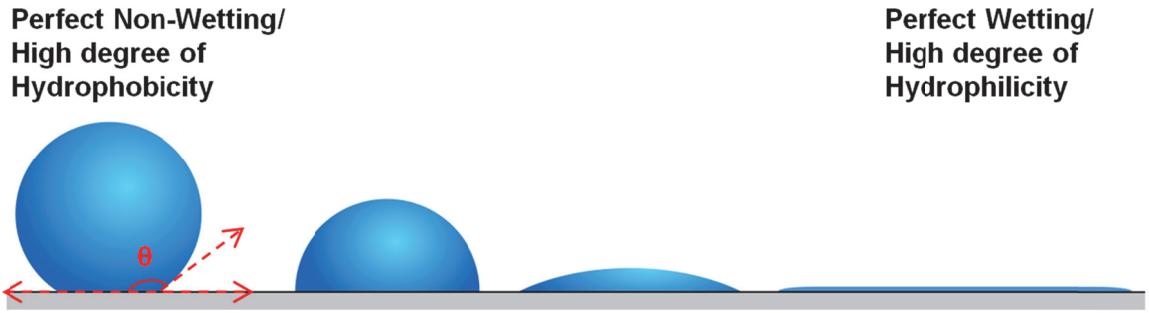

Figure 3.7 This figure depicts the wetting of different fluids on a surface.

3.4 Conclusion and Outlook

In conclusion, we have successfully prepared single crystals from six PMC precursors: compounds **10**, **11**, **12**, **16**, **35**, and **38**. During the course of this model study, in which the effect of geometry and length were varied, the crystal structures of the analyzed precursors revealed that the triangular precursors formed porous structures. These findings suggested that the trigonal geometry is required, along with hydrogen bonding and [π···π] stacking, to yield a porous framework.

The results of this study suggest that more triangular precursors should be synthesized as there is a good chance that these will yield porous frameworks. This study also opens up other avenues for future research, such as the development of an isoreticular series of more porous frameworks by extending the arms of **37** and **39**. Is it possible to replace the pyrazole end group with another end group capable of hydrogen bonding and still end up with a porous framework? It is also worth exploring what extent of fluorination is required for the [π···π] stacking interactions to effectively hold the framework together. If it is possible to remove some of the fluorine atoms from each of the fluorinated phenyl rings of the framework, this could allow access to a specific site on the framework where post synthetic modification can be attempted. Future work should also include the incorporation of the precursors that did not yield a porous framework into the development of MOFs and COFs. There is still more research to be conducted in this field and it is my hope that many generations of PMCs and other porous materials will be developed by this group in the near future.

3.5 Experimental Section

3.5.1 General Methods and Materials

Vials with PTFE/Liner caps were used as reaction vessels for the synthesis of precursors, while standard scintillation bottles were used as vessels for the solvothermal synthesis of porous molecular crystals. Solvents THF, Et_2O, and hexane were dried over activated alumina in an mBraun solvent purification system. Gas chromatography/mass spectrometry analyses were performed on a Shimadzu GCMS-QP5000 chromatograph equipped with a Restek column (Rtx-XLB, 30m×0.25mm internal diameter). Mass spectral measurements were performed by the Mass Spectrometry Facility of the Department of Chemistry and Biochemistry at the University of Texas at Austin. The ^{1}H and ^{19}F NMR spectra were recorded on JEOL ECA-600, ECA-500, or ECX-400P spectrometers, with working frequencies (for ^{1}H nuclei) of 600, 500, and 400 MHz, successively, and using the peaks of tetramethylsilane or residual solvent as standards.

Trifluorotoluene ($PhCF_3$, $\delta = -63.72$ ppm) was used as the internal standard in ^{19}F NMR spectra. All ^{13}C NMR spectra were recorded with the simultaneous decoupling of ^{1}H nuclei. Some ^{13}C NMR spectra were not included since they are not informative, due to the poor solubility of the prepared compounds and the extensive coupling between ^{13}C and ^{19}F nuclei; low intensities and many missing peaks were observed. Melting points were measured in a Barnstead International Mel-TEMP apparatus and are uncorrected. Infrared spectra were recorded on a Nicolet iS10 FT-IR spectrometer equipped with a Thermo Scientific iTR for multi-purpose ATR sampling. Microanalyses were conducted by Intertek USA Inc. Thermogravimetric analyses (TGA) were carried out on a TA

Instruments TGA 2050 thermogravimetric analyzer at a temperature ramping rate of 2 °C min^{-1} under the flow of N_2 or air. Crystalline samples were placed in a ceramic crucible, heated up to 300 °C and then cooled down to −150 °C at a rate of 20 °C min^{-1} under N_2.

3.5.2 Synthesis and Characterization of Molecular Crystals

Compound **32**

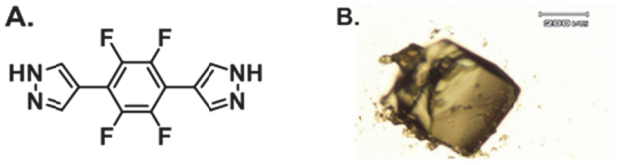

Figure 3.8 (A) Molecular structure of **32**. (B) Picture of a single cubic crystal of **32**.

The Boc-protected precursor **10** (5.0 mg, 0.01 mmol) was added to a 3 mL scintillation vial. Solvents DMF (0.6 mL) and MeOH (1.4 mL) were added to the solid and the bottle was capped and placed into an 80 °C oven for 1 d. The resulting colorless cubic crystals were washed with MeOH and air-dried to yield **32** (2.0 mg, 70%). ^{1}H NMR (500 MHz, $CDCl_3$): δ 13.41 (s, 2H), 8.23 (s, 2H), 7.92 (s, 2H) ppm. ^{19}F NMR (471 MHz, $CDCl_3$): δ –142.57 (s, 4F) ppm. HRMS (ESI/Q-TOF) *m*/*z*: $[M+Na]^+$ Calc'd for $C_{12}H_6F_4N_4Na$: 283.0683; Found 283.0601. Anal. Calc'd for $C_2H_{22}F_4N_4O_4$: C, 51.07; H, 2.14; N, 19.85. Found: C, 51.12; H, 2.21; N, 19.56.

Table 3.1. Crystal data and structure refinement data for **32**.

Empirical formula	$C_{12}H_6F_4N_4$	
Formula weight	282.21	
Temperature	123(2) K	
Wavelength	1.54178 Å	
Crystal system	Monoclinic	
Space group	P2 (1)/n	
Unit cell dimensions	a = 5.3834(3) Å	α = 90 °
	b = 5.7482(3) Å	β = 97.711(2) °
	c = 16.8992(8) Å	γ = 90 °
Volume	518.21(5) $Å^3$	
Z	2	
Density (calculated)	1.809 Mg/m^3	
Crystal size	0.35 × 0.35 × 0.06 mm^3	
Reflections collected	3385	
Independent reflections	974 [R(int) = 0.0177]	
Refinement method	Full-matrix least-squares on F^2	
Data / restraints / parameters	884 / 96 / 0	
Goodness-of-fit on F^2	1.090	
Final R indices [I>2sigma(I)]	R_1 = 0.0291, wR_2 = 0.0741	
R indices (all data)	R_1 = 0.0295, wR_2 = 0.0745	
Largest diff. peak and hole	0.280 and –0.201 e $Å^{-3}$	

Compound **33**

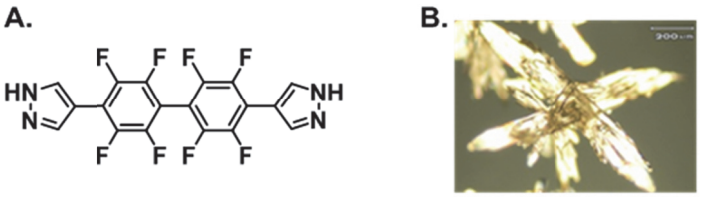

Figure 3.9 (A) Molecular structure of **33**. (B) Picture of a single cubic crystal of **33**.

The Boc-protected product **11** (7 mg, 0.01 mmol) was added to a 3 mL scintillation vial. Solvents DMF (0.1 mL) and MeOH (1.9 mL) were added to the solid and the bottle was capped and placed into an 80 °C oven for 1 d. The resulting colorless sea-urchin like crystals were washed with MeOH and air-dried to yield 33 (2.3 mg, yield 50 %). ^{1}H NMR (600 MHz, DMSO-d_6): δ 13.51 (s, 2H), 8.33 (s, 2H), 7.99 (s, 9H) ppm. ^{19}F NMR (564 MHz, DMSO-d_6): δ –139.83 to –139.87 (m, 4F), –140.61 to –140.64 (m, 4F) ppm. HRMS (ESI/Q-TOF) *m*/*z*: $[M+H]^+$ Calc'd for $C_{18}H_7F_8N_4$ 431.0543; Found 431.0537. Anal. Calc'd for $C_{18}H_6F_8N_4$: C, 50.25; H, 1.41; N, 13.02. Found: C, 49.96; H, 1.28; N, 12.46.

Table 3.2. Crystal data and structure refinement for **33**.

Empirical formula	$C_{18}H_6F_8N_4$	
Formula weight	430.27	
Temperature	123(2) K	
Wavelength	1.54178 Å	
Crystal system	Monoclinic	
Space group	P2 (1)/c	
Unit cell dimensions	a = 16.3930(5) Å	α = 90 °

	b = 14.5350(5) Å	β = 94.108(2) °
	c = 6.4865(2) Å	γ = 90 °
Volume	1541.58(9) Å^3	
Z	4	
Density (calculated)	1.854 Mg/m^3	
Crystal size	0.40 × 0.20 × 0.15 mm^3	
Reflections collected	10541	
Independent reflections	2718 [R(int) = 0.0243]	
Refinement method	Full-matrix least-squares on F^2	
Data / restraints / parameters	2607 / 278 / 0	
Goodness-of-fit on F^2	1.066	
Final R indices [I>2sigma(I)]	R_1 = 0.0274, wR_2 = 0.0719	
R indices (all data)	R_1 = 0.0318, wR_2 = 0.0764	
Largest diff. peak and hole	0.236 and –0.205 e Å^{-3}	

Compound **34**

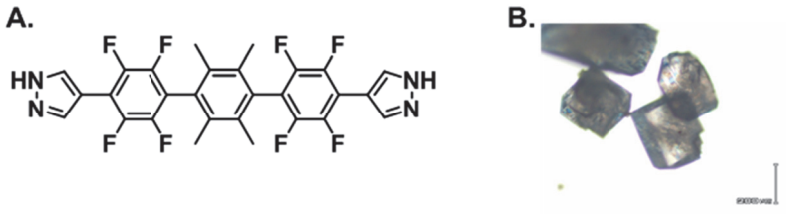

Figure 3.10 (A) Molecular structure of **34**. (B) Picture of a single cubic crystal of **34**.

The Boc-protected product **12** (100 mg, 0.26 mmol) was added to a 40 mL scintillation vial. Solvents DMA (6 mL) and MeOH (16 mL) were added to the solid and the bottle was capped and placed into an 80 °C oven for 1 d. The resulting colorless crystals were washed with MeOH and air-dried to yield **34** (64 mg, 87 %). ^{1}H NMR (600 MHz, DMSO-d_6): δ 13.46 (s, 2H), 8.30 (s, 2H), 7.99 (s, 2H), 2.00 (s, 12 H) ppm. ^{19}F NMR (564 MHz, DMSO-d_6): δ –141.28 to –141.32 (m, 4F), – 141.93 to –144.97 (m, 4F) ppm.

Table 3.3. Crystal data and structure refinement for **34**.

Empirical formula	$C_{28}H_{18}F_8N_4$	
Formula weight	762.70	
Temperature	150 K	
Wavelength	1.54178 Å	
Crystal system	Triclinic	
Space group	P 1	
Unit cell dimensions	a = 8.6710(4) Å	α = 93.693 °
	b = 8.9923(4) Å	β = 100.002(3) °
	c = 9.2524(3) Å	γ = 106.443(4) °
Volume	676.46(5) Å^3	
Z	1	
Density (calculated)	1.538 Mg/m^3	
Crystal size	0.20 × 0.20 × 0.15 mm^3	

Reflections collected	13822
Independent reflections	2771 [R(int) = 0.0397]
Refinement method	Full-matrix least-squares on F^2
Data / restraints / parameters	2607 / 278 / 0
Goodness-of-fit on F^2	0.990
Final R indices [I>2sigma(I)]	R_1 = 0.0397, wR_2 = N/A
R indices (all data)	R_1 = 0.0541, wR_2 = 0.1385
Largest diff. peak and hole	0.25 and –0.21 e Å^{-3}

Compound **36**

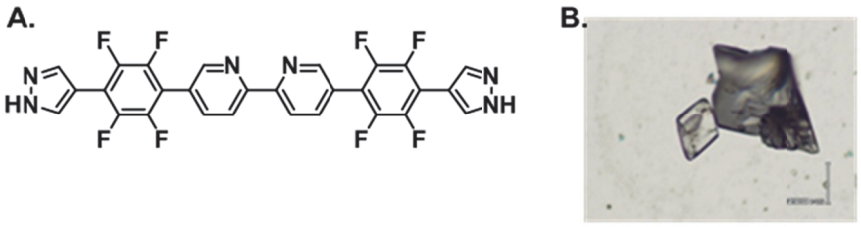

Figure 3.11 (A) Molecular structure of **36**. (B) Picture of a single cubic crystal of **36**.

The Boc-protected product **29** (10 mg, 0.13 mmol) was added to a 40 mL scintillation vial. Solvents DMF (1.8 mL) and MeOH (0.2 mL) were added to the solid and the bottle was capped and placed into an 80 °C oven for 1 d. The resulting colorless crystals were washed with MeOH and air-dried to yield **36** (5.1 mg, 68 %). Due to solubility issues it was difficult to obtain an NMR of **36**. Therefore, an NMR of the precursor **35** was reported. ^{1}H NMR (500 MHz, $CDCl_3$): δ 8.86 (s, 2H), 8.63 –8.65 (m, 4H), 8.24 (s, 2H), 8.03–8.02 (d, 2 H), 1.70 (s, 18 H) ppm. ^{19}F NMR (470 MHz, $CDCl_3$): δ –139.88 to –139.88 (m, 4F), – 143.51 to –143.59 (m, 4F) ppm.

Table 3.4. Crystal data and structure refinement for **36**.

Empirical formula	$C_{28}H_{12}F_8N_6$	
Formula weight	584.44	
Temperature	123(2) K	
Wavelength	1.54178 Å	
Crystal system	Monoclinic	
Space group	C 2/c	
Unit cell dimensions	a = 25.9168(6) Å	a = 90 °
	b = 10.2968(3) Å	b = 121.1150(10) °
	c = 19.6393(5) Å	γ = 90 °
Volume	4486.9(2) Å^3	
Z	8	
Density (calculated)	1.730 Mg/m^3	
Absorption coefficient	1.346 mm^{-1}	
F(000)	2352	
Crystal size	0.210 × 0.180 × 0.100 mm^3	
Reflections collected	10765	
Independent reflections	3853 [R(int) = 0.0191]	
Refinement method	Full-matrix least-squares on F^2	
Data / restraints / parameters	3853 / 0 / 379	
Goodness-of-fit on F^2	1.057	
Final R indices [I>2sigma(I)]	R_1 = 0.0351, wR_2 = 0.1012	

R indices (all data)	$R_1 = 0.0366$, w$R_2 = 0.1026$
Largest diff. peak and hole	0.248 and -0.198 e Å^{-3}

Compound **37**

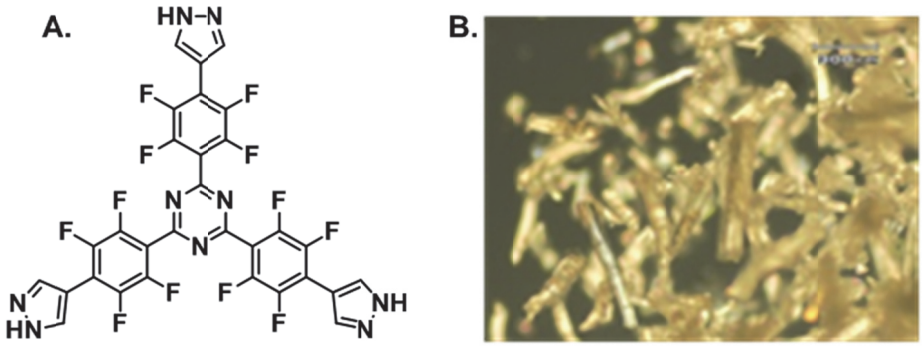

Figure 3.12 (A) Molecular structure of **37**. (B) Picture of a single cubic crystal of **37**.

The Boc-protected precursor **16** (100 mg, 0.098 mmol) was added to a 40 mL scintillation vial. Solvents DMA (10 mL) and EtOH (10 mL) were added to the solid and the bottle was capped. The vial was sonicated for 10 min and then sealed and placed into a variable temperature oven. The oven was programmed to heat the sample at 80 °C for 1 d and then to slowly cool it to room temperature by ~4 °C/h. The resulting colorless needle crystals (43 mg, 60 %) were washed with EtOH and air-dried. Mp: >350 °C (decomp). ^{1}H NMR (600 MHz, $CDCl_3$): δ 13.53 (s, 3H), 8.36 (s, 3H), 8.02 (s, 30H) ppm. ^{19}F NMR (564 MHz, $CDCl_3$): δ –138.97 to –139.05 (m, 6F), –141.04 to –141.13 (m, 6F) ppm. FT-IR (neat): ῡ 3147, 2827, 1648, 1514, 1471, 1407, 1364, 1320, 1257, 1207, 1175, 1032, 989, 964, 947, 871, 865, 831, 811, 705, 658, 609, 457 cm^{-1}.

Table 3.5. Crystal data and structure refinement for **37**.

Empirical formula	$C_{32.42}H_9F_{12}N_{9.35}O_{1.38}$

Formula weight	779.57	
Temperature	100(2) K	
Wavelength	1.54178 Å	
Crystal system	Monoclinic	
Space group	C 2/c	
Unit cell dimensions	a = 19.1610(7) Å	α = 90 °
	b = 34.1885(15) Å	β = 110.374(3) °
	c = 7.1304(4) Å	γ = 90 °
Volume	4378.8(4) Å^3	
Z	4	
Density (calculated)	1.183 Mg/m^3	
Crystal size	0.18 x 0.14 x 0.11 mm^3	
Reflections collected	15731	
Independent reflections	3937 [R(int) = 0.0427]	
Refinement method	Full-matrix least-squares on F^2	
Data / restraints / parameters	3937 / 15 / 260	
Goodness-of-fit on F^2	1.020	
Final R indices [I>2sigma(I)]	R_1 = 0.0726, wR_2 = 0.2396	
R indices (all data)	R_1 = 0.0884, wR_2 = 0.2592	
Largest diff. peak and hole	0.617 and −0.456 e Å^{-3}	

Compound **39**

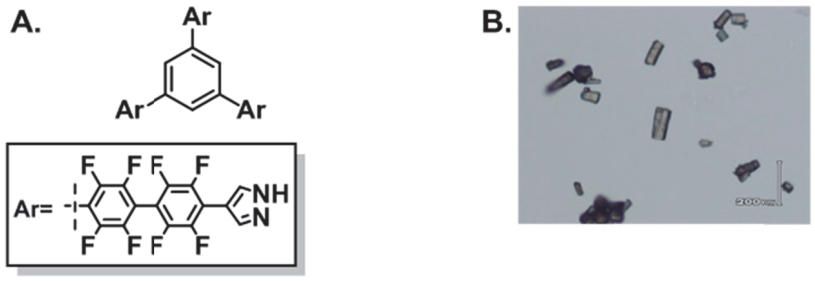

Figure 3.13 (A) Molecular structure of **39**. (B) Picture of a single cubic crystal of **39**.

The Boc-protected precursor **38** (20 mg) was added to a 3 mL dram vial in a DMF (0.4 mL) and MeOH (0.4 mL). The vial was sonicated for 10 min and then sealed and placed into a variable temperature oven. The oven was programmed to heat the sample at 80 °C for 1 d and then to slowly cool it to room temperature by ~4 °C/h. Crystals of **39** were formed (9.53 mg, 60% yield). ^{1}H NMR (600 MHz, $CDCl_3$) δ 13.53 (s, 3H), 8.34 (s, 3H), 8.15 (s, 3H), 8.00 (s, 3H) ppm. ^{19}F NMR (564 MHz, $CDCl_3$) δ –138.68 to –138.74 (m, 6F), –139.73 to –139.79 (m, 6F), –140.39 to –140.45 (m, 6F), –142.24 to –142.30 (m, 6F) ppm.

Table 3.5. Crystal data and structure refinement for **39**.

Empirical formula	$C_{102}H_{25}F_{48}N_{12}$	
Formula weight	2330.34	
Temperature	100(2) K	
Wavelength	1.54178 Å	
Crystal system	Orthorhombic	
Space group	*C*ccm	
Unit cell dimensions	a = 15.3843(10) Å	α = 90 °
	b = 93.285(7) Å	β = 90 °

	c = 53.370(4) Å γ = 90 °
Volume	76592(9) Å^3
Z	32
Density (calculated)	0.808 Mg/m^3
Crystal size	0.35 x 0.10 x 0.10 mm^3
Reflections collected	101140
Independent reflections	20264 [R(int) = 0.1896]
Refinement method	Full-matrix least-squares on F^2
Data / restraints / parameters	10627 / 1757 / 1624
Goodness-of-fit on F^2	1.088
Final R indices [I>2sigma(I)]	R_1 = 0.1250, wR_2 = 0.3162
R indices (all data)	R_1 = 0.1884, wR_2 = 0.3553
Largest diff. peak and hole	0.711 and −0.617 e Å^{-3}

3.5.3 ^{1}H and ^{19}F NMR Spectra of PMCs

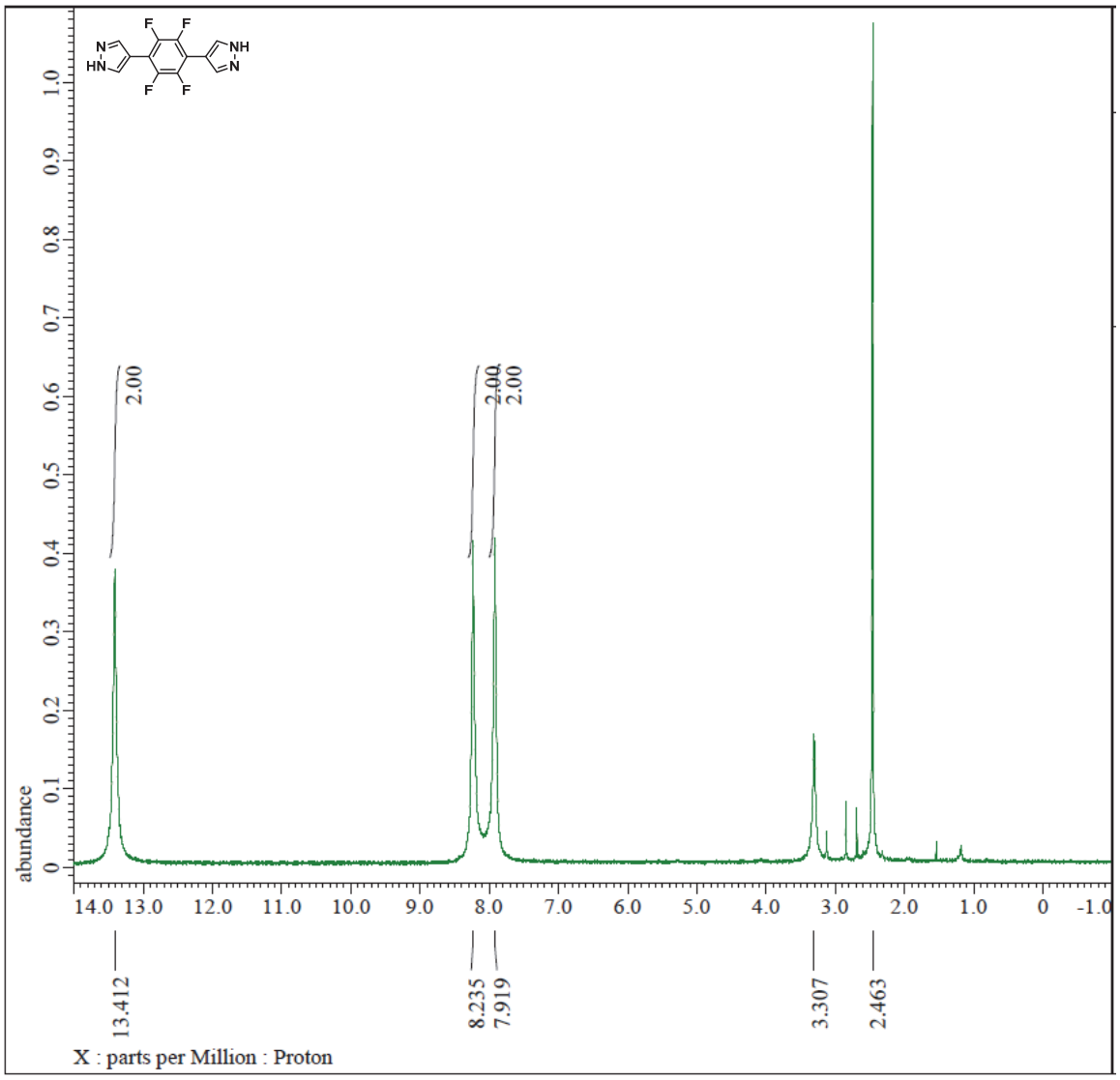

Figure 3.14 ^{1}H NMR Spectrum of **32**.

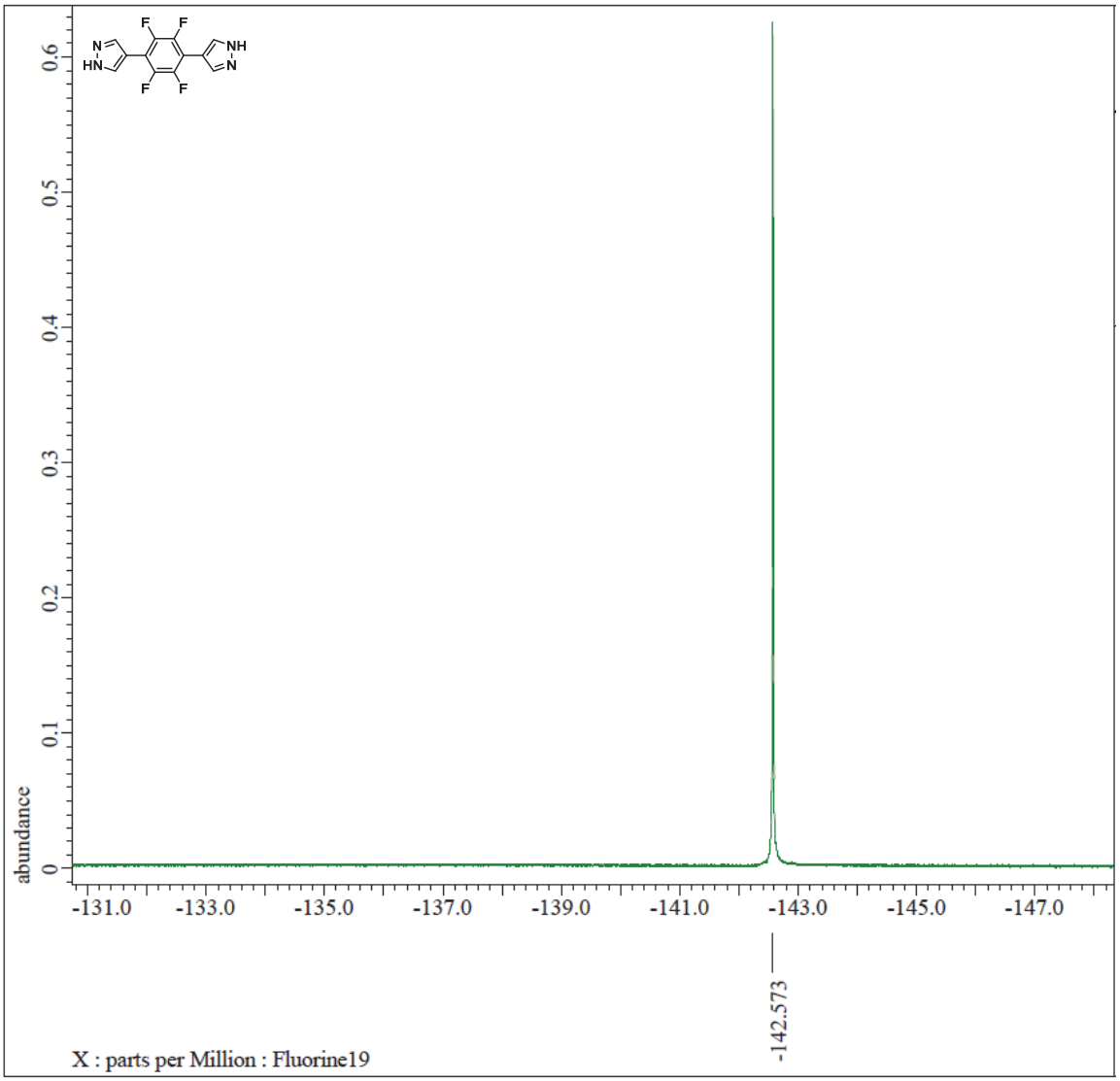

Figure 3.15 ^{19}F NMR Spectrum of **32**.

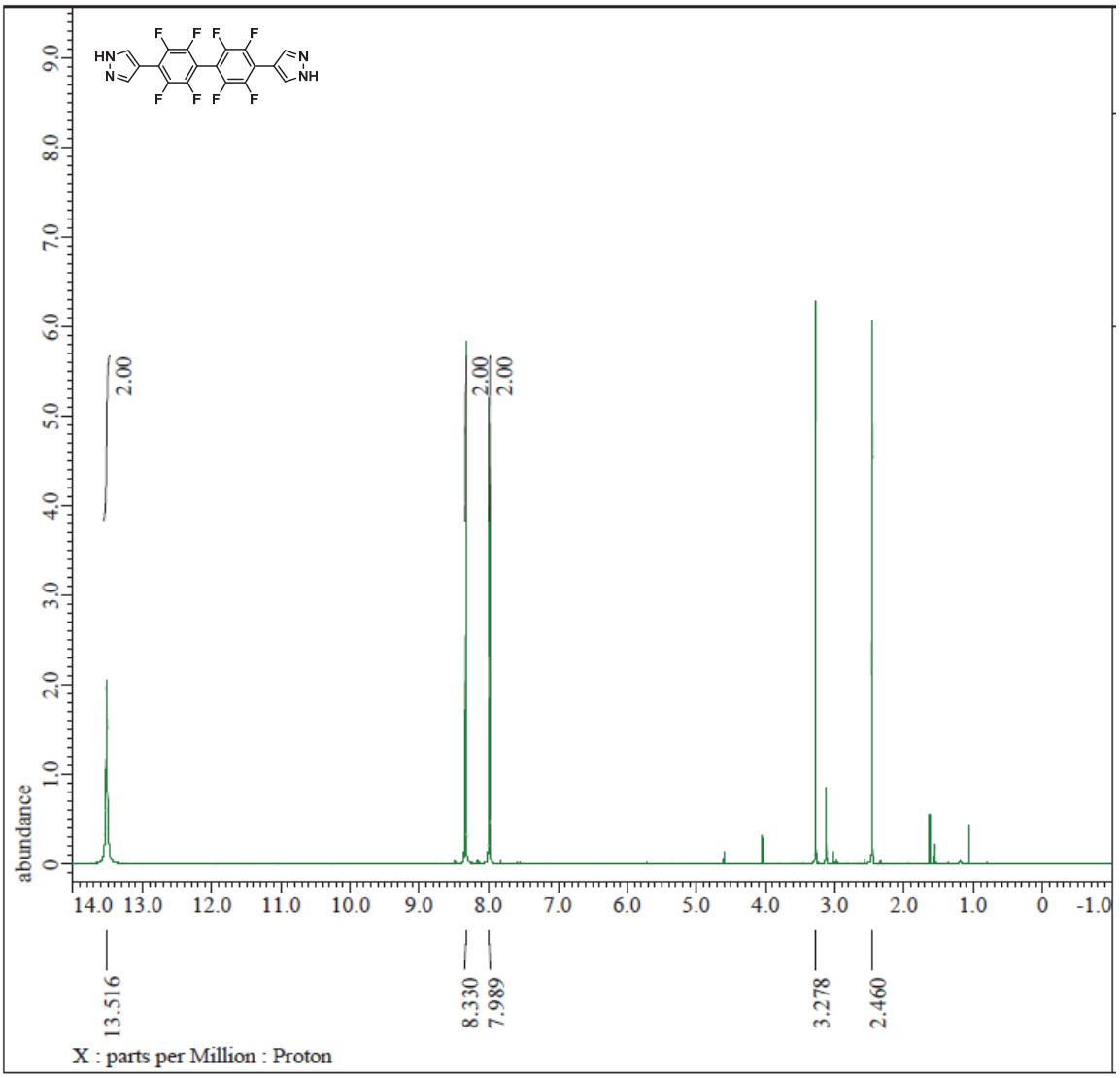

Figure 3.16 ^{1}H NMR Spectrum of **33**.

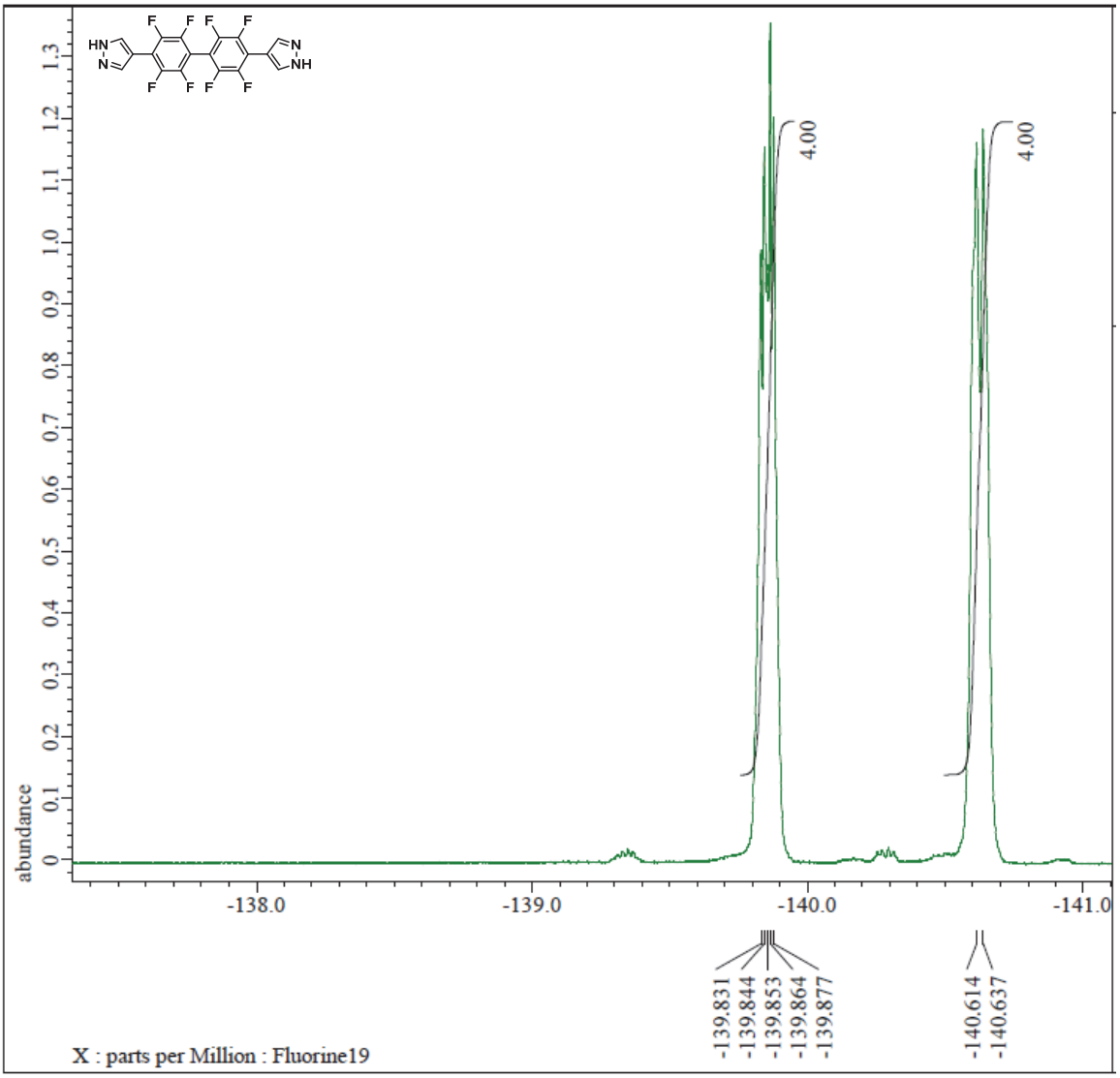

Figure 3.17 ^{19}F NMR Spectrum of **33**.

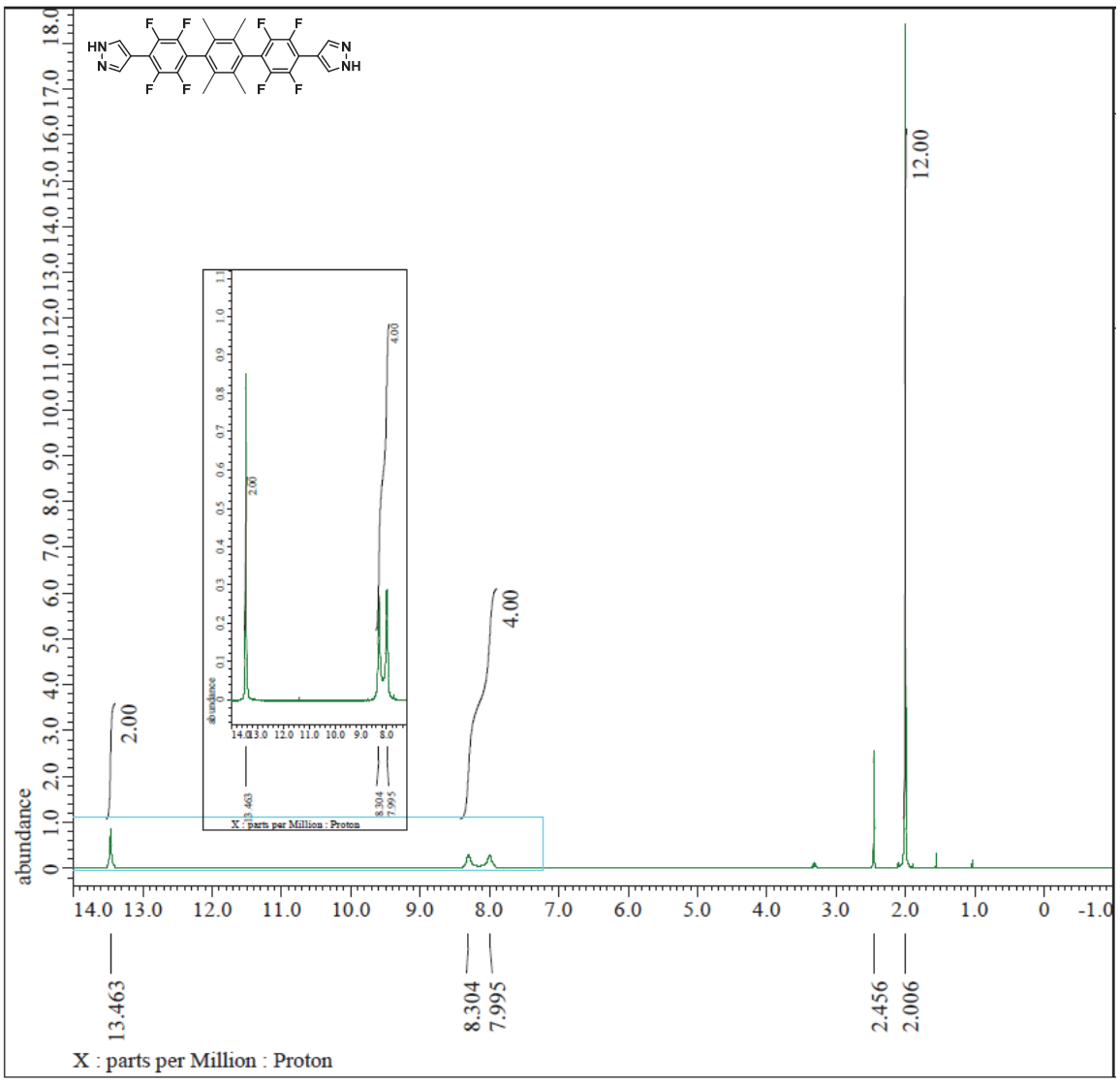

Figure 3.18 ^{1}H NMR Spectrum of **34**.

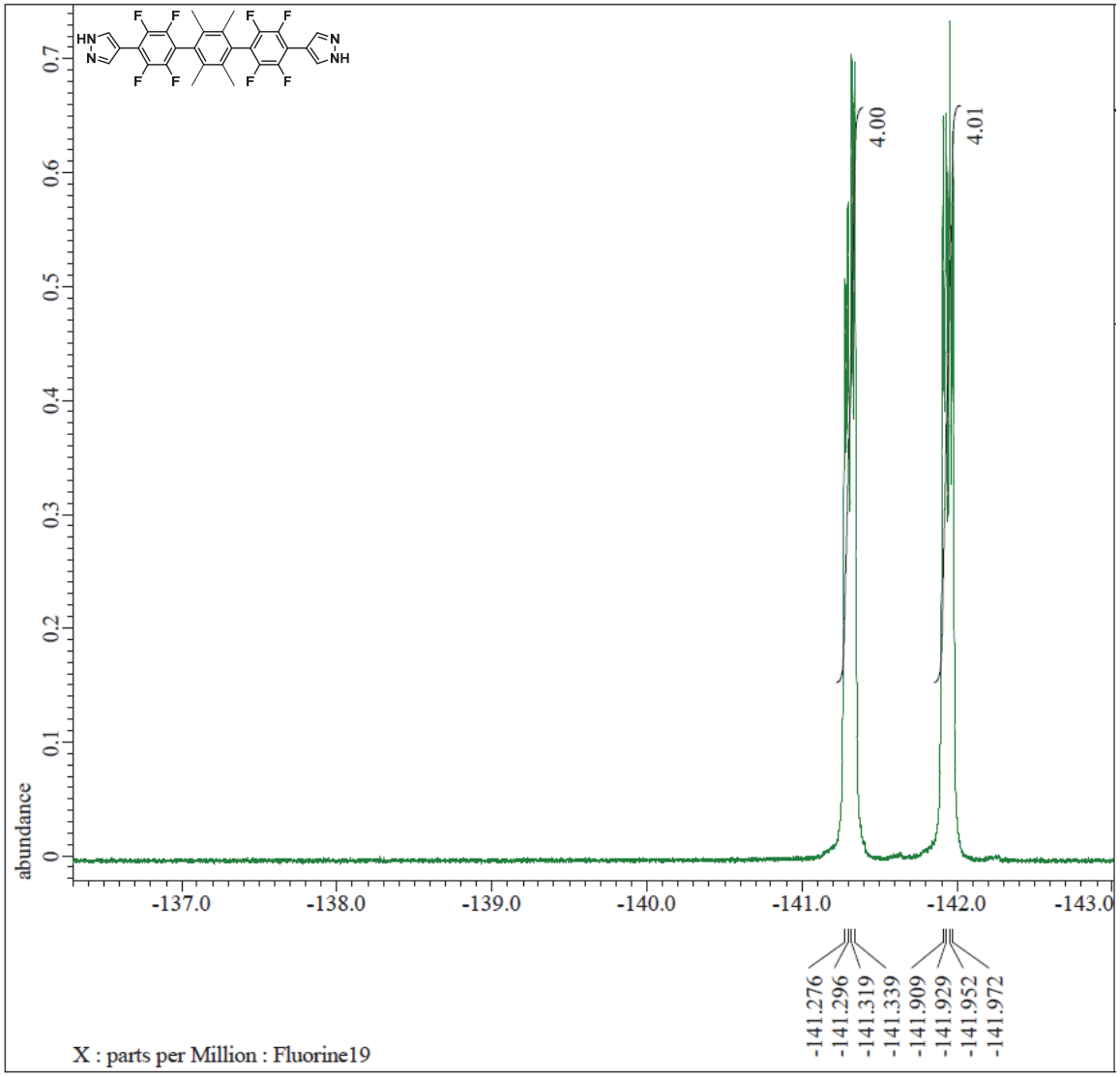

Figure 3.19 ^{19}F NMR Spectrum of **34**.

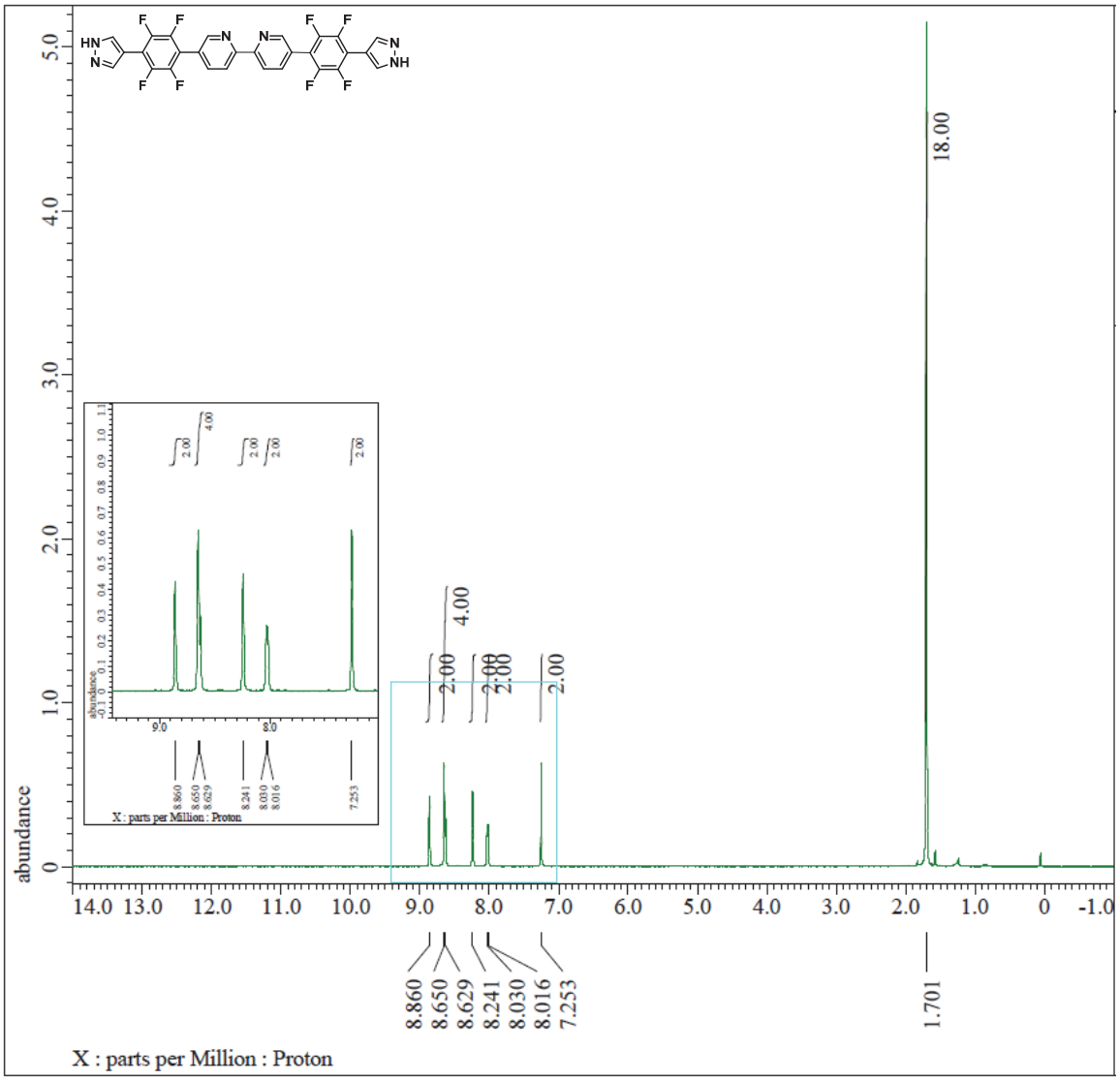

Figure 3.20 ^{1}H NMR Spectrum of **35.**

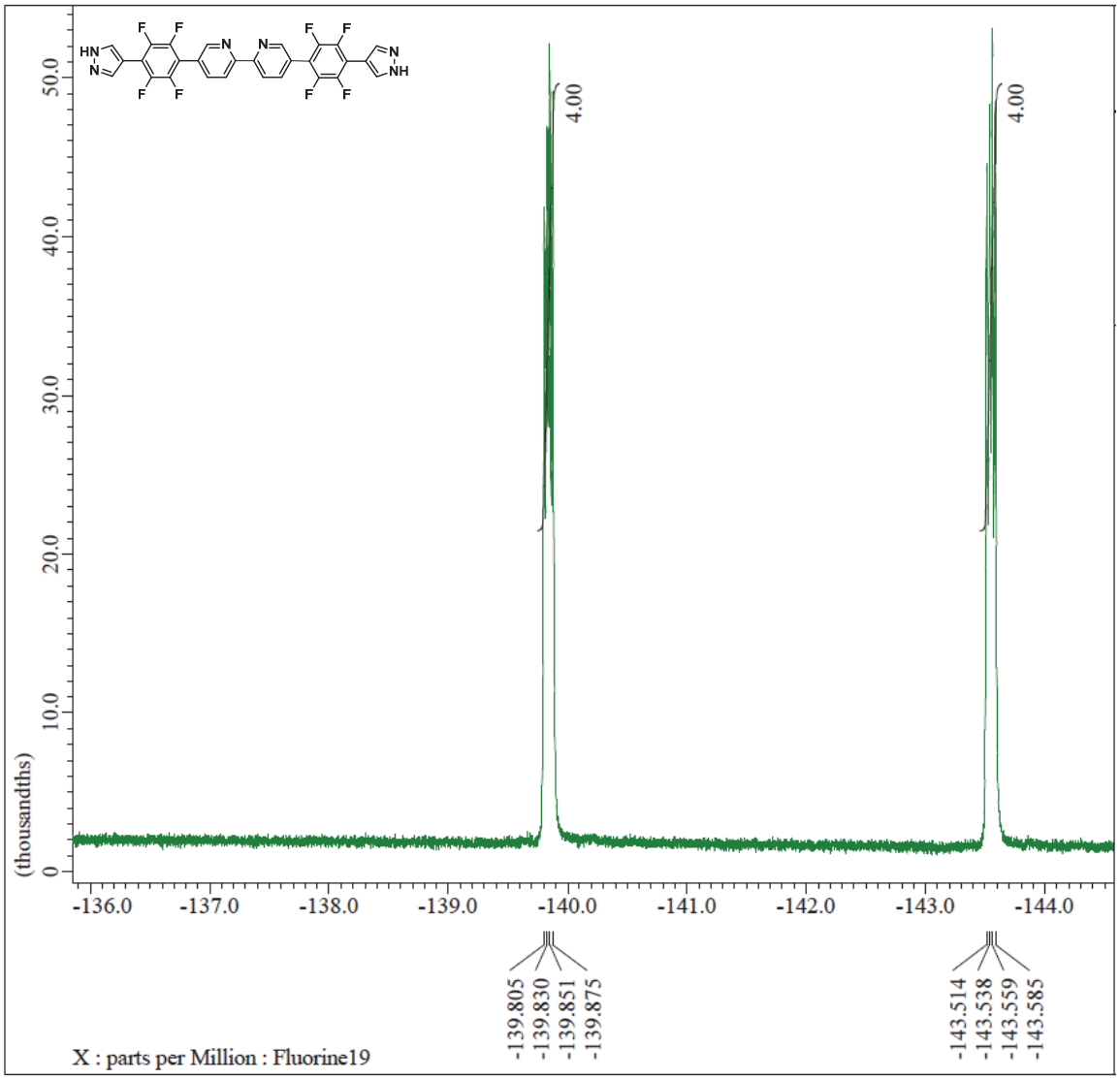

Figure 3.21 ^{19}F NMR Spectrum of **35.**

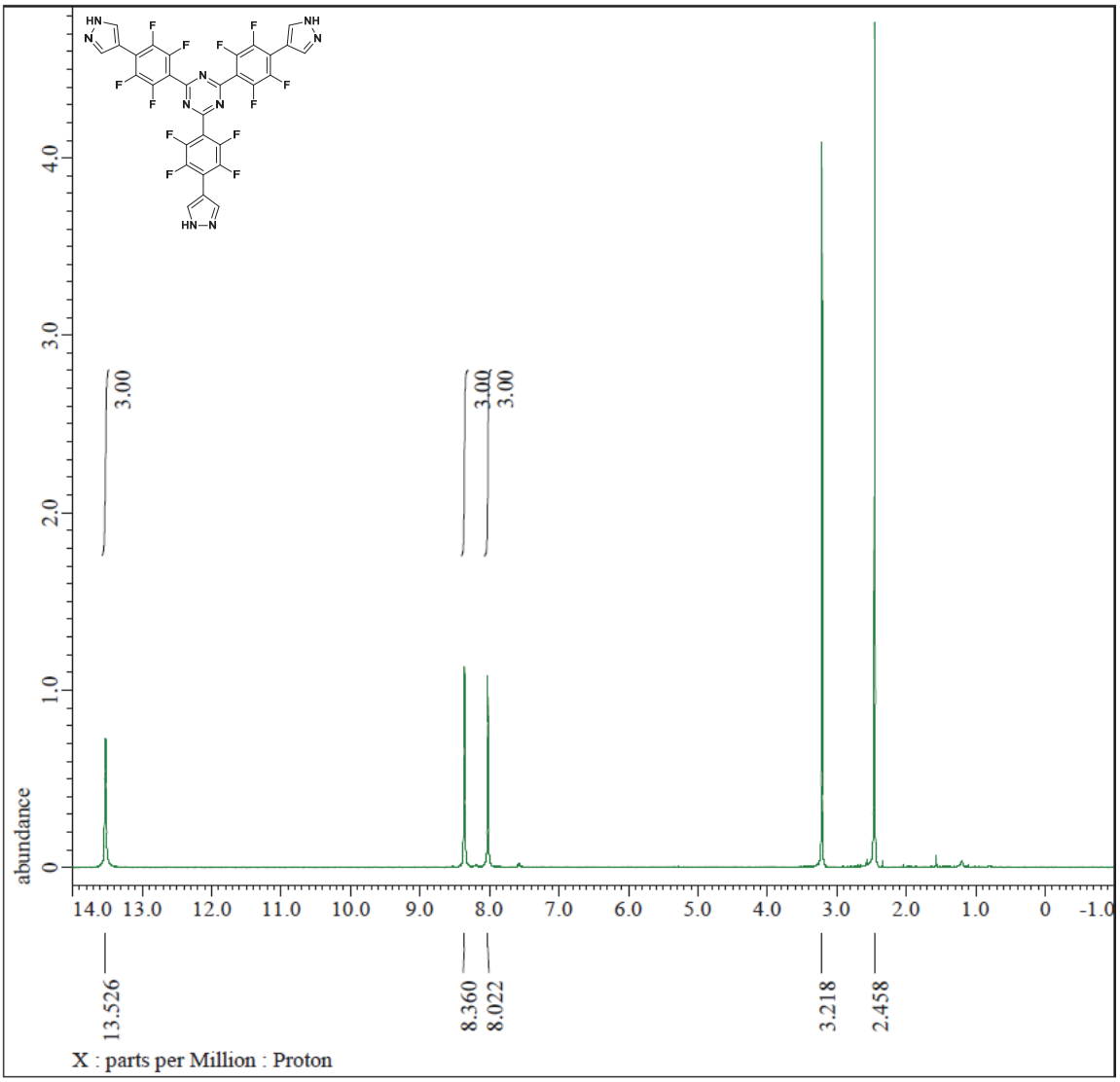

Figure 3.22 ^{1}H NMR Spectrum of **37**.

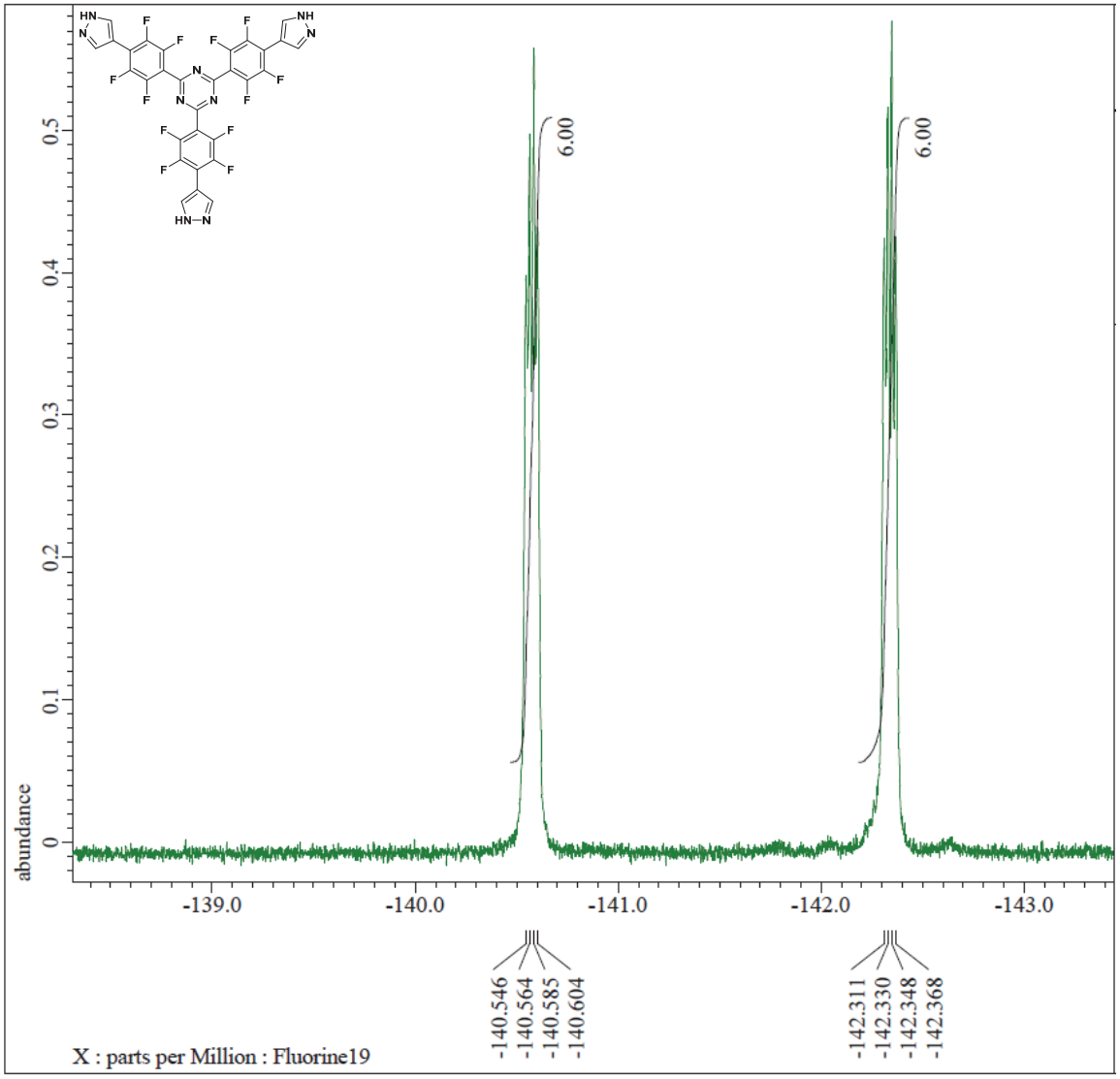

Figure 3.23 ^{19}F NMR Spectrum of **37**.

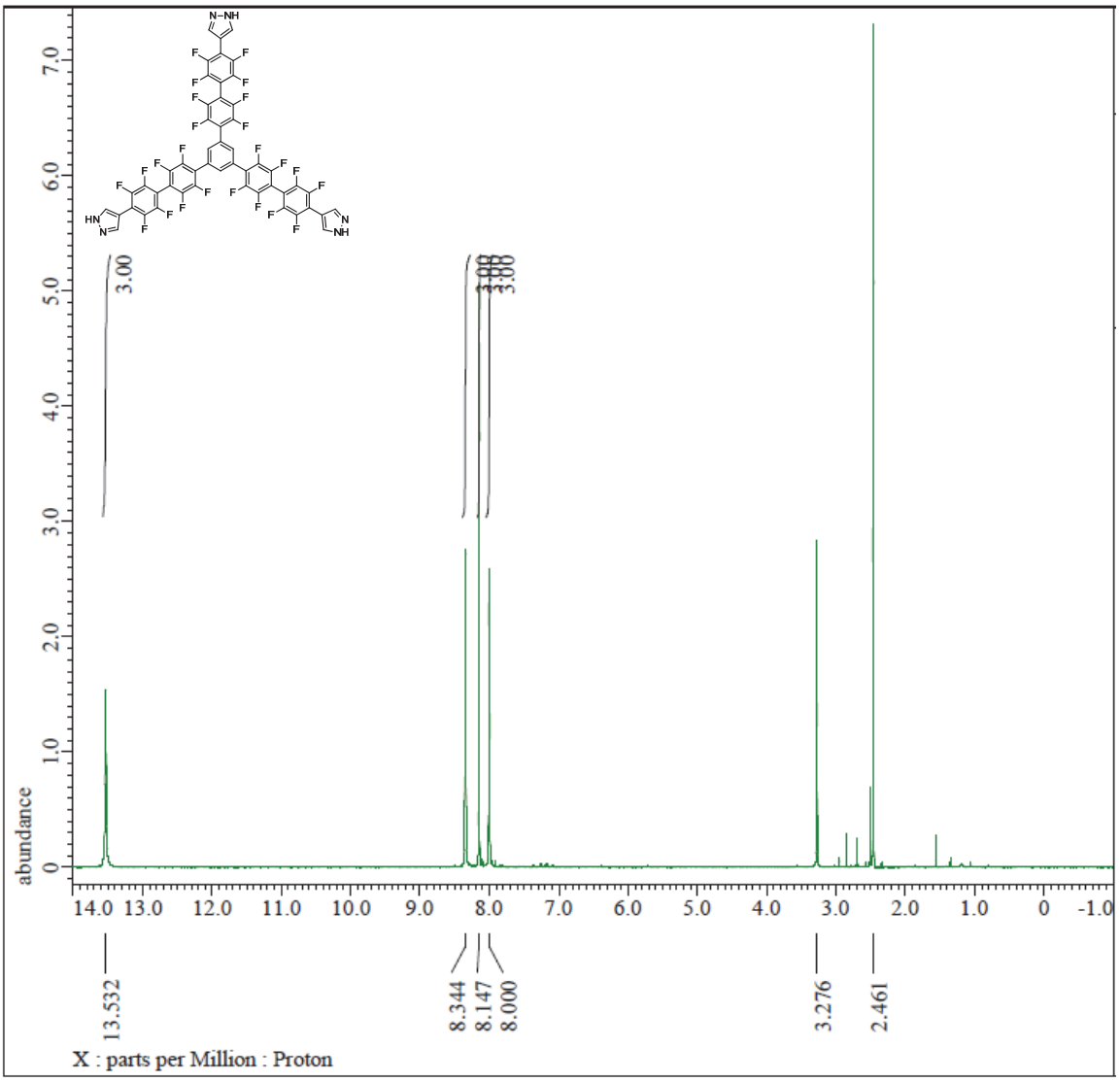

Figure 3.24 ^{1}H NMR Spectrum of **39**.

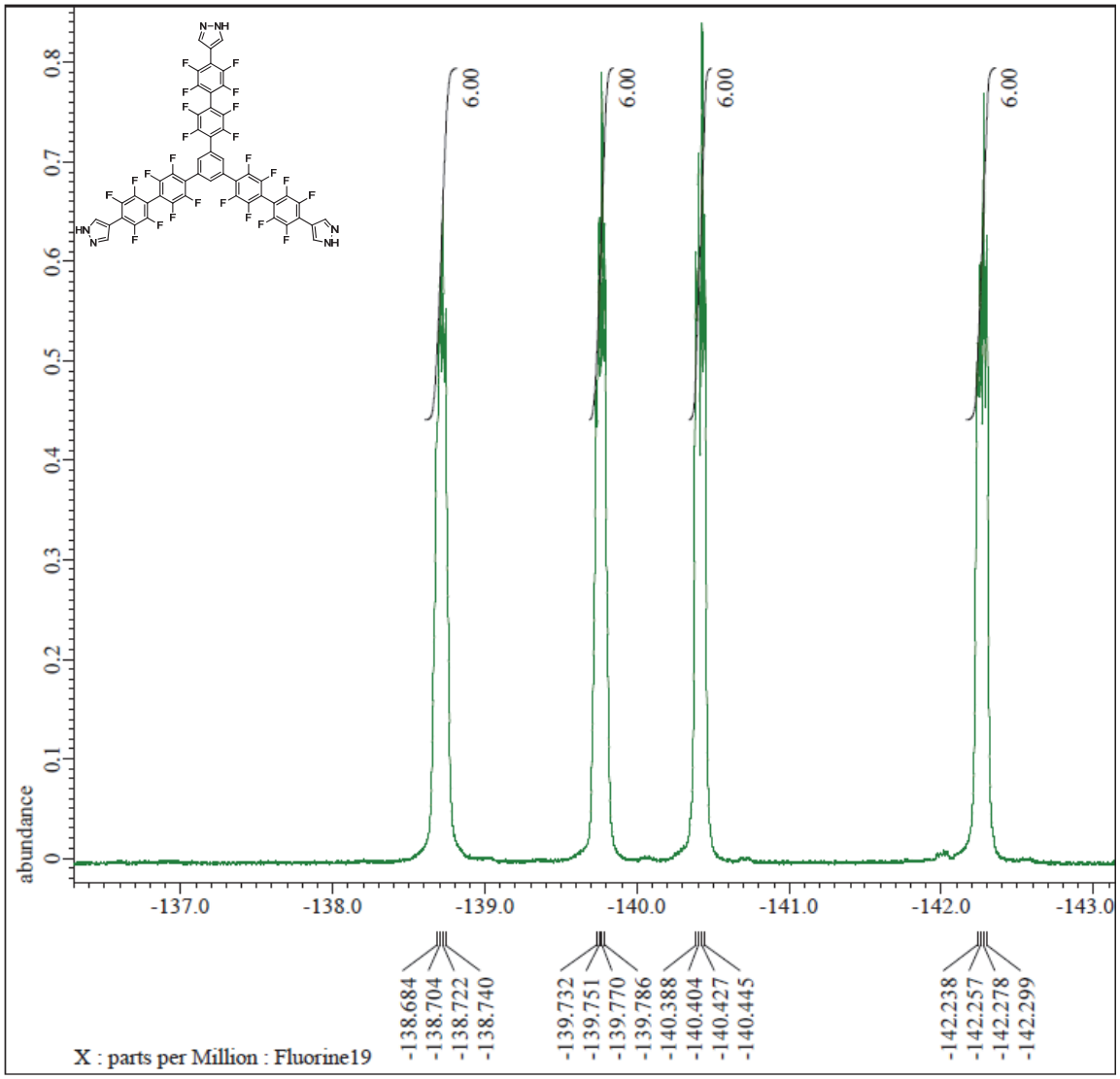

Figure 3.25 ^{19}F NMR Spectrum of **39**.

3.5.4 Thermogravimetric Analysis of 37 and 39

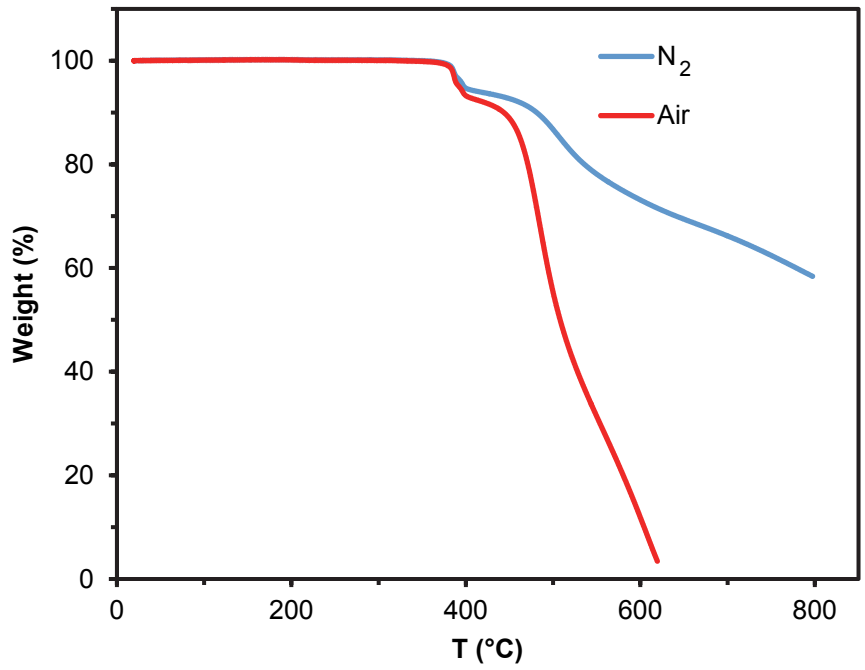

Figure 3.26 Thermogravimetric analysis of **37** in air (red trace) and nitrogen (blue trace).

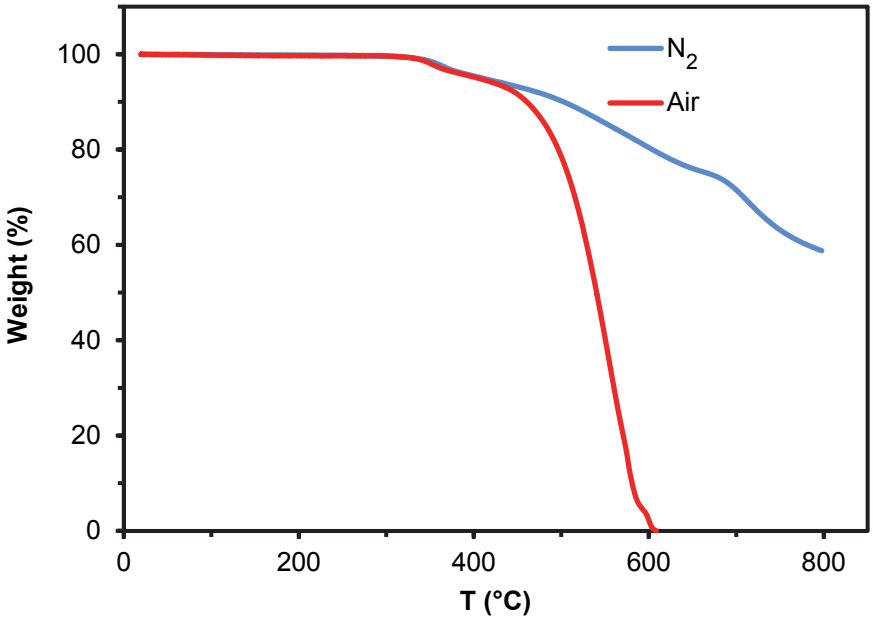

Figure 3.27 Thermogravimetric analysis of **39** in air (red trace) and nitrogen (blue trace).

3.5.5 Powder X-ray Diffraction

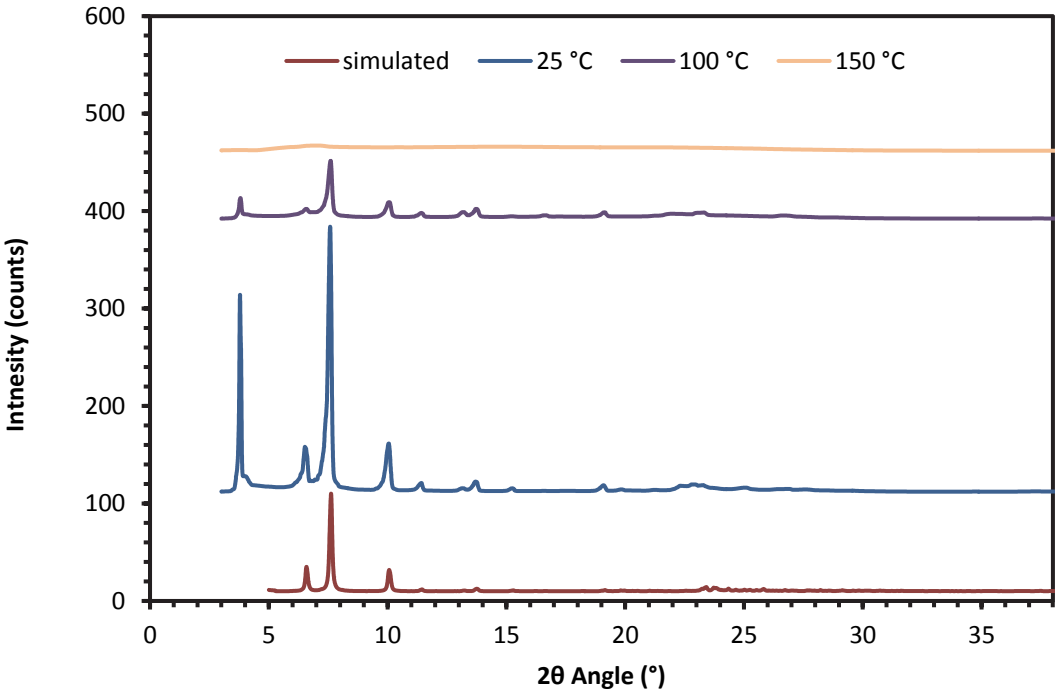

Figure 3.28 Variable temperature powder X-ray crystallography (PXRD) experiment conducted on a sample of **39** at different temperatures in order to determine the thermal stability of this crystal structure.

3.5.6 Gas Sorption Data of 37 and 39

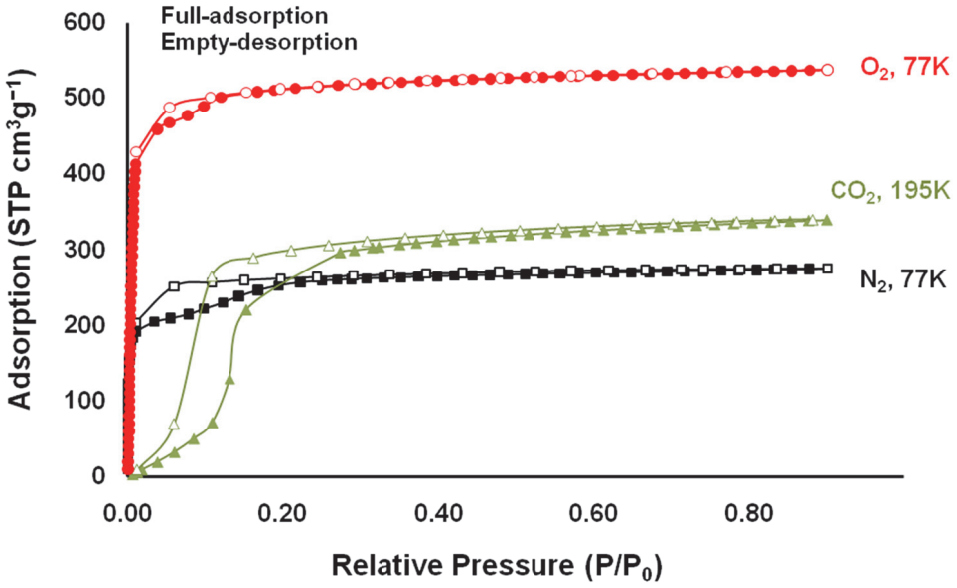

Figure 3.29 Gas sorption plot for crystals of **37** with different gases—oxygen (at 77 K), carbon dioxide (at 195K), and nitrogen (at 77 K). Filled symbols indicate adsorption, empty ones desorption.

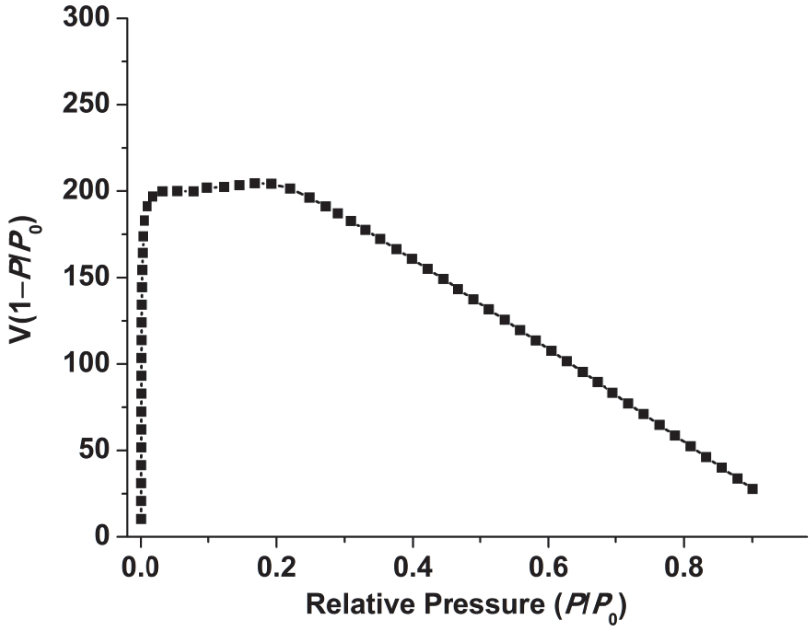

Figure 3.30 Rouquerol plot for gas sorption within the crystals of **37**.

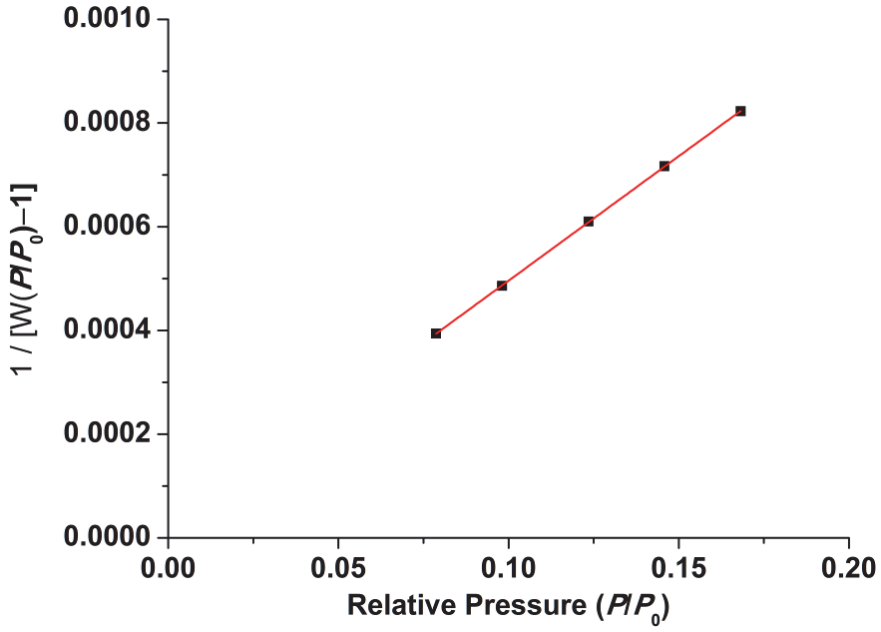

Figure 3.31 BET surface area plot for gas sorption within crystals of **37**. BET surface area: 903.65 ± 3.13 m^2 g^{-1}; *C* constant = 302.57; R_2 = 0.999982.

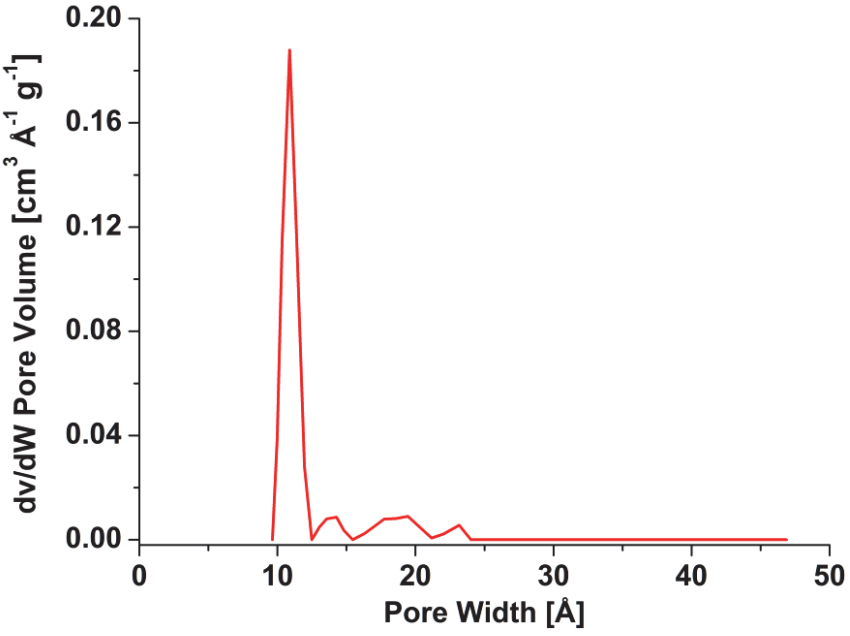

Figure 3.32 NLDFT pore size distribution for crystals of **37**.

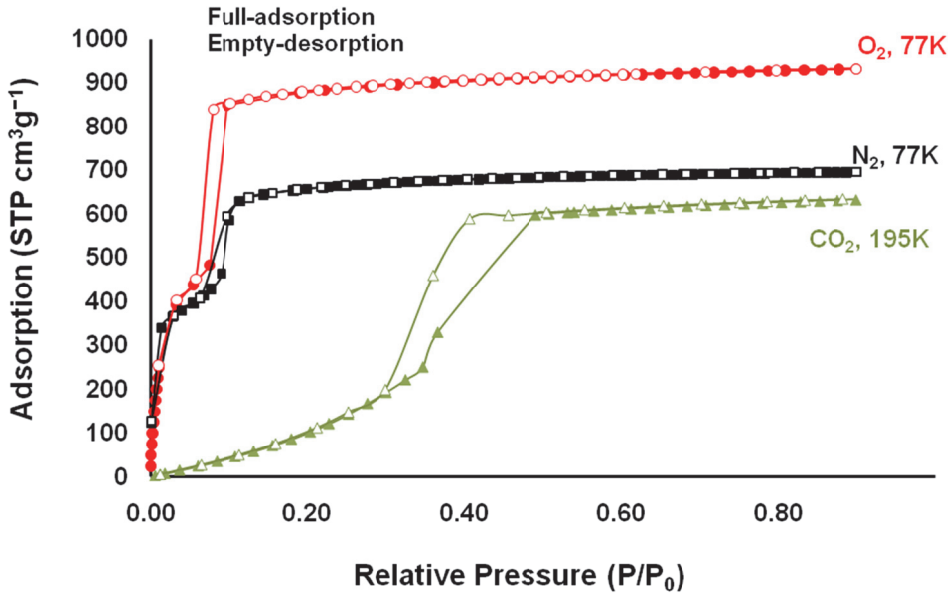

Figure 3.33 Gas sorption plot for crystals of **39** with different gases— xygen (at 77 K), carbon dioxide (at 195K), and nitrogen (at 77 K). Filled symbols indicate adsorption, empty ones desorption.

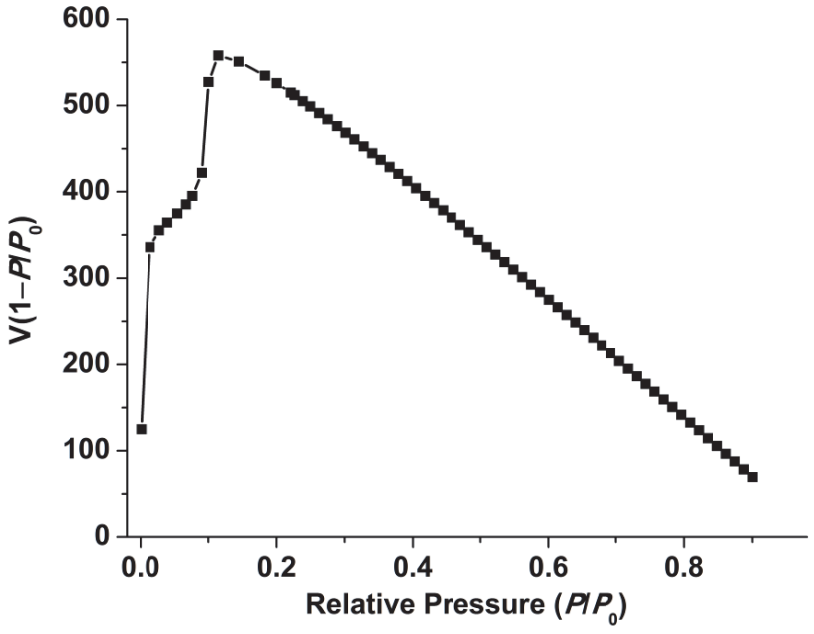

Figure 3.34 Rouquerol plot for gas sorption within the crystals of **39**.

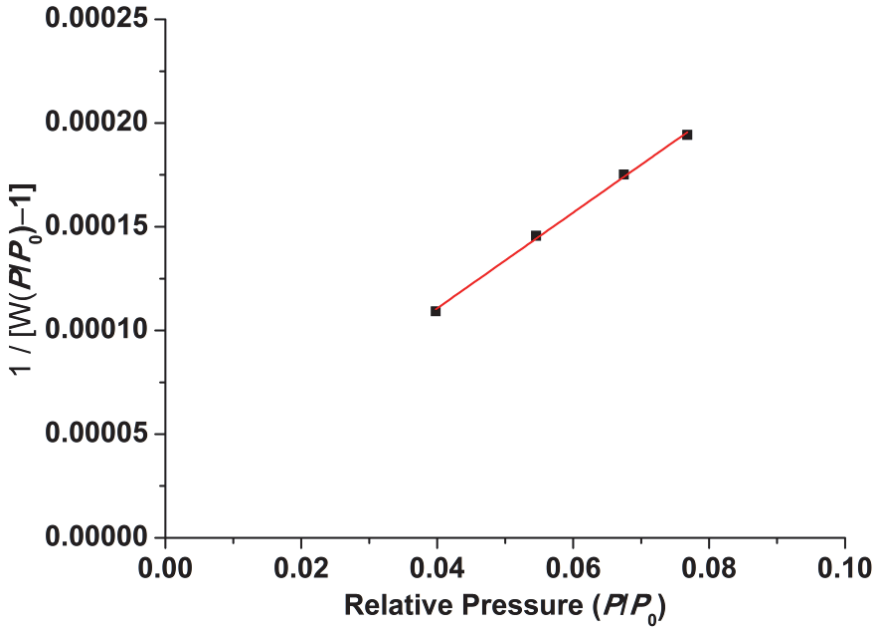

Figure 3.35 BET surface area for crystals of **39**. BET surface area: 1821.47±39.50 m^2 g^{-1}; *C* constant = 172.14; R_2 = 0.9993345.

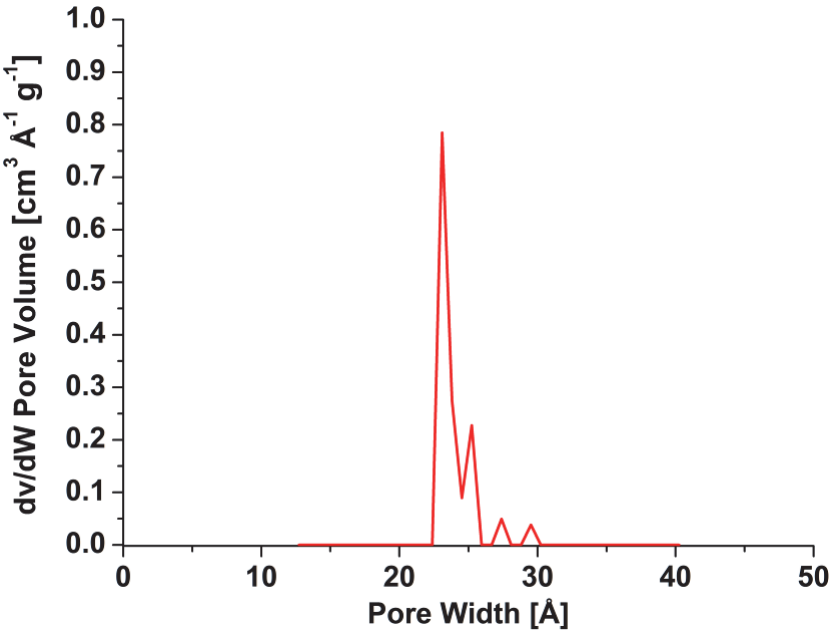

Figure 3.36 NLDFT pore size distribution for crystals of **39**.

3.5.7 Materials Studio Surface Area Calculations

The accessible surface area (S_{acc}) of **37** and **39** was estimated using the *Atoms Volume & Surfaces* calculation module within the Materials Studio package. The accessible surface area (S_{acc}) was calculated by a probe molecule with diameter equal to the kinetic diameter of N_2 (3.68 Å). Then a calculation was used to convert the accessible surface are from $Å^2$ to $m^2\ g^{-1}$ (shown below).

$$S_{acc} \times \text{Avogadro's Number} \times 1/\text{Molar Mass} \times 1/Z \times (Å^2 \text{ to } m^2 \text{ Conversion Factor})$$

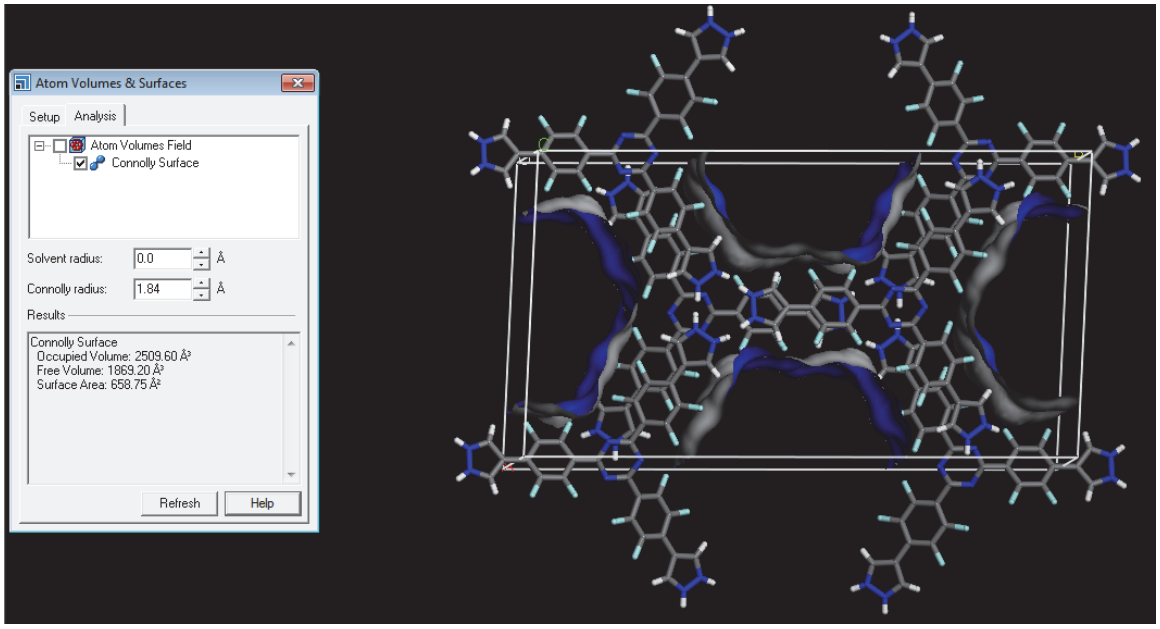

Figure 3.37 Materials Studio simulated image of occupied pore of **37**.

Theoretical Surface Area Calculation of **37**:

$$SA_{Theo} = 658.75\ Å^2 \times 6.022 \times 10^{23} \text{atoms} \times (1\ \text{mol}/725.46\ \text{g}) \times (1/4\ \text{atoms})$$

$$SA_{Theo} = 1.371 \times 10^{23}\ Å^2\ g^{-1}$$

$$SA_{Theo} = 1.371 \times 10^{23}\ Å^2 g^{-1} \times (1 \times 10^{-20}\ m^2/Å^2) = 1371\ m^2\ g^{-1}$$

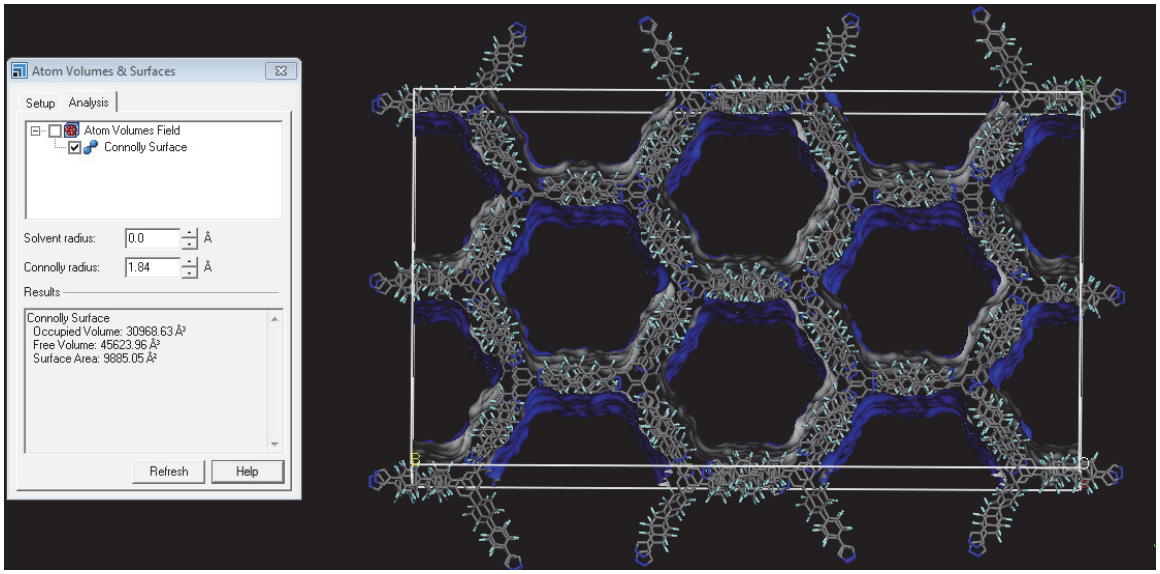

Figure 3.38 Materials Studio simulated image of occupied pore of **39**.

Theoretical Surface Area Calculation of **39**:

$$SA_{Theo} = 9885.05\ \text{Å}^2 \times 6.022 \times 10^{23}\ \text{atoms} \times (1\ \text{mol} / 1164.66\ \text{g}) \times (1 / 32\ \text{atoms})$$

$$SA_{Theo} = 1.598 \times 10^{23}\ \text{Å}^2\ \text{g}^{-1}$$

$$SA_{Theo} = 1.598 \times 10^{23}\ \text{Å}^2\text{g}^{-1} \times (1 \times 10^{-20}\ \text{m}^2 / \text{Å}^2) = 1598\ \text{m}^2\ \text{g}^{-1}$$

3.5.8 Contact Angles

Before the measurements, the crystals of **37** and **39** were vacuum dried for 24 h. Then the finely ground crystals were pressed between two Si(100) slides that had been previously rinsed with absolute EtOH and dried in a stream of nitrogen gas. After removing the upper slide, the exposed crystal surface was used for conducting contact angle measurements. Water was used as the contacting liquid and it was dispensed on the surface of the PMCs by using a Matrix Technologies micro-Electrapette 25 at the slowest speed of 1 μL/s. The measurements were performed at 293 K, with the pipet tip

remaining in contact with the drop. The reported data for each sample were the average of three measurements obtained from three different slides for each PMC with advancing contact angles recorded for both edges of the drop. The contact angles were measured using imageJ software.

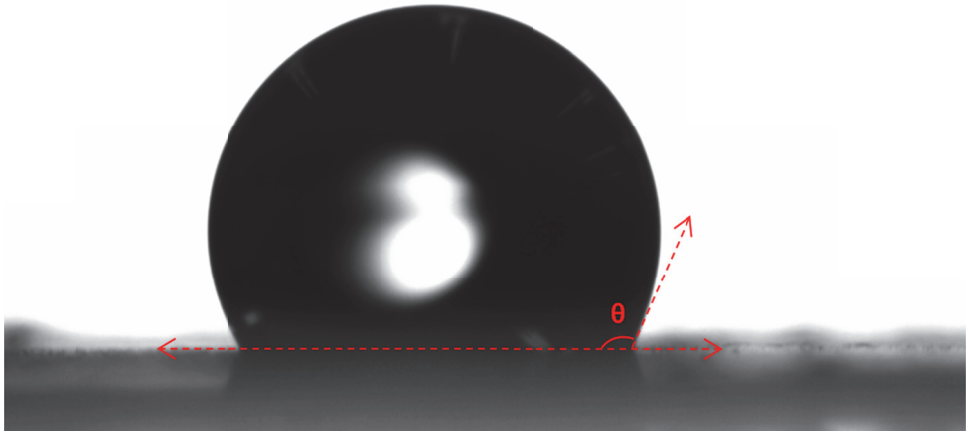

Figure 3.39 Black and white photo of a water droplet on the surface of **37**, displaying a contact angle value of 112.7 °.

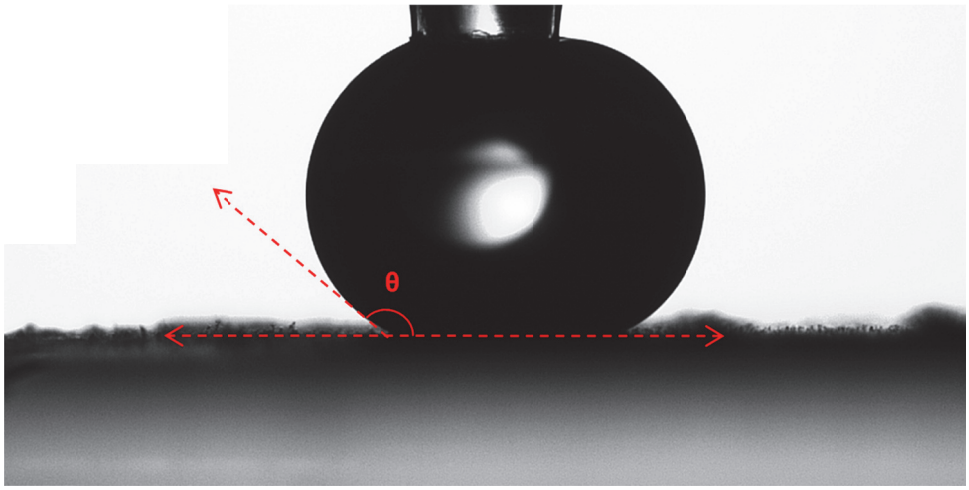

Figure 3.40 Black and white photo of a water droplet on the surface of **39**, displaying a contact angle value of 150.3 °.

References

1. Bindi, L.; Steinhardt, P. J.; Yao, N.; Lu, P. J. *Science* **2009**, *324*, 1306–1309.
2. Atkins, P.; Overton, T.; Rourke, J.; Weller, M.; Armstrong, F. *Inorganic Chemistry,* Oxford University Press: Oxford, GB, **2006**.
3. Wu, Y.; Xiang, J.; Yang, C.; Lu, W.; Lieber, C. M. *Nature* **2004**, *430*, 61–65.
4. Pei, H.; Wen, Z.; Li, Z.; Zhang, Y.; Yue, Z. *Appl. Surf. Sci.* **2018**, *440*, 790–803.
5. Li, Z.; Wen, Z.; Gao, H.; Wu, Y. *Materialwiss. Werkstofftech.* **2018**, *49*, 1193–1205.
6. Su, X.; Xu, Q.; Wang, R.; Xu, Z.; Liu, S.; Liu, B. *Mater. Des.* **2018**, *141*, 296–322.
7. Spittle, P. *Phys. Educ.* **2003**, *36*, 504–511.
8. Schmidt, G. M. J. *Pure Appl. Chem.* **1971**, *27*, 647–678.
9. Desiraju, G. R. *Angew. Chem. Int. Ed*. **2007**, *46*, 8342–8356.
10. Chen, T.-H.; Popov, I.; Kaveevivitchai, W.; Chuang, Y. C.; Chen, Y. S.; Daugulis, O.; Jacobson, A. J.; Miljanić, O. Š. *Nat. Commun.* **2014**, *5*, doi: 10.1038/ncomms6131.
11. Anderson, D.; Duncan, J.; Rossotti, F. *J. Chem. Soc.* **1961**, 140–145.
12. Wang, F.; Richards, V. N.; Shields, S. P.; Buhro, W. E. *Chem. Mater.* **2014**, *26*, 3212–3225.
13. Davey, R. J.; Schroeder, S. L. M.; ter Horst, J. H. *Angew. Chem. Int. Ed.* **2013**, *52*, 2166–2179.
14. Desiraju, G. R. *Nat. Mater.* **2002**, *1*, 77–79.

15. Wang, J.; Liang, Y.-L.; Qu, J. *Chem. Commun.* **2009**, 5144–5146.

16. Smith, B. J.; Dichtel, W. R. *J. Am. Chem. Soc.* **2014**, *136*, 8783−8789.

17. In all of the crystal structures, N−H and C−H bond lengths have been normalized to values obtained from neutron diffraction measurements. Refer to: Steiner, T. *Angew. Chem., Int. Ed.*, **2002**, *41*, 48−76.

18. Janiak, C. *J. Chem. Soc., Dalton Trans.*, **2000**, 3885–3896.

19. Wheeler, S. E.; Houk, K. N. *J. Am. Chem. Soc*. **2008**, *130*, 10854–10855.

20. Martinez, C. R.; Iverson; B. L. *Chem. Sci.* **2012**, *3*, 2191–2201.

21. Aldridge, B.; De Luca, G.; Edgar, M.; Emsley, J. W.; Furby, M. I. C.; Webster, M. *Liquid Cryst.* **1998**, *24*, 569−581.

22. Merritt, L. L.; Schroeder, E. *Acta Crystallographica.* **1956**, *9*, 801–804.

23. Hasell, T.; Chong, S. Y.; Schmidtmann, M.; Adams, D. J.; Cooper, A. I. *Angew. Chem. Int. Ed.* **2012**, *51*, 7154−7157.

24. Bosch, E.; Bowling, N. P.; Darko, J. *Cryst. Growth Des.* **2015**, *15*, 1634−1641.

25. Bojan, R. V.; Czerwieniec, R.; Laguna, A.; Lasanta, T.; López-de-Luzuriaga, J. M.; Monge, M.; Olmos, M. E.; Yersin, H. *Dalton Trans.* **2013**, *42*, 4267−4277.

26. Hashim, M. I.; Le, H. T. M.; Chen, T.-H.; Chen, Y.-S. Daugulis, O.; Hsu, C.-W.; Jacobson, A. J.; Kaveevivitchai, W.; Liang, X.; Makarenko, T.; Miljanić, O. Š.; Popovs, I.; Tran, H. V.; Wang, X.; Wu, C.-H.; Wu, J. I. *J. Am. Chem. Soc.* **2018**, *140*, 6014–6026.

27. Goodhand, N.; Hamor, T. A. *Acta Crystallogr., Sect. B: Struct. Crystallogr. Cryst. Chem.* **1982**, *38*, 1342−1345.

28. McDonald, T. M.; D'Alessandro, D. M.; Krishna, R.; Long, J. R. *Chem. Sci.* **2011**, *2*, 2022− 2028.

29. Nugent, P. S.; Rhodus, V. L.; Pham, T.; Forrest, K.; Wojtas, L.; Space, B.; Zaworotko, M. J. *J. Am. Chem. Soc.* **2013**, *135*, 10950−10953.

30. Patel, H. A.; Je, S. H.; Park, J.; Chen, D. P.; Jung, Y.; Yavuz, C. T.; Coskun, A. *Nat. Commun.* **2013**, *4*, doi: 10.1038/ncomms2359.

31. EL-Mahdy, A. F. M.; Kuo, C.-H.; Alshehri, A.; Young, C.; Yamauchi, Y.; Kim, J.; Kuo, S.-W. *J. Mater. Chem. A* **2018**, *6*, 19532–19541.

32. Owen, M. J. *Silicon* **2017**, *9*, 651–655.

33. Isimjan, T. T.; Wang, T.; Rohani, S. *Chem. Eng. J.* **2012**, *210*, 182−187.

34. Mo, C.; Zheng, Y.; Wang, F.; Mo, Q. *Int. J. Electrochem. Sci.* **2015**, *10*, 7380−7391.

35. Latthe, S. S.; Terashima, C.; Nakata, K.; Sakai, M.; Fujishima, A. *J. Mater. Chem. A* **2014**, *2*, 5548−5553.

36. Cully, P.; Karasu, F.; Muller, L.; Jauzein, T.; Leterrier, Y. *Surf. Coat. Technol.* **2018**, *348*, 111–120.

37. Banerjee, I.; Pangule, R. C.; Kane, R. S. *Adv. Mater.* **2011**, *23*, 690−718.

38. Gao, S.; Huang, J.; Li, S.; Liu, H.; Li, F.; Li, Y.; Chen, G.; Lai, Y. *Mater. Des.* **2017**, *128*, 1–8.

Chapter Four

Fluorescent Properties of Fluorinated Trispyrazoles

4.1 Fluorescence and Aggregation-Caused Quenching (ACQ)

Fluorescence is a form of luminescence that is caused by the absorption of high energy photons by the electrons of the material or compound. As a result of this absorption, electrons are promoted from the ground state to the singlet excited state. Then, as the electrons relax and return to the ground state, the system emits photons of a lower energy and longer wavelength than the absorbed photons at the beginning of this process. This phenomenon has many practical applications including biological imaging,[1,2,3] chemical sensors,[4,5,6] cosmic ray detection,[7] and fluorescent lamps. Recently, there has become a growing interest in organic molecules and polymers that are capable of emitting multicolor fluorescence in the solid phase for the use in organic light-emitting diodes (OLEDs)[8,9,10] and organic solid-state lasers.[11,12]

A range of fluorophores have been extensively studied in solution, but have found limited applications in the solid state due to the aggregation of these fluorophores and the non-radiative decay of the excited states in the aggregates effectively diminishing quantum yields.[13] This occurrence is known as the aggregation-caused quenching (ACQ) (photograph depicting this phenomenon is shown in Figure 4.1) and has been problematic for the development of solid state fluorescent organic materials. There have been numerous efforts exploited by researchers to circumvent ACQ. One approach involved the introduction of steric bulk to the fluorophore in order to obstruct this aggregation process.[14,15] Yamaguchi et al.[16] have reported that the incorporation of aromatic boryl

groups to the side positions of the electron-donating π-framework increases solid state emissions. This increase in emission is attributed to the bulky boron moiety preventing aggregation as well as it forming a donor-acceptor system with the fluorophore.

Shimizu et al.[17] have also shown that the twisted confirmation of their 1,4-bis(alkenyl)-2,5-dipiperidinobenzenes fluorophores were highly emissive in the solid state. Zhang et al.[18] recently developed a strategy to overcome ACQ of fluorophores by covalently bonding cellulose chains onto the molecule of interest and then ionizing this moiety. The cellulose chains separate the fluorophore molecules from one another and the ionization process results in the electrostatic repulsion of the molecules from one another effectively maintaining a distance between them. Both features synergistically hinder the effects of ACQ. While these approaches mitigate ACQ, they can result in other application-related problems. Hence, the development of solid organic fluorophores is still a very challenging task. However, there exists another way of solving the ACQ problem that is counter to this way of thinking. This approach takes advantage of a molecules' inherent tendency to form aggregates in high concentrations or in the solid state. This idea initiated research into the development of fluorophores that show an enhancement in emission upon aggregation, as a consequence of a phenomenon called aggregation-induced emission (AIE).

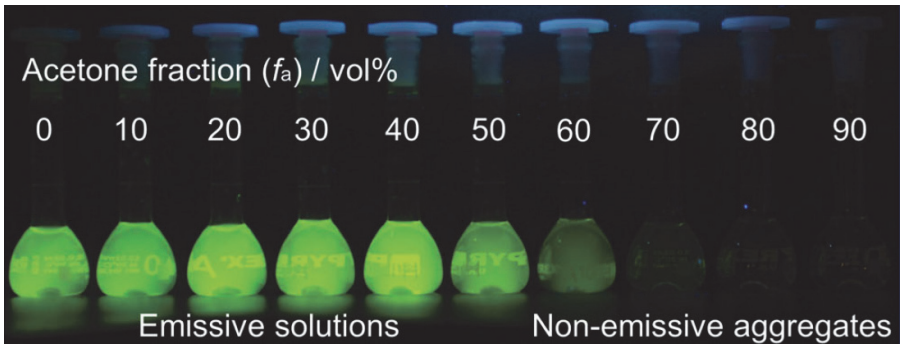

Figure 4.1 Fluorescence photograph of solutions and suspensions of fluorescein in acetone/water mixtures depicting ACQ.[19]

4.2 Aggregation Induced Emission (AIE)

AIE is a photophysical phenomenon that was reported in 2001 by Tang et al.[20] They noticed that hexaphenylsilole (HPS, **40**, Figure 4.2) was non-emissive when dissolved in a tetrahydrofuran solution but became highly fluorescent in concentrated solutions where aggregates formed (Figure 4.3). Further examination of HPS molecules revealed that they possess a non-planar twisted propeller-shaped structure. Hence, they inferred that in a dilute solution, the six phenyl arms of the HPS molecule can undergo dynamic intramolecular rotations leading to non-radiative decay rendering the solution non-emissive. While in the aggregate state the HPS molecules cannot pack through a [$\pi\cdots\pi$] stacking process due to the non-planar propeller shape of these molecules. However, the intramolecular rotations of the phenyl arms would be greatly restricted due to close proximity constraints. This restriction of intramolecular rotations (RIR) could obstruct the non-radiative decay pathways causing this molecule to be fluorescent in the aggregate state.[21,22] After this initial discovery, research into the development of AIE active molecules (Figure 4.2) has rapidly expanded with various applications in fields ranging from the detection of explosives[23] to DNA visualization.[24]

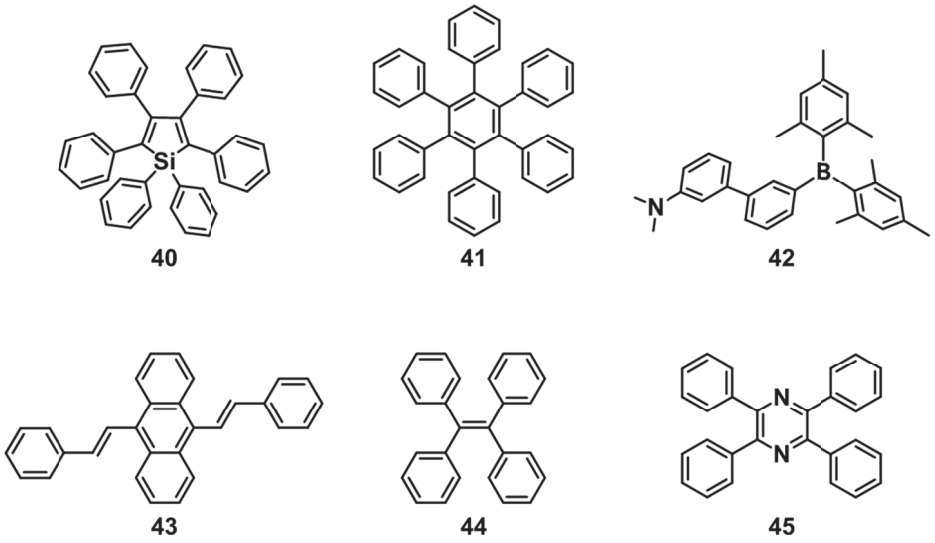

Figure 4.2 Representative structures of organic AIE molecules.

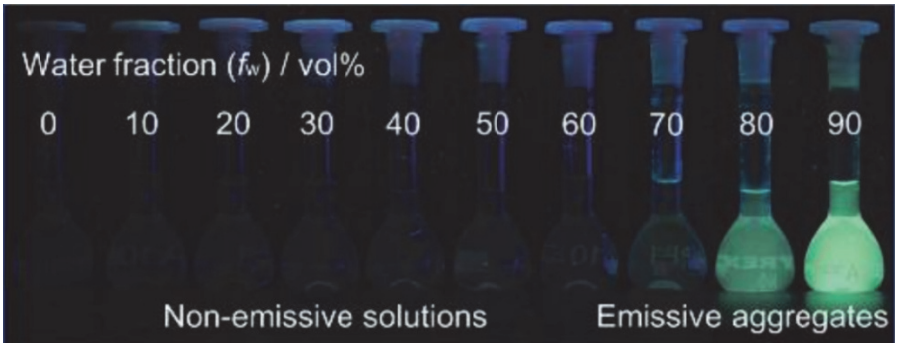

Figure 4.3 Fluorescence photograph of solutions and suspensions of HPS in THF/water mixtures.[19]

In order to better understand AIE and develop new AIE molecules, several mechanisms have been proposed. These mechanisms include the restriction of intramolecular motion (RIM),[21,25,26] *J*-aggregate formation,[27] twisted intramolecular charge transfer (TICT),[28,29] excited-state intramolecular proton transfer,[30] crystallization-induced emission,[31] and the recently proposed suppression of Kasha's rule.[32] Among these mechanisms, RIM is most commonly cited. According to the RIM definition, the

restriction of intramolecular rotation and vibration can suppress the radiationless decay of excited state species and cause an increase in radiative emission. The restriction can be controlled by both external and internal factors.[9,19] External factors can consist of factors such as lowering of the temperature,[21] increasing the pressure,[33] and the utilization of highly viscous solvents[21] to restrict intramolecular motion. Internally, factors such as the steric hindrance of bulky groups[34] and covalent tethering of rotatable groups[26] can be used to restrict intramolecular motion. The recent realization of AIE within porous materials, such as covalent organic frameworks (COFs) and metal organic frameworks (MOFs), could lead to the development of multifunctional and structurally robust materials.[35] In this chapter, the observation of aggregation induced emission within a class of extensively fluorinated aromatic pyrazoles which also form porous molecular crystals is reported.[36]

3.3 Results and Discussion

Our group has synthesized two extensively fluorinated aromatic compounds **4** and **37** (Figure 4.4 A and B), which assemble into porous solid-state structures that are held together by a combination of hydrogen bonding between terminal pyrazoles and [π···π] stacking between electron-rich pyrazoles and electron-poor tetrafluorobenzenes. Compounds **4** and **37** are very similar in their molecular and solid-state extended structures, and they both show solid state fluorescence (Fig. 4.4A and B). In the solid state, both **4** and **37** display a maximum wavelength at 336 nm in the excitation spectra and similar maximum wavelengths in their emission spectra, at 382 (for **4**) and 371 (for

37) nm. Both compounds fluoresce in the blue region in the solid state when excited at 365 nm with a handheld UV lamp (Figure 4.4C and D).

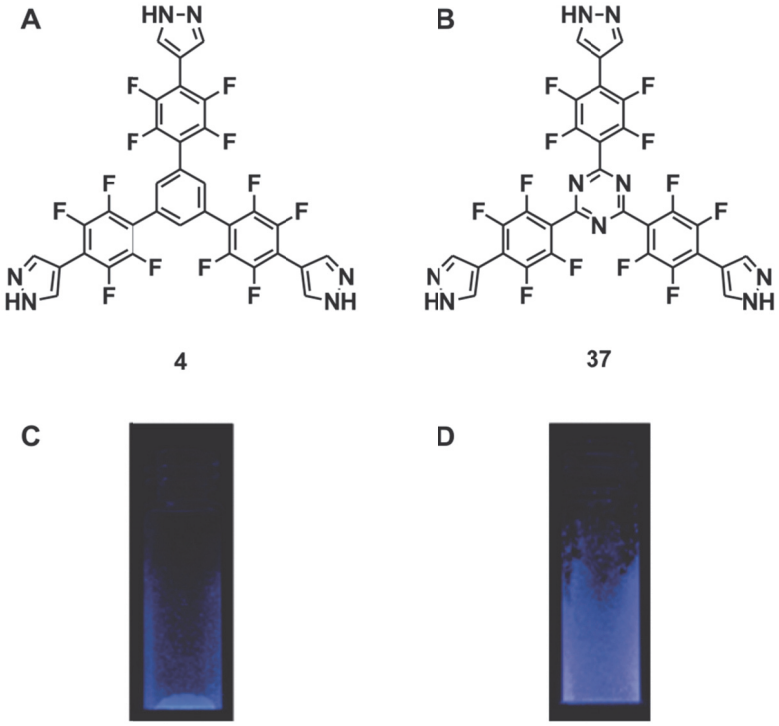

Figure 4.4 Chemical structure of molecules that make up (A) **4** and (B) **37**. Solid state fluorescence of (C) **4** and (D) **37**.

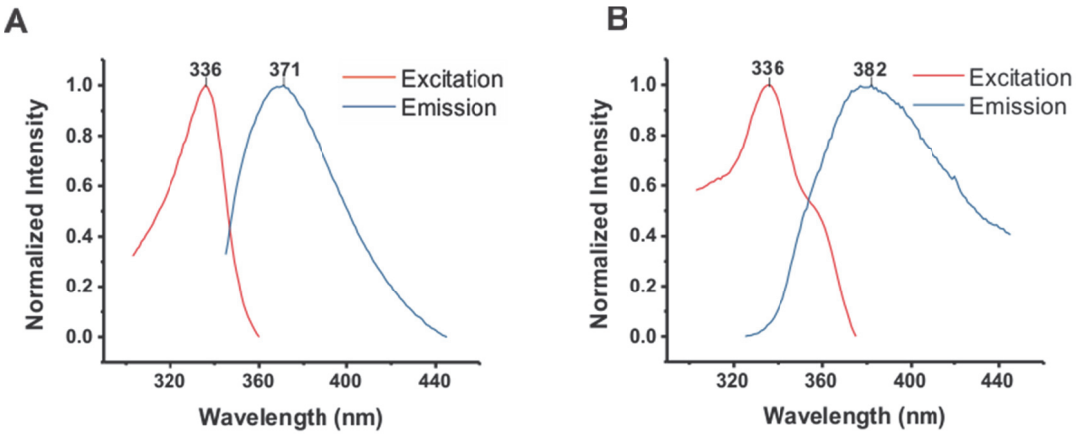

Figure 4.5 Solid-state excitation and emission spectra of (C) **4** and (D) **37**.

Since both **4** and **37** can be dissolved in hydrogen-bonding solvents without decomposition, we decided to explore their fluorescence behavior in solution. In order to establish the connection between the spectroscopic properties and different degrees of aggregation, both **4** and **37** were studied in a DMF/H_2O mixed solvent system. DMF played the role of a "good" solvent, while H_2O acted as the "bad" solvent which would induce the aggregation of hydrophobic **4** and **37**. In the case of **37**, the AIE phenomenon was observed (Figure 4.6). The initial solution of **37** in DMF was non-emissive. Unexpectedly, the emission intensity of the solution of **37** in DMF initially decreased by a third as the H_2O content was increased to 15% (Table 4.1). This could be due to a reduction in the space for free movement of solute molecules that occurred at this concentration. At the same time, this concentration was not high enough to yield substantial aggregation, which can restrict intramolecular motion (as indicated by the overlapping tails in the absorption spectra of the samples with 0% and 15% H_2O, Figure 4.7). As the content of H_2O increased beyond 15%, the emission intensity considerably increased, as H_2O promoted aggregation.

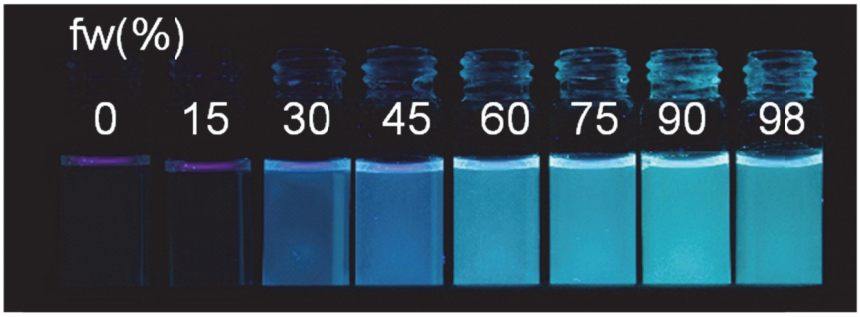

Figure 4.5 Photographs of the fluorescence of solutions of **37** in DMF/water mixtures.

f_w(%)	λ_{abs}(nm)	λ_{ems}(nm)	Stokes shift (cm^{-1})	Relative intensity
0	322	444	8553	1
15	322	429	7746	0.66
30	318	441	8771	3.9
45	323	436	8024	8.8
60	324	458	9030	11.4
75	325	473	9628	13.5
90	324	477	9900	14.6
98	320	475	10197	11.4

Table 4.1 Emission and absorption spectral data of **37** (10 μM) in DMF/H_2O with different H_2O volume percentages. (The relative intensity in the table is the ratio of the intensity integrated area from 330 nm to 700 nm between a certain sample).

The presence of aggregation can be further verified from the normalized absorption spectra (Figure 4.6B) as the tails of this spectra level off. This leveling off has been attributed to aggregate scattering and is typically associated with AIE.[37,38] The relative intensity of emissions continued to increase until a maximum value was reached at 90% H_2O. The resulting emission was 14.6 times stronger than that observed for the sample with 0% H_2O. The addition of H_2O also caused a change in the observed emission color from deep-sea blue to turquoise under irradiation at 365 nm (Figure 4.5). Finally, when the H_2O content increased from 90% to 98%, the emission intensity dropped

slightly, from 14.6 to 11.4. This decrease of emission intensity does not appear to be a consequence of ACQ, but instead can be attributed to the onset of precipitation of **37**. This precipitation could lead to a decrease in the amount of aggregates in the tested area. It was also observed that the absorption maximum λ_{abs} did not shift significantly, but the emission maximum λ_{ems} did. The λ_{ems} showed a red shift and an increase in Stokes shift when the H_2O percentage was increased. This suggests that the structure difference between the ground state and the excited state increases with the polarity of the solvent[39] and could demonstrate the influence of a possible TICT mechanism under these specific circumstances. Hence, it can be concluded **37** is AIE active and it can be hypothesized that **4** would also be AIE active due to the similarities in structure and solid-state fluorescence.

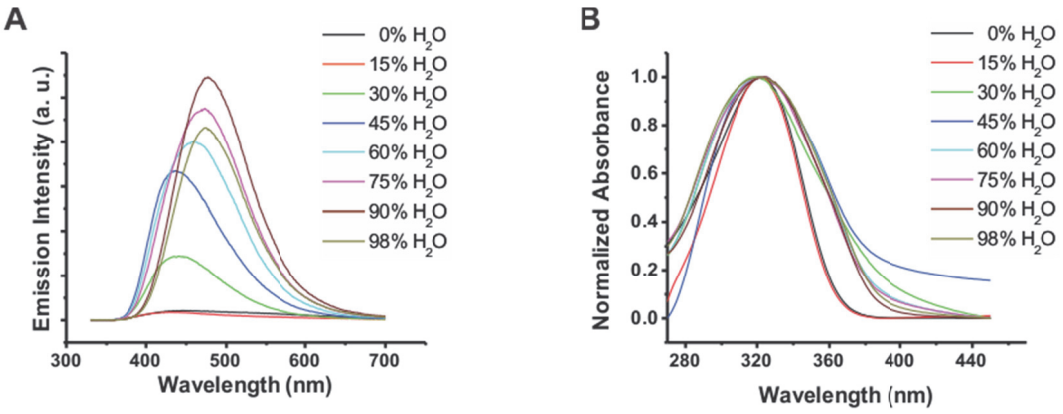

Figure 4.6 Graphical representation of the (A) emission spectra and (B) absorption spectra of **37**.

However, the experiments conducted on **4** in the same mixed solvent system gave a different result (Figure 4.7). As the H_2O content was increased from 0 to 98%, aggregation did occur and this was confirmed by the level-off of tails in the absorption spectra (Figure 4.8 B). The dissimilarity to **37** was related to the relative emission

intensity that changed minimally with increasing H_2O content in the solution of **4**. The intensity ranged from 0.78 to 1.52 times the emission at 0% H_2O content (Table 4.2). Even when dissolved in pure DMF, the emission spectrum of **4** showed a strong fluorescence peak (Figure 4.8 A). In addition, the emission maximum λ_{ems} shifted towards the red from 381 to 411 nm, while the absorption maximum λ_{abs} was not influenced greatly by the increase in solvent polarity, further suggesting that **4** is not AIE active. Since both **4** and **37** displayed a similarly high value of Stokes shifts (Table 4.1 and 4.2), this is indicative of a significant structural change taking place upon excitation. Therefore, it can be concluded that these compounds are not rigid and that there is a noteworthy difference in intramolecular rotation of their aromatic rings relative to one another.

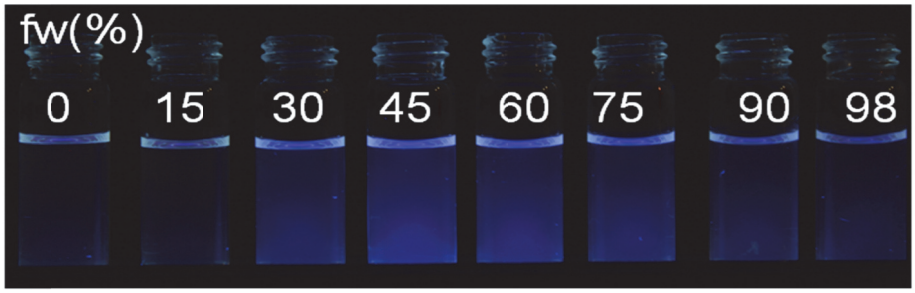

Figure 4.7 Fluorescence photograph of solutions of **4** in DMF/water mixtures.

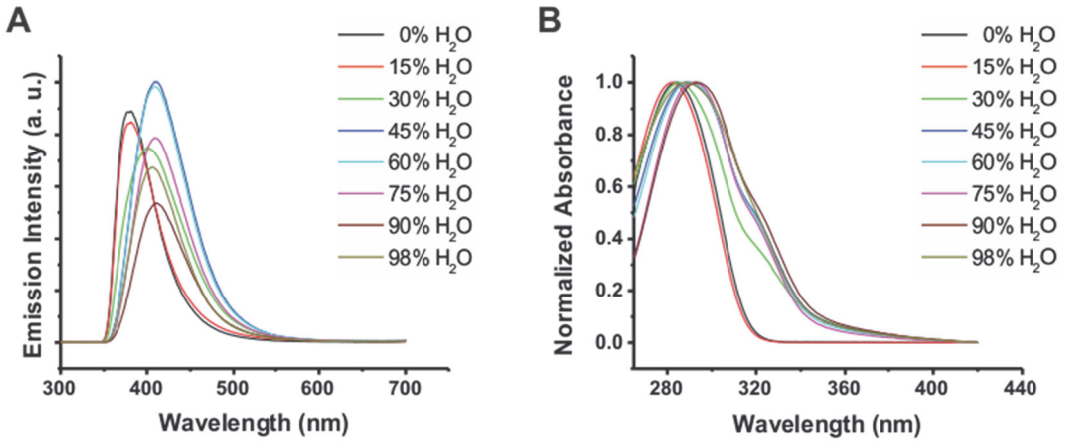

Figure 4.8 Graphical representation of the (A) emission spectra and (B) absorption spectra of **4**.

fw(%)	λabs(nm)	λems(nm)	Stokes shift (cm^{-1})	Relative intensity
0	284	381	8964	1
15	282	382	9283	1.02
30	285	400	10088	1.21
45	289	411	10271	1.52
60	290	410	10093	1.48
75	292	410	9856	1.16
90	292	411	9916	0.78
98	288	406	10092	0.95

Table 4.2 Emission and absorption spectral data of **4** (10 μM) in DMF/H_2O with different H_2O volume percentages.

Examination of crystal structure of **37** revealed the presence of two conformers (one of them is shown in Figure 4.9 A). The dihedral angles between the central plane of the triazine and the planes of tetrafluorobenzenes range from 30 to 45.6 °, depending on the conformer. In contrast, the tetrafluorobenzene group and the pyrazole group on the

same arm are almost coplanar, with the dihedral angles ranging from 8.2–11 °, depending on the conformer. Crystals of **4** reveal the presence of four slightly different conformers in the framework (one of them is shown in Figure 4.10A). The dihedral angles between the planes of the central benzene ring and the tetrafluorobenzene rings range between 30.5 and 50.8 °. The tetrafluorobenzene group and the pyrazole group in the same branch are almost coplanar, with the dihedral angles ranging from 7.2 to 141 °.

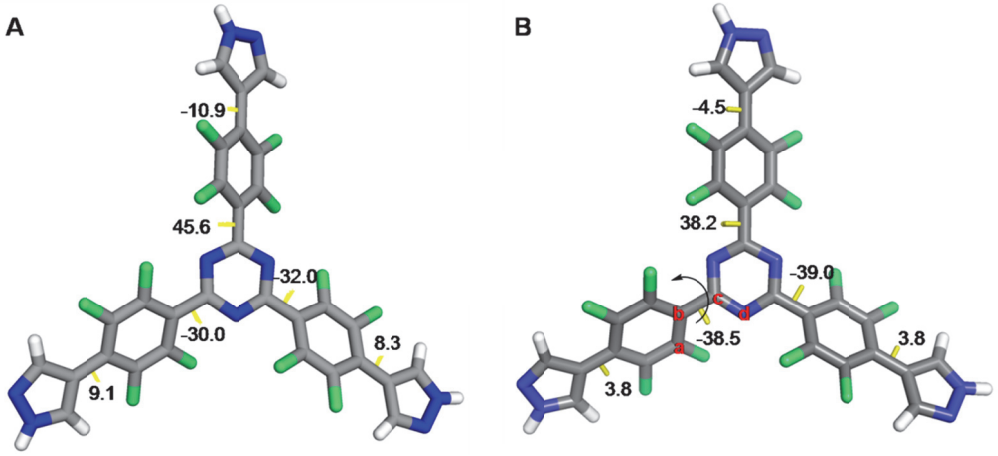

Figure 4.9 (A) Structure of one of the two conformer molecules found in the crystal of **37**. (B) Optimized structure of this conformer used to probe intramolecular dynamics. Element colors: H—white, N—blue, C—gray, F—green.

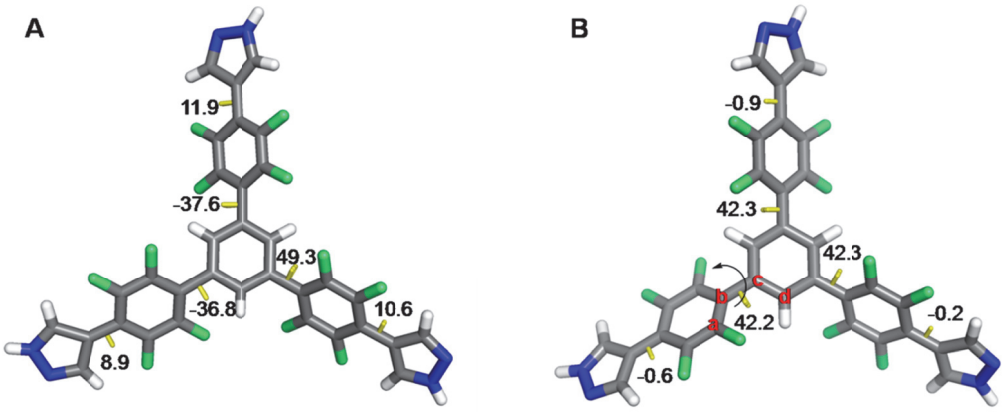

Figure 4.10 (A) Structure of one of the two conformer molecules found in the crystal of **4**. (B) Optimized structure of this conformer used to probe intramolecular dynamics. Element colors: H—white, N—blue, C—gray, F—green.

Next we decided to probe the intramolecular dynamics of **37** and **4** in a dilute solution, which was expected to be the cause of their different AIE behavior. The structures were optimized in the gas state by using the B3LYP/B-31G(d) function of the Gaussian 09 software package. The optimized structures were then scanned rigidly along the dihedral angle a–b–c–d (shown in Figure 4.9B and 4.10B) to obtain the barriers of rotation. For **37**, the most stable structure has a dihedral angle of 38.5 ° between the triazine and tetrafluorobenzene planes, and was chosen as the 0 kcal mol^{-1} reference point. The rotational barrier appears when the dihedral angle is near 90, 180, 270, and 360 °, indicating that the tetrafluorobenzene ring is either coplanar or perpendicular to the triazine plane (graph of the rotational energy barriers shown in Figure 4.11). The maximum energy barriers ($\Delta E_2 = \Delta E_4 = 2.54$ kcal mol^{-1}) occur at the coplanar positions as the distance between the lone pair of triazine nitrogens and the *ortho*-fluorine atoms is shortest at that point, causing the greatest repulsion. The perpendicular positioning of the

two groups disrupts the π conjugation, resulting in energy maxima (ΔE_1 = 1.94 and ΔE_3 = 1.92 kcal mol^{-1}). All of the rotation barriers in compound **37** are less than 3 kcal mol^{-1}, suggesting that intramolecular rotation along the C–C bond between the central triazine and three arms of the molecule can readily occur at room temperature.

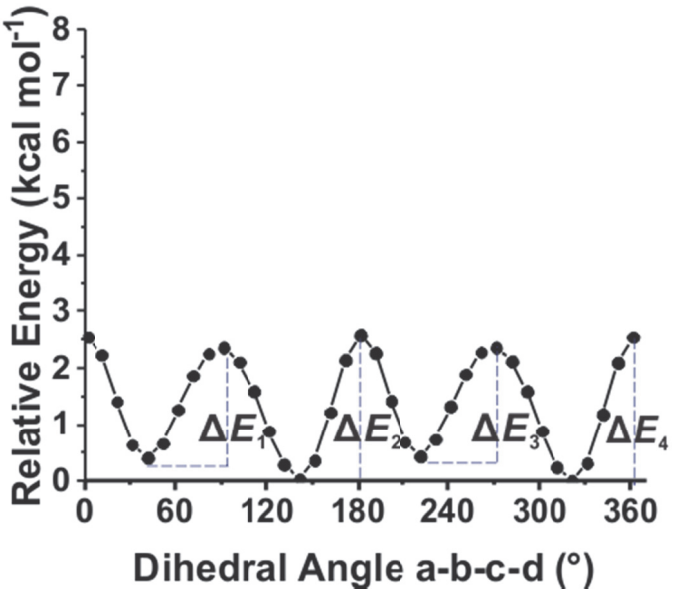

Figure 4.11 Graphical representation of the relative energy conformations of **37** as a function of the dihedral angle a-b-c-d (shown in Figure 4.9B).

As for **4**, the most stable calculated structure displayed a dihedral angle of 42.2, and this was chosen as the 0 kcal mol^{-1} reference point. The energy maxima also occurred when the tetrafluorobenzene and core benzene rings were coplanar and perpendicular to one another (graph of the rotational energy barriers shown in Figure 4.12). At the perpendicular positions, they are ΔE_1 = 2.21 and ΔE_3 = 2.16 kcal mol^{-1}, which was similar to the values found for **37** and presumably caused by an analogous loss in conjugation overlap. However, the maximum energy barriers at the coplanar positions

were ΔE_2 = 6.74 and ΔE_4 = 6.72 kcal mol^{-1}, which are approximately 2.6 times greater than the values observed for **37**. The reason for the higher rotational energy barriers at the coplanar position for **4** was likely due to the steric repulsion between the hydrogen atoms of the central benzene ring and the *ortho*-fluorines. These two atoms rotate past one another with a minimal F–H distance of 1.81 Å.[18] These calculation results indicate that a stronger vicinal repulsion in **4** resulted in a higher rotational energy barrier, thereby limiting the intramolecular rotation to a higher extent compared to **37**. Therefore, **4** is more rigid and restricted in its rotation to conformations closely resembling that observed in the solid crystal structure. Meaning that its fluorescence does not change much with the introduction of solvent, or with a transition from the solution to the solid state. In contrast, the more flexible **37** must have its rotation restricted by the addition of H_2O in order for its fluorescence to turn on, as suggested by the RIM mechanism.

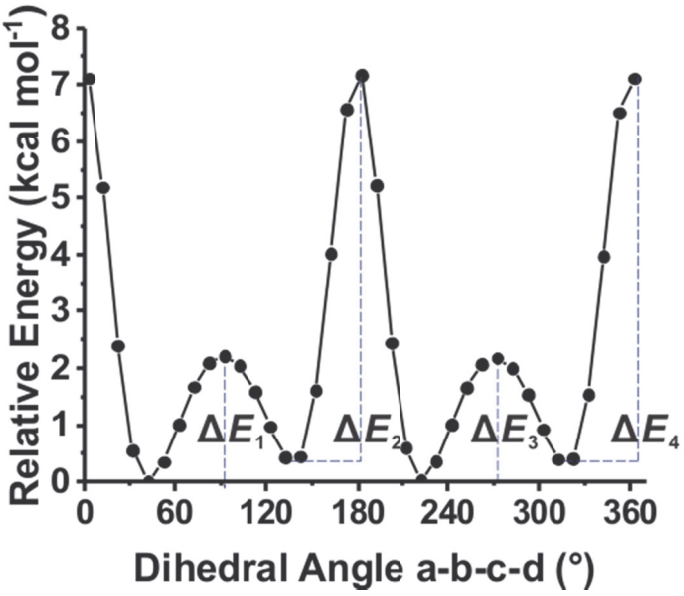

Figure 4.12 Graphical representation of the relative energy conformations of **4** as a function of the dihedral angle a-b-c-d (shown in Figure 4.10 B).

Factors other than aggregation can restrict intermolecular motions and turn on the fluorescence of AIE-active molecules. It has been reported in the literature that AIE active molecules can fluoresce due to the formation of complexes[41,42,43,44] and oligomers[45] without causing aggregation. Hence, we decided to utilize AIE active **37** and take advantage of the known interaction between pyrazoles and dicarboxylic acids.[46,47] The hope was that **37** could function as a fluorescent sensor for dicarboxylic acids. We began this study by testing the fluorescence response of **37** toward different carboxylic acids (Figure 4.13).

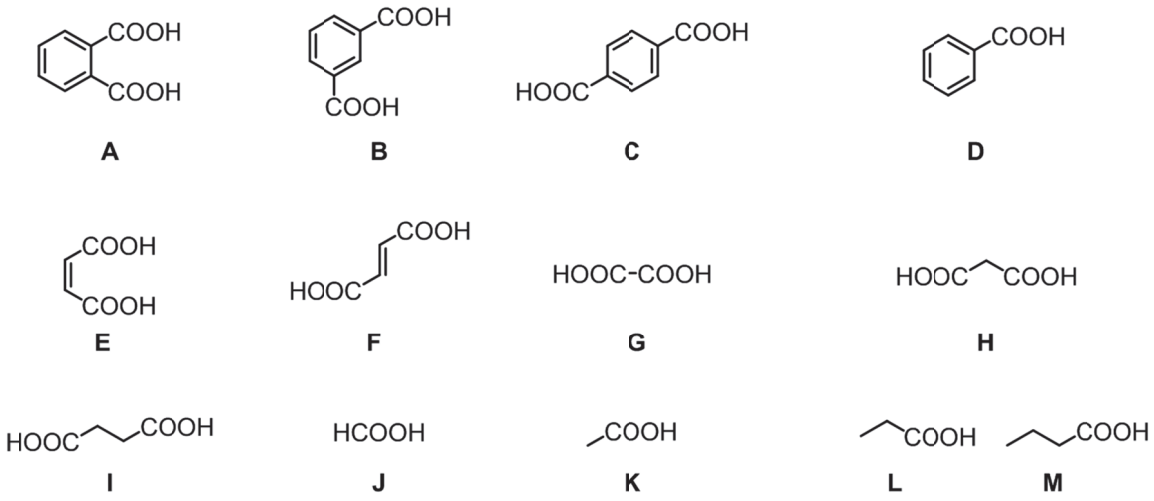

Figure 4.13 Chemical structures of the carboxylic acids used in this study.

The emission and absorption spectral responses of **37** to **A** were tested first (Figure 4.14 A, B, and Table 4.3). The addition of **A** (up to 3 eq) into a solution of **37** resulted in a decrease of the relative integrated emission intensity (I/I_0) to 0.68 with λ_{ems} shifting from 438 to 440 nm. However, with the further addition of **7** (3–12 eq), the integrated emission intensity increased to 4.40 displaying a significant bathochromic shift of λ_{ems} to 490 nm. A visible turn ON aquamarine fluorescence was also observed (Figure

4.15 A). Further addition of **7** (up to 48 eq), resulted in a decrease in the fluorescence intensity to 1.5 (Figure 4.15 B) along with a hypochromic shift of λ_{ems} to 484 nm. The change in the emission intensity and λ_{ems} indicated that the excited state decay was influenced by the addition of **A**. As for absorption spectra, the representative peak of **37** (λ_{abs} = 323 nm) continued to appear at 323 or 324 nm after the addition of **A**, indicating that the conjugation the system of was minimally influenced by **A**. The peaks that appeared around 284 and 292 nm were the signals from **A**, and as was expected their intensity increased with the addition of **A**. The leveling off of the tails in the long wavelength side of the absorption spectra was not observed during the addition of **A**, suggesting that no aggregation occurred.

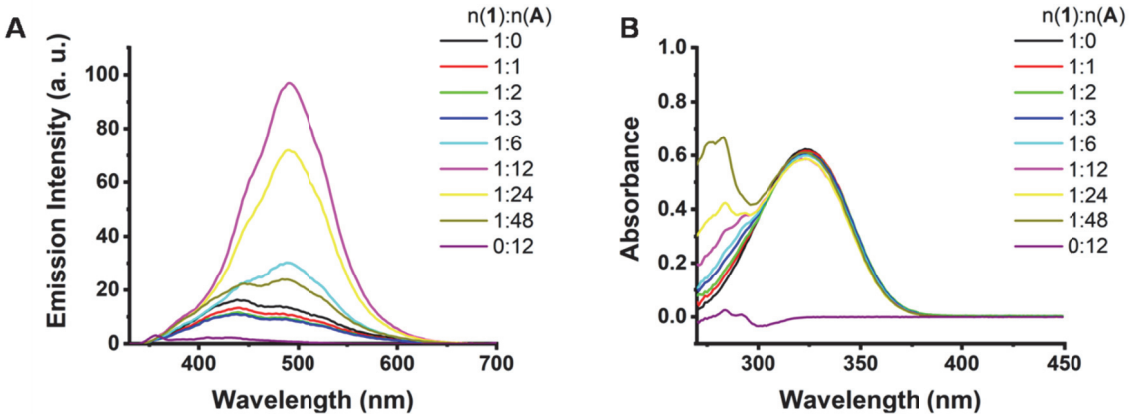

Figure 4.14 Graphical representation of the (A) emission spectra and (B) absorption spectra of **37** with different equivalents of **A** in DMF.

fw(%)	λems (nm)	λabs (nm)	I/I_0
0	439	323	1.00
1	440	323	0.82
2	440	324	0.71

3	438	324	0.68
6	489	324	1.63
12	490	324	4.40
24	490	323	3.39
48	484	323	1.50

Table 4.3 Emission and absorption spectral data of **37** (10 μM) in DMF with different equivalents of **7.**

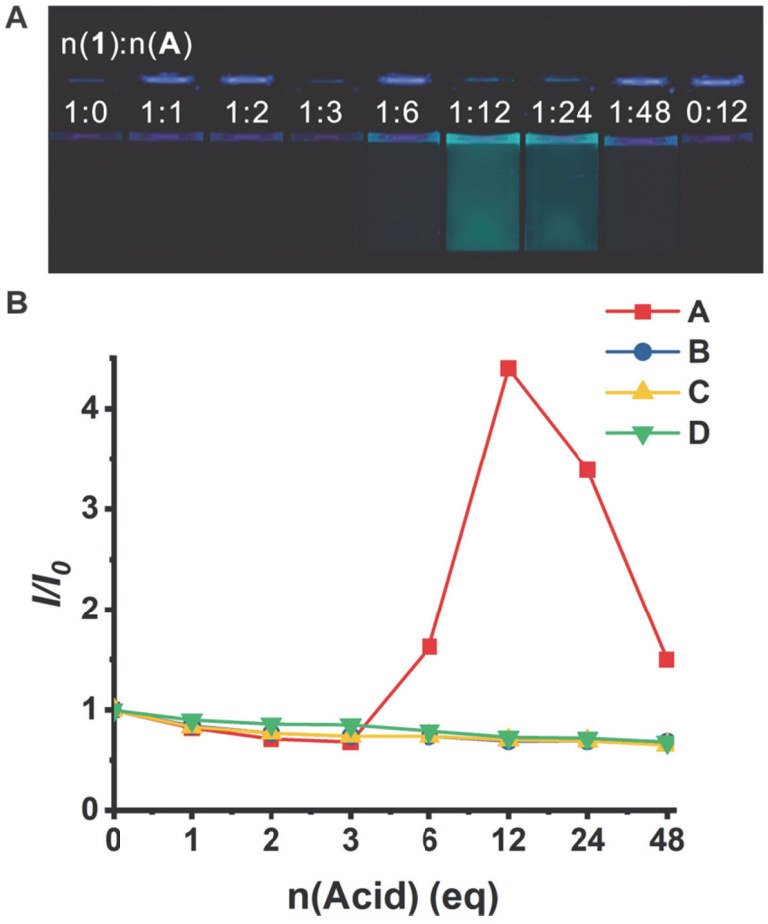

Figure 4.15 (A) Fluorescence photograph under UV irradiation (λ_{exc} = 365 nm) of **37** (10 μM, 1eq) with different equivalents of **A** in DMF. (B) Graphical representation of the

relationship between the relative emission intensity and the acid amount for **A**–**D**, where *I* is the integrated emission intensity ranging from 330 to 700 nm.

Due to the response of **A**, other aromatic isomers **B** and **C** along with carboxylic acid **D** were tested. The relative integrated emission intensity continuously decreased with the increased addition of these compounds from ranging from 0 to 48 equivalents. (Table 4.4). No significant bathochromic or hypochromic shift in the λ_{ems} was observed for these compounds. The question then arises why does **A** turn on the fluorescence of **37** while structurally similar compounds **B**, **C**, and **D** do not?

	Compound B			**Compound C**			**Compound D**		
fw(%)	λ_{ems}	λ_{abs}	I/I_0	λ_{ems}	λ_{abs}	I/I_0	λ_{ems}	λ_{abs}	I/I_0
0	439	323	1.00	439	323	1.00	439	323	1.00
1	440	323	0.84	439	325	0.84	439	325	0.90
2	440	324	0.77	442	323	0.77	440	325	0.86
3	438	324	0.74	445	325	0.74	443	324	0.85
6	489	324	0.74	440	324	0.74	439	323	0.79
12	441	324	0.69	434	324	0.69	442	325	0.73
24	441	323	0.69	437	324	0.69	438	325	0.72
48	439	323	0.68	435	324	0.68	437	324	0.68

Table 4.4 Emission and absorption spectral data of **37** (10 μM) in DMF with different equivalents of **B**, **C**, and **D** (each mixed separately with **37**).

NMR studies were then conducted to further study the interactions between each of the aromatic carboxylic acids and **37**. The ^{1}H NMR spectrum showed that the protons H_a and H_b of the pyrazole endgroups in **37** (which appeared at 8.40 and 8.04 ppm in DMSO-d_6) started to merge into one signal at 8.22 ppm when 2–3 eq of **A**–**C** or 6 eq of **D** were added (Figure 4.16B). These results implied that protonation of the pyrazole nitrogens of **37** occurred. This is consistent with the lower pK_{a1} values of **A**–**C** (2.9, 3.7, and 3.5, respectively) and the higher pK_a value of monoacid **D** (4.2).[48]

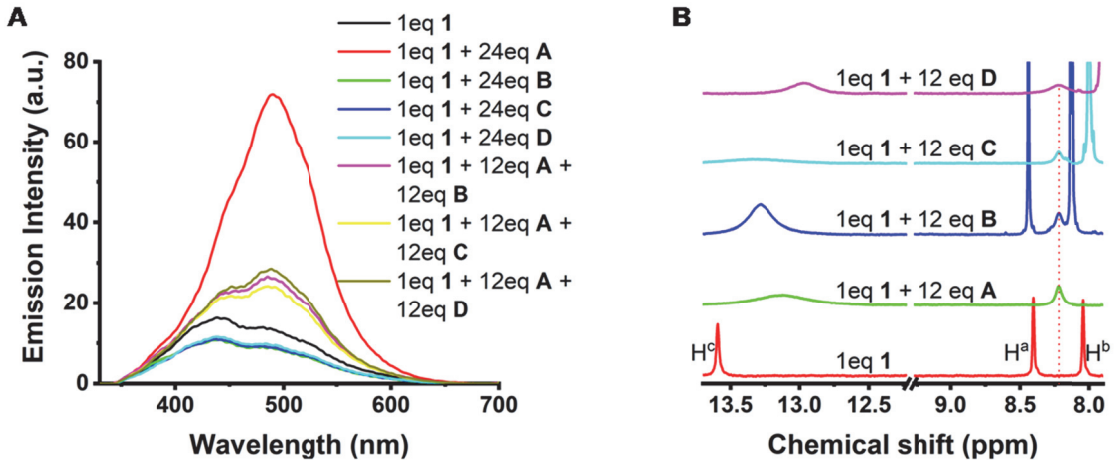

Figure 4.16 (A) Emission spectra of **37** (10 μM, 1 eq) mixed with 24 eq of one or two aromatic acids. (B) The influence of 12 eq of an aromatic acid on the ^{1}H NMR of **37** in DMSO-d_6.

The next course of action was to determine if **37** can recognize **A** in a mixture with **B**, **C**, or **D**. This was accomplished by the addition 12 eq of **A** and 12 eq of **B**, **C**, or **D** into a DMF solution of **37**. The results (Figure 4.16A) revealed that the fluorescence response of **37** increased to 1.56, 1.46, and 1.62 with the λ_{ems} shifting bathochromically to 486–489 nm for the mixture of **A** with **B**, **C**, and **D**, respectively. However, if only 24 eq

of **B**, **C**, or **D** were added to the **37** solution in DMF, the fluorescence was quenched and the λ_{ems} change was negligible. Notably the relative integrated emission values of the samples with the mixture of **A** and another aromatic acid were significantly smaller than that of the sample with 24 eq of **A** alone (I/I_0 = 3.39), this could be indicative of a competition occurring between **A** and the other aromatic acids, as all the acids were capable of protonating **37** (Figure 4.16B). The result also provides further corroboration that fluorescence response was not only due to the existence of a protonated **37** species. Even though the fluorescence intensity only increased to a smaller degree in the mixture of acids, the existence of **A** still can be determined, due to the increase of the integrated emission values and the red shift of λ_{ems}. Accordingly, **37** can successfully recognize **A** selectively in a mixture with its respective isomers.

Based on the models of the single crystal structure of **37** and optimized complexes between **37** and **A** conducted by our collaborator Dr. Chia-Hua Wu.[49] It is believed that in the solution state *J*- and *H*-stacking dimers along with other complexes exist. Based on this a possible mechanism for the turn ON fluorescence of **37** with the addition of **A** was proposed (Scheme 4.1). According to this mechanism, the initial addition of **A** (0–3 eq) caused the formation of a flexible non-emissive complex **3;** coupled with the simultaneous decomposition *H*- or *J*-stacking dimers yielding complex **2** resulted in the quenching of the fluorescence. An increase in the amount of **A** from 3 to 12 eq can lead to the formation of more complexes **3**, **4**, and **5**, which causes the fluorescence of this system to turn ON, due to the presence of rigid complexes **4** and **5** that restrict the intramolecular rotation of **37**. Further increasing the amount of **A** (12–48 eq), resulted in

each pyrazolium group of **37** complexing with its own dicarboxylate, thereby decomposing the rotation-restricted complexes **4** and **5** into flexible **6–8**, decreasing the fluorescence intensity of the system.

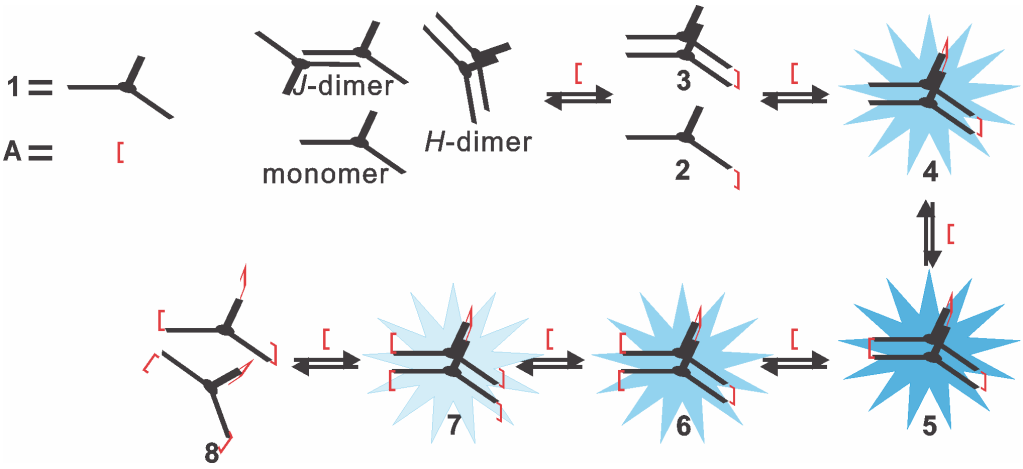

Scheme 4.1 Proposed mechanism that explains the turn ON and OFF fluorescence of **37** upon exposure to **A**.

The decisive steps in this mechanism are the formation of fluorescent complexes such as **4** and **5**. Consequently, if this mechanism is rational, maleic acid (**E**) that possesses two carboxyl groups in the *cis*-form (sterically similar to **A**), should exert a similar influence over the turn ON fluorescence of **37**. To test this hypothesis, the emission spectra of **37** (1 eq) with 12 eq of **E** or its *trans*-isomer **F** were collected. The addition of **E** produced a visible turn ON of aquamarine fluorescence (Figure 4.17A and B) with an integrated emission value of 5.77 and a bathochromic shift of λ_{ems} to 493 nm. The addition of **F** on the other hand quenched the fluorescence, resulting in a relative integrated emission value of 0.71, along with minimal change in the λ_{ems}. *Cis*-isomer **E** caused the two molecules of **37** to stack together, thereby restricting the intramolecular

rotation and turning on the fluorescence. The *trans*-isomer **F** however, could not form such stacks, resulting in flexible complexes with **37** that were capable of rotation, effectively quenching the fluorescence.

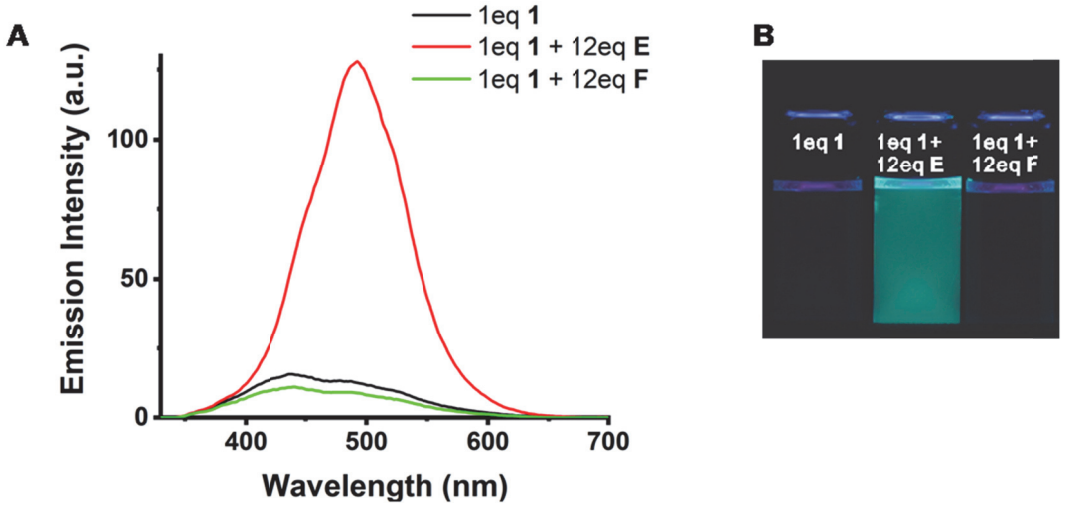

Figure 4.17 (A) Emission spectra (λ_{exc} = 320 nm) of **37** (10 μM, 1eq.) mixed 12 eq. of **E** or **F**. (B) Fluorescence photograph under UV irradiation (λ_{exc} = 365 nm) of **37** (10 μM, 1eq.) with 12 eq of **E** or **F** in DMF.

Aliphatic carboxylic acids were also tested to see if they could induce a fluorescent response from **37**. These aliphatic acids should form complexes and bring two molecules of **37** together and restrict the rotation of this complex. Initially, monoacids **J**–**M** of varying lengths were tested. These acids quenched the fluorescence of **37**. These results were expected as earlier testing with **D** indicated that a monoacid could not induce a fluorescence response. Thus monoacids **J**–**M** of varying length provided further corroboration of that notion. Next aliphatic diacids **G**–**I** were tested. The emission spectra of **37** mixed with 12 eq. of these diacids showed a fluorescent response and a decrease in the fluorescence intensity that correlated to the distance between the COOH groups

(Figure 4.18A and B). The relative integrated emission values these diacids displayed were 2.12, 1.13, and 0.70, respectively. The addition of **G**—the shortest among the aliphatic diacids—also caused a bathochromic shift of λ_{ems} to 489 nm. This observation was consistent with the fluorescent species proposed in the mechanism (Scheme 4.1), as the shorter distance between the two molecules of **37**, controlled by the separation between the COOH groups of aliphatic dicarboxylic acid, restricted the intramolecular rotation more effectively and produced a stronger turning ON of the fluorescence.

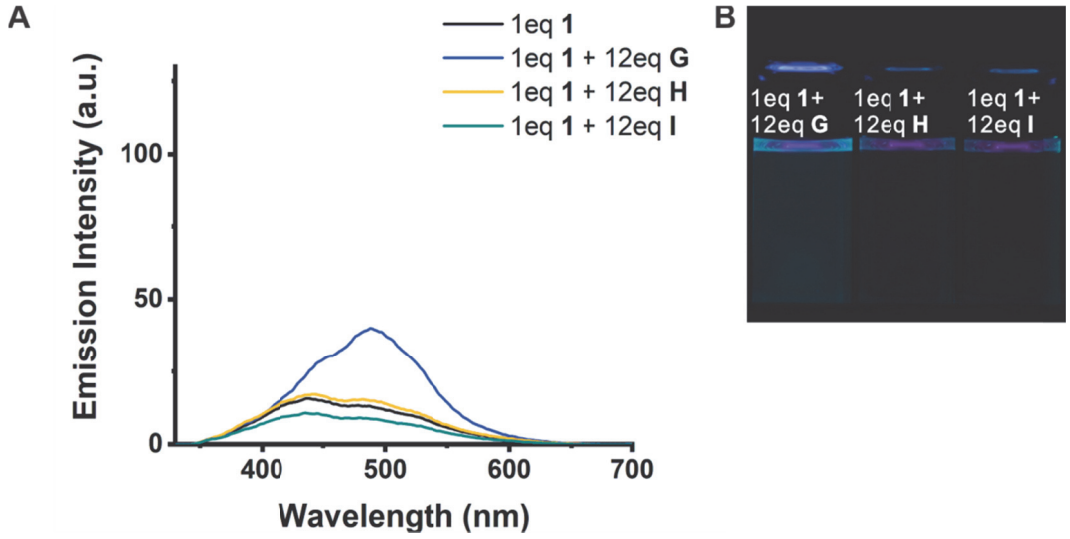

Figure 4.18 (A) Emission spectra (λ_{exc} = 320 nm) of **37** (10 μM, 1eq.) mixed 12 eq. of **G**, **H**, or **I**. (B) Fluorescence photograph under UV irradiation (λ_{exc} = 365 nm) of **37** (10 μM, 1eq.) with 12 eq. of **G**, **H**, or **I** in DMF.

4.4 Conclusions and Outlook

In conclusion, our research of the fluorescent properties of the isostructural **37** and **4** allowed the discovery of an unexpected difference in the aggregation-induced emission between these two molecules. This difference was caused by a subtle influence of the steric bulk on the central ring of these molecules, which restricted the intramolecular rotation in one precursor, while allowing it in the other. Overall, each structural element of the **37** and **4** plays a functional role, illustrating the subtlety of supramolecular chemistry. The fluorescent properties displayed by **37** caused us to speculate if it could be used as a fluorescent sensor. This thought led to the discovery that **37** can selectively differentiate between dicarboxylic acids with closely positioned COOH groups (including **A** and **E**) from their isomers. It is believed that two molecules of **37** are held together by the dicarboxylic acids and is likely the cause of the turn ON fluorescence behavior observed.

References

1. Carr, J. A.; Franke, D.; Caram, J. R.; Perkinson, C. F.; Saif, M.; Askoxylakis, V.; Datta, M.; Fukumura, D.; Jain, R. K.; Bawendi, M. G.; Bruns, O. T. *Proc. Natl. Acad. Sci.* **2018**, *115*, 4465–4470.
2. Poß, M.; Eva, Z.; Anna, M.; Ute, S.; Claus, F. *Bioconjugate Chem.* **2018**, *29*, 2818−2828.
3. Bhargava, S.; Chu, J. J. H.; Valiyaveettil, S. *ACS Omega* **2018**, *3*, 7663−7672.
4. Zhang, H.; Zhang, G.; Xu, J.; Wen, Y.; Ming, S.; Zhang, J.; Ding, W. *Spectrochim. Acta A* **2018**, *191*, 79–87.
5. Bao, X.; Cao, Q.; Wu, X.; Shu, H.; Zhou, B.; Geng, Y.; Zhu, J. *Tetrahedron Lett.* **2016**, 57, 942−948.
6. Bao, X.; Cao, X.; Nie, X.; Xu, Y.; Guo, W.; Zhou, B.; Zhang, L.; Liao, H.; Pang, T. *Sens. Actuator B, Chem.* **2015**, *208*, 54–66.
7. Arqueros, F.; Hörandel, J. R.; Keilhauer, B. *Nucl. Instr. Meth. Phys. Res. A* **2008**, *597*, 23–31.
8. Mullen, K.; Scherf, U. *Organic Light-Emitting Devices. Synthesis Properties and Applications*, Wiley-VCH, Weinheim, **2006**.
9. Mei, J.; Leung, N. L. C.; Kwok, R. T. K.; Lam, J. W. Y.; Tang, B. Z. *Chem. Rev.* **2015**, *115*, 11718–11940.
10. Wang, K.; Shi, Y.-Z.; Zheng, C.-J.; Liu, W.; Liang, K.; Li, X.; Zhang, M.; Lin, H.; Tao, S.-L.; Lee, C.-S.; Ou, X.-M.; Zhang, X.-H. *ACS Appl. Mater. Interfaces* **2018**, *10*, 31515−31525.

11. Zhao, Z.; Mhibik, O.; Leang, T.; Forget, S.; Chenais, S. *Opt. Express* **2014**, *22*, doi:10.1364/oe.22.030092.

12. Samuel, I. D. W.; Turnbull, G. A. *Chem. Rev.* **2007**, *107*, 1272−1295.

13. Birks, J. B. *Photophysics of Aromatic Molecules*, Wiley-Interscience, London, **1970**.

14. Hecht, S.; Fréchet, J. M. J. *Angew. Chem. Int. Ed.* **2001**, *40*, 74–91.

15. Wang, J.; Zhao, Y.; Dou, C.; Sun, H.; Xu, P.; Ye, K.; Zhang, J.; Jiang, S.; Li, F.; Wang, Y. *J. Phys. Chem. B* **2007**, *111*, 5082–5089.

16. Wakamiya, A.; Mori, K.; Yamaguchi, S. *Angew. Chem., Int. Ed.* **2007**, *46*, 4273–4276.

17. Shimzu, M.; Takeda, Y.; Higashi, M.; Hiyama, T. *Angew. Chem., Int. Ed.* **2009**, *48*, 3653–3656.

18. Tian, W.; Zhang, J.; Yu, J.; Wu, J.; Nawaz, H.; Zhang, J.; He, J.; Wang, F. *Adv. Optical Mater.* **2016**, *4*, 2044–2050.

19. Mei, J.; Hong, Y.; Lam, J. W. Y.; Qin, A.; Tang, Y.; Tang, B. Z. *Adv. Mater.* **2014**, *26*, 5429–5479.

20. Luo, J.; Xie, Z.; Lam, J. W. Y.; Cheng, L.; Chen, H.; Qiu, C.; Kwok, H. S.; Zhan, X.; Liu, Y.; Zhu, D.; Tang, B. Z. *Chem. Commun.* **2001**, 1740–1741.

21. Chen, J.; Law, C. C. W.; Lam, J. W. Y.; Dong, Y.; Lo, S. M. F.; Williams, I. D.; Zhu, D.; Tang, B. Z. *Chem. Mater.* **2003**, *15*, 1535−1546.

22. Zhang, G.-F.; Chen, Z.-Q.; Aldred, M. P.; Hu, Z.; Chen, T.; Huang, Z.; Meng, X.; Zhu, M.-Q. *Chem. Commun*. **2014**, *50*, 12058−12060.

23. Li, D; Liu, J.; Kwok, R. T. K.; Liang, Z.; Tang, B. Z.; Yu, J. *Chem. Commun.* **2012**, *48*, 7167–7169.

24. Li, Y.; Kwok, R. T. K.; Tang, B. Z.; Liu, B. *RSC Adv.* **2013**, *3*, 10135−10138.

25. Leung, N. L. C.; Xie, N.; Yuan, W.; Liu, Y.; Wu, Q.; Peng, Q.; Miao, Q.; Lam, J. W. Y.; Tang, B. Z. *Chem. Eur. J.* **2014**, *20*, 15349–15353.

26. Liu, Z.; Bo, Z.; Dong, Y. Q.; Tang, B. Z. *Chem. Commun.* **2012**, *48*, 10675–10677.

27. An, B.; Kwon, S.; Jung, S.; Park, S. Y. *J. Am. Chem. Soc.* **2002**, *124*, 14410–14415.

28. Hu, R.; Lager, E.; Aguilar-Aguilar, A.; Liu, J.; Lam, J. W. Y.; Sung, H. H. Y.; Williams, I. D.; Zhong, Y.; Wong, K. S.; Penã-Cabrera, E.; Tang, B. Z. *J. Phys. Chem. C* **2009**, *113*, 15845–15853.

29. Gao, B.; Wang, H.; Hao, Y.; Fu, L.; Fang, H.; Jiang, Y.; Wang, L.; Chen, Q.; Xia, H.; Pang, L.; Ma, Y.; Sun, H. *J. Phys. Chem. B* **2010**, *114*, 128–134.

30. Shigemitsu, Y.; Mutai, T.; Houjou, H.; Araki, K. *J. Phys. Chem. A* **2012**, *116*, 12041–12048.

31. Yu, Z.; Duan, Y.; Cheng, L.; Han, Z.; Zheng, Z.; Zhou, H.; Wu, J.; Tian, Y. *J. Mater. Chem.* **2012**, *22*, 16927–16932.

32. Qian, H.; Cousins, M. E.; Horak, E. H.; Wakefield, A.; Liptak, M. D.; Aprahamian, I. *Nat. Chem.* **2017**, *9*, 83–87

33. Fan, X.; Sun, J.; Wang, F.; Chu, Z.; Wang, P.; Dong, Y.; Hu, R.; Tang, B. Z.; Zou, D. *Chem. Commun.* **2008**, 2989–2991.

34. Li, Z.; Dong, Y.; Mi, B.; Tang, Y.; Haussler, M.; Tong, H.; Dong, Y.; Lam, J. W. Y.; Ren, Y.; Sung, H. H. Y.; Wong, K. S.; Gao, P.; Williams, I. D.; Kwok, H. S.; Tang, B. Z. *J. Phys. Chem. B* **2005**, *109*, 10061–10066.

35. Dalapati, S.; Gu, C.; Jiang, D. *Small* **2016**, *12*, 6513–6527.

36. Zhang, Z.; Hashim, M. I.; Miljanić, O. Š. *Chem. Commun.* **2017**, *53*, 10022–10025.

37. Chen, Z.; Zhang, J.; Song, M.; Yin, J.; Yu, G.; Liu, S. H. *Chem. Commun.* **2015**, *51*, 326–329.

38. Xu, B.; He, J.; Dong, Y.; Chen, F.; Yu, W.; Tian, W. *Chem. Commun.* **2011**, *47*, 6602–6604.

39. Yang, Y.; Su, X.; Carroll, C. N.; Aprahamian, I. *Chem. Sci.* **2012**, *3*, 610–613.

40. Dincă, M.; Dailly, A.; Tsay, C.; Long, J. R. *Inorg. Chem.* **2008**, *47*, 11‑13.

41. Sinha, N.; Stegemann, L.; Tan, T. T. Y.; Doltsinis, N. L.; Strassert, C. A.; Hahn, F. E. *Angew. Chem. Int. Ed.* **2017**, *56*, 2785–2789.

42. Yan, X.; Cook, T. R.; Wang, P.; Huang, F.; Stang, P. J. *Nat. Chem.* **2015**, *7*, 342–348.

43. Noguchi, T.; Roy, B.; Yoshihara, D.; Tsuchiya, Y.; Yamamoto, T.; Shinkai, S. *Chem. Eur. J.* **2014**, *20*, 381–384.

44. Zhao, J.; Yang, D.; Zhao, Y.; Yang, X.-J.; Wang, Y.-Y.; Wu, B. *Angew. Chem. Int. Ed.* **2014**, *53*, 6632–6636.

45. Liu, Y.; Deng, C.; Tang, L.; Qin, A.; Hu, R.; Sun, J. Z.; Tang, B. Z. *J. Am. Chem. Soc.* **2011**, *133*, 660–663.

46. López, C.; Claramunt, R. M.; García, M. Á.; Pinilla, E.; Torres, M. R.; Alkorta, I.; Elguero, J. *Cryst. Growth Des.* **2007**, *7*, 1176–1184.

47. Basu, T.; Sparkes, H. A.; Mondal, R. *Cryst. Growth Des.* **2009**, *9*, 5164–5175.

48. Rumble, J. R. *CRC Handbook of Chemistry and Physics*, CRC Press/Taylor & Francis, Boca Raton, FL, 98th Ed., Internet Version **2018**.